Demolding of Hot Embossed Polymer Microstructures

By

Matthew E. Dirckx

S.M. Mechanical Engineering, Massachusetts Institute of Technology, 2005
B.S. Mechanical Engineering, University of Oklahoma, 2003

Submitted to the Department of Mechanical Engineering
in Partial Fulfillment of the Requirements for the Degree of

Doctor of Philosophy in Mechanical Engineering

at the

Massachusetts Institute of Technology

June 2010

Signature of Author . . . .
Department of Mechanical Engineering
May 19, 2010

Certified by . . . .
David E. Hardt
Ralph E. and Eloise F. Cross Professor of Mechanical Engineering
Thesis Supervisor and Committee Chair

Accepted by . . . .
David E. Hardt
Chairman, Department Committee on Graduate Students

Demolding of Hot Embossed Polymer Microstructures
by
Matthew E. Dirckx

Submitted to the Department of Mechanical Engineering on May 19, 2010
in Partial Fulfillment of the Requirements for the Degree of
Doctor of Philosophy in Mechanical Engineering

ABSTRACT

Polymer-based microfluidic "lab on a chip" technology promises to reduce cost and extend access to medical diagnostic tests that formerly required expensive and labor-intensive lab work. The predominant methods for manufacturing these devices are miniaturized molding processes including casting, injection molding, and hot embossing. These techniques have in common the use of a mold to define the shape of functional features (fluidic channels), the separation of the part from the mold as a process step (demolding), and the intended re-use of the mold to produce additional parts. The demolding step in particular poses significant challenges for mass production. Demolding affects several issues including production rate, part quality, and mold lifetime, and demolding-related defects are frequently observed. Despite its importance, there has been no comprehensive effort to analyze demolding theoretically or experimentally.

This thesis aims to deepen the understanding of demolding of polymer microstructures in order to facilitate mass manufacturing of polymer-based devices with micro-scale functional features, such as microfluidic chips. A theory of demolding mechanics has been proposed that combines the effects of thermal stress, friction, and adhesion in a unified framework. A metric by which demolding can be characterized experimentally—the demolding work—has been proposed by analogy with interfacial fracture and has been related to underlying physical mechanisms. Finite element simulations based on this theory of demolding have been performed to investigate the effects of important parameters, including demolding temperature and feature geometry. A test method for characterizing demolding by directly measuring the demolding work for individual microstructures has been developed and applied to hot embossing to study the effects of process parameters such as demolding temperature, the effects of feature geometry and layout, and the impacts of mitigation strategies such as low-adhesion mold coatings.

The results of these demolding experiments broadly agree with expected trends based on the theory of demolding mechanics proposed herein. A dimensionless parameter aggregating the effects of feature geometry and layout has been identified and related to the occurrence of demolding-related defects, the demolding process window, and the demolding temperature that minimizes the demolding work. These findings have been generalized to provide processing and design guidance for industrial application of polymer micro-molding.

Thesis supervisor: David E. Hardt

Title: Ralph E. & Eloise F. Cross Professor of Mechanical Engineering

Acknowledgements

First, I wish to thank my parents for their love and guidance. With their unending support and encouragement, and by their example, I have gone far.

I would like to thank my advisor, Dave Hardt, for his thoughtful mentorship, and my thesis committee, Lallit Anand, Duane Boning, and Todd Thorsen, for their insight and advice.

I would also like to thank all of my friends and colleagues at MIT for their help and companionship.

Finally, I would like to thank the Singapore-MIT alliance for funding this work and making my studies at MIT possible.

Table of contents

List of figures

11

12

13

15

16

1 Introduction

This thesis presents a study of demolding of hot embossed polymer microstructures—such as microfluidic channels—including a theory of demolding mechanics, finite element simulations of demolding, a demolding test method, and the results of demolding experiments. This work is motivated by the goal of improving the understanding of demolding to facilitate high-volume manufacturing of polymer-based micro-devices such as microfluidic chips at high quality and low cost, and so the findings are generalized to provide demolding guidelines and design rules for industrial application.

1.1 Contributions of this thesis

This thesis presents a number of new contributions to the understanding of demolding in the field of polymer microfabrication.

A theory of demolding mechanics is presented, which relates the energy dissipated during demolding to specific mechanisms, namely adhesion, friction, and thermal stress. This theory of demolding is used to make testable predictions, including the existence of an optimal demolding temperature. A metric by which demolding can be characterized experimentally—the demolding work and demolding toughness—is proposed and related to physical mechanisms. Finite element simulations encapsulating this theory of demolding have been performed and used to investigate the effects of parameters such as the friction coefficient, adhesion strength, and feature geometry.

A test method for characterizing demolding by directly measuring the demolding work for individual microstructures has been developed and evaluated. This method is adapted from the well-established cantilever fracture test. Test equipment, including temperature-controlled platens and demolding fixtures have been designed and fabricated. Test molds have been designed and produced to study specific effects of feature geometry, including feature height, width, and spacing. The test method has been evaluated with respect to the repeatability of the measured demolding work and found to be useful for studying demolding of polymer microstructures.

This test method has been used to study the effects of demolding temperature and feature geometry experimentally, and these results have been found to be consistent with the finite element simulations and the predictions of the theory of demolding developed here, including the existence of an optimal demolding temperature.

The demolding process window has been identified, along with the physical mechanisms that define its boundaries. For a given pattern, the lower limit on demolding temperature is set by local distortion of features caused by thermal stress. The upper limit of the demolding window is set by the degradation of adhesion between the part and the mold. The demolding window is influenced by the pattern geometry. A geometric parameter has been derived from the demolding theory, and is related to the demolding process window and the optimal demolding temperature.

The development of a reliable demolding test method has enabled mitigation strategies, such as mold surface coatings and feature edge treatments, to be evaluated. The effect of these treatments on the demolding work has been tested.

These theoretical and experimental findings have been generalized to develop demolding guidelines and design rules for industrial applications, such as manufacturing microfluidic chips.

1.2 Microfluidics

As defined by one of the field's early pioneers, microfluidics is the "science and technology of systems that process or manipulate small…amounts of fluids, using channels with dimensions of tens to hundreds of micrometers," [1]. Various terms for microfluidic devices, such as "Lab on a Chip" or "Micro Total Analysis Systems" encapsulate the aspiration of the field to miniaturize and integrate a large number of chemical or biochemical processes onto a single, small device. Such devices may be designed for massively parallel experiments on protein crystallization [2], low-cost, automated medical diagnostics [3], or any of an endless variety of other applications, as can be seen from the table of contents of any issue of journals like *Lab on a Chip* and *Microfluidics and Nanofluidics*.

Microfluidics as a concept was partly inspired by the miniaturization and integration that characterized the microelectronics industry [4, 5], and many of the earliest microfluidic devices were produced using similar processes in glass and silicon [6]. The high cost of these materials and processes, among other factors, has led to a shift to polymer materials, especially the thermosetting elastomer polydimethylsiloxane (PDMS), and transparent amorphous

thermoplastics such as polymethyl methacrylate (PMMA), polycarbonate (PC), polystyrene (PS), and cyclo-olefin polymers (COP) [7-10]. In addition to their low material cost, transparency, and biocompatibility, a key advantage of polymer materials for microfluidics is their ability to be manufactured using high-volume and low-cost replication or molding processes, such as casting [11], injection molding [12-15], and hot embossing [16-21].

1.3 Hot embossing

Hot embossing in particular is a very promising process for manufacturing microfluidic devices. In this process, a thin polymer workpiece is first heated above the material's glass transition temperature (T_g). A heated mold with the inverse of the desired feature pattern (e.g. ridges and posts where channels and wells are desired in the final part) is pressed into the part, and the pressure is maintained over sufficient time for the material to deform around and replicate the mold features. The embossing pressure is maintained while the part and mold are cooled to the demolding temperature, whereupon the part is separated from the mold. The trajectories of temperature and force over time in hot embossing are illustrated in Figure 1.1.
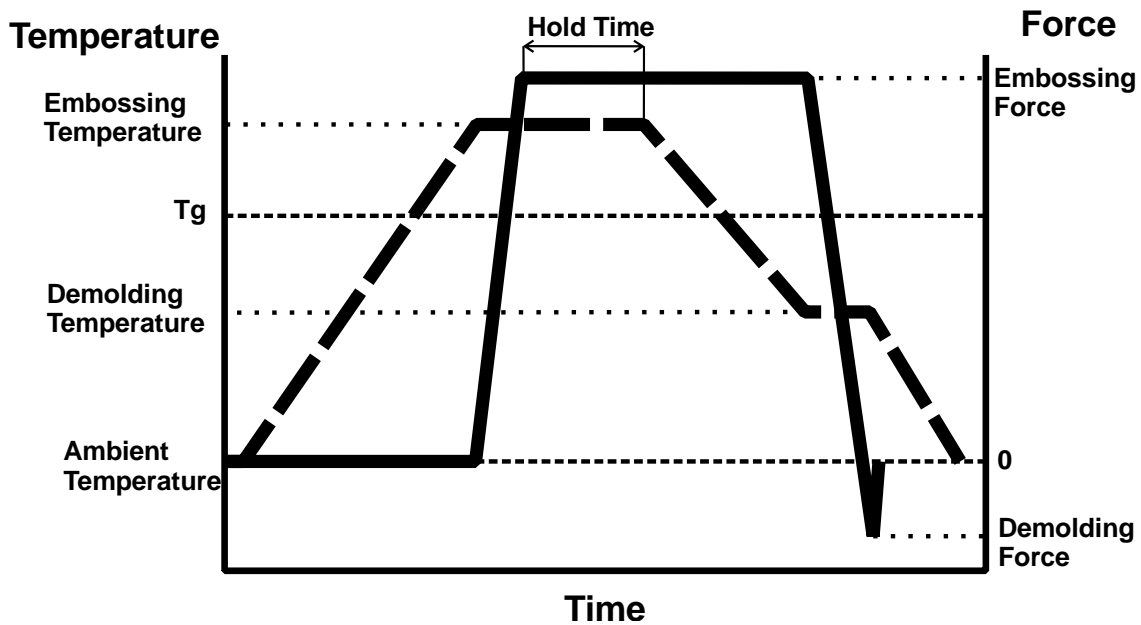
Figure 1.1 Temperature and force trajectory in HME.

Casting, especially of PDMS, is the predominant process used in prototyping microfluidic devices and low-volume production for research [22]. This process is not well-suited for high-volume manufacturing, mainly because of long cycle times (several minutes to

several hours), a labor intensive multi-step processing protocol (mixing polymer precursors, degassing, casting, and curing), and a lack of equipment or automation [23], although recent efforts have been made to address these issues [24, 25]. In contrast, injection molding is a well-established high-volume manufacturing process, but it has high initial costs associated with mold design and fabrication, so this process not well suited for prototyping or low-volume production [22, 26].

Hot embossing is uniquely able to bridge this gap between low- and high-volume manufacturing of microfluidic devices. Compared with casting, hot embossing has higher initial costs associated with purchasing (or fabricating) the required equipment and producing molds, but embossing has drastically shorter cycle times than casting [23] and only two process steps (blank production and embossing). Because embossing equipment is inherently flexible, initial costs (other than molds) can be spread over a large number of different prototypes. Embossing equipment can also be used for downstream processes such as input/output port punching [27] and thermal bonding [28]. While embossing molds are subject to greater loads than molds used in casting, prototype embossing molds can be made using many of the same techniques as molds for casting, so these costs need not be markedly different [29].

Compared with injection molding, hot embossing has much simpler and less expensive equipment. This difference is related to both the lower temperatures (T_g vs. melting) and pressures (~few MPa vs. tens to hundreds of MPa) required in embossing. Embossing requires only heated, aligned platens and a means of applying sufficient pressure, compared with the inherent complexity of injection molding machines [26]. Hot embossing has somewhat longer cycle times (typically 1-10 minutes vs. 10-100 seconds for injection molding) [23], and production-ready embossing machines are still expensive (though less so than injection molding machines) and not widely available. Hot embossing also does not benefit from a well-developed manufacturing science foundation compared with injection molding, which has been more intensively studied [30]. Because of these limitations, injection molding is more likely to be adopted for very-high volume manufacturing ($>10^5$ parts), with hot embossing filling the niche in low- to medium-high-volume manufacturing [31]. At the same time, it is worth noting ongoing efforts in the research community to reduce embossing cycle times [32, 33], reduce equipment complexity and cost [34], and develop production-ready, automated embossing systems [35, 36], which aim to make hot embossing more competitive with injection molding.

1.4 Demolding of polymer microstructures

All of the molding processes that may be used to produce microfluidic chips and other polymer-based devices with micro-scale features have in common the use of a mold, and thus the need to separate the part from the mold at the end of the process. Demolding is a critical step in these processes, since any distortion or damage of the part during demolding can result in degraded quality or even render the part useless, regardless of how well the part was originally formed.

1.4.1 Demolding-related defects

Several researchers have observed demolding-related defects including broken or distorted features in hot embossing [37-42], injection molding of microfeatures [43, 44], and PDMS casting [45]. Demolding-related defects have also been observed in the related process of nanoimprint lithography (NIL) [46, 47], in which a thin layer (a few micrometers thick or less) of polymer is spin-cast onto a silicon wafer and embossed to define features that serve as a mask layer for subsequent etching [48].

In hot embossing, a very commonly observed defect is a bulge on one side of a feature, as shown in Figure 1.2. These defects are widely attributed to thermal stress associated with differential thermal contraction of the part and mold during cooling [37, 39, 40, 42].

Similar defects have been observed in injection molding of micro-features, as in Figure 1.3. These bulges are problematic in microfluidic devices because they can prevent cover-plates from sealing channels.

Other defects commonly observed are broken mold features, as in Figure 1.4, which can render a mold unusable. Parts can also fail in demolding, potentially leaving material behind on the mold, as in Figure 1.5, which can also make a mold unusable. Mold failures such as these can be particularly costly, since the mold must be replaced.

(a)

Bulge defect

10 µm deep, 300 µm wide hexagon feature

2.3kV   X430   50µm   19 48 SEI

(b)

Bulge defects

Acc.V Spot Magn Det WD   50 µm
5.00 kV 2.0 650x   SE 26.0
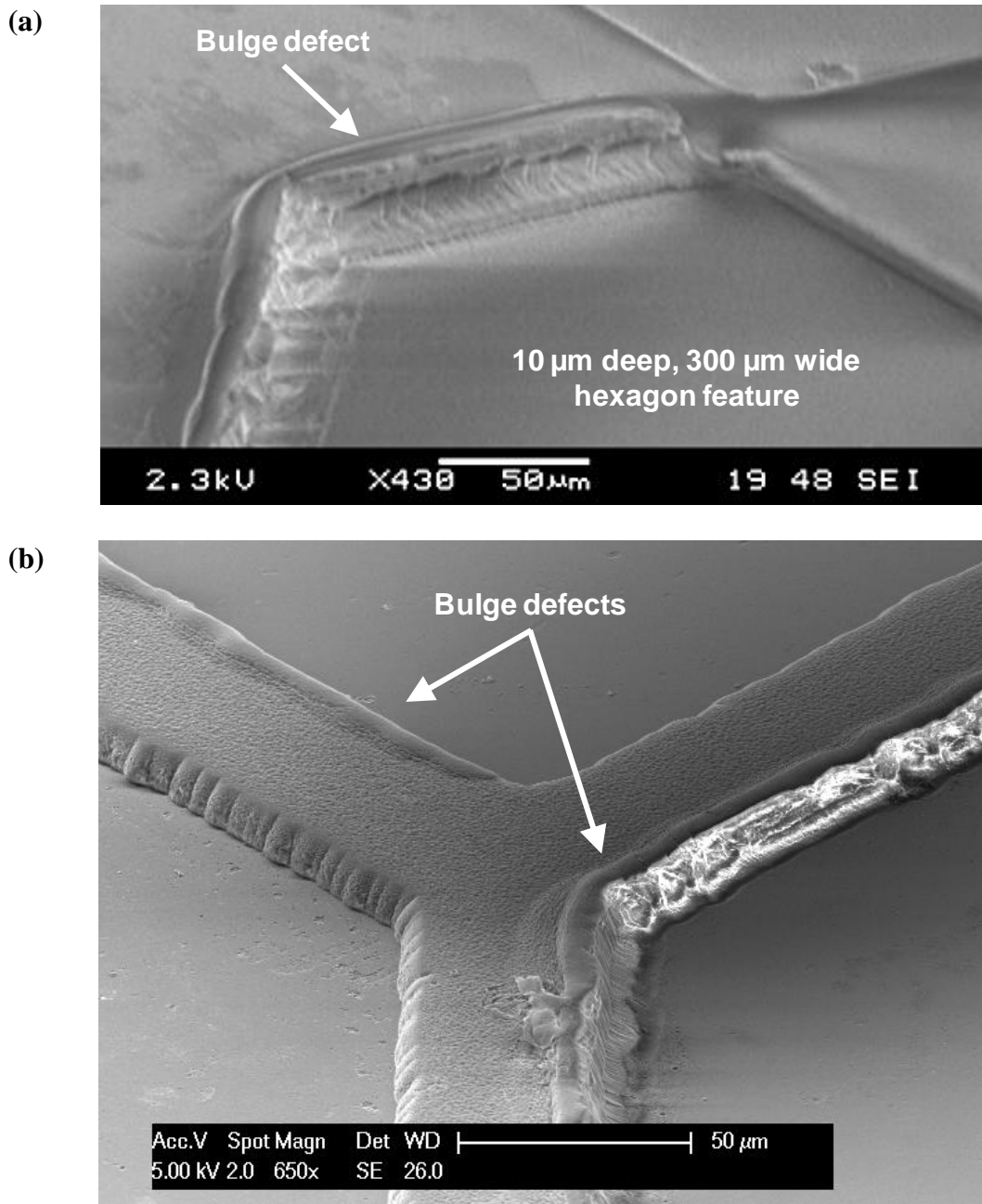
Figure 1.2 Scanning electron micrographs of embossed features with bulge defects most likely caused by thermal contraction; (a) 10 µm deep, 300 µm wide hexagon feature embossed in PMMA with a bulge defect, (image courtesy Hayden Taylor); (b) 10 µm tall, 50 µm wide raised feature embossed in polycarbonate at 160°C and demolded at 130°C.
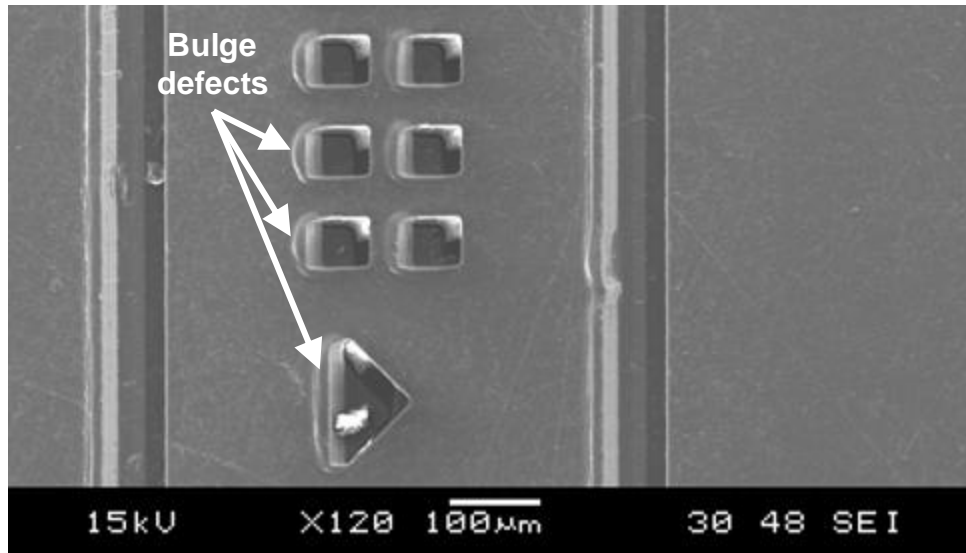
Figure 1.3 Scanning electron micrograph showing bulge defects in 50 µm deep, 50 µm wide features in an injection molded PMMA part demolded at 40°C (Image courtesy Fu Gang).
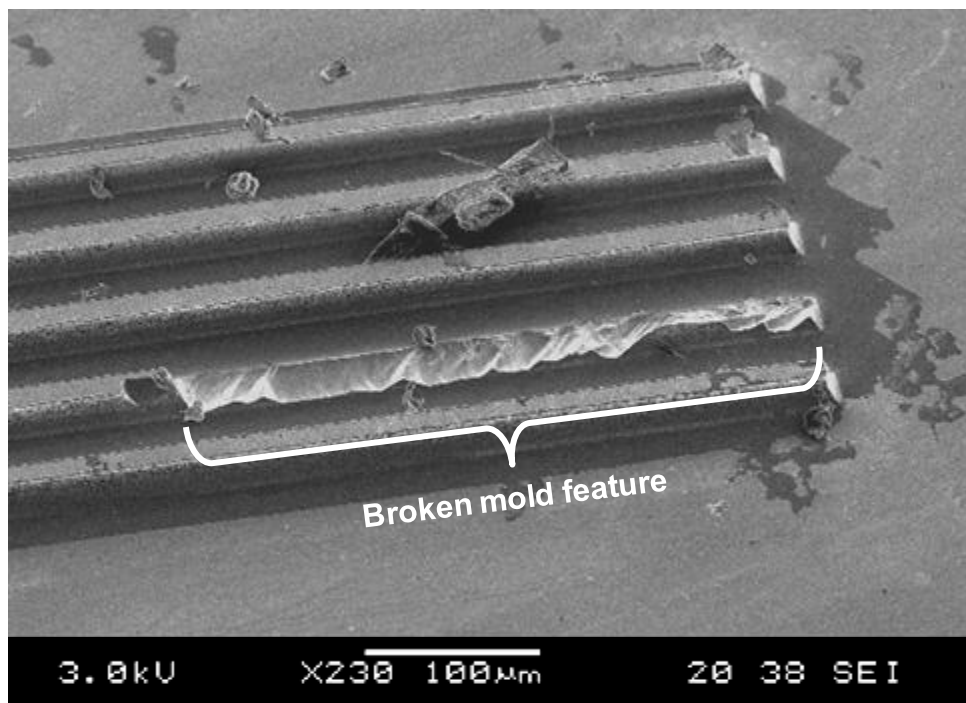
Figure 1.4 Scanning electron micrograph of a broken feature on a silicon mold that was used to hot emboss PMMA. The feature was a 30 µm wide by 30 µm deep channel (Image courtesy Hayden Taylor).
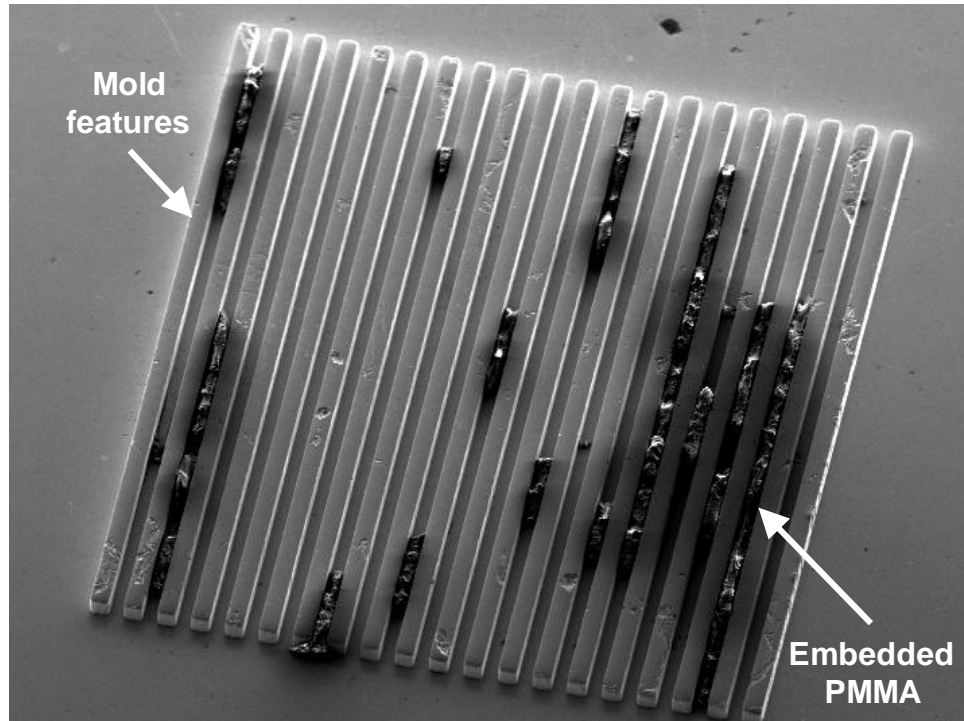
Figure 1.5 Scanning electron micrograph of an embossing mold made of bulk metallic glass with 40 μm deep, 25 μm wide ridges spaced 25 μm apart. PMMA has been embedded between closely spaced features after an embossing cycle.

1.5 Review of demolding research

1.5.1 Hot embossing

Quantitative research on demolding of hot embossed polymer microstructures has so far been limited to finite element simulation of the demolding process. Several researchers have developed two-dimensional [38, 42, 49] or three-dimensional [41, 50] finite element simulations of polymer parts adhered to embossing molds combining the effects of thermal stress and sidewall friction. These simulations generally find that the stresses caused by thermal contraction mismatch and sidewall friction are concentrated at the edges of features, and are generally high enough that deformation of the polymer is likely. These simulations have been used to check the effect of varying sidewall friction on the simulated stresses in the part and mold or on the demolding forces, where reducing friction in the model also reduces demolding forces. These works have not systematically studied the effects of feature geometry (for instance, feature spacing or height) on simulated demolding.

Experimental studies of demolding in hot embossing have consisted of qualitative evaluations of the effects of mold materials [51, 52], coatings [38, 53], the demolding

temperature [39], or the effect of barrier features [42]. No direct measurements of demolding forces in hot embossing seem to have been made to date, nor has the effect of feature geometry on demolding difficulty or on the occurrence of feature distortion been studied systematically.

In one interesting contribution, Worgull et al. describe a specialized test apparatus they have used to characterize friction between embossed polymers and mold materials [54]. This test apparatus is similar to the one used by Pouzada et al.. to characterize friction between thermoplastic polymers and steel molds [55]. In Worgull's apparatus, a polymer foil is pressed between heated platens and then cooled. One of the platens is then displaced in a direction parallel to the surface of the polymer while a small normal load is maintained, and the frictional force between the mold and the polymer is measured. They found that the dynamic friction coefficient is somewhat affected by the mold material and its surface roughness (Brass with Ra=20 nm and 200 nm or Nickel), while the static friction coefficient is affected by the embossing temperature (110-170°C) and pressure (2.5-7.5 MPa), the sliding velocity (1 mm/min vs. 5 mm/min), and the presence of an unspecified "release agent." The dynamic friction coefficient was generally ~0.6, except for the less rough Brass mold (1.0) and the Nickel mold (1.2). The static friction coefficient ranged between 0.6 (when sliding at 5 mm/min) and 2.2 (when embossing at 170°C). They did not test the effect of the demolding temperature or the presence of features on the molds (these experiments seem to have been motivated by a need to calibrate the friction coefficient used in their finite element simulations).

1.5.2 Injection molding of microstructures

Michaeli et al.. performed a qualitative study of demolding of injection molded polymer microstructures (PMMA and PC), including different mold patterns and different means of demolding [43]. Hexagonal pillars 100 μm high in a honeycomb array spaced 2.5 μm apart were always difficult to demold successfully, but larger patterns of lines of unspecified size (apparently hundreds of μm) were demolded easily. Insufficient demolding force could be generated via vacuum, so mechanical demolding was the only feasible means. Applying ultrasonic vibration during demolding had no observable effect.

Fu et al.. performed a comprehensive study of demolding a square array of 100 μm diameter pillars spaced 200 μm apart produced by micro powder injection molding (μPIM) [44]. The forces on ejector pins were measured during demolding. The peak demolding force followed

a decreasing trend with demolding temperature until it reached an optimal value, after which demolding force increased with decreasing temperature. This behavior was attributed to the combined and antagonistic effects of thermal contraction during cooling and hydrostatic expansion when the packing pressure was released. The optimal demolding temperature depended on the magnitude of the packing pressure, with higher packing pressures leading to lower optimal demolding temperature. These results were consistent with finite element simulations also discussed in that work.

1.5.3   Nanoimprint lithography

Similar to the case for hot embossing, research on demolding in nanoimprint lithography has been largely limited to finite element simulations based on thermal stress and friction [47, 56, 57]. Some studies have applied fracture mechanics tests including pull tests (see section 4.3.1) [46, 58] and asymmetric cantilever tests (see section 4.3.5) [59] to measure the adhesion strength between featureless molds and nanoimprint resists and to assess the effects of anti-adhesive coatings.

A fracture mechanics test (the razorblade test, see section 4.3.4) was adapted by Landis et al.. [60] to study demolding in nanoimprint lithography. In this study, a silicon mold with an array of 200 nm deep and 500 nm wide trenches was imprinted into a 280 nm thick layer of poly(hydroxystyrene)-based resist on a silicon wafer at 120°C and 1.5 MPa for 60 s. The razorblade tests were conducted at room temperature. They found that patterned molds exhibited greater adhesive strength than un-patterned molds, and that molds with features with their long dimension oriented perpendicular to the crack front exhibited less adhesion than those with features oriented parallel to the crack front.

They attributed the increase in toughness for patterned vs. unpatterned molds to frictional dissipation on the feature sidewalls. They proposed a relation between the feature dimensions, the sidewall stress, and the surplus toughness attributed to friction dissipation (Eq. 1-1).

$$G_{\text{fric}} = \sigma_{\text{sw}}h^2\frac{2}{P}$$

<div align="right">1-1</div>

where

G_{fric}	Toughness surplus attributed to friction
σ_{sw}	Sidewall stress
h	Feature height
P	Feature pitch

Without testing the effect of different feature heights and pitch, however, this relation remains hypothetical. They attributed the difference in toughness associated with feature orientation to a difference in sidewall stress, but did not propose an explanation for this difference in sidewall stress. They did not study the effect of varying feature dimensions or demolding temperature.

Demolding forces for full-wafer (100 mm diameter) nanoimprinting were studied by Trabadelo et al. using a commercial imprinting machine (Jenoptik HEX03) from the brief "jump" in the recorded force during demolding (similar to pull tests, see section 4.3.1) [61]. They observed a great deal of variation in the apparent demolding force between test runs with the same conditions. They used etched silicon molds with arrays of 2 µm wide square features in an orthogonal array spaced 4 µm apart, both holes 150-700 nm deep and pillars 500 and 1000 nm high, imprinting into a 4.5 µm thick layer of PMMA spin-cast onto another silicon wafer. The demolding force appeared to be related to the pattern geometry, with deeper holes requiring higher demolding forces and showing more demolding defects, and pillars demolding easily. They also found that the demolding force decreased with decreasing temperature until reaching an optimal value, then increased with decreasing temperatures; however, they only tested four temperatures for a single pattern of 500 nm high square pillars. They speculated that this trend was caused by changes in the adhesion strength between the PMMA and the mold with temperature.

Along with finite element simulations [57], Song performed demolding tests similar to those by Trabadelo et al., but using a custom laboratory imprinting machine [62, 63]. Song's experiments used an etched silicon mold with a sparse pattern combining dots and lines 3-9 µm wide and 100 nm high imprinted into a 300 nm thick PMMA layer on a 100 mm diameter silicon wafer. Only three demolding temperatures were tested, but the demolding force followed a

similar trend with temperature to that found by Trabadelo et al. [61]. Song did not test different mold geometries.

1.5.4   Curable liquid resin casting of microstructures

Yeo et al. studied demolding for curable liquid resin casting of UV-curing polyurethane [64, 65] and PDMS [45], including both finite element simulations and peel test experiments. Unlike the other simulation studies discussed above, Yeo's simulations used cohesive surface elements rather than Coulomb friction to model the interaction between the part and the mold. The finite element simulation results suggest that shrinkage during curing (related to the crosslink density and the cure time) served to degrade the adhesion between the part and mold, but that excessive shrinkage could cause distortion [65]. Peel tests were used to measure the adhesion strength between the part and the mold (demolding toughness, see section 2.7). Peel tests of UV-curing polyurethane demolding from nickel molds found an increasing trend of demolding toughness with cure time, except for 90° peel tests, which suggested an optimal cure time ~30 s [64]. Peel tests also showed that plasma-polymerized fluorocarbon coatings reduced the demolding forces for PDMS cast on silicon molds with high aspect ratio features [45].

1.5.5   Demolding in macroscopic injection molding

Demolding is also important in macroscopic injection molding. Several researchers have used finite element simulations combining thermal contraction and friction to estimate the demolding force for injection molded parts and compared these with measured demolding forces [66-72]. This approach is not much different from that given by Glanvill in 1973, where the ejection force is estimated from the forces on the mold due to thermal contraction and an assumed friction coefficient [73]. When demolding temperature is considered, demolding forces have been found to follow an increasing trend with decreasing temperature.

1.6 Motivation for this work

While demolding is a critical step in all polymer micro-molding processes, it has not yet been studied comprehensively. Simulation approaches that have been long used for macroscopic molding have been applied to micro-molding [38, 41, 42, 44, 47, 56, 57, 74], but few researchers have extended this work to consider the effects of adhesion [65], and none have considered the

combined effects of thermal stress, friction, and adhesion. There is a need for an over-arching explanatory framework relating observable effects to physical mechanisms—a theory of demolding mechanics.

Most studies of demolding have been qualitative, usually comparing electron microscope images of parts made under different conditions (e.g. different mold materials [52]). A few researchers have made quantitative measurements of demolding forces [45, 61-63] or toughness [60, 64], but these studies have been limited to a small set of parameters. None has tested the effects of feature geometry and demolding temperature across a wide range. No studies have quantitatively related defects to processing conditions or feature geometry. A standardized test method for characterizing demolding of polymer microstructures is needed to promote comparison of results from multiple studies and facilitate research on the effects of factors including feature geometry, processing conditions, material properties.

Interpretation of demolding experiments has largely been speculative [45, 60-64]. Without a over-arching theory of demolding mechanics nor a standardized test method, it has so far not been possible to compare theoretical predictions with experimental results to validate or disprove hypotheses.

Mitigation strategies are usually proposed based on these hypothetical demolding mechanisms. Understanding of the physical mechanisms responsible for energy dissipation in demolding will guide the implementation of mitigation strategies (e.g. if friction is dominant, low-friction coatings or materials would be recommended). A standardized test method would also enable comparative studies of mitigation strategies (e.g. different coatings) and a cost-benefit analysis to evaluate the usefulness of these treatments.

The ultimate purpose of research on polymer micro-molding processes is to facilitate their profitable use in industry in manufacturing products. It is essential that research findings are generalized and interpreted with industrial application in mind. There is currently no equivalent of the *Machinery's Handbook* [75] for polymer micro-molding processes. Process development is currently conducted on an *ad hoc*, trial-and-error basis relying on individual experience and intuition [76]. Manufacturers need guidelines and design rules for successful micro-molding, including the demolding step. Research findings on demolding need to be interpreted with respect to metrics such as production rate, part quality, cost, process flexibility, and environmental impact.

1.7 Overview of the thesis

This chapter (Chapter 1) has introduced the topic of demolding of polymer microstructures and reviewed the relevant backround of microfluidics and the existing research in this field. This chapter has also discussed the motivation for and contributions of the present work.

Chapter 2 presents a brief review of relevant mechanics and their application to demolding. A theory of demolding mechanics combining thermal stress, friction, and adhesion, along with a metric for demolding (the demolding work and toughness) are presented). The theory of demolding mechanics is used to make testable predictions, including the existence of an optimal demolding temperature and the effects of feature geometry including height, width, and spacing.

Chapter 3 presents the results of finite element simulations of demolding. Thermal stress in the part and mold is considered along with the potential for local distortion. Demolding work for single features is estimated using simulations, and the effects of friction coefficient, adhesion strength, material properties, and feature geometry are investigated and compared with theoretical predictions.

Chapter 4 reviews demolding in practice, along with existing test methods for evaluating adhesion. The test method developed in this work is described along with the equipment that has been designed and fabricated. Test mold designs and experimental procedures are described. The test method is evaluated for its repeatability.

Chapter 5 presents experimental results. These results are discussed and compared with theoretical predictions. Feature distortion defects are observed and related to a geometric factor that has been identified in this work. The observed effects of demolding temperature and feature geometry are compared with theory. The demolding processing window is identified, and its boundaries are defined with reference to physical mechanisms. The effects of mold coatings and feature edge quality are evaluated.

Chapter 6 summarizes this thesis and presents conclusions on demolding mechanics, simulation, and experimental results. The findings of this thesis are adapted and generalized to develop demolding guidelines and design rules for industrial application in hot embossing extended to similar micro-molding processes. Future work is proposed.

2 Mechanics of demolding

2.1 Introduction to the chapter

One consequence of hot embossing is the formation of a bonded interface between the mold and the part. The goal of demolding is to destroy this bond. The failure of bonded interfaces is relevant to many problems in many fields, and has been studied extensively. Sections 2.2-2.4 below summarize the relevant parts of this body of knowledge. Sections 2.5-2.6 discuss the application of fracture mechanics to the problem of demolding. Section 2.7 proposes a metric by which demolding can be characterized by analogy with fracture: the demolding work.

2.2 Causes of adhesion in hot embossing

Adhesion is a complex phenomenon that involves several different mechanisms. Adhesion can arise from chemical interaction such as covalent bonding, acid-base interaction, or inter-diffusion, as well as molecular interactions such as van der Waals forces or hydrogen bonding. Mechanical interaction or interlocking of surface roughness or asperities also contribute to adhesion [77]. These various mechanisms of adhesion result in loads on the mold during the demolding step, shown schematically in Figure 2.1. Mechanical adhesion can arise from friction on feature sidewalls, and from interlocking of undercut features, surface roughness, or asperities. Differential strains between the mold and the part, such as those caused by thermal contraction mismatch or shrinkage during curing, can increase the forces on sidewalls and exacerbate the effects of friction.
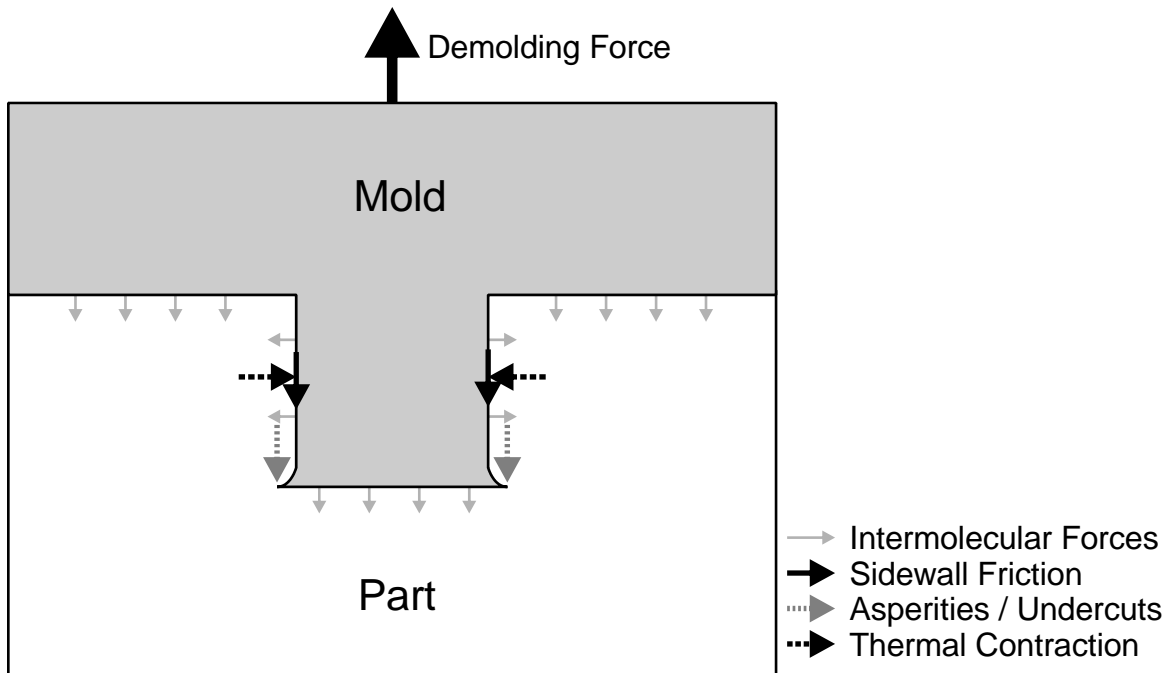
Figure 2.1 Schematic of forces acting on a mold during the demolding step in hot embossing.

Certain clues provide evidence that one or several of these phenomena contribute to part-mold adhesion. It is often observed that different pairs of mold and part materials exhibit different demolding behavior. Coatings such as fluorocarbon films [78], molecular monolayers [79-81], and diamond-like carbon [53] have shown some success in improving demolding in hot embossing as well as in casting of UV-curing thermosets [82], suggesting that friction and/or adhesion caused by chemical or molecular interactions are partially responsible for mold-part adhesion.

Such molecular interactions generally require that the two surfaces be in "intimate contact." Hot embossing has demonstrated the capability to replicate 10 nm features [83] and is often observed to replicate the nano-scale scalloped texture in the sidewalls of silicon molds produced by deep reactive ion etching [39, 84] and the texture of machined metal molds (Figure 2.2, Figure 2.3). Casting of thermal curing elastomers (polydimethylsiloxane, or PDMS) has demonstrated replication of features as small as 2 nm across [85]. All polymer micro- and nano-molding processes are valued for their ability to replicate very small features, so it is reasonable to consider the part and mold to be in sufficiently intimate contact for molecular forces to be potentially relevant to demolding.
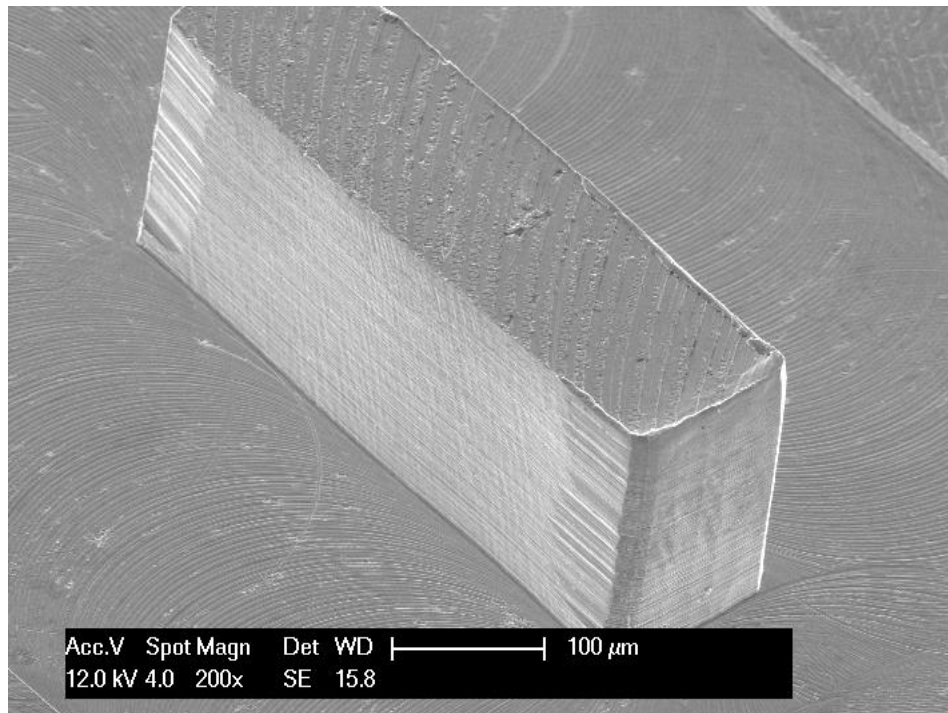
Figure 2.2 Scanning electron micrograph of a mold feature; note the sidewall texture. The mold was produced by micro-milling Aluminum 6061 (see section 4.6). The feature is 200 µm tall, 100 µm wide, and 500 µm long.
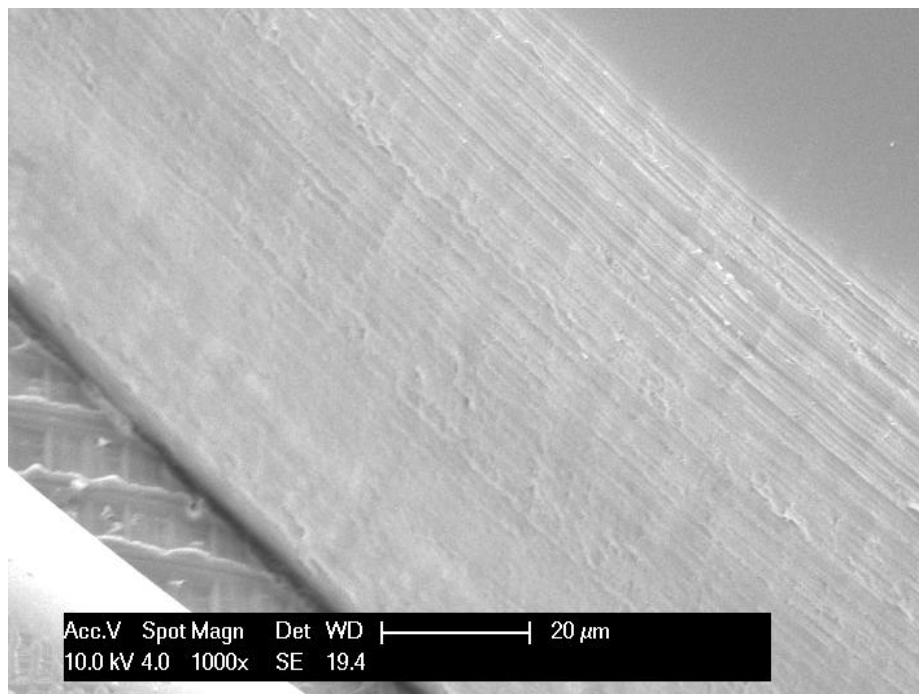
Figure 2.3 Scanning electron micrograph of the sidewall of an embossed feature in PMMA. The bottom of the feature is at the lower-left of the image. The part was embossed at 135°C under a pressure of 1 MPa for 30 s, then cooled to 25°C and demolded. The excellent replication of the sub-micrometer scale sidewall texture suggests the part and mold were in intimate contact.

The high-fidelity replication of nano-scale surface textures often observed in hot embossing also suggests that mechanical interaction of asperities contributes to adhesion. If mold features are undercut (Figure 2.4), the part can become "locked" onto the mold, and deformation or failure will occur during demolding. This failure can occur in the part (Figure 2.4 and Figure 1.5) or the mold (Figure 1.4). Although the sidewalls of silicon molds produced by the Bosch process (deep reactive ion etching or DRIE) are often nearly vertical, the scalloped texture will produce some undercut areas that can serve to "lock" the polymer onto the mold. Sidewall roughness can also contribute to friction between the part and mold that must be overcome during demolding. It has been observed that molds with a draft angle such as silicon molds produced by KOH etching can be demolded more easily [84, 86], further suggesting that friction related to mechanical asperity interaction is involved in mold-part adhesion.
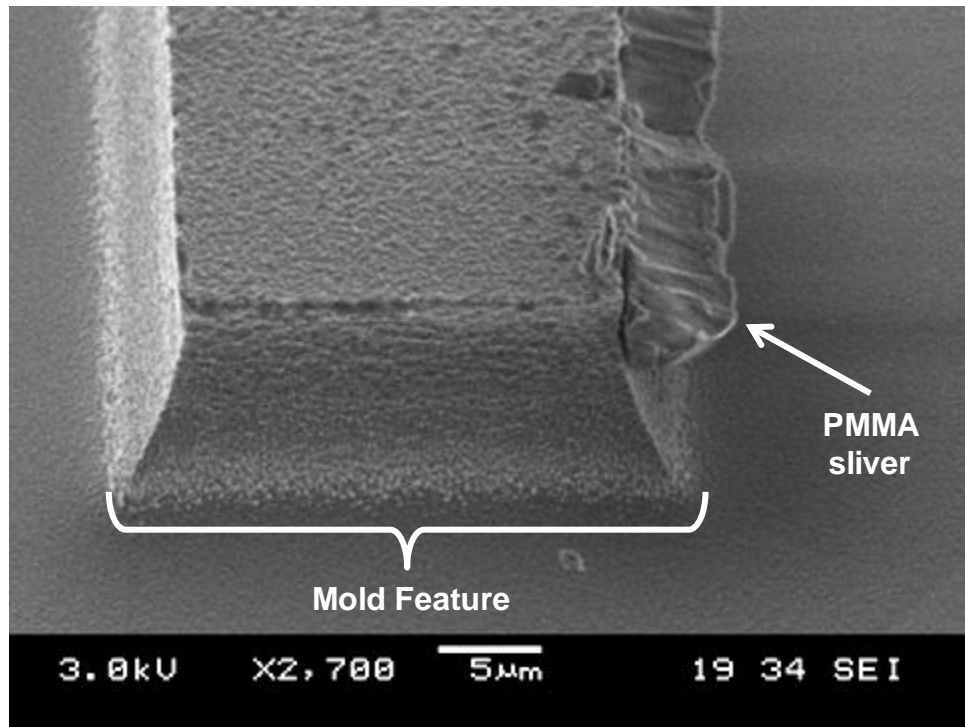
Figure 2.4 Scanning electron micrograph of an undercut feature on a silicon mold. The feature is slightly undercut, and a sliver of PMMA that was ripped out of the part during demolding is adhered to the right edge of the feature (Image courtesy Hayden Taylor).

Mechanical stresses caused by differential thermal contraction [39, 42, 47, 74] or shrinkage during curing [87] are also very important in demolding. In hot embossing, mold and part materials often have quite different thermal contraction behavior. This differential contraction during cooling can impose a load on feature sidewalls normal to their surfaces. This

36

load will magnify any friction force that may be present between the part and mold, whatever the source of this friction. The thermal stress developed during cooling can result in damage to both the part [39, 42, 47] (Figure 2.5) and the mold [80]. In addition to wear or fracture of mold features, thermal stress can result in gross mold failure if the mold material is brittle (Figure 2.6).
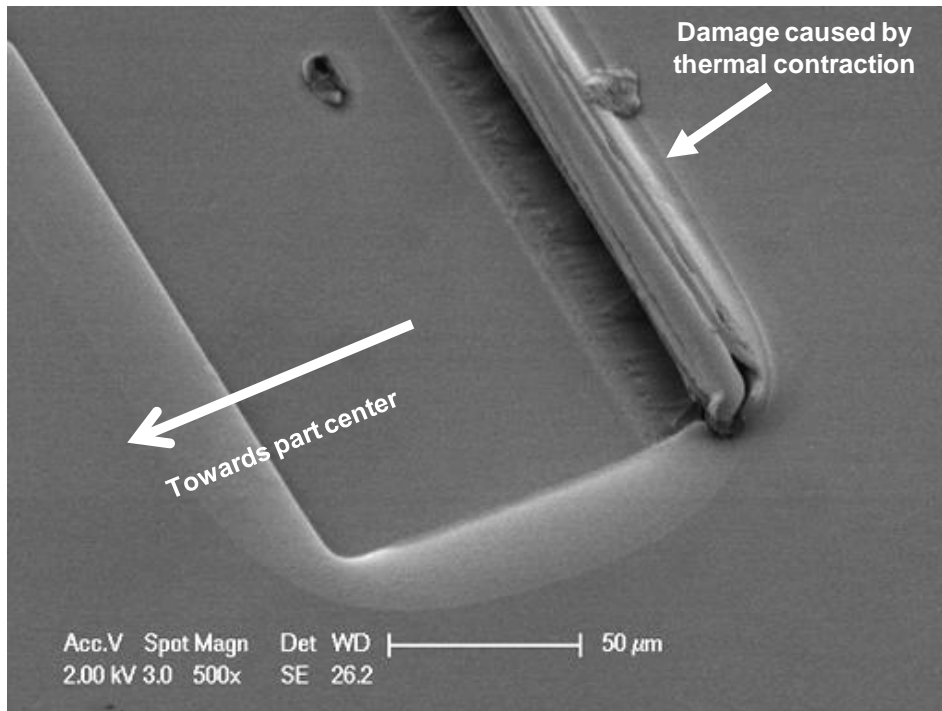
Figure 2.5 Damage to a PMMA part caused by thermal contraction during hot embossing [39]. The part was embossed with a silicon mold at 120°C under a pressure of 4 MPa for 60 s, then cooled to 50°C and demolded. The feature shown is the end of a long rectangle, 100 μm wide and 15 μm deep.
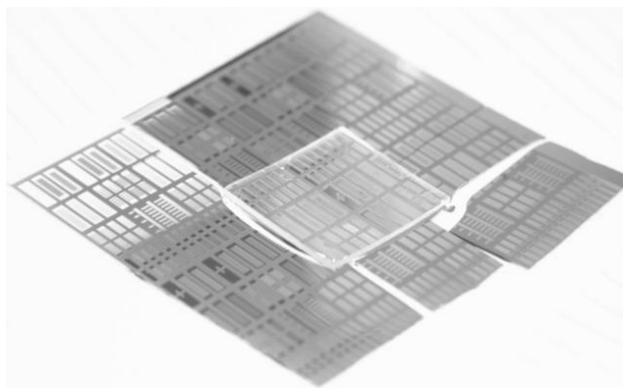
Figure 2.6 Gross mold failure caused by thermal stress in hot embossing. The ~30 mm square PMMA part was embossed with the 100 mm square silicon mold with dense, 100 μm high features at 120°C, then cooled to 50°C and removed from the embossing machine. As the part cooled to room temperature, bending stress induced by thermal contraction mismatch caused the mold to shatter.

2.3 Fracture mechanics background

The present work proposes an analogy between the failure of the bonded interface between the part and the mold during demolding and the brittle fracture of an adhesive bond between two materials. Through this analogy, the mechanics of fracture are applied to the mechanics of demolding. Fracture mechanics is a large and varied discipline with numerous dedicated journals and conferences. A thorough review of this field, or even the sub-discipline of interfacial fracture mechanics, is well beyond the scope of the present work. There are many excellent texts available, some of which are cited below. For the most part, derivations that can be found elsewhere will not be repeated here.

2.3.1 Strain energy approach

Many situations involving fracture can be satisfactorily described using the energy balance approach laid out by Griffith [88, 89]. Consider an existing crack with area A within a deformable body subject to external loads (Figure 2.7). Energy conservation requires that the sum of the work performed by the external loads should equal the sum of the change in internal energy of the body, the kinetic energy of the body, and the energy consumed by increasing the crack area [90]. For the quasi-static case where kinetic energy can be neglected, and for ideally brittle fracture where plastic deformation is negligible, this relationship can be stated in terms of changes in crack area:

$$\frac{\partial W}{\partial A} - \frac{\partial U}{\partial A} = \frac{\partial \Gamma}{\partial A}$$

2-1

where
A   Crack area
W   External work
U   Elastic strain energy
Γ   Energy consumed to create new surface
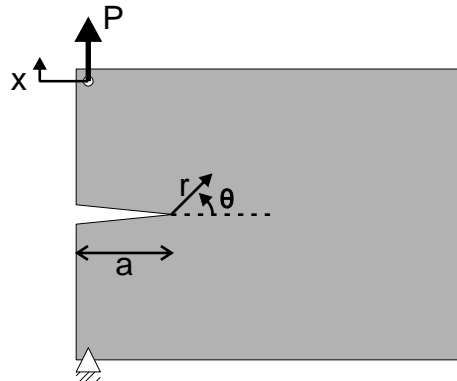
Figure 2.7 Edge crack in an elastic body subject to external loads.

A particularly relevant special case arises when the locations on the body subject to external loads are effectively stationary while the crack propagates (the so-called "fixed-grips" condition) and the external work is thus negligible [90]. This situation is found in fracture tests where the grips are moving under displacement control. In this case, the energy consumed in extending the crack is supplied by the strain energy stored in the system. The second term in Eq. 2-1 is thus referred to as the strain energy release rate. If the stored energy exceeds the amount required, the crack will grow. This observation leads to the Griffith fracture criterion, stated in Equation 2-2. In Griffith theory, the energy required to extend the crack is attributed to the surface energy of the material (2γ in Equation 2-2 to account for the two crack surfaces) [88, 89].

Orowan later extended the Griffith criterion to ductile materials where plastic deformation is not negligible. Orowan partitioned the critical strain energy release rate between surface energy and plastic/dissipative mechanisms [91]. The critical strain energy release rate in Equation 2-2 is considered equivalent to the fracture toughness measured experimentally, where any departure from the theoretical surface energy is attributed to other (dissipative) mechanisms.

$$-\frac{\partial U}{\partial A} \geq G_C = \begin{cases} 2\gamma & \text{Griffith} \\ 2\gamma + \partial U^P/\partial A & \text{Orowan} \end{cases} \qquad \textbf{2-2}$$

where
A   Crack area
U   Elastic strain energy
G_C Critical strain energy release rate
γ Surface energy
U^P Plastic work, or Dissipative work

The fracture criteria concepts set forth by Equations 2-1 and 2-2 are depicted graphically in Figure 2.8 and Figure 2.9. The strain energy release rate of Equation 2-2 is the slope of the curve $U(a,x_0)$ under fixed-grips conditions. A stable crack of length a_0 corresponds to the minimum of the total energy of the system, and this minimum occurs where the strain energy release rate is equal to the fracture resistance, as given by the fracture criterion G_C in Equation 2-2. When the system is changed, for instance by applying a greater displacement (x), the energy curve shifts, and the crack will grow to the new stable length (Figure 2.9). The fracture resistance must be overcome by consuming some of the strain energy stored in the system, corresponding to the shaded area ΔU.
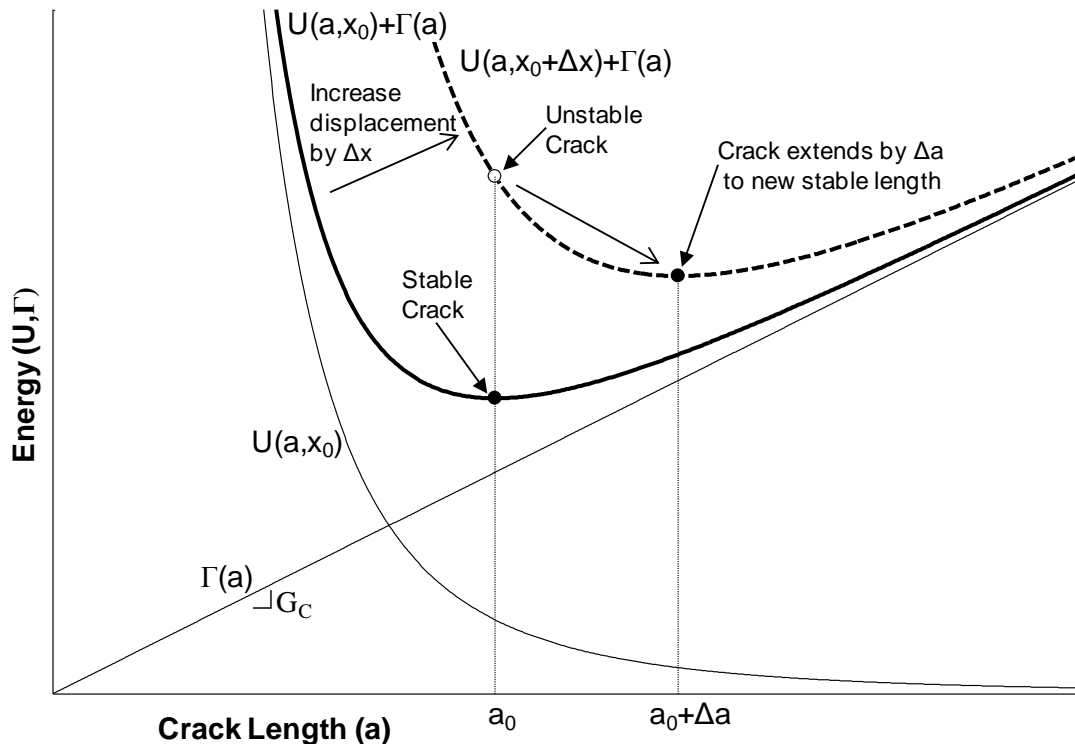
Figure 2.8 Schematic representation of strain energy fracture criterion. A stable crack length corresponds to the minimum energy condition of the system.
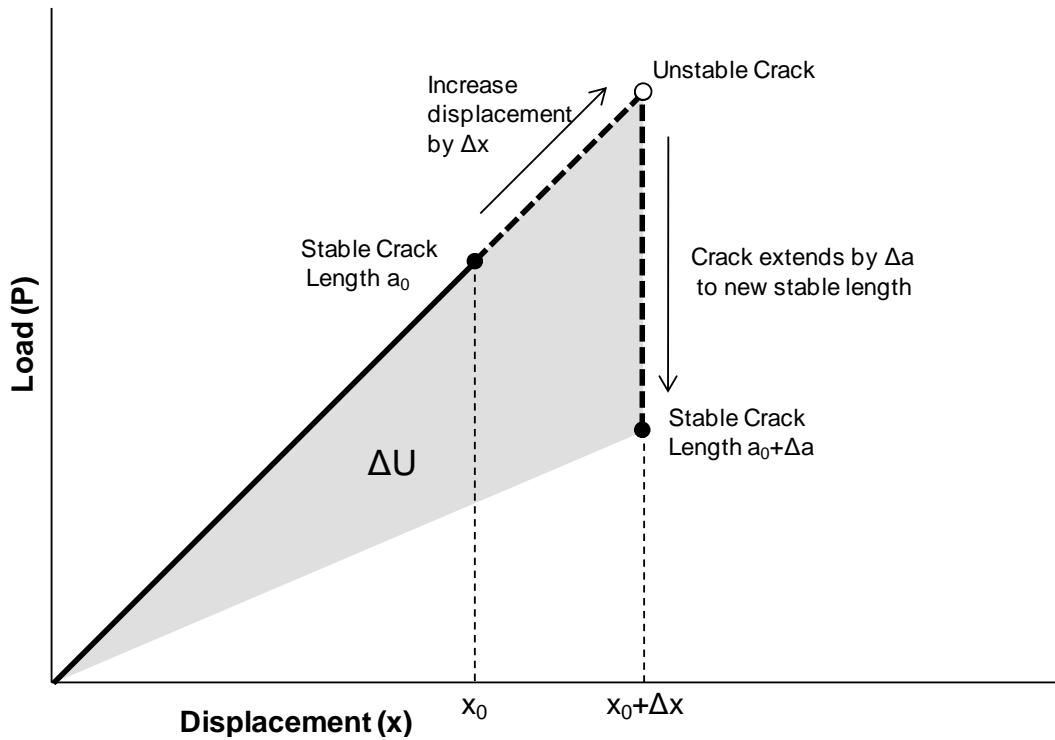
Figure 2.9 Schematic representation of load and displacement for strain energy fracture criterion. Additional displacement can cause the crack to grow. The energy consumed by this growth comes at the expense of the strain energy stored in the system.

2.3.2 Stress intensity approach

An alternative to the strain energy approach considers the stress field in the vicinity of the crack. Many derivations and solutions for stresses and strains in cracked bodies can be found in fracture mechanics texts. The solutions for the stress field have the form of Equation 2-3, where f is a function of the angular coordinate θ (Figure 2.7) [92], and the stress intensity factor K is a function of material properties, geometry, and loads. As an example, for the system shown in Figure 2.7, the radial stress component σ_r is given by Equation 2-4, and the stress intensity factor K is given by Equation 2-5 [90].

$$\sigma_i = \frac{K}{\sqrt{2\pi r}} f(\theta) \qquad\qquad\qquad \textbf{2-3}$$

$$\sigma_r = \frac{K}{\sqrt{2\pi r}} \left[\frac{5}{4} \cos\left(\frac{\theta}{2}\right) - \frac{1}{4} \cos\left(\frac{3\theta}{2}\right) \right] \qquad\qquad \textbf{2-4}$$

$$K = 1.12\, \sigma_0 \sqrt{\pi a} \qquad\qquad\qquad \textbf{2-5}$$

where

σ_i Stress component
K   Stress intensity factor
r   Radial coordinate measured from crack tip
θ Angular coordinate measured from plane of crack
f Function of angle θ
σ_0 Far-field tensile stress due to applied load
a   Crack length

Examining Equation 2-4, it is clear that the stress goes to infinity at the tip of the crack (r=0). This stress singularity makes it impossible to compare the stresses due to different crack geometries or different loads, or to develop a fracture criterion based on maximum stress. The key insight of the stress intensity approach is the similitude of the crack tip stress fields, which means that despite differences in far-field loading, two systems that share the same stress intensity factor will have the same stress field near the crack. Systems can therefore be compared on the basis of their stress intensity factor. A fracture criteria based on the stress intensity factor approach is based on a critical value K_C, above which a crack will propagate.

Practitioners of the stress intensity approach define orthogonal loading modes for which stress intensity factors can be computed [90]. These are Mode I (tensile load normal to the plane of the crack), Mode II (shear load in the plane of the crack and parallel to the crack extension direction) and Mode III (shear load in the plane of the crack and perpendicular to the crack extension direction). Three corresponding fracture criteria are proposed. This analysis assumes linear elastic behavior, so the stress fields can be superposed resulting in "mixed-mode" loading.

By substituting the stress field solution into the equations for strain energy, one can arrive at Equations 2-6 and 2-7, which show that the strain energy and stress intensity approaches are, in fact, equivalent [90, 93].

For single-mode loading:

$$G_I = \frac{\kappa + 1}{8\mu} K_I^2$$

$$G_{II} = \frac{\kappa + 1}{8\mu} K_{II}^2 \qquad \qquad \textbf{2-6}$$

$$G_{III} = \frac{K_{III}^2}{2\mu}$$

For plane problems with mixed-mode loading:

$$G = \frac{K_I^2}{E'} + \frac{K_{II}^2}{E'} + \frac{\mathcal{C}(1 + v)K_{III}^2}{E'} \qquad \qquad \textbf{2-7}$$

where

G   Strain energy release rate
K   Stress intensity factor
κ Bulk modulus
μ Shear modulus
E'   Effective modulus (E' = E for plane stress and $E/(1-v^2)$ for plane strain)
$\mathcal{C}$ $\mathcal{C} = 0$ for plane stress and 1 for plane strain

2.4 Interfacial fracture mechanics

The above analysis assumes a homogenous elastic body, but in demolding, there are two bodies bonded along an interface. At the interface, there is a discontinuity in material properties, and there may be a discontinuity in stress state. Despite these discontinuities, in many cases the energy balance approach remains useful [94].
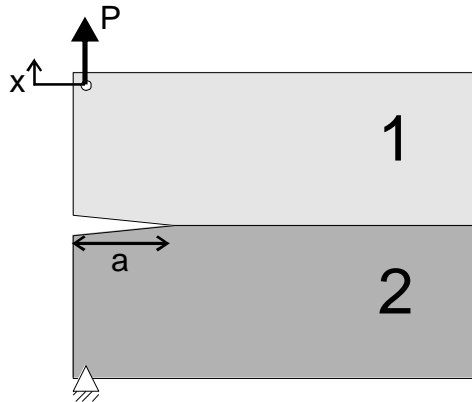
Figure 2.10 Bonded bodies with an interfacial crack.

2.4.1 Surface energy of interfaces

For dissimilar materials, the surface energy in Equation 2-2 is replaced by the Work of Adhesion (W_A), which is a characteristic of the material pair. Work of adhesion is defined as the

"decrease of Gibbs free energy per unit area when an interface is formed from two individual surfaces" [95]. In other words, the work of adhesion is the reversible work per unit area required to separate two surfaces that have adhered. The work of adhesion is attributed to van der Waals forces, and is related to the surface energies of the two materials (γ_i) and the interfacial energy between the materials (γ_{ij}) by the Dupré relation (Equation 2-8) [96].

$$W_A = \gamma_1 + \gamma_2 - \gamma_{12} \qquad \textbf{2-8}$$

where
W_A Work of Adhesion
γ_i Surface energy of material i
γ_{ij} Interfacial surface energy between materials i and j

The work of adhesion can often be approximated from the polar (dipole-dipole, induced-dipole, etc.) and dispersive (non-polar) components of surface energy. For low-energy systems such as polymers bonded to metals, this approximation is given by Equation 2-9 [95].

$$W_A = 4 \left[\frac{\gamma_1^p \gamma_2^p}{\gamma_1^p + \gamma_2^p} + \frac{\gamma_1^d \gamma_2^d}{\gamma_1^d + \gamma_2^d} \right] \qquad \textbf{2-9}$$

where
W_A Work of Adhesion
γ_i^p Polar component of surface energy of material i
γ_i^d Dispersive component of surface energy of material i

2.4.2 Stress intensity factors for interfaces

The elastic mismatch at the interface between two materials can result in shear loads at the interface even when the far-field stresses are purely tensile [97]. This means that even for single-mode loading, the interfacial crack will experience mixed-mode conditions. The Dunders parameters α and β defined in Equation 2-10 are dimensionless groups that characterize the elastic mismatch and simplify many other expressions in interfacial fracture mechanics [94]. The constant α is related to the tensile mismatch, while β is related to the coupling of tension and shear at the interface. For a homogenous material, β=0 and far-field tension will not produce shear loading on the crack. Larger values of β (greater mismatch) will result in shear loads at the interface (Mode II) even when far-field loads are purely tensile (Mode I).

44

$$\alpha \equiv \frac{\mu_2(\kappa_1 + 1) - \mu_1(\kappa_2 + 1)}{\mu_2(\kappa_1 + 1) + \mu_1(\kappa_2 + 1)}$$

2-10

$$\beta \equiv \frac{\mu_2(\kappa_1 - 1) - \mu_1(\kappa_2 - 1)}{\mu_2(\kappa_1 + 1) + \mu_1(\kappa_2 + 1)}$$

where

α, β	Dunders constants
μ_i	Shear modulus of material i
κ_i	Bulk modulus of material i

The stress state near an interfacial crack is a complex function involving a complex stress intensity factor (Equation 2-11) [97, 98]. For a crack in a homogenous body, K_1 and K_2 reduce to the conventional stress intensity factors K_I and K_{II}. The determination of the values of K_1 and K_2 is quite complicated, and is often approachable only through numerical means. In the absence of Mode III loading, the strain energy release rate for a bimaterial crack is related to the complex stress intensity factor by Equation 2-13 [99].

$$\sigma_{22} + i\sigma_{12} = \frac{K_1 + iK_2}{\sqrt{2\pi r}} r^{i\epsilon}$$

2-11

$$\epsilon = \frac{1}{2\pi} \ln\left(\frac{1 - \beta}{1 + \beta}\right)$$

2-12

$$G = \frac{1 - \beta}{2}\left(\frac{1}{E_1'} + \frac{1}{E_2'}\right)(K_1^2 + K_2^2)$$

2-13

where

i	$\sqrt{-1}$
σ_{ij}	Stress component
K_i	Components of the complex stress intensity factor
r	Radial coordinate measured from crack tip
ϵ	Bi-material constant
β	Dunders constant (see Eq. 2-10)
G	Strain energy release rate
E'	Effective modulus (E' = E for plane stress and $E/(1-v^2)$ for plane strain)

The relative contributions of shear and tensile (Mode I and II) loading are characterized by the phase angle of loading (ψ) defined in Equation 2-14 [94].

45

$$\psi \equiv \tan^{-1}\left(\frac{K_2}{K_1}\right)$$

<div align="right">**2-14**</div>

where

ψ	Phase angle of loading
K_i	Components of the complex stress intensity factor

In experimental studies of the effect of mixed-mode loading, the observed toughness of an interface has been found to increase with increasing shear loads (increasing ψ) [100, 101]. This effect has been attributed to changes in the shape of the plastic zone at the crack tip [101], electrostatic effects near the crack tip [102], frictional interaction of asperities [103], and shielding of the crack tip by asperities [100]. Of these explanations, asperity interaction is the most relevant to demolding.

2.5 Application to demolding

The present work considers the mechanics of demolding by analogy with interfacial fracture mechanics. The part and mold are considered to be adhered together, with the interface corresponding to the surface where they are in contact.

2.5.1 Strain energy approach applied to demolding

Consider a thin, rectangular polymer part adhered to a thick metallic mold (Figure 2.11). This part is being demolded by a load applied at its end (see section 4.2 for a discussion of demolding in practical applications). For this preliminary analysis, features on the mold are assumed to be very small compared to the size of the part/mold system, and are assumed not to affect the macroscopic behavior. There is an initial crack of length a at the edge of the part. The part is much wider than its thickness (b ≫ t), so the part is modeled as a built-in cantilever of length a subject to plane strain (Figure 2.12).
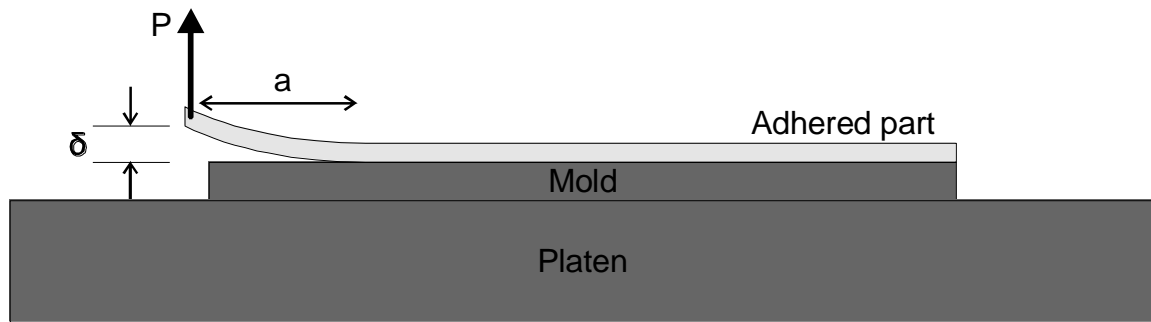
Figure 2.11 Schematic diagram of basic demolding configuration for analysis.
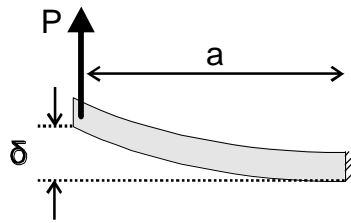
Figure 2.12 Part being demolded is modeled as a built-in cantilever beam.

Following the strain energy approach for interfacial fracture, the Griffith fracture criterion is given in terms of the applied force by Equation 2-15 and in terms of the tip displacement by Equation 2-16 (neglecting the contribution of shear in the beam for simplicity). For fracture in a homogenous material, the surface energy is doubled because two surfaces are created in the crack, but the work of adhesion is a property of the interface, so it is not doubled (compare to Eq. 2-2 and Eq. 4-1).

$$G = \frac{\partial U}{\partial A} = \frac{\partial(P^2 C/2)}{\partial A} = \frac{P^2}{2}\frac{\partial C}{\partial A} = \frac{P^2}{2b}\frac{\partial C}{\partial a} = \frac{6P^2 L^2}{E'b^2 t^3} \geq W_A \qquad \textbf{2-15}$$

$$G = \frac{\partial U}{\partial A} = \frac{\partial(\delta^2/2C)}{\partial A} = \frac{\delta^2}{2C^2}\frac{\partial C}{\partial A} = \frac{\delta^2}{2C^2 b}\frac{\partial C}{\partial a} = \frac{3\delta^2 E' t^3}{8a^4} \geq W_A \qquad \textbf{2-16}$$

where
G   Strain energy release rate
U   Strain energy
A   Crack area
P   Force applied at beam end
δ Displacement of beam end
C   Beam compliance (δ/P)
a   Crack length
b   Part width (into the page)
t   Part thickness
E'   Effective modulus (E' = E for plane stress and $E/(1-v^2)$ for plane strain)
v Poisson's Ratio
W_A Work of Adhesion

The calculated values for work of adhesion for some common pairs of tool and part materials in micro-and nano-molding processes are listed in Table 2.1. Taking as an example a PMMA part adhered to a Nickel mold, where the part is 1.58 mm thick, 10 mm wide, and has an initial crack of 5 mm, and using material properties at 25°C (E=3.1 GPa, v=0.35), the critical load (P) corresponding to the Griffith criterion (Eq. 2-15) is 0.82 N, and the critical tip displacement (δ) is 2.9 μm. If the tip is forced beyond this critical displacement, the crack will extend. For an Aluminum mold, the corresponding force and displacement are 0.70 N and 2.5 μm.

Table 2.1 Works of adhesion in J/m^2 for selected material pairs calculated by Eq. 2-8. Surface energy data and references for these calculations are available in appendix A.1.

	Nickel	Silicon	Aluminum
PMMA	71	70	54
PC	76	70	52
COP	74	43	17
PS	77	63	41

Equation 2-15 and Equation 2-16 can be augmented to account for the contribution of shear stress in the beam to the strain energy as well as the non-ideal constraint at the root of the

cantilever (see section 4.3.5 and Eq. 4-2 and Eq. 4-3). Even so, this analysis leaves out one of the most important factors to consider in demolding: the effect of temperature.

2.5.2 Thermal effects

Hot embossing depends on changes in temperature to soften the polymer parts and facilitate replication and to subsequently "freeze in" these deformations. This requires a thermal cycle where demolding occurs at a lower temperature than embossing. Hot embossing exploits the drastic changes in material properties with temperature that amorphous polymers experience, and these changes must also be considered in demolding.

The surface energy of polymers is known to change with temperature [104], for instance, the total surface energy (sum of polar and dispersive components) of PMMA decreases from about 0.041 J/m^2 at 25°C to about 0.032 J/m^2 at 135°C. This change causes a 13% reduction in the work of adhesion between PMMA and Nickel over this temperature range, and a similar reduction for PMMA and Aluminum.

Amorphous polymers experience even greater changes in elastic properties with temperature, especially when the change spans the glass transition temperature (T_g). For instance, the elastic modulus of PMMA (T_g = 110°C) changes from about 3 GPa at 25°C to about 5 MPa at 135°C, a change of three orders of magnitude [105]. The yield strength also changes significantly over this range (Figure 2.13). The thermal expansion coefficient roughly doubles through the glass transition. The behavior of PMMA changes from essentially elastic at 25°C, to viscoelastic near 100°C, to rubbery at 135°C. Recalling the role of material properties in interfacial fracture mechanics, temperature will have a drastic effect on the behavior of the polymer part during demolding.
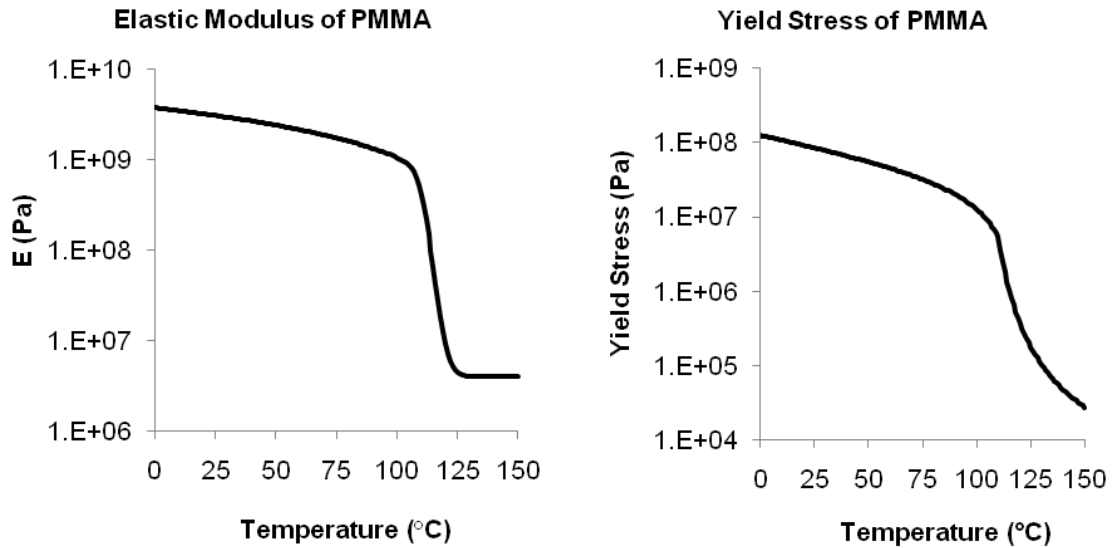
Figure 2.13 Properties of PMMA vs. temperature in the hot embossing process range, calculated according to models developed by Ames [105].

Equally important are the changes in *relative* properties between the mold and part. Embossing molds may be made of silicon, metals, or polymers, though the former two are the most common. Metal molds in particular are most likely to be used for high-volume manufacturing because of their balance of excellent durability and moderate cost [29]. Metals have quite different properties from polymers, generally having elastic moduli one or two orders of magnitude higher (at room temperature), and thermal expansion coefficients one to three orders lower. The metals used for embossing molds undergo far less drastic changes in properties over the processing temperature range; in fact, their properties are nearly constant.

One very important consequence of the property mismatch between metal molds and polymer parts in hot embossing is the development of thermal stresses during cooling. Kendall considered the effects of volumetric strain in an adhesive layer caused by shrinkage during curing or by thermal contraction [106]. In the worst case where change in shape of the adhesive layer is prevented by the constraint of the relatively rigid adherend, residual stress will contribute to the strain energy of the system just as external loads would. Kendall proposed that the toughness of the interface (Eq. 2-2) should be replaced by the adjusted toughness in Equation 2-17, in which the intrinsic toughness of the interface is reduced by the energy contribution from volumetric strain.

$$G_C = G_0 - \frac{\kappa \epsilon^2}{2} t \qquad\qquad \textbf{2-17}$$

where

G$_C$ Adjusted toughness or critical strain energy release rate
G$_0$ Toughness at zero volumetric strain
κ Bulk modulus of adhesive
ε Volumetric strain of adhesive
t   Adhesive layer thickness

Similarly, Cannon et al.. studied cracks at the edges of residually stressed thin films and gave the strain energy release rate and crack-extension criterion as Equation 2-18 for cracks that are long compared to the film thickness [107]. Treating the mold as rigid and substituting for thermal stress to apply this criterion to hot embossing gives Equation 2-19.

$$G = \frac{\sigma^2(1-v)t}{E} \geq G_C \qquad\qquad \textbf{2-18}$$

$$G = E(1-v)(\alpha \Delta T)^2 t \geq G_C \qquad\qquad \textbf{2-19}$$

where

G   Strain energy release rate
G$_C$ Toughness of interface
σ Biaxial residual stress
v Poisson's ratio
t   Film thickness
E   Elastic modulus
α Linear thermal expansion coefficient
ΔT Change in temperature

Figure 2.14 shows a plot of G calculated according to Equation 2-19 for a 1.58 mm thick layer of PMMA adhered to a rigid mold while cooling from an embossing temperature of 135°C. Works of adhesion for PMMA on Aluminum and Nickel (adjusted for temperature) are shown for comparison. Accounting for thermal expansion and elasticity of the mold would not alter this calculation significantly, since the metal mold is three orders of magnitude stiffer and has a thermal expansion coefficient one order lower. After cooling less than 15°C, the strain energy due to thermal stress in the PMMA layer exceeds the work of adhesion, and spontaneous

demolding would be expected if the toughness of the interface were equal to the work of adhesion.
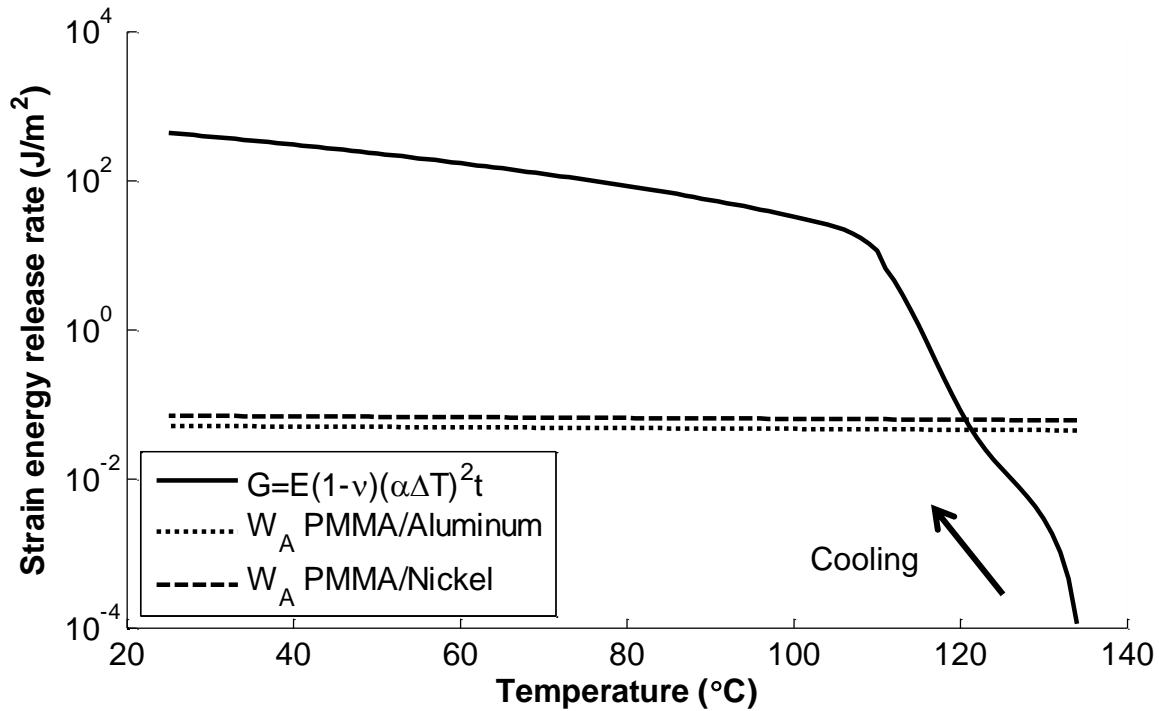
Figure 2.14 Strain energy release rate for a 1.58 mm thick PMMA part adhered to a rigid mold cooling from 135°C where G is calculated as in Eq. 2-19 after Cannon et al. [107], using PMMA properties according to Ames [105].

2.5.3 Stress concentration factors and mode mixity in demolding

Thermal contraction mismatch between the mold and part not only produces residual stress in the part, but shear loads at the interface. These loads result in mixed-mode conditions at the crack tip, which have been found to alter fracture behavior [100, 101]. Suo and Hutchinson considered the case of a semi-infinite crack between two infinite elastic layers subject to general loads, as shown in Figure 2.15 [108].
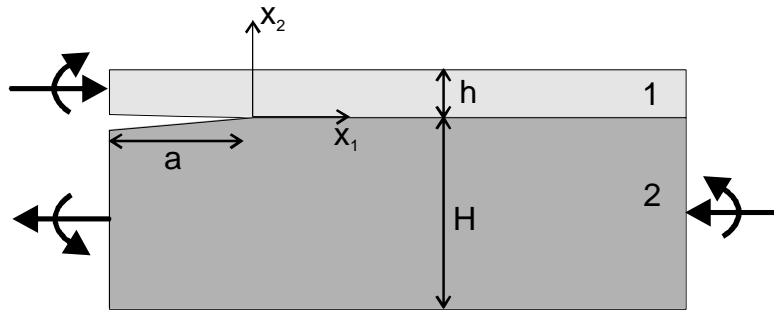
Figure 2.15 Semi-infinite interfacial crack between two infinite elastic layers subject to general loading.

Suo and Hutchinson developed an analytical solution for the complex stress intensity factor that depends on a real scalar parameter that is independent of loading [108]. This parameter was then found from the numerical solution for one load condition. For a thin layer adhered to a thick substrate (h≪H) where the layer is subject to thermal mismatch stress, they give the complex stress intensity factor as Equation 2-20.

$$K = K_1 + iK_2 = \sigma \left(\frac{1 - \alpha}{1 - \beta^2} \frac{h}{2} \right)^{1/2} h^{-i\epsilon} e^{i\omega} \qquad \textbf{2-20}$$

where

i	$\sqrt{-1}$
K_i	Components of the complex stress intensity factor
σ	Thermal mismatch stress
α, β	Dunders constants (see Eq. 2-10)
h	Layer thickness (h≪H)
ϵ	Bi-material constant (Eq. 2-12)
ω	Numerical parameter (function of α, β, and h/H, tabulated in [108].)

The assumption that h≪H is justified because in hot embossing the metal mold is usually bolted to the much larger platen assembly. The numerical parameter ω is an angle that is a function of the Dunders constants α and β and the ratio h/H, which must be evaluated numerically. This function was tabulated by Suo and Hutchinson for various values of the input parameters. For a PMMA layer and a metal substrate, $\alpha \sim -1$ and $\beta \sim 0$ above T_g and $\beta \sim -0.2$ below T_g. From Suo and Hutchinson's Table 1, for h≪H, ω is ~55° and ~47° above and below T_g, respectively [108].

The strain energy release rate can be calculated from the stress intensity factor given by Eq. 2-20. This value is plotted in Figure 2.16 along with the strain energy release rate calculated from 2-18 and the temperature-adjusted work of adhesion between PMMA and Aluminum. The two values of G are within ±20% of one another.
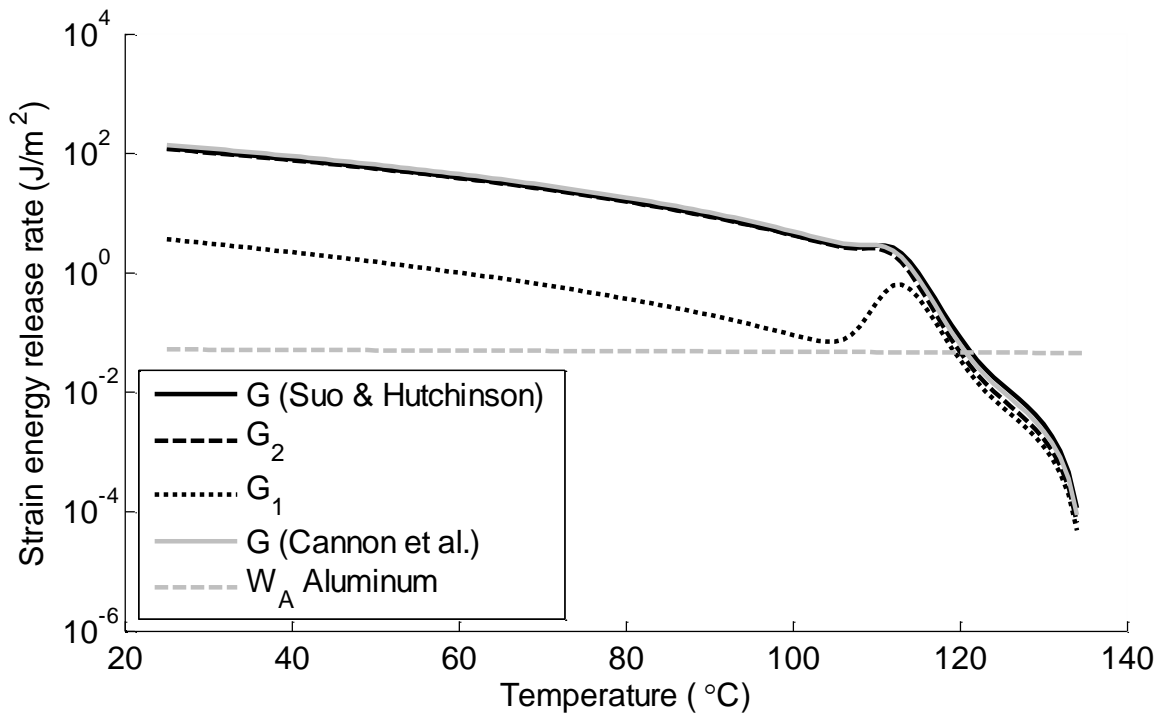
Figure 2.16 Comparison of strain energy release rates calculated from different models for a 1.58 mm PMMA layer adhered to a thick Aluminum mold cooling from 135°C. G_1 and G_2 are the strain energy release rates associated with K_1 and K_2 calculated from Eq. 2-20.

The benefit of calculating the stress intensity factor is that the phase angle of loading can be determined. This parameter is plotted in Figure 2.17. Above T_g, the phase angle is about 50°, corresponding to Mode I and Mode II loading in roughly equal proportion. Below T_g, however, the phase angle is about 80°, corresponding to dominant Mode II loading. This result matches the intuitive expectation that thermal mismatch stress would produce severe shear loads at the interface. The large jump at T_g is related to the rapid increase in the elastic modulus of PMMA through the glass transition.
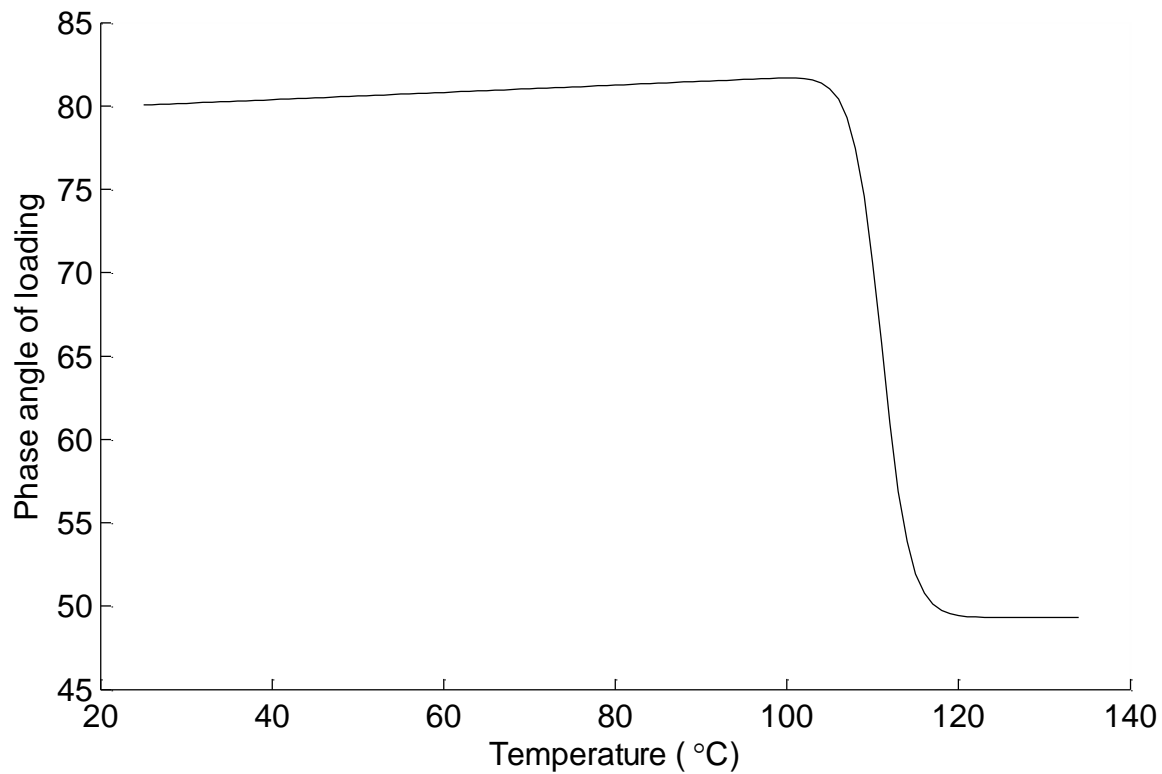
Figure 2.17 Phase angle of loading for 1.58 mm thick PMMA adhered to a thick Aluminum mold and cooling from 135°C calculated from Eqs. 2-20 and 2-14. The jump at 110°C is caused by the rapid increase in stiffness of the PMMA below T$_g$.

The approach of Suo and Hutchinson can be modified to add the effect of a demolding force. Their approach is based on infinite elastic layers, so the demolding force is modeled as a moment applied to the adhered part. Their Appendix III details how different loads may be superposed to determine the complex stress intensity factor [108]. Applying a line moment (moment per unit width into the page) to the semi-infinite model equivalent to the concentrated moment associated with displacing the tip of the finite cantilever model in Figure 2.11 by a fixed amount results in Equation 2-21. The equivalent moment based on simple beam theory is given by Equation 2-22.

$$K = K_1 + iK_2 = \left(\sigma - \frac{i\sqrt{3}}{2}\frac{M}{h^2}\right)\left(\frac{1-\alpha}{1-\beta^2}\frac{h}{2}\right)^{1/2} h^{-i\epsilon}e^{i\omega} \qquad \textbf{2-21}$$

$$M = \frac{E'\delta h^3}{a^2} \qquad \textbf{2-22}$$

where

i $\sqrt{-1}$

K_i Components of the complex stress intensity factor

σ Thermal mismatch stress

M   Applied moment

α, β Dunders constants (see Eq. 2-10)

h   Layer thickness (h≪H)

ϵ Bi-material constant (Eq. 2-12)

ω Numerical parameter (function of α, β, and h/H)

E'   Effective modulus (E' = E for plane stress and $E/(1-v^2)$ for plane strain)

δ Displacement of beam end

a   Length of initial crack

The effect of this applied "demolding moment" is to increase the overall strain energy release rate (Figure 2.18). If cooling alone has not exceeded the fracture resistance of the interface, the additional strain energy from tip deflection will overcome it and the part will be demolded.
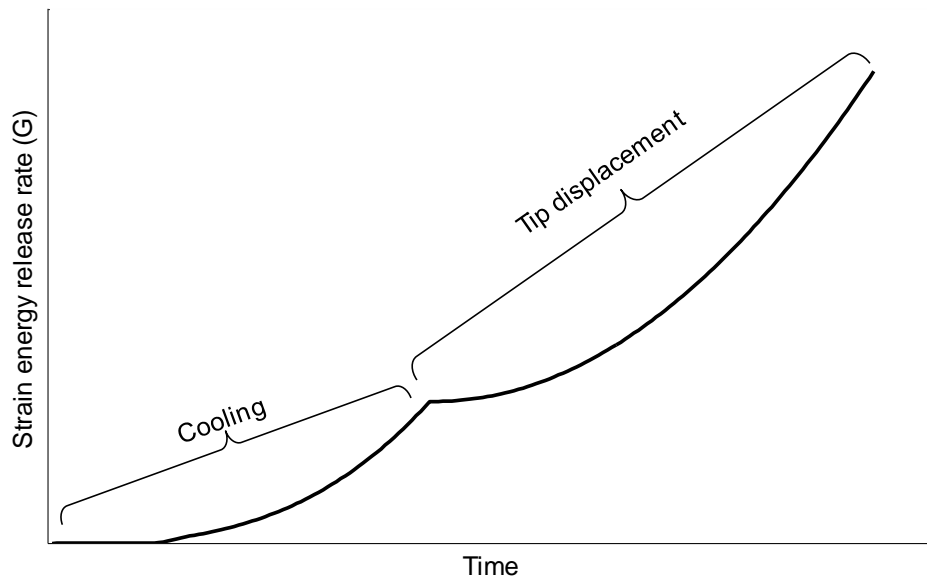
Figure 2.18 Combined effects of cooling and tip displacement on strain energy release rate for an adhered part.

This increase is not evenly divided between Mode I and Mode II loading. The applied moment increases the Mode I loading as expected, but decreases the Mode II loading. The latter effect is unexpected, but is reasonable in light of the fact that the (tensile) bending stress at the bottom surface of the part counteracts the thermally induced shear stress at the interface. The result is that the phase angle is reduced as tip displacement (and the corresponding moment) increases. The phase angle is plotted as a function of temperature and tip displacement in Figure 2.19 and Figure 2.20 for a 1.58 mm thick PMMA layer adhered to a thick Aluminum mold with an initial crack 8 mm long. During cooling, the phase angle progresses along the horizontal axis (tip displacement = 0). Then, when the demolding temperature has been reached and the tip displacement is applied, the phase angle moves along a vertical line in Figure 2.19 (or follows the marked contours in Figure 2.20), until the fracture resistance of the interface is overcome and the crack propagates.
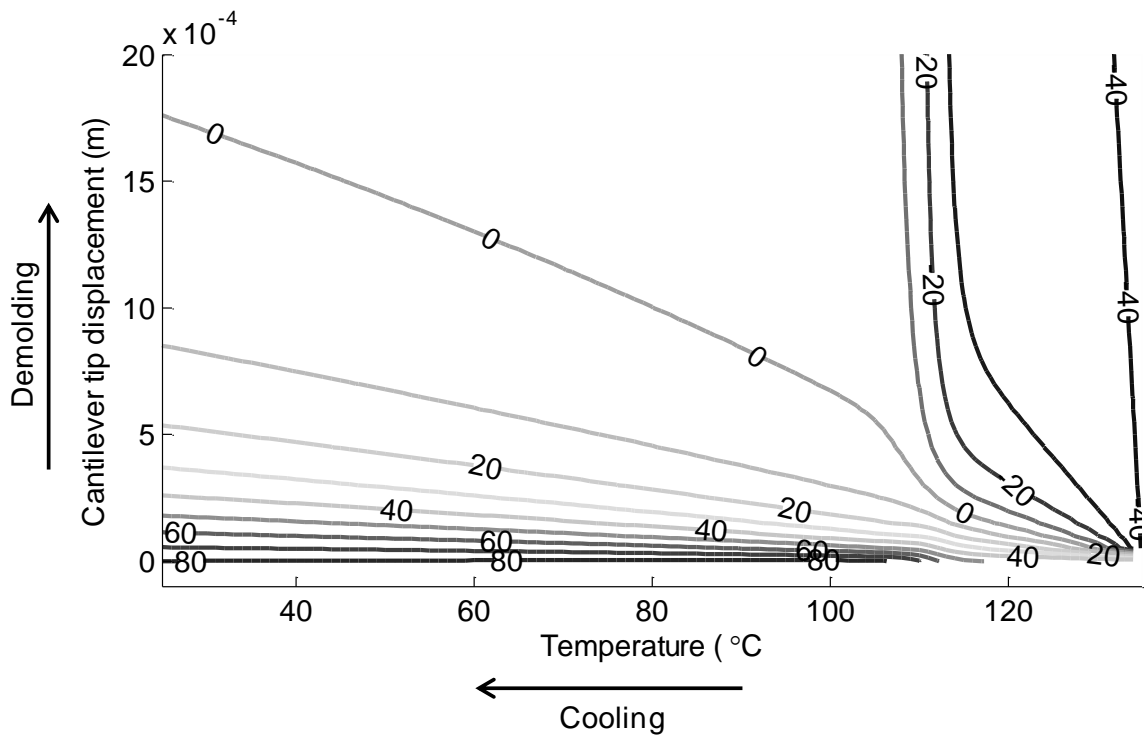
Figure 2.19 Contour plot of phase angle during cooling and demolding for a 1.58 mm thick PMMA part adhered to a thick Aluminum mold with an 8 mm initial crack cooling from 135°C.

57
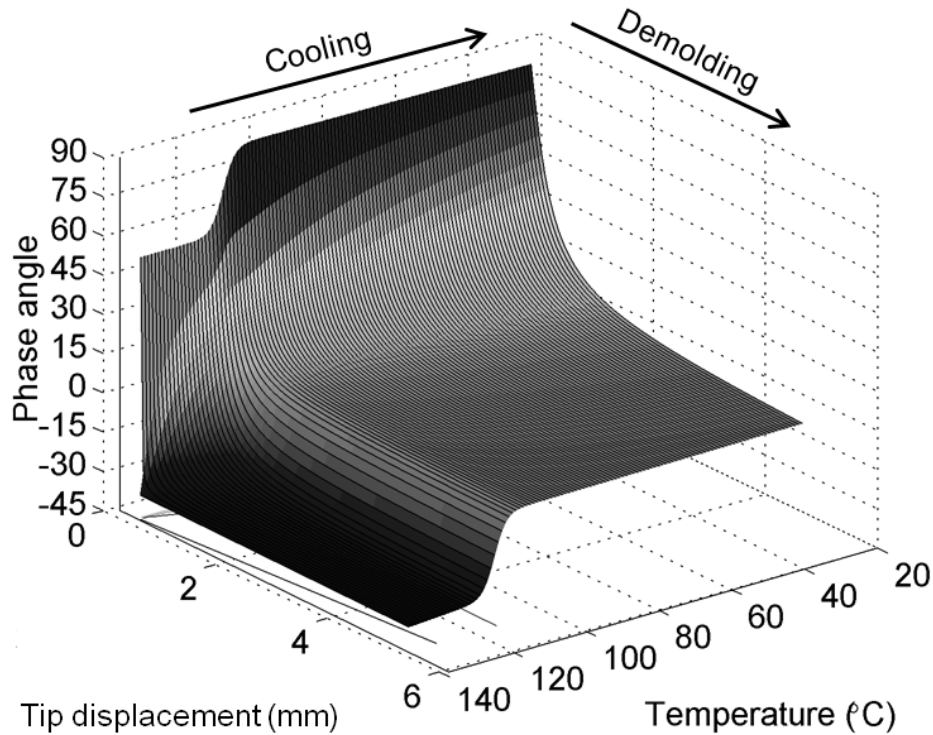
Figure 2.20 Surface plot of phase angle for a 1.58 mm thick PMMA part adhered to a thick Aluminum mold with an 8 mm initial crack cooling from 135°C.

2.6 Effects of mold features

From the calculated strain energy release rate plotted in Figure 2.14 and Figure 2.16, it can be seen that that even for apparently minor reductions in temperature, thermal stress in the polymer part is more than sufficient to overcome the strength of simple surface-to-surface adhesion expected from the work of adhesion. In fact, if the interface toughness was ten, one hundred, or even several thousand times greater than the work of adhesion, the interface would still fail during cooling, before any external demolding load was applied. These results strongly suggest that mechanisms other than adhesion are also operating at the interface.

This section abandons the assumption prevailing in the above sections that the smallness of the mold features relative to the size of the macroscopic mold-part system renders their effects negligible. Given the apparent weakness of surface adhesion and the significant shear loads present at the mold-part interface during cooling and demolding, the effects of features, and the loads on them, must be considered. This conclusion is reinforced by the fact that many of the

defects observed in embossed parts that are related to cooling and demolding are associated with individual features (see sections 1.4.1 and 2.2).

2.6.1 Effect of asperities in mixed-mode fracture

The hypothesis of crack tip shielding by asperities introduced by Evans et al. is particularly relevant for demolding [100, 103, 109]. They propose that, for a brittle interface with a sharp crack tip, there will be a region near the tip where the separation between the crack faces is on the order of the roughness amplitude of the surfaces (Figure 2.21).
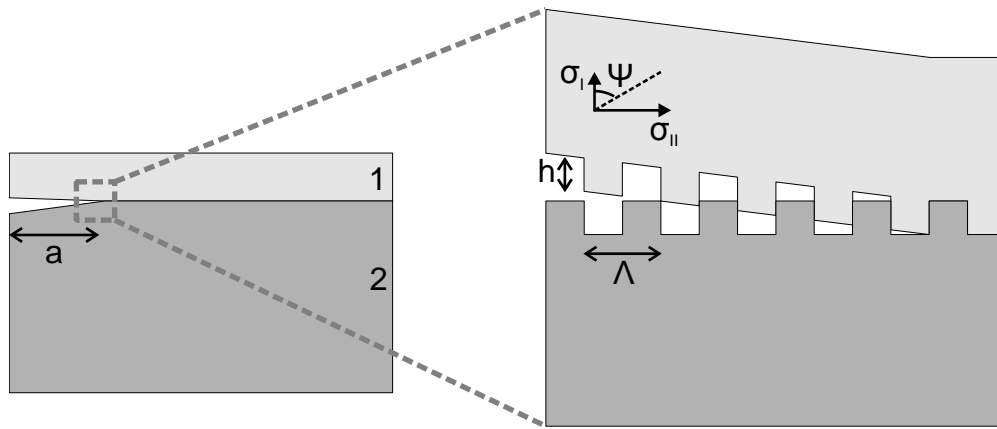
Figure 2.21 Asperity interaction near the crack tip as proposed by Evans et al.. [100, 103].

Shear loading (caused by mixed-mode loading or elastic mismatch) will cause asperities on the surfaces to come into contact laterally. This contact region has the effect of shielding the crack tip from some of the shear loads, leading to an increase in the apparent toughness as measured for the macroscopic system. Friction between the asperities can also have the effect of increasing the measured toughness by providing an additional dissipative mechanism.

Evans et al.. relate the increase in apparent toughness to a proposed dimensionless parameter, χ (Equation 2-23) [100, 109].

$$\chi = \frac{Eh^2}{\Lambda\Gamma_0}$$

2-23

where
χ	Dimensionless parameter related to crack tip shielding
E	Elastic modulus
h	Amplitude, or height of roughness
Λ	Wave length, or spacing of roughness
Γ_0	Intrinsic fracture toughness of the interface

They assert that for low values of this parameter ($\chi \lesssim 10^{-4}$), no shielding is evident until $\psi \sim \pi/2$. Above a threshold ($\chi > 1$), the effect of shielding saturates and additional roughness amplitude does not increase the apparent toughness any further. Their relation depends on Γ_0, the intrinsic fracture toughness of the interface, which they attribute to the work of adhesion. Their proposals imply that for $\psi = 0$ the measured toughness should equal the intrinsic toughness.

It is interesting to note that the crack tip shielding parameter proposed by Evans et al. [100, 109] for the geometry tested by Landis et al. [60] (section 1.5.3) has a value of ~50, suggesting strong crack tip shielding (conservatively assuming a modulus E=1 GPa and using Γ_0=0.274 J/m^2 measured by Landis et al. for an unpatterned stamp).

For materials and geometry typical of microfluidic chips (E~3 GPa, h=10-200 μm, Λ=0.5-5 mm, Γ_0=0.05-50 J/m^2) the parameter χ varies between 1.2 and 2.4×10^7. By this analysis, a large increase in apparent toughness with increasing loading angle would be expected except for very soft materials (E≪3 GPa), very sparse patterns (Λ≫5 mm), or very small features (h≪10 mm). No researchers seem to have attempted to verify the predictive capacity of the parameter χ proposed by Evans et al.. by systematically varying the roughness of an interface. From the calculated values for χ, it is clear that demolding of hot embossed polymer microstructures belongs to an extreme regime compared to the roughness-related crack tip shielding studied by Evans et al.. and that mechanical interactions of features will be important in demolding.

2.6.2   Estimation of forces on feature sidewalls by contact mechanics

Whatever surface-to-surface adhesion that may be present between the part and the mold is easily overcome by thermal stress. Thermal stress creates intense shear loads at the interface, and these loads must be borne by the features. In the previous analysis of thermal stress effects, the part was assumed to be perfectly adhered to the mold. In reality, this constraint is not perfect. Once the part has cooled sufficiently to break the adhesive bond with the mold, the only constraint against thermal contraction is provided by the interlocking of the features, as shown in Figure 2.22a. This interlocking is an imperfect constraint, since the elasticity of the part will permit localized deflections around the features. Such deflection will partially relieve the thermal stress by allowing some contraction of the part. The balance between the thermal stress and the local elasticity can be modeled by the lumped-parameter spring system shown in Figure 2.22b.
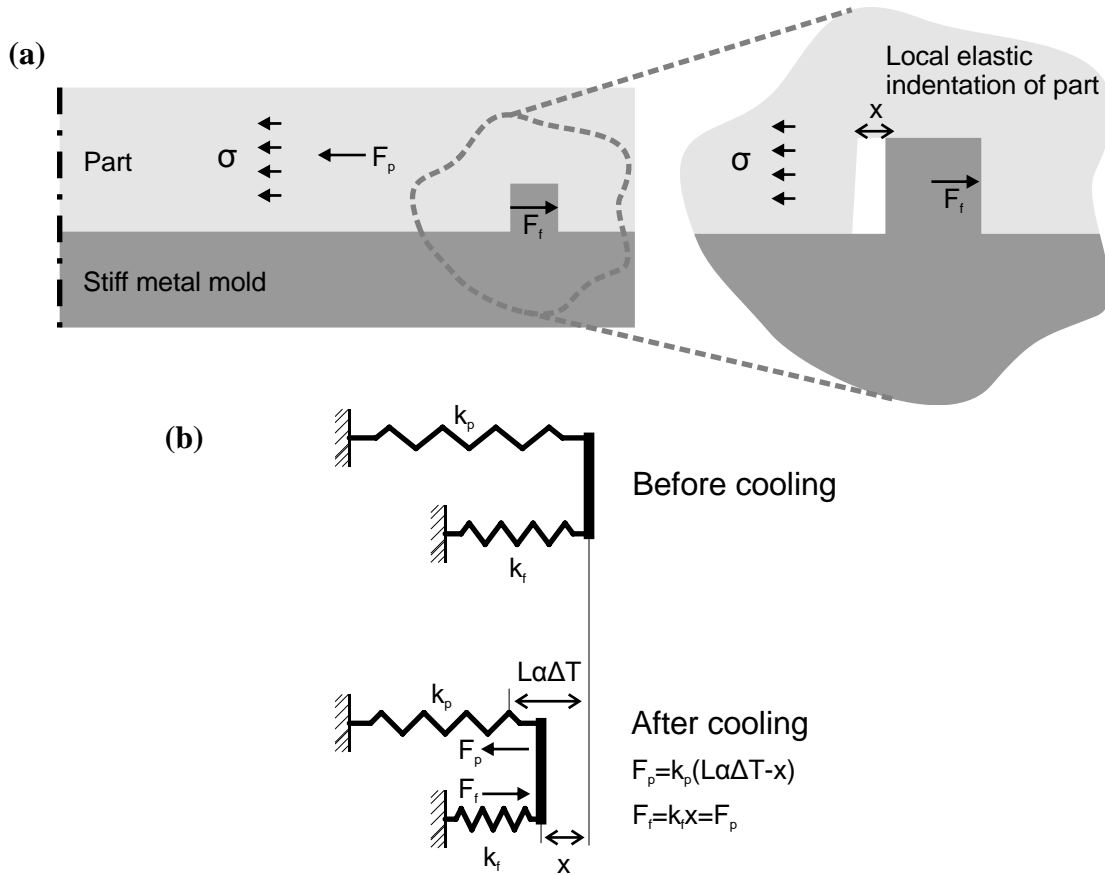
Figure 2.22 (a) Model for sidewall force estimation: PMMA part adhered to a rigid mold with a single feature. Scale is exaggerated. Forces are drawn from the frame of reference of the part, where F_p is the force that arises from the remaining thermal stress in the bulk of the part, while F_f is the force on the feature in the part (sidewall force) (b) The lumped-parameter stiffnesses k_p and k_f correspond to the stiffness of the bulk of the part and the local stiffness of the region near the part feature, respectively, and x represents the amount of local indentation of the part feature.

Consider a part adhered to a rigid mold with a single feature near the edge, as in Figure 2.22, being cooled by an amount ΔT. The part is sufficiently wide so that plane strain conditions prevail. If the part is completely constrained from contracting, thermal stress will build up according to Equation 2-24. If the interlocked feature is assumed to provide this constraint, then the force on the feature must equal the tensile force in the bulk of the part (Equation 2-25).

$$\sigma_{Th} = E\alpha\Delta T \hspace{4cm} \textbf{2-24}$$

$$F_{feat} = \sigma_{Th}A = E\alpha\Delta TA_p \hspace{3cm} \textbf{2-25}$$

where

σ_{Th} Thermal stress
E   Elastic modulus
α   Linear coefficient of thermal expansion
ΔT Change in temperature
F_{feat} Force on the feature
A_p Cross-sectional area of the part

In fact, the interlocked feature will not be able to totally constrain the part from contracting. The force on the feature will cause a local indentation of the part near the feature, which will permit a small amount of contraction. This contraction, in turn, relieves some of the thermal stress. If this local indentation is elastic, the balance between the local stiffness of the part near an interlocked feature and the stiffness of the bulk of the part will result in an equilibrium force given by Equation 2-26, which is derived from the parallel-spring lumped parameter model in Figure 2.22b. The stiffness of the bulk of the part is given by Equation 2-27, but the local stiffness of the interlocked feature is more difficult to determine.

$$F_{part} = F_{feat} = \frac{k_p k_f}{k_p + k_f} L\alpha\Delta T \hspace{3cm} \textbf{2-26}$$

$$k_p = \frac{E w_p t_p}{L} \hspace{4cm} \textbf{2-27}$$

where

F_{part} Force within the part
F_{feat} Force on the feature
k_p Bulk stiffness of the part
k_f Local stiffness of the part near the interlocked feature
L   Distance from feature to center of contraction
α   Linear coefficient of thermal expansion
ΔT Change in temperature
w_p, t_p Width of part (into the page), thickness of the part
E   Elastic modulus

In the limit of a perfectly rigid feature ($k_f \rightarrow \infty$), Equation 2-26 reduces to Equation 2-25. The elasticity of the mold is neglected here, but with an elastic modulus more than ten times

greater than that of the part and with a much larger cross-sectional area, the stiffness of the mold would have a negligible effect on the estimated sidewall force.

To estimate the local stiffness of the part near the interlocked feature (k_f), the load on the feature is modeled as a line load on the surface of a semi-infinite plane, as depicted in Figure 2.23. The deflection at the surface for a given line load (force per unit width into the page) is given by Equation 2-28 [110]. The local stiffness is estimated from the stiffness of the contact mechanics model, given by Equation 2-29.
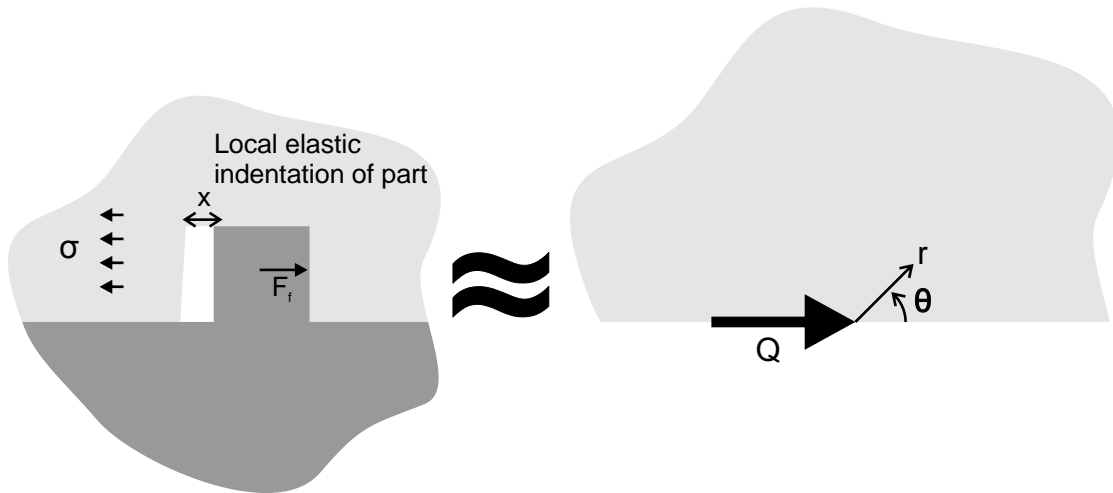
Figure 2.23 Line load applied parallel to the surface of a semi-infinite plane model used to estimate the local stiffness of the part near an interlocked feature [110].

$$x_r|_{\theta=0} = \frac{(1-v^2)}{\pi E} 2Q \ln\left(\frac{r_0}{r}\right)$$

<div align="right">2-28</div>

$$k_f \approx \frac{Qw_f}{x_r|_{\theta=0}} = \frac{\pi E w_f}{(1-v^2)2\ln\left(\frac{r_0}{r}\right)}$$

<div align="right">2-29</div>

where
x   Local deflection
Q   Tangential line load applied to semi-infinite plane
E   Elastic modulus
v   Poisson's ratio
r_0 Reference distance
r   Radial coordinate
k_f Local stiffness of the part near the interlocked feature
w_f Width of feature into page

As in fracture mechanics, this contact mechanics approach produces a singularity at the origin (the point where the load is applied). Values of r and r_0 must be selected to calculate k_f. The parameter r_0 arises from the boundary conditions used to derive this relation; it is a reference distance from the origin where deflection is set to zero. The variable r is the distance from the origin where the deflection is evaluated. As r goes to zero, the deflection becomes infinite, and the stiffness goes to zero. Values for r and r_0 were chosen as 1 μm and 1 mm respectively. The sidewall force calculated in Equation 2-26 is not very sensitive to the values chosen for these parameters, varying less than ±8% when r and r_0 are separately varied by a factor of $10^{\pm 2}$.

Substituting Equation 2-29 into Equation 2-26, the estimated force on the feature can be corrected for the local stiffness. The distance from the feature to the center of the part is 25 mm. The force on the feature estimated by these models is plotted in Figure 2.24.
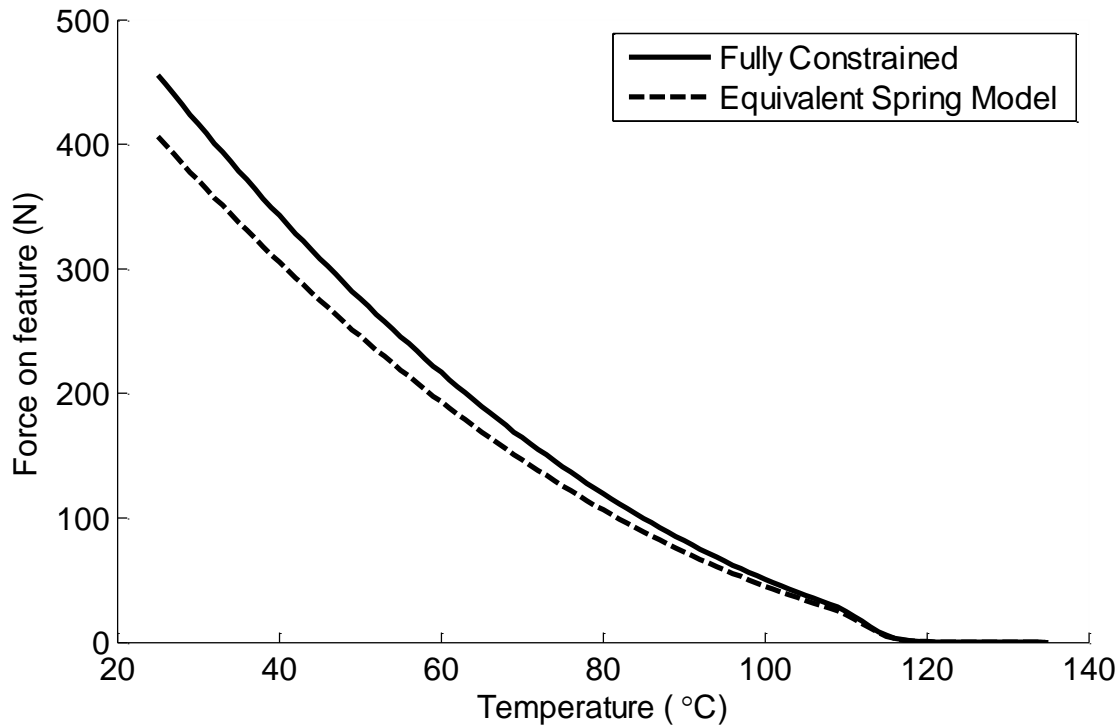
Figure 2.24 Plot of estimated sidewall forces for a 1.58 mm thick and 10 mm wide PMMA against a rigid mold with a single feature near the edge cooling from 135°C. Fully constrained model calculated from Eq. 2-25, equivalent spring model calculated from Eq. 2-26.

The calculated values for sidewall force are quite large. This is mainly attributed to the large distance between the center and the feature (25 mm). Real embossing molds have several features, and so the thermal stresses will be distributed among the outer and inner features. The equivalent spring model in Figure 2.22b can be repeated to represent a mold with multiple

features, as in Figure 2.25. Equation 2-26 can then be stated in matrix form as Equation 2-32, where k_p is calculated from Equation 2-27 where L is replaced by the inter-feature spacing, Λ.
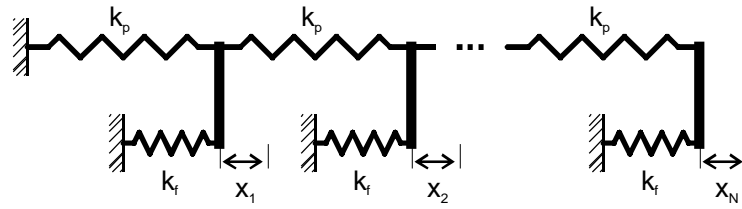
Figure 2.25 Equivalent spring model for multiple features.

$$\overline{\overline{K}}\overline{x} = \Sigma\overline{F}$$

$$\begin{bmatrix} k_f & -k_p & & \\ k_p & k_f & -k_p & \\ & \ddots & \ddots & \ddots \\ & & k_p & k_f + k_p \end{bmatrix}\begin{bmatrix} x_1 \\ x_2 \\ \vdots \\ x_n \end{bmatrix} = \begin{bmatrix} 0 \\ 0 \\ \vdots \\ k_p\Lambda\alpha\Delta T \end{bmatrix}$$
  2-30

$$\overline{F} = k_f\overline{x}$$
  2-31

where
k_p Bulk stiffness of the part
k_f Local stiffness of the part near the interlocked feature
x_i Local elastic indentation
Λ Inter-feature spacing
α Linear coefficient of thermal expansion
ΔT Change in temperature
F   Forces on features

Equation 2-30 can be solved for the local displacements, and the forces can be found by multiplying the local displacements by the local stiffness k_f as in Equation 2-31. The estimated force on each feature for a part embossed with a mold with 12 features spaced 2 mm apart is plotted in Figure 2.26. The load on each feature decreases from outer to inner (the mold is assumed to be symmetric, with 24 features in total).
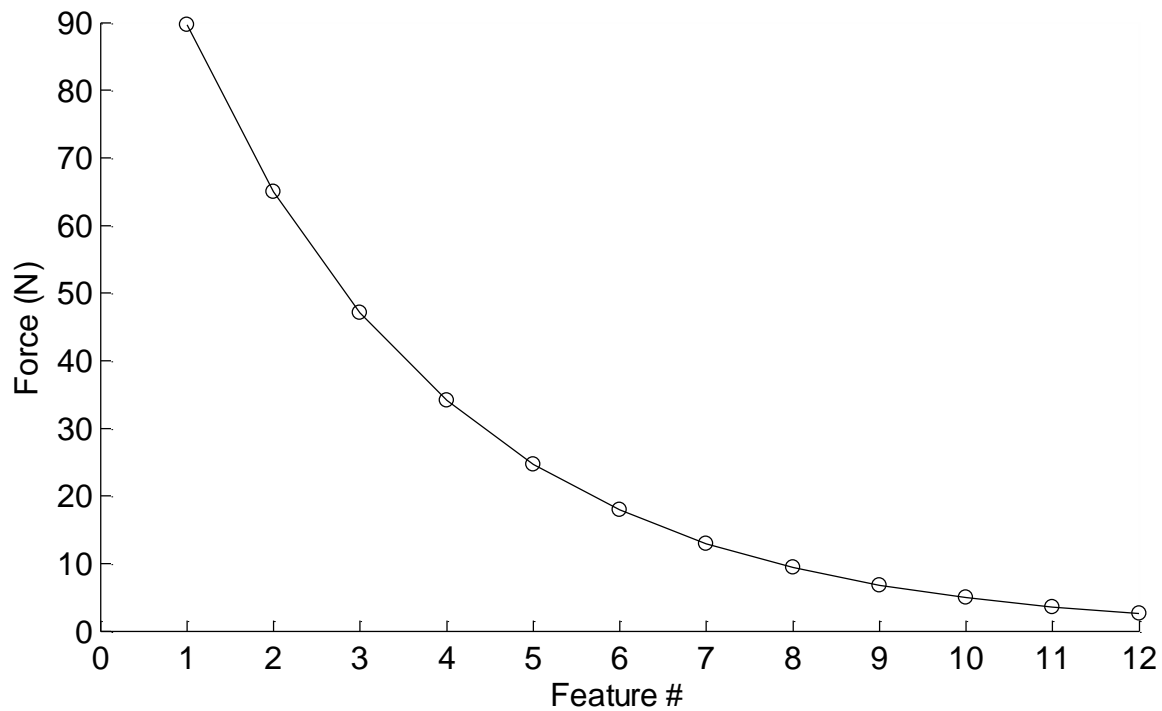
Figure 2.26 Estimated sidewall forces according to Eq. 2-30 and 2-31. Feature #1 is the outermost. 1.58 mm thick and 10 mm wide PMMA cooling from 135°C to 25°C, half of a symmetric rigid mold for a mold with 24 features spaced 2 mm apart.

Although the overall part size is similar (24 mm vs. 25 mm for the symmetric half), the maximum force on the outer feature is much lower than for the single-feature mold (about 90 N vs. 400 N). This reduction is attributed to sharing of the load among multiple features. It is interesting to note that if the number of features in Equation 2-30 is reduced by one, the maximum force is nearly unchanged. This means that during demolding, when the outermost feature is released, the maximum load transfers to the next feature. At least for the several outer features, the local loading condition is the same for each feature immediately before it is demolded. Furthermore, the local conditions immediately before demolding do not depend on the number of features or the overall size of the part, but only on the local inter-feature spacing.

2.7 The Demolding Work

Demolding is the process of releasing the part from the mold by overcoming the bond between them. This process consumes energy, just like fracturing a homogenous body or a bonded interface between two bodies. By analogy with the fracture energy, the energy consumed in demolding, or the "Demolding Work" is proposed as a measure of the strength of the bond

66

between the mold and the part. The demolding work could be measured in a demolding experiment similar to an interfacial fracture experiment (see Chapter 4). Demolding work normalized by area is the "Demolding Toughness."

The demolding work combines the effects of surface-to-surface adhesion (such as the work of adhesion), the energy dissipated by sidewall friction, and potentially the energy dissipated through plastic deformation of features or of parts. This concept is restated as Equation 2-32, where the total demolding work is the sum of the energies contributed by the various mechanisms.

$$DMW = W_A A + W_{fric} + W_{deform}$$
$$\Gamma_{DM} = \frac{DMW}{A} = G_A + G_{fric} + G_{deform}$$

2-32

where
DMW Demolding work
Γ_{DM} Demolding toughness
W_A Work of adhesion, function of Temperature & materials
A Adhered area of part
W_{fric} Energy dissipated by friction, function of temperature, materials, geometry
W_{deform} Energy dissipated by plastic deformation, function of temperature, materials, geometry
G_A Toughness associated with adhesion
G_{fric} Toughness associated with friction
G_{deform} Toughness associated with deformation

These mechanisms are expected to depend on the demolding temperature, the materials involved, as well as the geometry of the features. The contribution of adhesion, for instance, is expected to be minimal at lower demolding temperatures because of the accumulated thermal stress in the adhered part. Similarly, the effect of friction is expected to increase at lower temperatures because of the greater loads on feature sidewalls. Indeed, because of the relative weakness of the work of adhesion, feature sidewall effects are expected to play the dominant role in part/mold adhesion and in determining the difficulty of demolding.

The demolding work associated with adhesion can be estimated as the original adhesive strength degraded by the accumulated thermal stress, after the approach proposed by Kendall [106] by combining Equations 2-17 and 2-19, as in Equation 2-33. The demolding toughness associated with adhesion is plotted as a function of demolding temperature in Figure 2.27 using the measured adhesion strength between PMMA and Aluminum at 135°C (see section 5.4.1).

According to this model, the adhesion component of the demolding toughness is completely degraded at ~60°C.

$$G_{Adhesion} = G_0 - E(1-\nu)(\alpha \Delta T)^2 t \qquad \textbf{2-33}$$

where
G_0 Original adhesive strength
E   Elastic modulus
ν Poisson's ratio
t   Film thickness
α Linear thermal expansion coefficient
ΔT Change in temperature
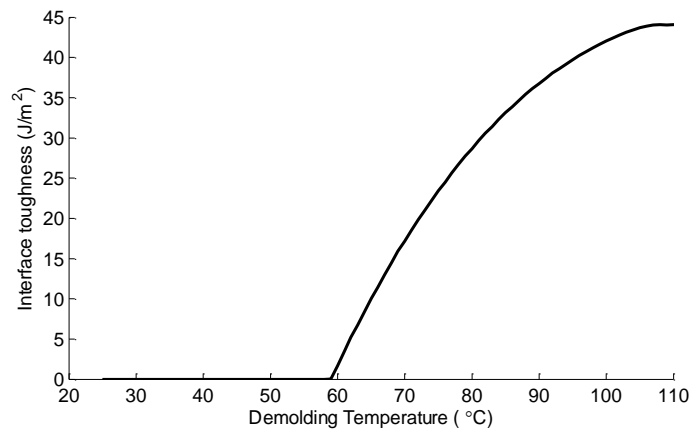
Figure 2.27 Demolding work associated with adhesion as a function of temperature assuming a 1.58 mm thick PMMA part adhered to an Aluminum mold cooling from 135°C using the measured adhesion strength of 50 J/m^2 (see section 5.4.1).

The energy dissipated by friction could be estimated as in Equation 2-34. This estimate assumes that the force on the feature remains constant, and that the energy dissipated while demolding the feature is equal to the product of the frictional force and the feature height (since this is the distance over which the friction force operates), and assumes Coulomb-type friction. The force on the feature would be a function of the demolding temperature, the material properties, and the geometry of the feature (via its local stiffness). Given the very high estimates for the force on the feature, the shear load due to sliding friction could saturate at a maximum shear stress. If that were the case, the energy dissipated by friction would be estimated by Equation 2-35. The value of the maximum shear stress could be a function of temperature. It is important to note that these hypothetical functions for the energy dissipated by friction (W_{fric})

have different dependency on the geometry of the mold. Most importantly, the Coulomb friction model suggests that the demolding work should be independent of the width of the mold features (because Coulomb friction does not depend on the apparent area of contact). Therefore, the results of experiments in which mold geometry is varied systematically could shed light on the specific mechanism (friction, shear stress, etc.) that accounts for the demolding work.

$$W_{fric} = F_{feat}\mu h \qquad \textbf{2-34}$$

$$W_{fric} = \frac{\tau_{max}b_f h^2}{2} \qquad \textbf{2-35}$$

$$G_{fric} = W_{fric}/w_p\Lambda \qquad \textbf{2-36}$$

where

W_{fric}	Energy dissipated by friction, function of temperature, materials, geometry
μ	Friction coefficient
h	Feature height.
τ_{max}	Maximum frictional shear stress
b_f	Width of feature
w_p	Width of part
Λ	Inter-feature spacing

The demolding toughness associated with friction estimated from Equation 2-36 is plotted as a function of temperature for a PMMA part embossed with a 100 μm deep channel in Figure 2.28 assuming a friction coefficient of 0.2.
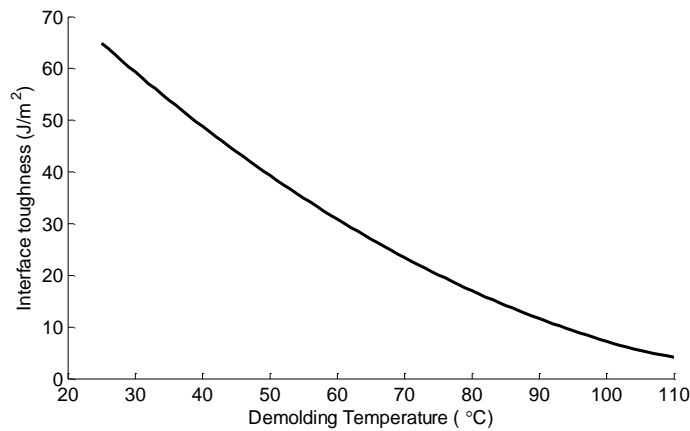
Figure 2.28 Demolding toughness associated with friction for a 100 μm deep channel feature embossed into PMMA, assuming a friction coefficient of 0.2.

The combined effects of adhesion and friction can be given by Equation 2-32, and are plotted in Figure 2.29. There is a clear minimum in the combined demolding toughness at the transition between adhesion-dominant and friction-dominant demolding. The temperature where this transition occurs (~60°C in this case) would be the optimal demolding temperature for this mold pattern.
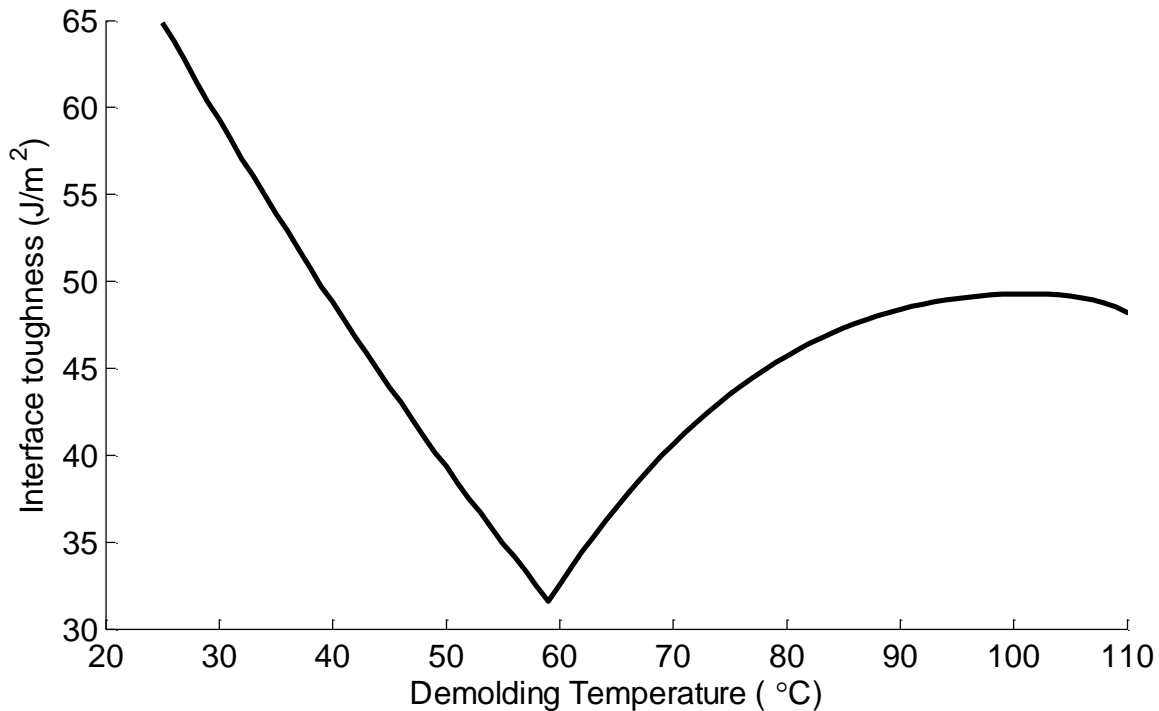
Figure 2.29 Combined effects of friction and adhesion in demolding at temperatures from 25-110°C. There is a clear minimum demolding toughness at the transition between adhesion-dominant and friction-dominant demolding. This point at ~60°C would be the optimal demolding temperature.

Again, by analogy with fracture, the demolding work is considered to be the "fracture resistance" of the part/mold interface, which must be overcome by external loads. Thus, if one knows the demolding work (or toughness), one can estimate the loads required to demold a part. The demolding toughness Γ_{DM} would take the role of the critical strain energy release rate G_C in Equation 2-2.

2.8 Conclusions on mechanics

Adhesion in general is a complex phenomenon related to several mechanisms. The destruction of the adhesive bond between the part and the mold during demolding can be treated as an interfacial fracture problem. Accordingly, it is found that the thermal stress that results

from thermal contraction mismatch between the polymer part and typically metallic molds is the dominant characteristic of demolding. This thermal stress easily overcomes the expected work of adhesion between the part and the mold, but causes severe forces on feature sidewalls. While this result was anticipated in the literature on interfacial fracture, the size of typical features in hot embossing (e.g. microfluidic channels) is much greater than the scale of typical surface roughness, and the effects of sidewall interactions can be considered an extreme case of asperity interaction in interfacial fracture.

Again, by analogy with fracture, the Demolding Work is proposed as a metric of the difficulty of demolding. This demolding work has a physical origin in the combined effects of the work of adhesion and energy dissipated by friction at interlocked feature sidewalls. Because of the dominant effect of thermal stress, demolding temperature is expected to strongly influence the demolding work. The effects of adhesion and friction combine to produce a minimum demolding work at the temperature where demolding transitions from an adhesion-dominated regime to friction-dominated.

At lower temperatures, feature sidewalls are subject to very large loads, which may result in localized deformation. The influences of temperature, feature geometry, and material properties are explored in subsequent chapters through finite element simulation (Ch. 3) and experiments (Ch. 4 & 5).

3 Simulating demolding via the finite element method

3.1 Introduction to the chapter

One obstacle in the way of a total understanding of demolding is the breadth of physical scale involved, from molds and parts that are several tens of millimeters in size, to individual features of tens to hundreds of micrometers, to sub-micrometer and nanometer-scale surface textures and roughness, and finally molecular-scale interactions such as van der Waals forces. The lumped-parameter, part-scale models presented in the previous chapter represent one approach for studying the mechanics of demolding. This chapter presents an intermediate compromise, where local stresses in the region of individual features are modeled using the finite element method, while the properties and interactions at the interface between the part and the mold are still treated in a lumped-parameter fashion as friction coefficients and adhesive constitutive laws. This compromise permits a greater scrutiny of local, feature-scale effects at the expense of the global, part-scale perspective of the previous chapter, but does not permit much exploration of the nano- and micro-scale mechanisms that contribute to friction and adhesion.

Finite element analysis (FEA) is a well-known and widely applied method, so its fundamentals need not be reviewed here. For a deeper discussion of this method, the textbook by Bathe [111] and the documentation for the FEA software package ABAQUS [112] are excellent sources. The simulations discussed below were carried out using ABAQUS version 6.8.1. The subsequent sections describe the FE models that have been used to simulate different aspects of demolding.

3.2 Modeling approach

Within the present work, the purpose of simulation is not to produce a perfect numerical replica of the experimental situation, but to give insights into local effects and mechanisms that operate during an experiment, to test the predictions of various models of the interaction

mechanism between the mold and the part, and to probe the trends in experimental metrics as parameters of the models are varied.

A full representation of an entire part and mold in three dimensions as a finite element model would be impractical both in terms of computational cost and model complexity. A tradeoff can be made against completeness in favor of simplicity and flexibility by restricting the scope of the model. The goals of this simulation effort can be met with a two-dimensional model of a region of the part-mold system encompassing a single feature and the material in its vicinity. Restricting the scope of the simulation to this sub-region helps to mitigate some of the difficulty associated with the wide range of length scales. The plane of the model is parallel to the direction of crack extension, and perpendicular to the plane of the mold surface (Figure 3.1). Because the part and mold are substantially wider in the out-of-plane direction than the in-plane dimensions, plane-strain conditions are assumed.
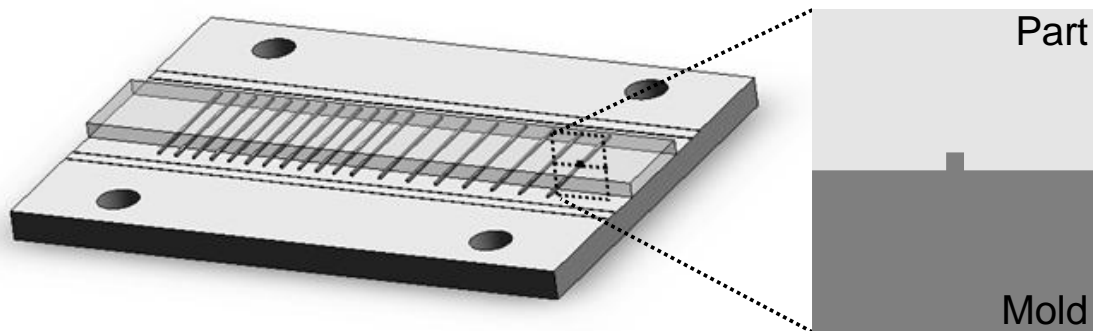
Figure 3.1 Schematic diagram of the two-dimensional plane strain sub-region model used in finite-element simulations.

Another modeling decision to be made is the selection of either an implicit or explicit integration scheme for numerically solving for the stresses and displacements, implemented as ABAQUS/Standard and ABAQUS/Explicit, respectively. This topic is discussed at length by other authors [111, 112]. In both methods, the model history is broken up into simulated time increments.

The implicit method is generally less computationally intensive because it permits larger time increments and thus a smaller number of computations overall. The iterative solution process helps to reduce the impact of computational errors. Implicit simulations, however, do not handle abrupt changes in the system well. This limitation is especially relevant in simulating

demolding, where the moment of separation between the part and the mold is an abrupt transition. Such abrupt changes in the system state can cause the computation to diverge.

Explicit integration can simulate dynamic, abrupt changes, but at greater computational cost. Explicit methods are sensitive to computational errors, which can accumulate and cause the simulated results to diverge. To ensure a stable computation, the time increments must be shorter than the maximum stable increment, which can be estimated from Equation 3-1 [112]. The maximum stable time increment depends on the ratio of the size of the smallest element in the model to the dilatational wave speed in the material (the denominator in Equation 3-1).

$$\Delta t_{max} \lesssim \frac{L_{min}}{\sqrt{\frac{\lambda + 2\mu}{\rho}}}$$

3-1

where
Δt_{max} Maximum stable time increment
L_{min} Minimum element size
λ First Lamé parameter: $\lambda = E\nu/[(\nu + 1)(2\nu - 1)]$
μ Shear modulus: $\mu = E/[2(\nu + 1)]$
ρ Density

Because of the relationship between the maximum stable time increment and the size of the smallest element, explicit simulations of phenomena that span a wide range of length scales require very short time increments and are thus computationally costly. Most of the processes important in demolding, such as the development of thermal stresses during cooling, are slow enough to be treated as quasi-static and can be easily simulated using implicit methods. Implicit integration as implemented in ABAQUS/Standard is used for the finite element simulations in the present work. Although demolding represents an abrupt transition, it has been found that an implicit scheme gives adequate results under certain circumstances.

3.3 Description of the model

The models used for finite element simulations consist of two bodies representing the part and the mold, respectively. For simplicity, the simulation begins at the end of the holding step and the beginning of the cooling step in the hot embossing process. Simulating the large deformations that occur during embossing is itself a difficult problem, which has been addressed by Ames [105] and Srivastava [113], among others.

The part is modeled with an existing feature that replicates the feature on the mold. The part and mold begin the simulation at the embossing temperature, and they are held together with a force that simulates the embossing pressure. The model is cooled to the demolding temperature, and the part is separated from the mold. The specific characteristics of the part and mold, the material properties, and the loads and boundary conditions are discussed in the sections below.

The model dimensions are scaled so that the simulated units are as follows: length= micrometer; force=microNewton; pressure/stress=MegaPascal; energy=picoJoule (1 microNewton · micrometer, or 10^{-12} Joule). Because the model is two-dimensional, the forces and energies are calculated per unit width. The quantitative results that are presented in the sections below have been re-scaled from the simulation units back to conventional units for consistency, and forces and energies have been adjusted for parts that are 10 mm wide, corresponding to the size of most experimental specimens.

3.3.1   Part model

The part is modeled as a two-dimensional deformable body in plane strain (Figure 3.2). The pre-existing feature is a 100 μm wide by 100 μm deep channel. The corners of the channel feature are rounded to reduce computational difficulties associated with sharp corners. The modeled region is 1500 μm high, approximating the thickness of the experimental specimens (section 4.7.1). The modeled region width ranges from 1100 μm to 4640 μm, representing different feature spacing.
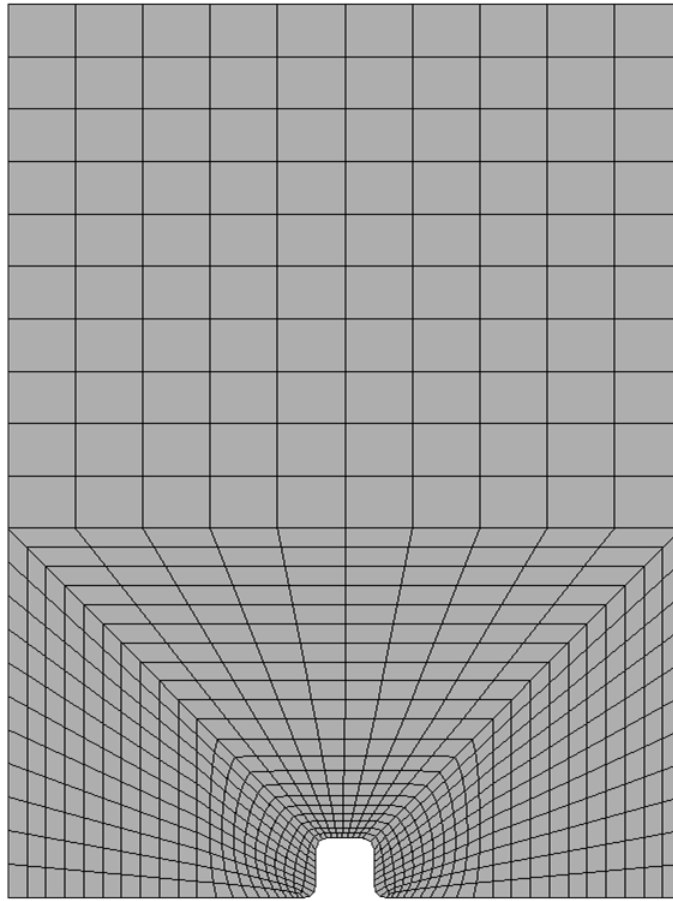
Figure 3.2 Diagram of a part model used in finite element simulations. The model is 1.5 mm high and 1.1 mm wide, and the feature is 100 μm wide and 100 μm deep.

The part is meshed with quadrilateral, linear-order plane strain elements (ABAQUS/Standard element type CPE4R with default settings). The mesh is finer in the region near the feature and coarser elsewhere. Linear-order elements are selected because they present fewer difficulties when subject to contact interactions between solid bodies [112].

3.3.2 Mold model

Depending on the specific purpose of each simulation, the mold is sometimes modeled as perfectly rigid, and other times it is modeled as a deformable body just like the part. The model of the mold has a protruding feature that matches the channel feature in the part (Figure 3.3). The mold models are generally wider than the part models to ensure the nodes at the edges of the part model remain in contact with the mold surface. The deformable mold model is meshed with the same element type as the part, and the mesh is finer in the region near the feature.

(a)

(b)
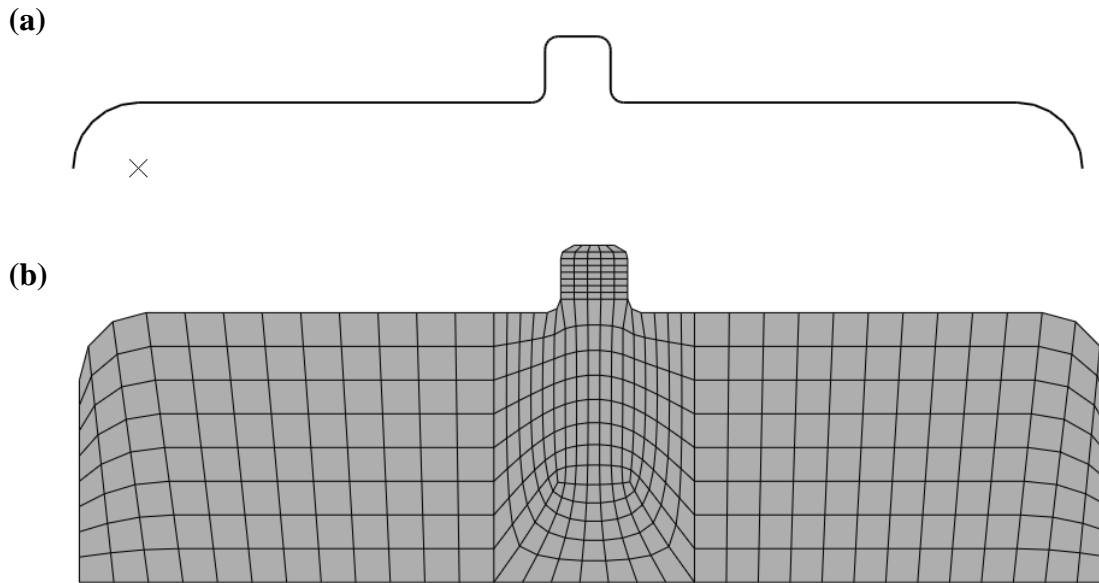
Figure 3.3 Diagrams of mold models used in finite element simulations: (a) analytical rigid model (the "X" is the reference point of the model), (b) deformable solid model.

3.3.3   Material properties

The amorphous thermoplastics that are commonly used in hot embossing exhibit complicated, nonlinear stress-strain behavior that is strongly dependent on the temperature and strain rate. For simplicity and reduced computational cost, the part is modeled as an isotropic rate-independent elastic material with temperature-dependent elastic modulus, Poisson's ratio, and thermal expansion coefficient. The values of the elastic parameters over the simulated temperature range are determined from the models developed by Ames [105] for PMMA subject to quasi-static deformation (strain rate 3×10^{-4}/s). The values of the thermal expansion coefficient over this temperature range are based on data from Wunderlich [114] and smoothly interpolated across the glass transition using an inverse tangent function following the method of Ames [105]. The material properties were calculated at 1°C increments over the range 0-150°C, and these tables were used in the finite element simulations, with intermediate values linearly interpolated by the software as needed. Some simulations used an elastic-perfectly-plastic material model to study plastic deformation; these are discussed in sections 3.4.4 and 3.5.4.

When the mold is modeled as a deformable body, it is given isotropic rate-independent elastic material properties consistent with Aluminum 6061-T6 that are constant over the

simulated temperature range. All of the material properties used for these simulations are tabulated in Appendix A.2.

3.3.4 Interaction properties

The interaction between the mold and the part is a key component of these finite element simulations. For most of the simulations presented below, the interaction between the mold and part is modeled as basic Coulomb friction using the most common implementation in ABAQUS/Standard. The contact pair is defined with the mold surface as the master. Node-to-surface discretization is used with finite-sliding slip tracking, with all other contact formulation settings at their default values [112]. The contact interaction is defined as "hard" in the normal direction, giving zero contact loads when the surfaces are not in contact, and enforcing zero penetration of the master surface by slave nodes when the surfaces are in contact. Tangential interactions are modeled as Coulomb friction with a constant friction coefficient using the penalty friction formulation [112]. Unless otherwise noted, simulations used a friction coefficient of 0.4.

3.3.5 Boundary conditions and loads

For convenience, the simulated model history is separated into several loading steps. In the first step, the initial conditions are applied. These include a uniform temperature for both bodies corresponding to the embossing temperature, horizontal symmetry on the left edge of the model, and vertical symmetry on the bottom edge of the mold. When a rigid mold is used, all of the mold's degrees of freedom are fixed. These boundary conditions are illustrated in Figure 3.4.
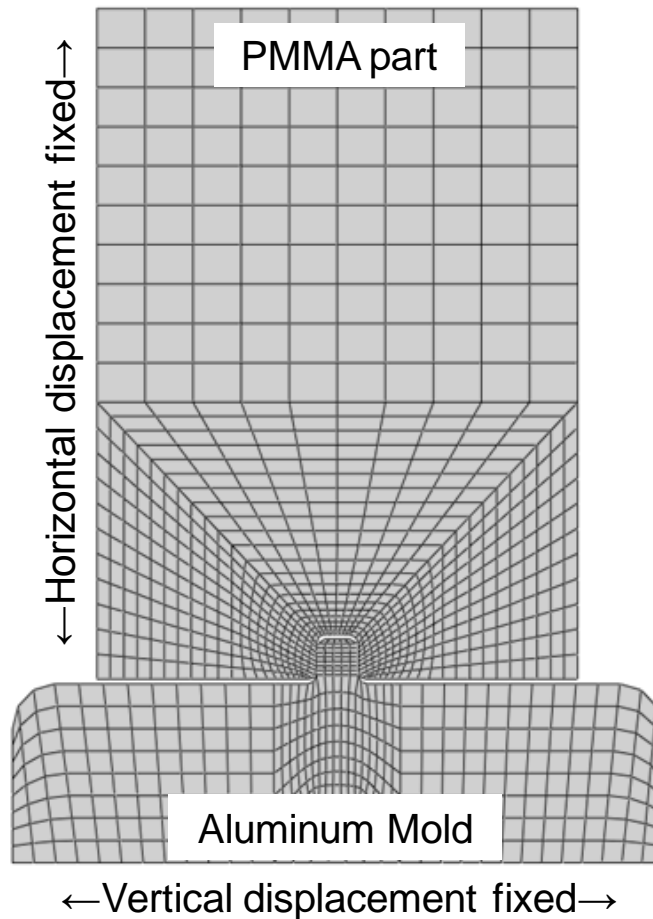
Figure 3.4 Schematic diagram of boundary conditions for finite element simulations.

In the next two steps, a small displacement is applied to the top surface of the part to ensure it is firmly in contact with the mold and to prevent unconstrained rigid-body motion while the part is coming into contact. This displacement is then replaced by a load that simulates the embossing pressure. This load is maintained during the next step, in which the temperature of both bodies is ramped down to the demolding temperature. Heat conduction and thermal gradients are not modeled, and the temperature change is applied uniformly to every element. In actual demolding, the part is thin enough that temperature gradients within it during cooling are not significant, and thermal equilibrium is quickly achieved once the platens are cooled to the demolding temperature (see section 4.5.3).

3.4 Simulated sidewall forces

During the cooling step, the part's contraction is constrained by the interlocked feature, and large stresses develop near the feature. A contour plot of the von Mises stress near the feature for a purely elastic model with a rigid mold cooled from 135°C to 25°C is shown in Figure 3.5. The width of this model region corresponds to an inter-feature spacing of 3 mm, which approximates the spacing of some experimental molds (see section 5.2). The maximum stress (765 MPa) is far in excess of the yield strength of PMMA at this temperature (112 MPa), and the local indentation of the mold feature into the part is significant (compare with Figure 2.22a). This figure also shows separation between the part and the mold after cooling and before demolding.
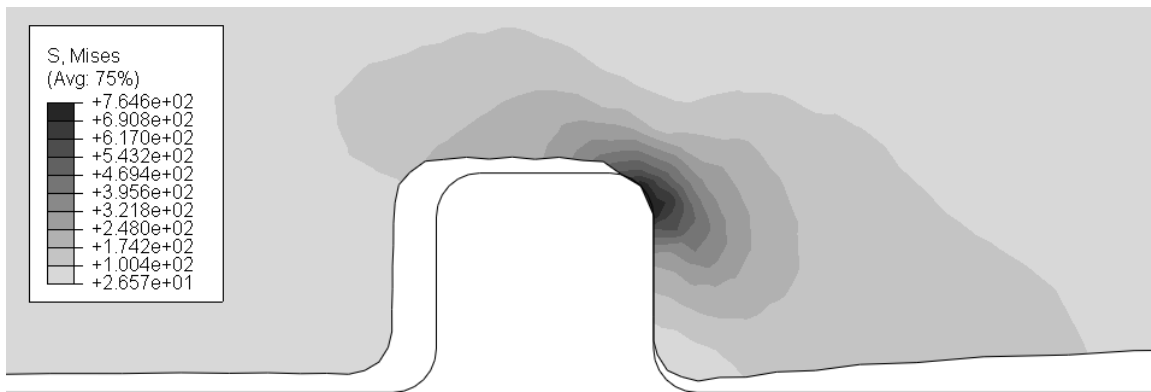
Figure 3.5 Contour plot of von Mises stress in the region near the feature for a PMMA part cooled from 135°C to 25°C while in contact with a rigid mold (thin black line). Overall contraction is towards the left.

The magnitude and components of the contact forces on the defined contact pair are available as standard outputs of the finite element computation. The component of the contact force that is normal to the contact surface (ABAQUS/Standard output parameter CNORMF) is shown in Figure 3.6. The total load on the sidewall adjusted for a 10 mm wide part is 242 N.
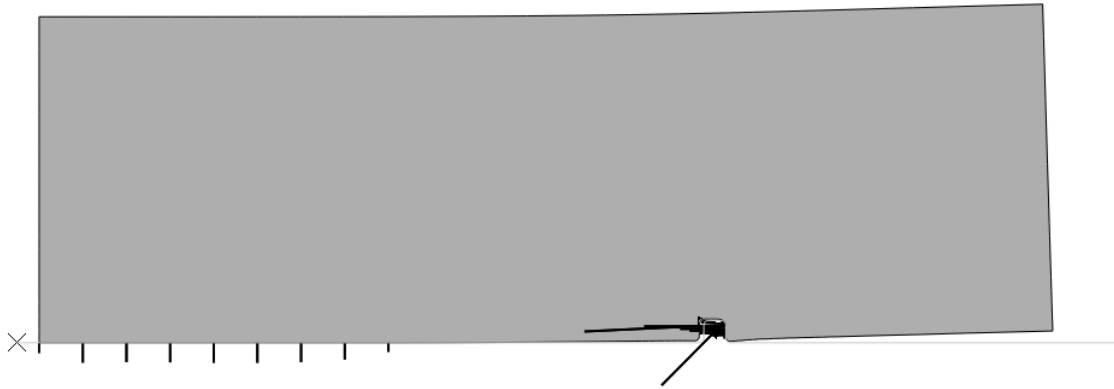
Figure 3.6 Vector plot of normal contact loads for a PMMA part cooled from 135°C to 25°C while in contact with a rigid mold (thin grey line). Overall contraction is towards the left.

The constraint provided by the interlocked feature is imperfect, and so some thermal contraction of the part is allowed. The displacement of the part in the horizontal direction is shown in Figure 3.7. The constraint provided by the interlocked feature also causes some rotation of the part on the right of the feature. This effect qualitatively corresponds to the introduction of Mode I (tensile) loading at the crack tip during cooling, as discussed in section 2.5.3.
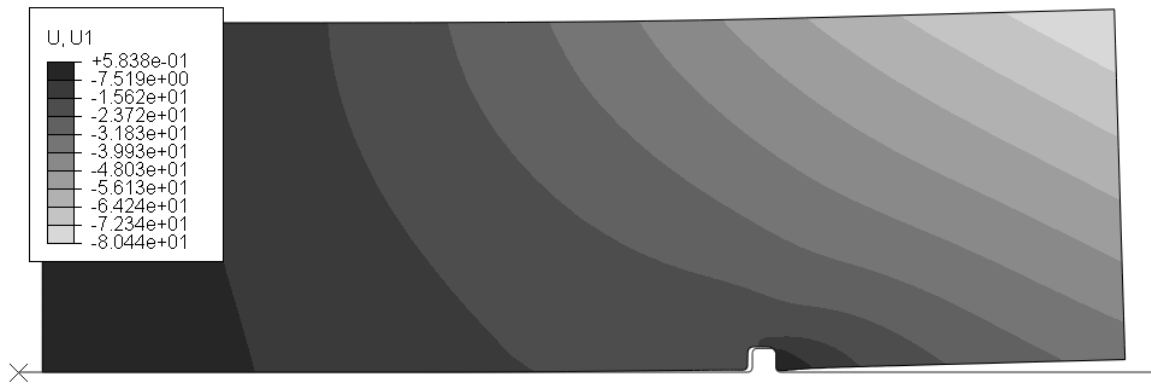
Figure 3.7 Contour plot of deflection in the horizontal direction for a PMMA part cooled from 135°C to 25°C while in contact with a rigid mold (thin black line). Overall contraction is towards the left.

3.4.1   Effects of temperature

As the temperature decreases, the load on the feature increases. The sidewall load from this simulation is plotted in Figure 3.8 along with comparable results (for 3 mm inter-feature spacing) from the lumped-parameter models discussed in Section 2.6.2. This plot shows good agreement (within 10%) between the finite element results and the single-feature lumped

parameter model, with the largest difference in behavior around the glass transition temperature (110°C).
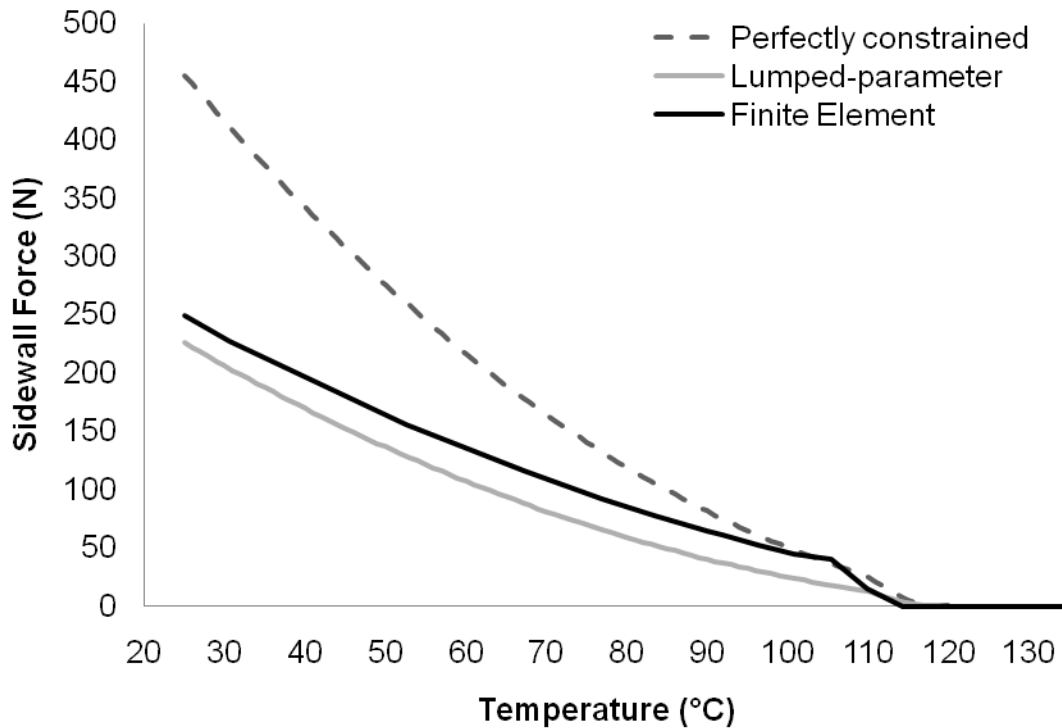
Figure 3.8 Comparison of sidewall force on a single feature simulated by different models. Perfectly constrained model calculated from Eq. 2-25, Lumped-parameter model for a single feature from Eq. 2-26 with the model length set to 3 mm. The load increases for decreasing temperature because of increasing thermal contraction and temperature dependent properties of PMMA.

The lumped-parameter approach models the local indentation of the part in the vicinity of the interlocked feature as a concentrated tangential force at the surface of a semi-infinite body. The overall deflection of the part and the equilibrium sidewall force are determined from the parallel spring model in Figure 2.22. The overall stiffness of the finite element model (determined from the ratio of the sidewall force to the average horizontal deflection of the line between the feature and the top of the part) is plotted in Figure 3.9 along with the overall stiffness of the parallel-spring lumped parameter model. The overall stiffness of the finite element and lumped-parameter models show good agreement (within 10%), with the largest difference in behavior evident near the glass transition.
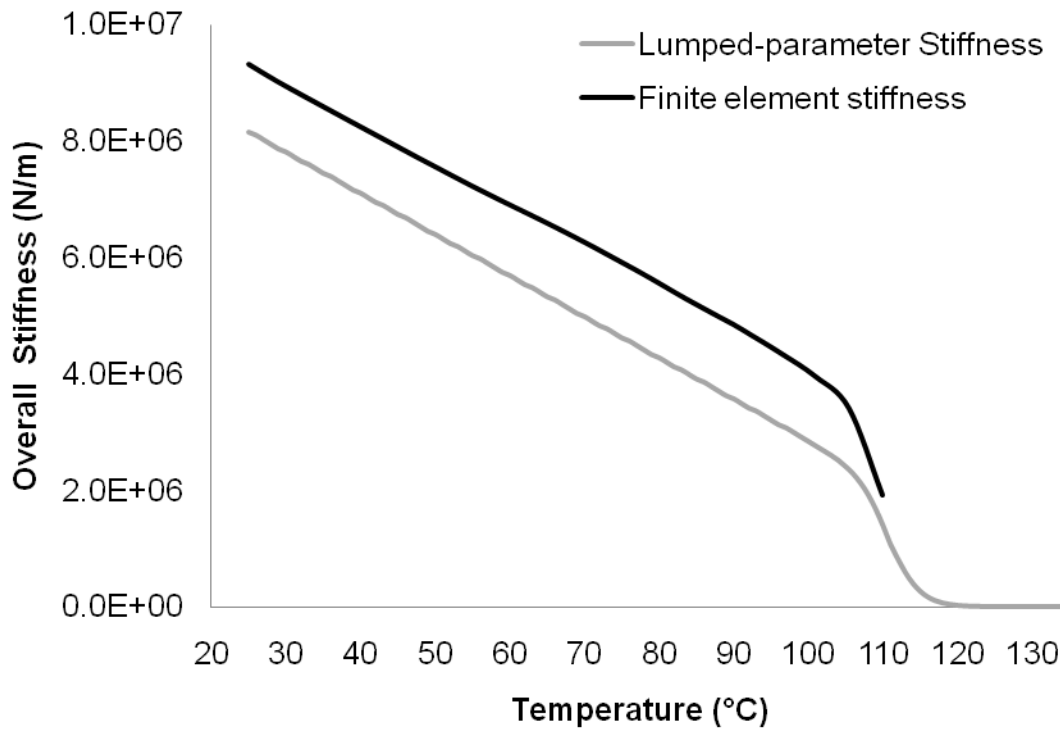
Figure 3.9 Comparison of overall stiffness of the part from different models. Lumped-parameter stiffness (F/x) from Eq. 2-26. The models show good agreement, except near the glass transition temperature (see text). The stiffness increases at cooler temperatures because of the temperature-dependent properties of PMMA.

3.4.2   Effects of multiple features

Real embossing molds have multiple features, and the thermal stresses will be distributed among them. To simulate this effect, a model with three features was created. The features are identical to those discussed in the previous section (100 µm by 100 µm), and are spaced 2 mm apart, which is the same as in some molds used in experiments (section 5.2). This model is shown in Figure 3.10, which also shows the von Mises stress distribution after the model has cooled from 135°C to 75°C. The finite element computations for this model would not converge for lower temperatures.
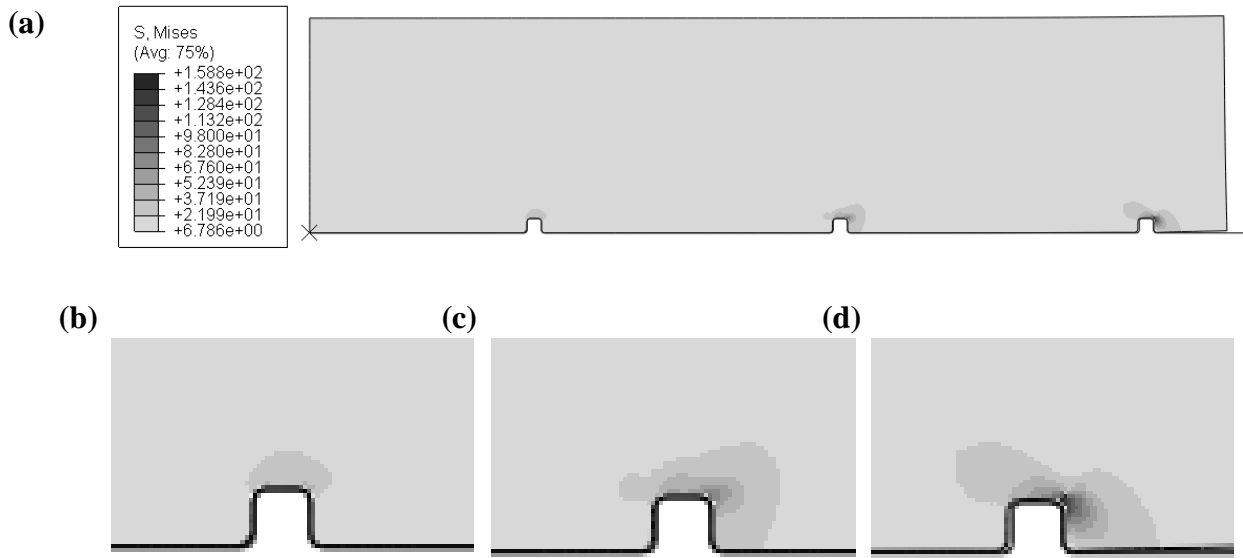
Figure 3.10 (a) Contour plot of von Mises stress in a PMMA part against a rigid tool cooled from 135°C to 75°C. Spacing between features is 2 mm. Overall contraction is towards the left. Detailed views of the stresses near the (b) outer (c) middle and (d) inner features.

As is evident from Figure 3.10, the loads are not evenly distributed among the three features. Figure 3.11 compares the sidewall forces predicted by this model with those given by the lumped parameter model for multiple features (Eq. 2-30). Both models agree in the qualitative trend of higher forces on the outer features, but the finite element model predicts higher force magnitudes. Comparing the force on the outermost feature, the finite element model result falls between those of the single-feature and multiple-feature lumped parameter models (both calculated for 2 mm spacing and 75°C). Increasing the number of features in the finite element model may produce better agreement with the lumped parameter multi-feature model.
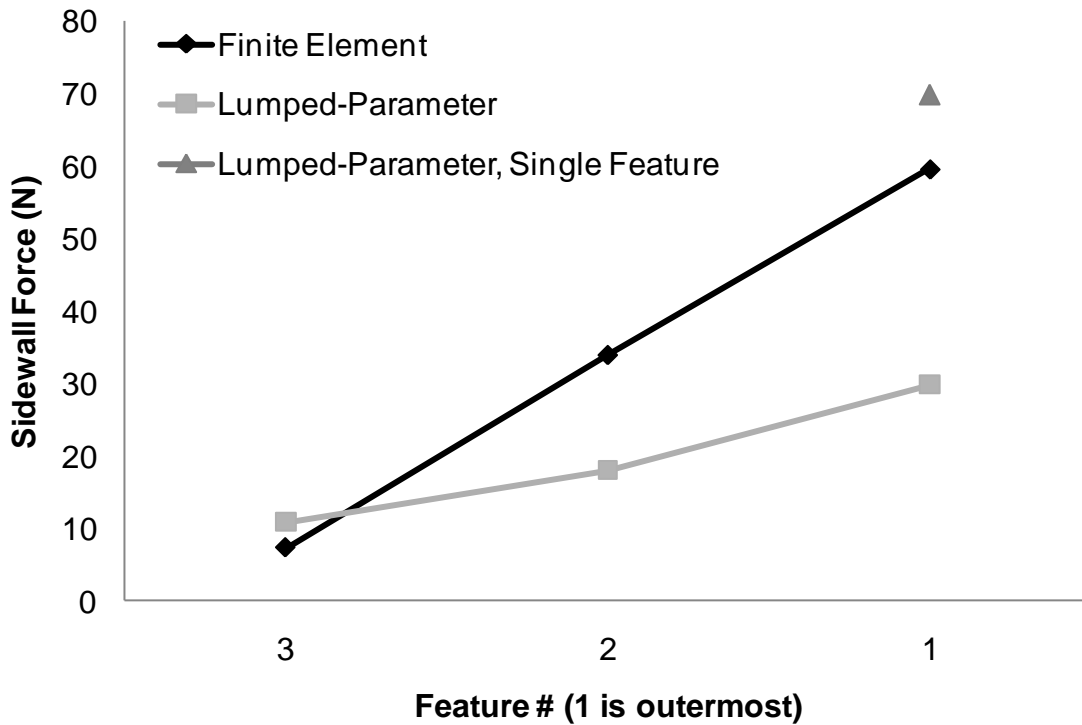
Figure 3.11 Comparison of sidewall forces from different models of parts cooled from 135°C to 75°C. Lumped-parameter multi-feature model from Eq. 2-30 with feature spacing 2 mm. Lumped-parameter model for a single feature from Eq. 2-26 with the model length set to 2 mm.

3.4.3 Effects of spacing

Feature spacing plays an important role in the lumped-parameter models, and this is also the case in finite element models. Sidewall force results from the finite element and single-feature lumped parameter models are compared in Figure 3.12. Sidewall forces increase with feature spacing.
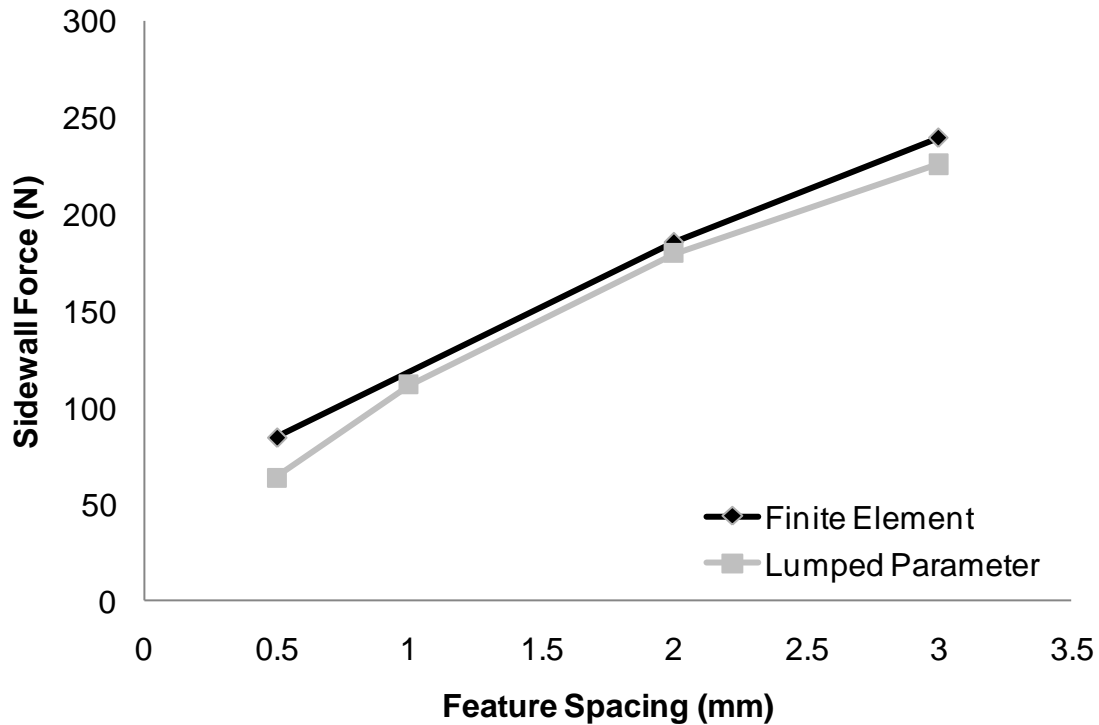
Figure 3.12 Comparison of sidewall force for different feature spacing (model length for single-feature lumped parameter model) for PMMA cooled from 135°C to 25°C against a rigid mold.

3.4.4 Plastic deformation

Recalling Figure 3.5, the concentrated stress in the part near the feature often exceeds the expected yield strength of the material. To investigate permanent deformation during cooling, simulations were carried out using an isotropic rate-independent elastic-perfectly-plastic material model with a von Mises plastic flow rule. This model uses the same values for the elastic constants and expansion coefficient as the purely elastic model. The temperature-dependent yield stress in the plastic model is taken from a linear least-squares fit to empirical data from quasi-static compression experiments below the glass transition temperature (Figure 3.13 and Figure 3.14) [105]. The large-deformation behavior of PMMA is complex, but any amount of deformation would result in a "failed" part, and so the onset of yielding is the most important phenomenon to capture. To accurately simulate the onset of yielding, the initial peak of the stress-strain curve is used as the yield stress in the plastic material model.
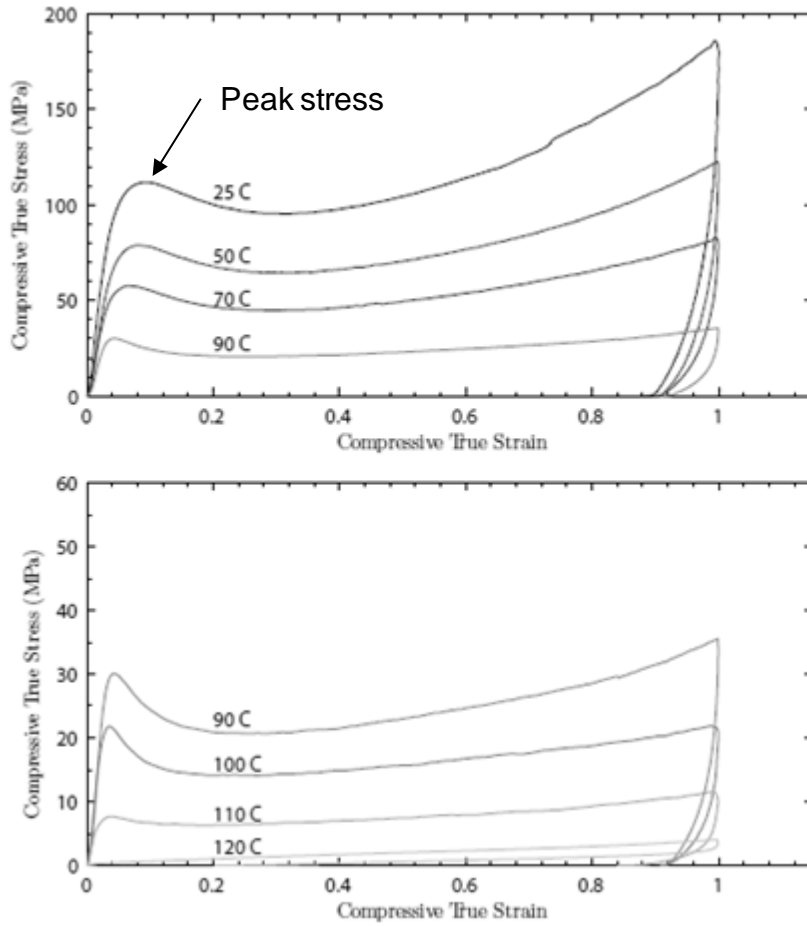
Figure 3.13 Stress-strain data for simple compression experiments on PMMA at several temperatures and a strain rate of 3×10^{-4}/s. The peak stress is used as the yield stress in finite element simulations. Plots from Ames [105].
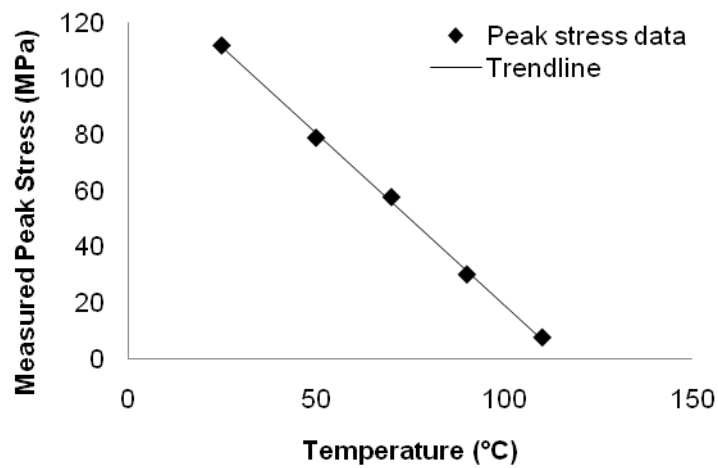
Figure 3.14 Peak stress data from quasi-static compression experiments on PMMA [105] used for the linear elastic perfectly plastic material model in finite element simulations.

The plastic strain in the region of the outermost feature of the three-feature finite element model (Figure 3.10) is shown in contour plots at different temperatures in Figure 3.15. At 100°C, slight plastic strain (~5%) is evident where the stress is concentrated at the corner of the feature. As the part cools and loads from thermal stress increase, local yielding near the feature becomes more pronounced. At 50°C, a large "bulge" can be seen where part material has been compressed against the feature. Such a bulge would be considered a serious manufacturing defect, since it could prevent adequate sealing with a cover-plate.

The middle feature does not experience such extreme thermal loads because it is partly shielded by the outer feature. A contour plot of the maximum principal component of plastic strain at 25°C is shown in Figure 3.16.

The normal force on the sidewalls of the three features at 75°C is plotted in Figure 3.17, along with the same results from the purely elastic model. The force on the outer feature is somewhat reduced because the local yielding of the part around the feature has allowed some of the thermal stress to relax.

(a)

PE, Max. Principal
(Avg: 75%)
+5.463e-02
+4.917e-02
+4.370e-02
+3.824e-02
+3.278e-02
+2.732e-02
+2.185e-02
+1.639e-02
+1.093e-02
+5.463e-03
+0.000e+00

100°C

(b)

PE, Max. Principal
(Avg: 75%)
+1.192e-01
+1.073e-01
+9.534e-02
+8.342e-02
+7.151e-02
+5.959e-02
+4.767e-02
+3.575e-02
+2.384e-02
+1.192e-02
+0.000e+00

75°C

(c)

PE, Max. Principal
(Avg: 75%)
+4.581e-01
+4.123e-01
+3.665e-01
+3.206e-01
+2.748e-01
+2.290e-01
+1.832e-01
+1.374e-01
+9.161e-02
+4.581e-02
+0.000e+00

50°C

(d)

PE, Max. Principal
(Avg: 75%)
+7.091e-01
+6.382e-01
+5.673e-01
+4.964e-01
+4.254e-01
+3.545e-01
+2.836e-01
+2.127e-01
+1.418e-01
+7.091e-02
+0.000e+00

25°C

Figure 3.15 Contour plots of maximum principal component of plastic strain near outermost feature for PMMA part against a rigid mold cooling from 135°C to (a) 100°C, (b) 75°C, (c) 50°C, (d) 25°C. Overall contraction is towards the left. Note that the scale for the contours in each plot is different.
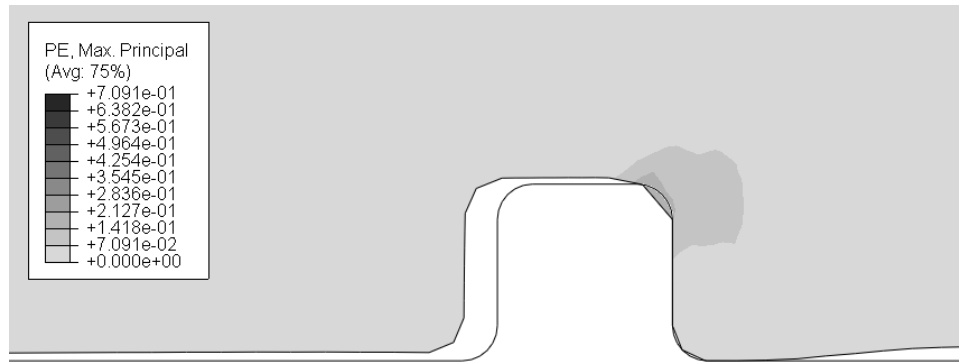
Figure 3.16 Contour plot of maximum principal component of plastic strain near middle feature for PMMA part against a rigid mold cooling from 135°C to25°C. Overall contraction is towards the left. Note that the scale for the contours in this plot is the same as in Figure 3.15(d).
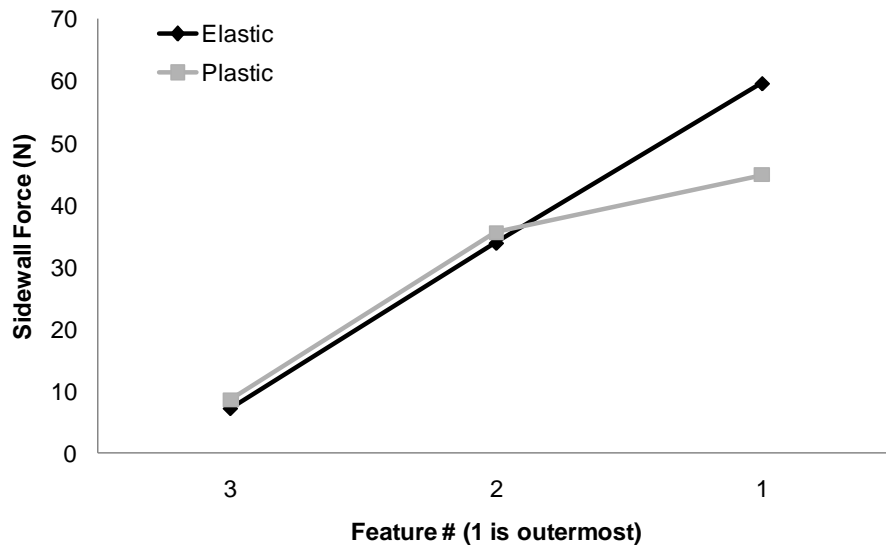
Figure 3.17 Comparison of sidewall forces for elastic and elastic-plastic materials in finite element models of PMMA against a rigid mold cooled from 135°C to 75°C. The force on the outermost feature is somewhat reduced because the local yielding has allowed some of the thermal stress to relax.

3.4.5   Mold elasticity

As discussed in Section 3.3.2, the mold has also been modeled as an elastic body with material properties representing Aluminum 6061-T6, the same material used for many of the experimental molds (Section 4.6). The finite element model shown in Figure 3.6 (single feature with 3 mm effective spacing) has been adapted to include an elastic mold. The resulting stresses in the part and mold at 30°C using a purely elastic material model are shown in Figure 3.18.

90
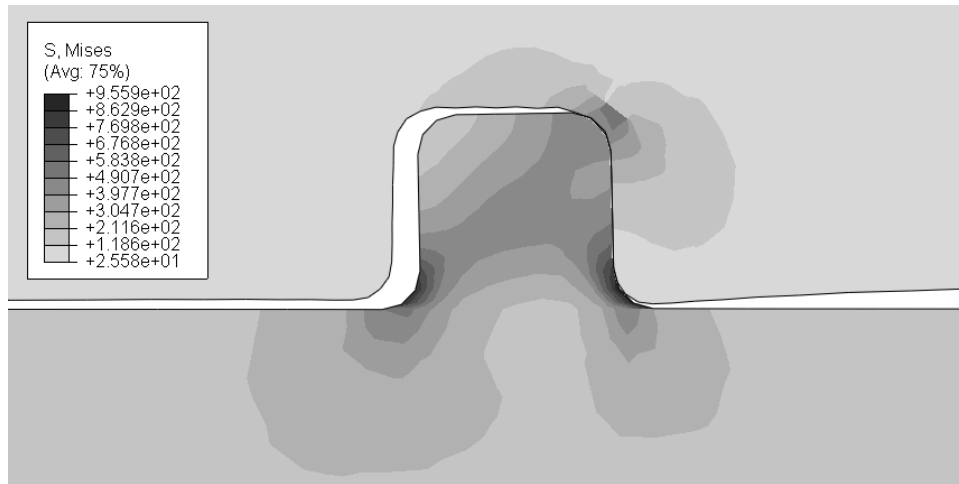
Figure 3.18 Contour plot of von Mises stress distribution in Aluminum mold and purely elastic PMMA part after cooling from 135°C to 30°C. Overall contraction is towards the left.

Figure 3.19 shows the von Mises stress distribution in the part and the mold after cooling to 25°C using an elastic-plastic material model for the part. Comparing Figure 3.19 and Figure 3.18, the stresses for the plastic model are lower.
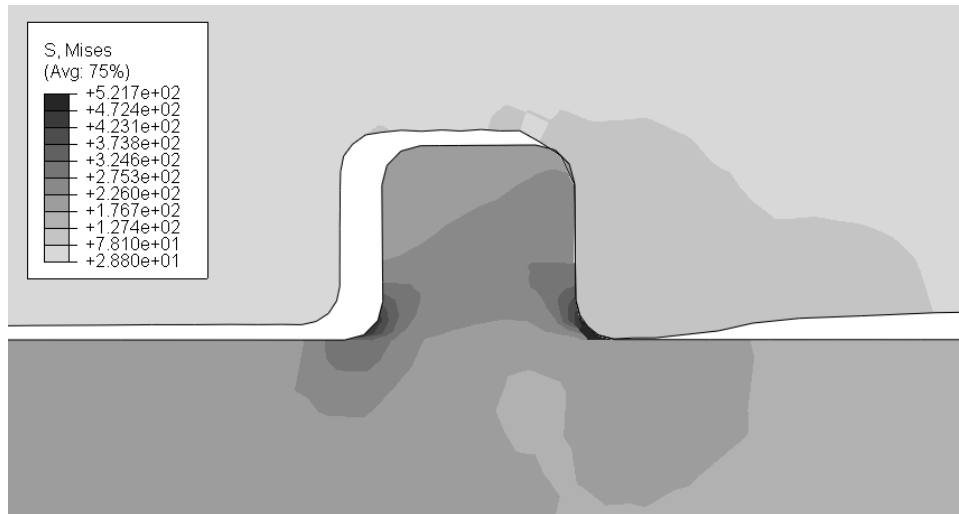
Figure 3.19 Contour plot of von Mises stress distribution in Aluminum mold and elastic-plastic PMMA part after cooling from 135°C to 25°C. Note the "bulge" in the part surface to the right of the mold. Overall contraction is towards the left.

The maximum principal plastic strain in the region near the feature is shown in contour plots at different temperatures in Figure 3.20. Large changes in the profile of the part's surface are not evident until about 50°C.

(a) 100°C
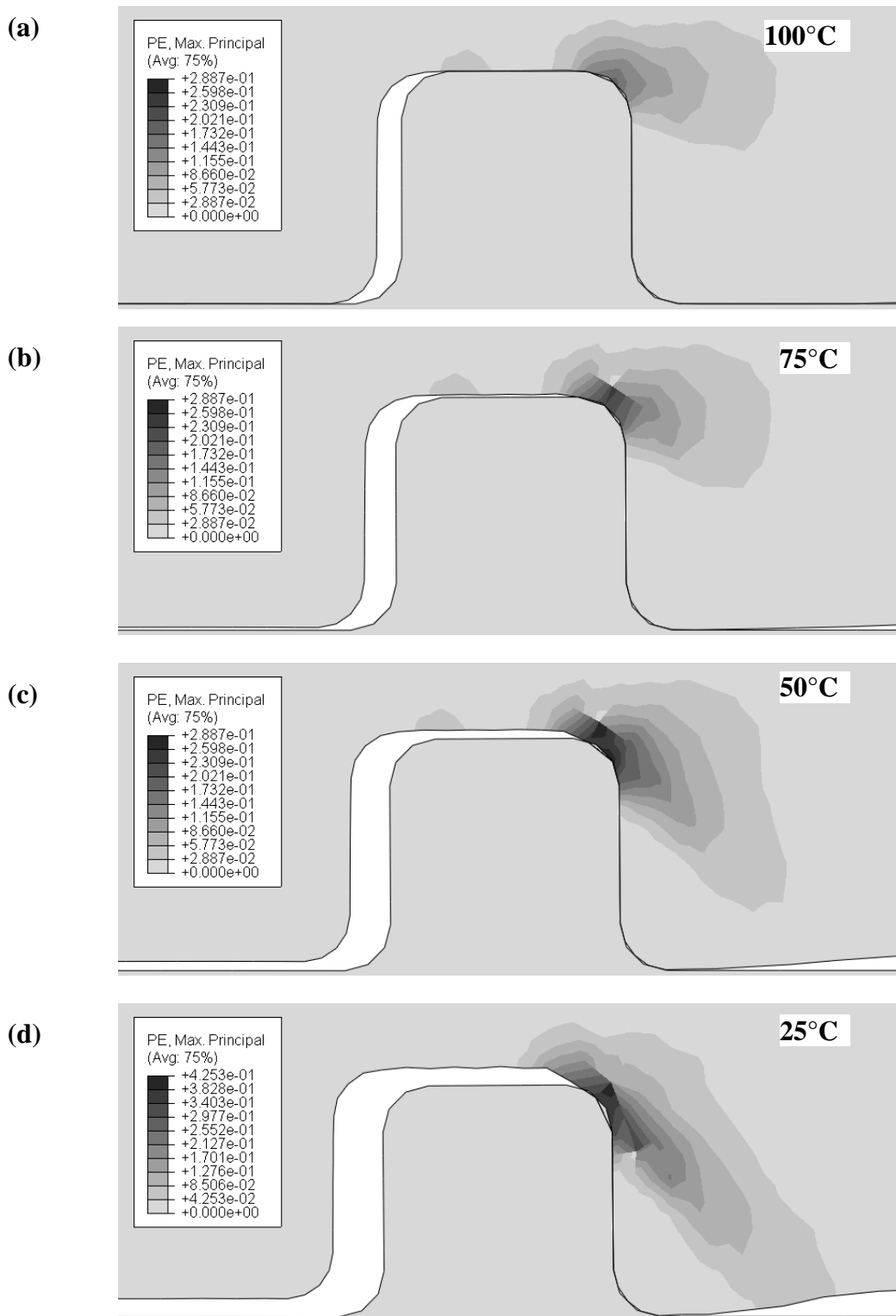
(b) 75°C

(c) 50°C

(d) 25°C

Figure 3.20 Contour plots of maximum principal component of plastic strain near the feature for a PMMA part against an Aluminum mold cooling from 135°C to (a) 100°C, (b) 75°C, (c) 50°C, (d) 25°C. Overall contraction is towards the left. Note that the scale for the contours in each plot is different.

With an elastic mold, the deflection of the mold and its thermal contraction both serve to relieve some of the thermal stresses compared with a perfectly rigid mold. The sidewall forces predicted by models based on rigid and elastic molds and elastic and elastic-plastic material models are compared in Figure 3.21.
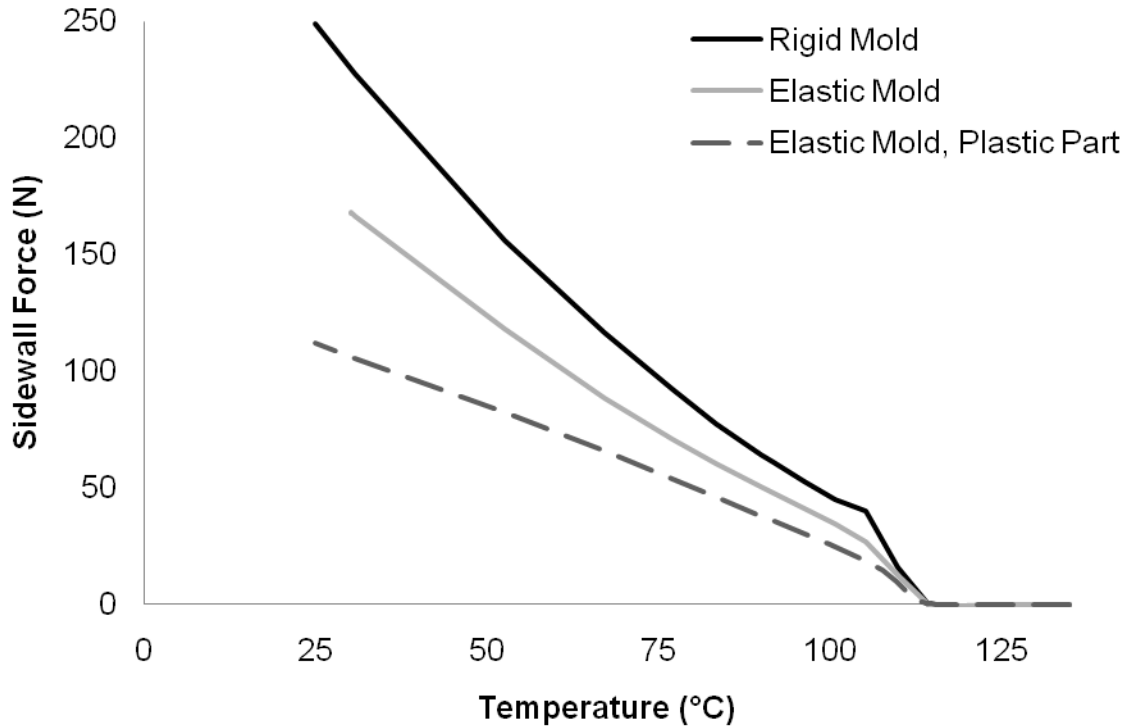
Figure 3.21 Comparison of sidewall force for single-feature finite element models with 3 mm effective feature spacing.

3.5 Simulated demolding

The simulations discussed above end once the part has been cooled to the demolding temperature. To investigate the conditions during demolding, a final step is added to the model history in which the embossing pressure is removed and a displacement is applied in a ramp mode to the upper right node of the part. Because of the highly nonlinear effects of contact constraints changing as the part is forced off of the mold, and because of the abrupt transition when the part is finally free of the mold, some simulations could not proceed through the last demolding step, especially those with higher sidewall forces. The model depicted in Figure 3.2 with a width of 1.1 mm (corresponding to 0.5 mm spacing) and an elastic mold was selected for demolding simulations. The results for this model may not be directly comparable to experiments

on other mold geometries, but this model should still accurately reflect the trends associated with specific parameters and the effects of the various mechanisms (thermal contraction, sidewall friction, etc.).

Figure 3.22 shows contour plots of the von Mises stress in the PMMA part and the Aluminum mold at different stages of demolding. In this model, the friction coefficient between the part and the mold is 0.4, and the model was cooled from 120°C to 25°C prior to demolding. Throughout demolding, the highest stress in the part is adjacent to the top corner of the mold protrusion. This observation suggests that the edge quality and shape of the protrusion (burrs, roughness, rounded corners, etc.) could have a disproportionate effect on demolding. This expectation has been confirmed by experimental results (see section 5.9.2).

Several measures of interest are available from the simulation output, including contact force magnitudes and components on the interface between the part and mold, the applied demolding force, the energy dissipated by friction, and the total external work applied to the model. These output metrics are available as standard options, and are computed by the finite element software [112]. The external work applied to the model during demolding is analogous to the demolding work, which is the amount of energy input required to separate the part from the mold (section 2.7).
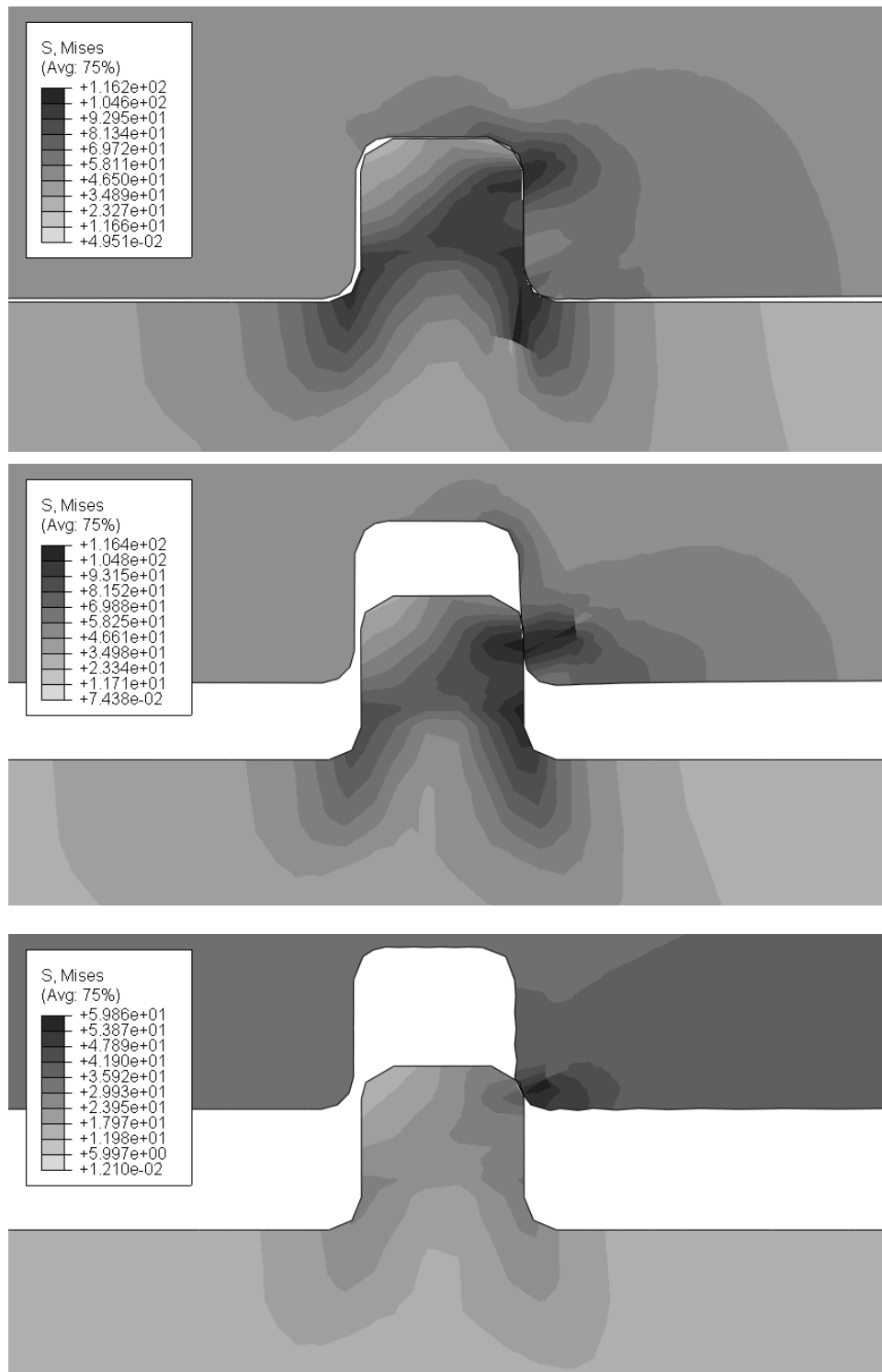
Figure 3.22 Contour plots of von Mises stress distribution in purely elastic PMMA part and Aluminum mold at different stages of demolding after cooling from 120°C to 25°C. Note that the contour scales are different in each plot. Overall contraction is towards the left.

Some of the important forces in the model are plotted in Figure 3.23. The demolding force is balanced by the sidewall shear force. During demolding, the sidewall shear force remains in a constant ratio with the normal force determined by the friction coefficient.
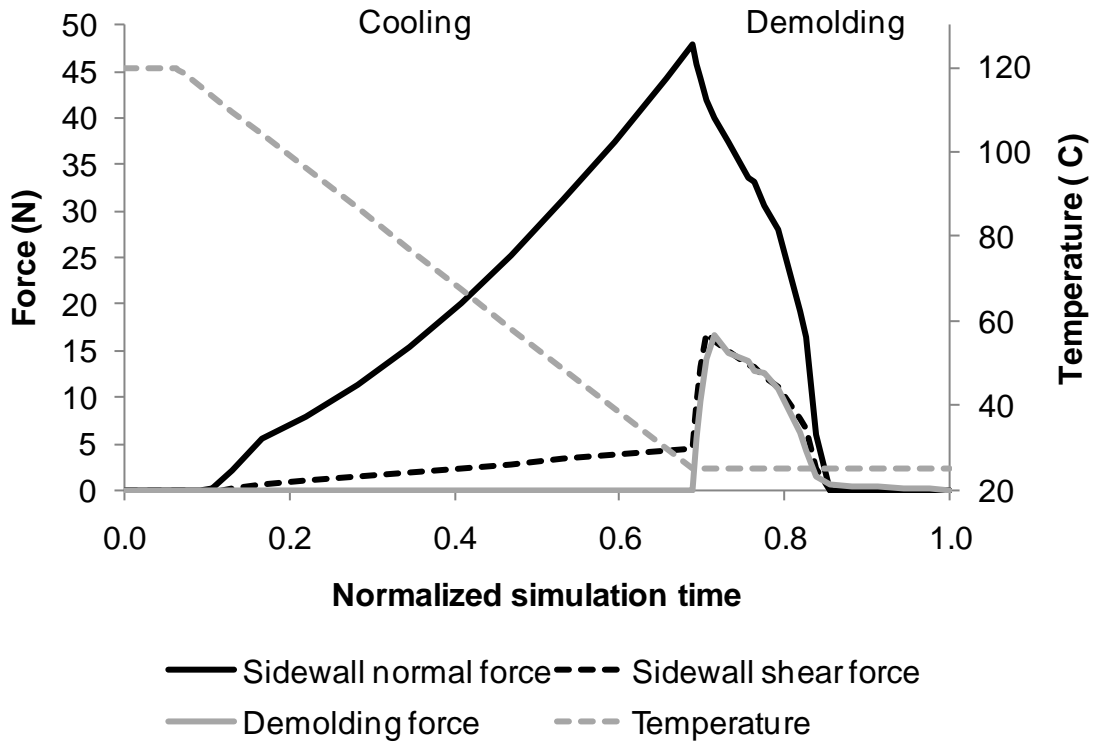
Figure 3.23 Plot of forces operating during demolding an elastic PMMA part from an Aluminum mold after cooling from 120°C to 25°C.

The energy dissipated by friction within the finite element model is plotted in Figure 3.24 along with the external work applied to the model. Some of the energy dissipated by friction comes from elastic strain energy that is stored in the model during cooling, accounting for the difference in the final value of the two energy measures. The external work applied during demolding is analogous to the demolding work for a single feature that might be measured in an experiment.
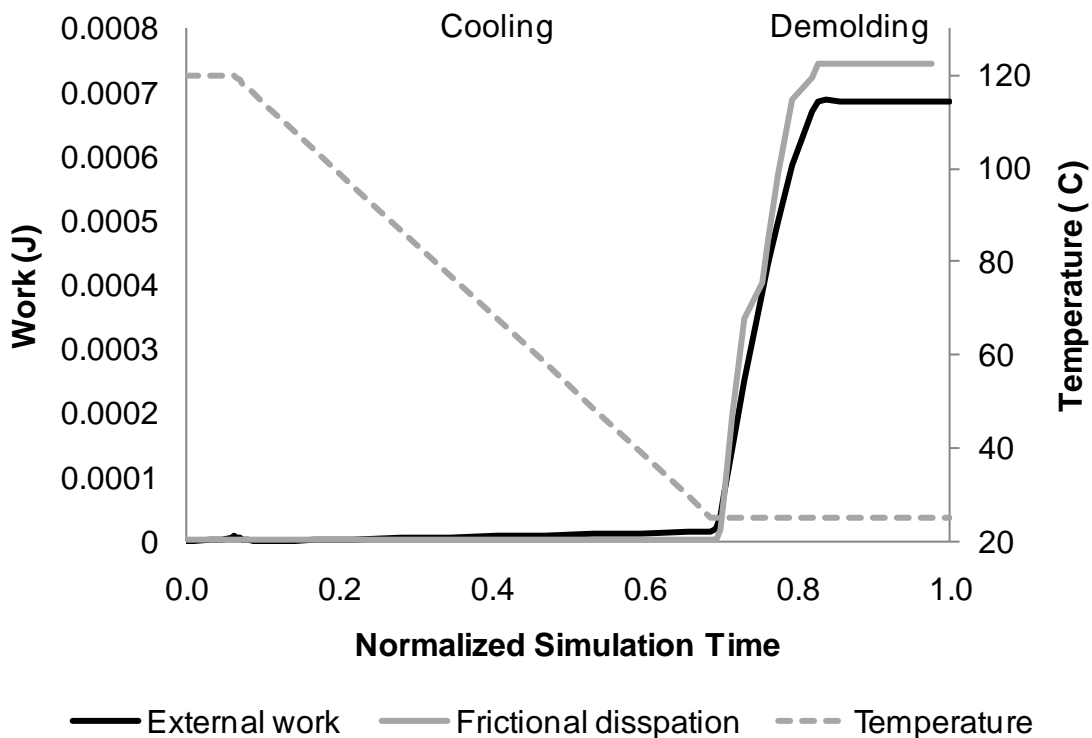
Figure 3.24 Plot of external work applied to the finite model and energy dissipated by friction within it. Some of the energy dissipated by friction comes from strain energy stored in the model during cooling, accounting for the discrepancy with external work.

The amount of work required to demold the finite element model (0.69 mJ) is less than what might be estimated from Equation 2-34 (1.9 mJ) using only the maximum sidewall normal force (48 N). This difference is caused by the reduction in the sidewall force during demolding, as shown in Figure 3.23.

3.5.1 Effects of temperature and friction coefficient

In these finite element simulations, the interaction between the part and the mold is modeled as Coulomb friction. It is expected that the energy consumed during demolding is entirely a result of frictional dissipation as the channel in the part slides off of the mold protrusion. The amount of energy dissipated would depend on the normal force on the sidewall, the friction coefficient, and the height of the feature, as in Equation 2-34. Because the sidewall force depends on temperature, the demolding work is also expected to depend on temperature. The demolding work determined from the finite element model is plotted in Figure 3.25 for two different friction coefficients at several demolding temperatures. The demolding work increases with increasing friction coefficient and decreasing temperature, as expected.
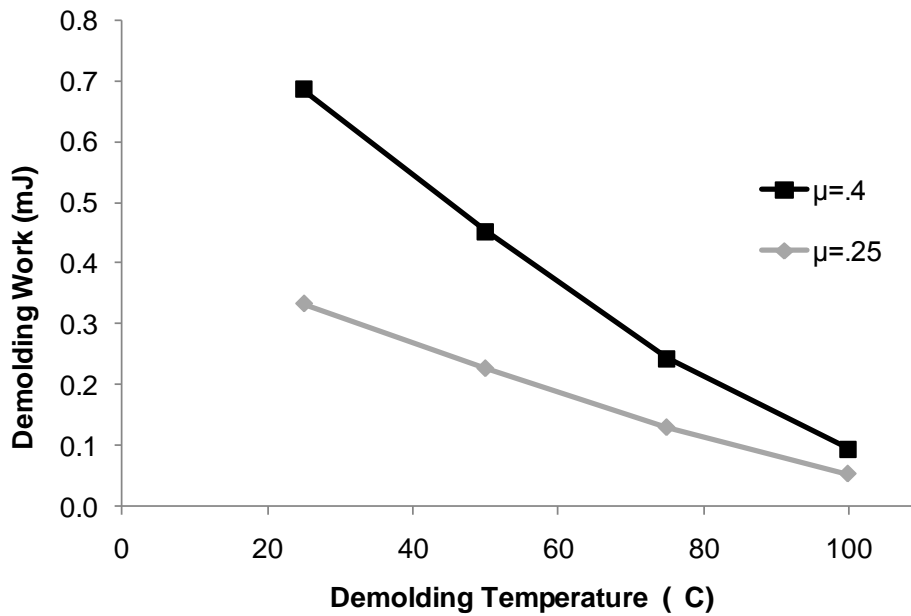
Figure 3.25 Plot of demolding work from finite element model of elastic PMMA part and Aluminum mold cooling from 120°C. Demolding work increases with increasing friction coefficient and decreasing temperature.

The effects of friction coefficient can be isolated by looking at a single demolding temperature. Figure 3.26 shows the effect of friction coefficient on the demolding work for this model at a demolding temperature of 25°C.
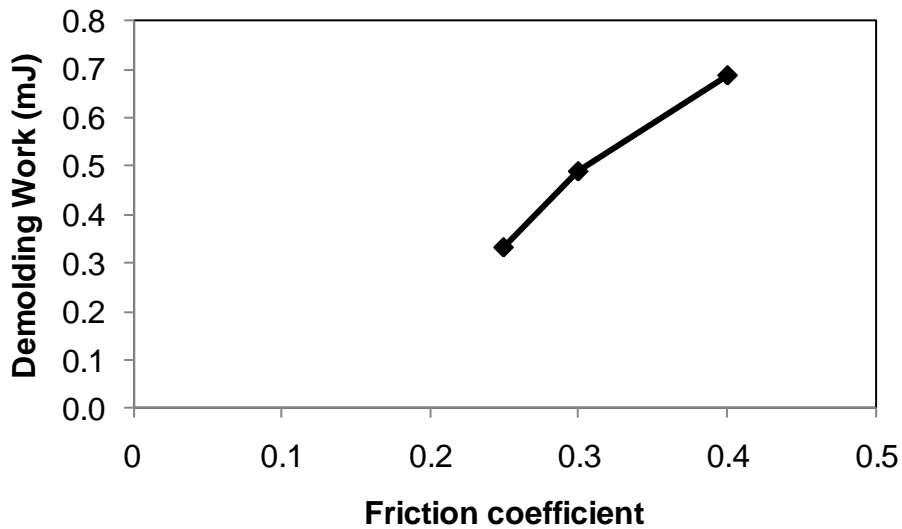
Figure 3.26 Effect of friction coefficient for PMMA and Aluminum mold cooled from 120°C to 25°C.

Since the amount of thermal contraction is partly determined by the initial temperature, the effect of embossing temperature on demolding work was tested within the finite element model. From the plot in Figure 3.27, it can be seen that the demolding work is slightly increased for higher embossing temperatures, but this effect is much smaller than that of demolding temperature or friction coefficient.
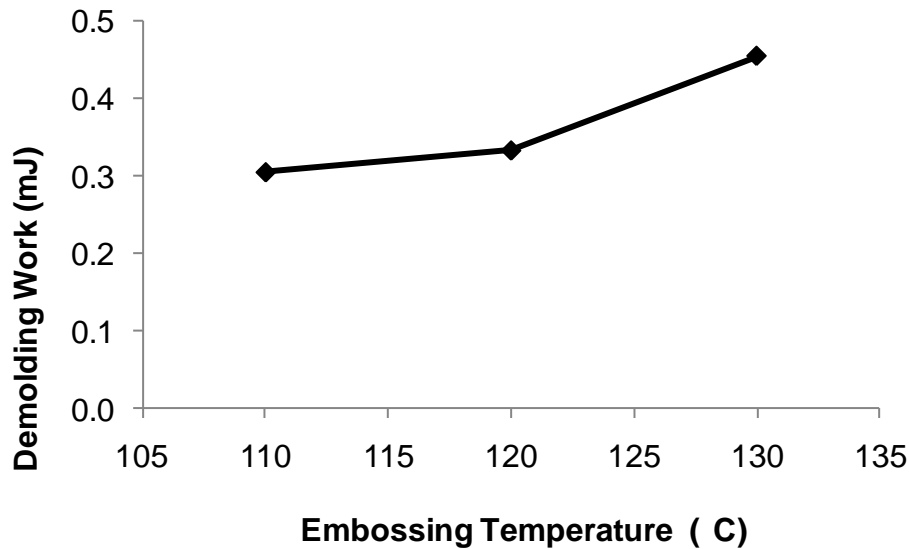
Figure 3.27 Effect of embossing temperature on demolding work at 50°C.

3.5.2 Effects of mold properties

The amount of thermal stress in the part—and the force on the feature sidewall—is largely determined by the temperature and the thermal contraction mismatch between the mold and the part. The properties of the mold in the finite element model were adjusted to reflect different materials: Silicon, Aluminum, and polycarbonate, and the resulting demolding work at 50°C for a friction coefficient of 0.25 is plotted in Figure 3.28. The polycarbonate mold has the least thermal contraction mismatch with the PMMA part (68 µm/m°C for PC vs. 83 µm/m°C for PMMA) and has the lowest demolding work as well. The polycarbonate also has the lowest elastic modulus, and the elastic properties of the mold also affect the sidewall force, and therefore the demolding work (section 3.4.5). The interaction between the mold material and part in terms of friction coefficient and adhesion would also have a strong effect on demolding work, but this is not modeled here.
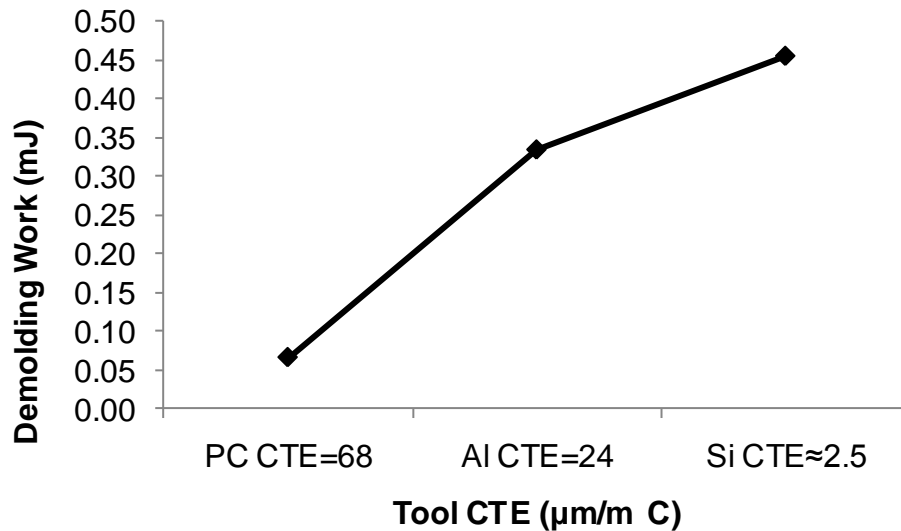
Figure 3.28 Effect of mold material on demolding work at 50°C and with a friction coefficient of 0.25. Thermal contraction mismatch is the dominant factor.

3.5.3 Effects of feature height

Because the demolding work is associated with the energy dissipated while the part feature slides off of the mold protrusion, the height of the protrusion on the mold (channel depth) is also expected to have an important effect. The feature dimensions of the finite element model were changed to investigate this effect. Figure 3.29 shows one such model, where the feature has been enlarged to 200 μm high. For simplicity, a rigid mold was used in the models with different feature heights.

Simulations were performed for models with features 100 μm, 150 μm, and 200 μm high. The friction coefficient was set at 0.4, and the demolding temperature was 50°C. The sidewall and demolding forces were not affected by the changes in feature heights (Figure 3.30), but the demolding work was strongly affected by the feature height (Figure 3.31). The sidewall shear force and demolding force are largely determined by the underlying Coulomb friction model for the surface interaction, in which the friction force is independent of the apparent area of contact. By contrast, the demolding work also depends on the distance over which the friction force operates, and so the work depends on feature height (Eq. 2-34).
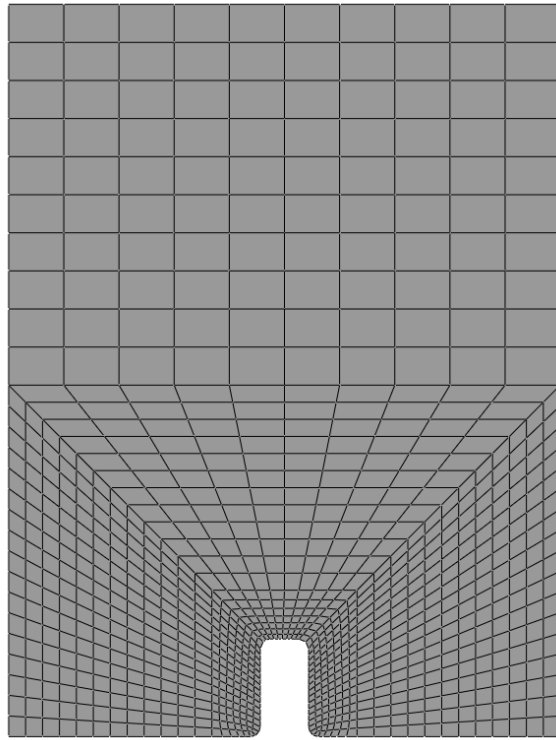
Figure 3.29 Diagram of finite element model with a 200 μm high feature.
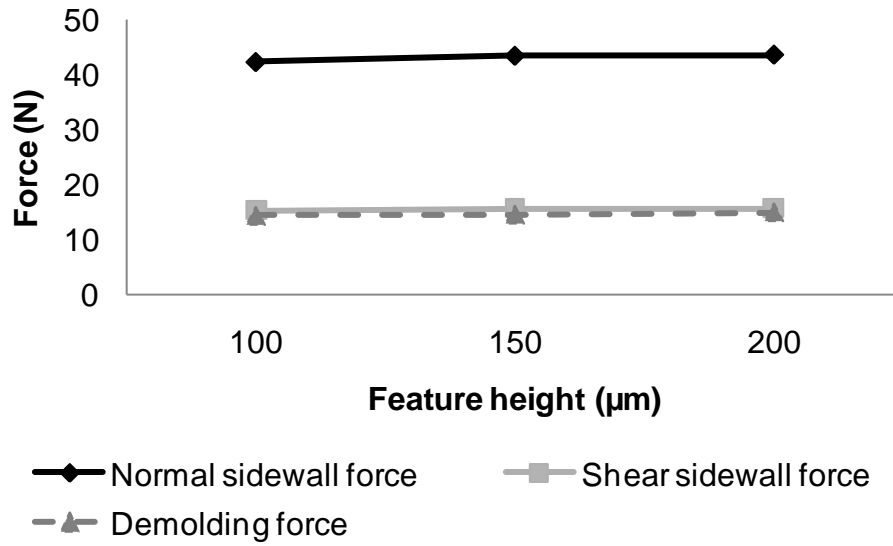
Figure 3.30 Forces on PMMA parts and rigid molds at 50°C are unaffected by different feature heights.
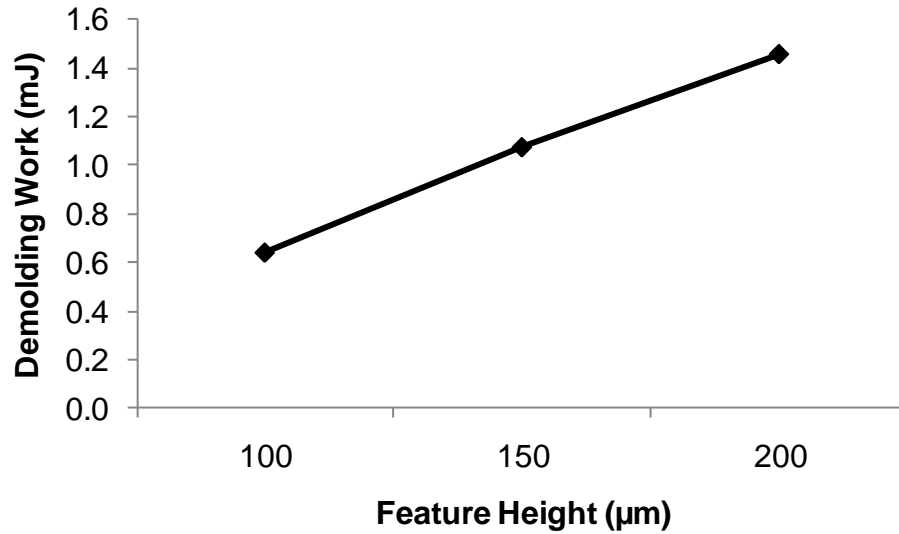
Figure 3.31 Demolding work for a PMMA part and a rigid mold at 50°C is strongly affected by the feature height.

3.5.4 Plasticity in demolding

Plastic deformation in the part serves to reduce sidewall forces by relieving some of the thermal stress (Figure 3.21), but it also provides an additional mechanism through which energy can be dissipated. To test the effects of plastic deformation during demolding, an elastic perfectly plastic material model was used for the PMMA part (as in section 3.4.4). Contour plots of the maximum principal component of plastic strain in a PMMA part at various stages of demolding from a rigid mold at 25°C are shown in Figure 3.32. As the part is demolded, the concentrated stress at the top corner of the feature progressively extends the yielded region along the feature sidewall. The overall effect of plasticity in the part is to slightly reduce the demolding work, as shown in Figure 3.33.
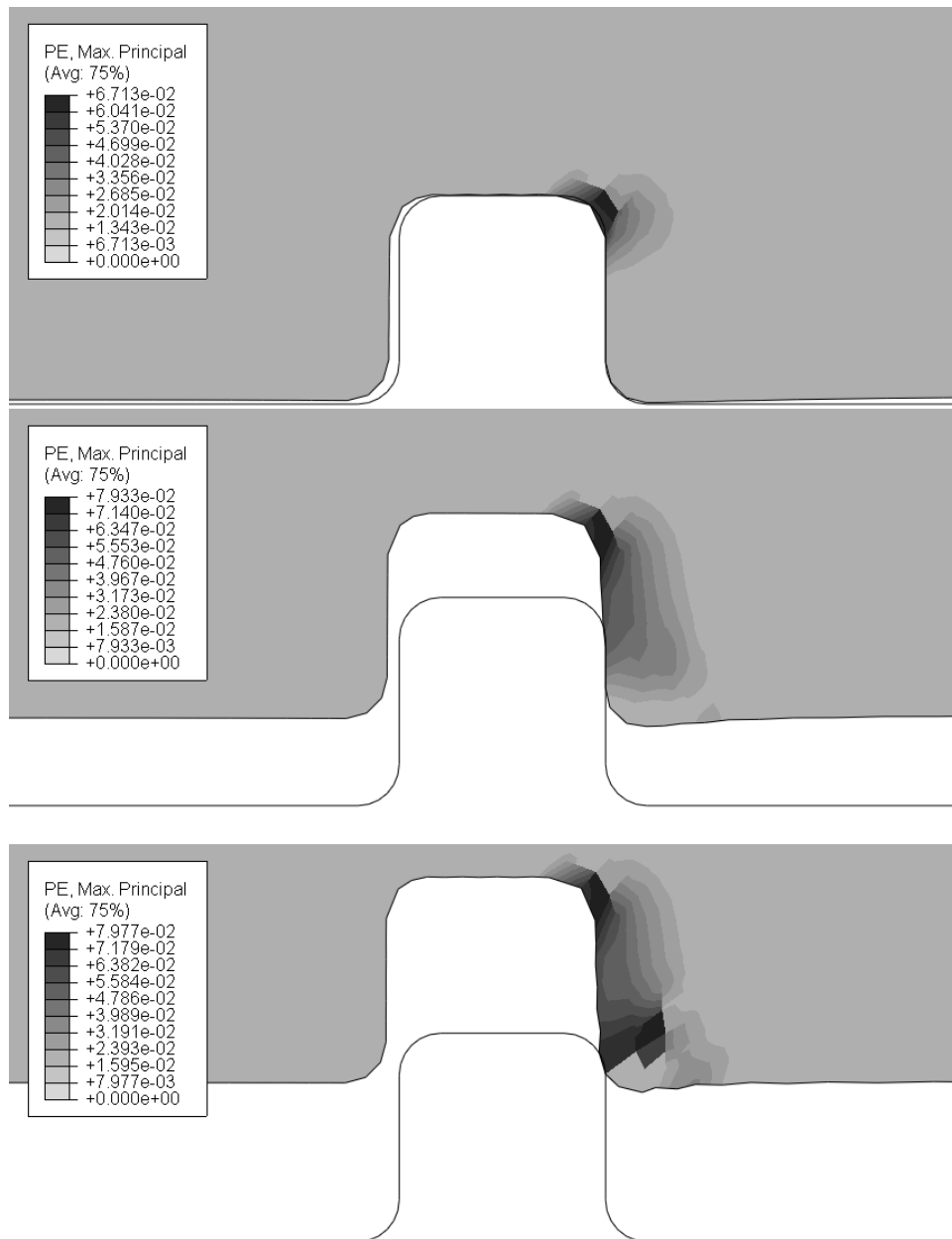
Figure 3.32 Contour plots of maximum principal component of plastic strain in a PMMA part demolding from a rigid mold at 25°C. Note the contour scales are different for each plot.
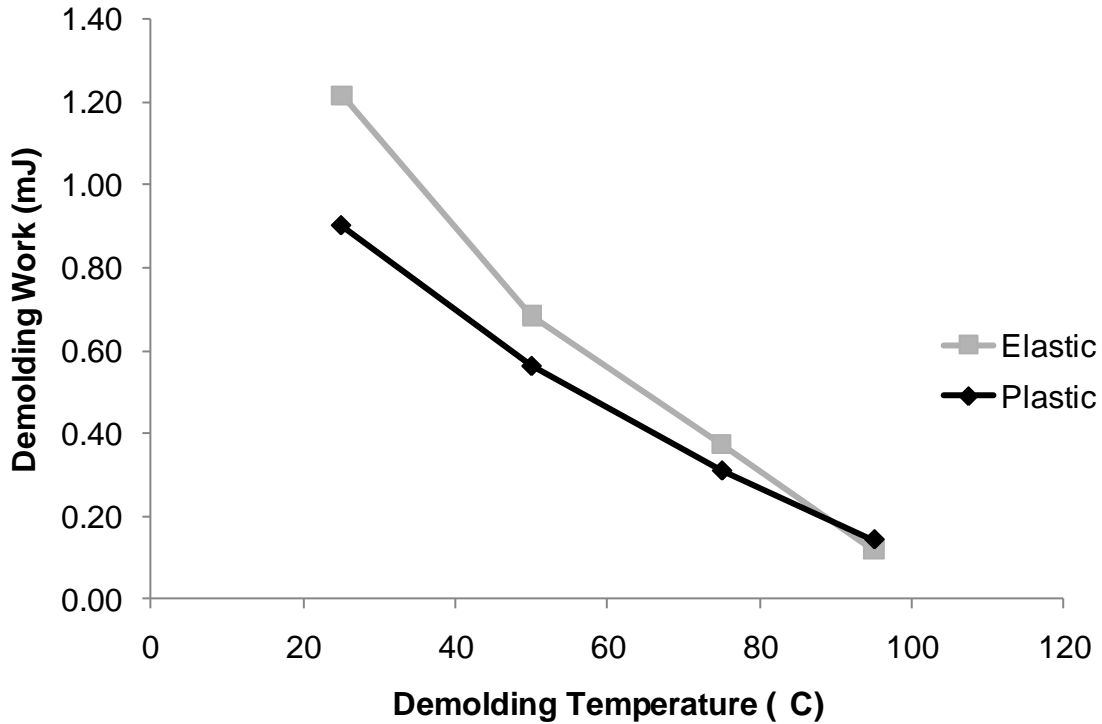
Figure 3.33 Plasticity in the part has the net effect of slightly reducing the demolding work for PMMA demolding from a rigid mold.

3.6 Adhesion

Along with friction, adhesion between the mold and the part plays an important role in demolding. Adhesion can be modeled in ABAQUS/Standard with a cohesive surface interaction [112]. Unlike conventional contact modeling, this approach allows for tensile loads between surfaces as they are displaced apart. A constitutive relation for the separation between surfaces and the traction between the surfaces is defined and applied to individual nodes on the contacting surfaces. Figure 3.34 shows a schematic of a one-dimensional cohesive traction-separation behavior, where σ_{max} is the maximum traction the bond can transmit, K is the initial stiffness of the bond, and G_C (the area under the curve) is the toughness of the bond.
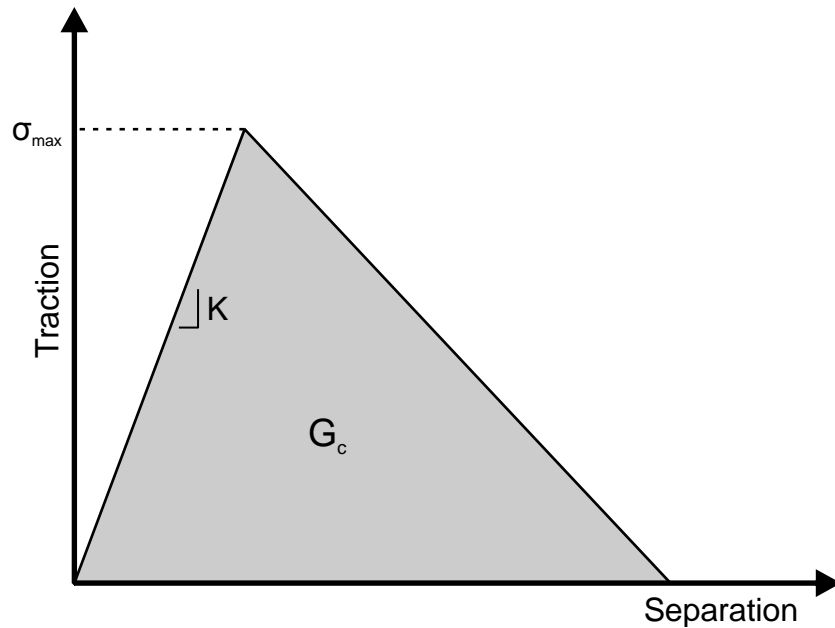
Figure 3.34 Constitutive traction-separation relation for cohesive surface modeling.

In the two-dimensional implementation of this model, the failure criterion for the adhesive bond between nodes is given by Equation 3-2 (the MAXS damage initiation criterion in ABAQUS/Standard) [112]. According to this criterion, once either the shear or normal load on the surface exceeds the adhesion strength, the bond will begin to degrade as the surfaces continue to separate.

$$\max\left(\frac{\sigma_N}{\sigma_{max}}, \frac{\sigma_S}{\sigma_{max}}\right) \geq 1 \qquad \textbf{3-2}$$

where

σ_{max} Maximum strength of adhesive bond
σ_N Normal traction on surface
σ_S Shear traction on surface

Once this failure criterion is exceeded, the load transmitted across the bond decays linearly with separation so that the total area under the traction-separation curve is equal to the defined bond toughness (Figure 3.34) (the ENERGY damage evolution type in ABAQUS/Standard) [112]. The failure stress and toughness for the cohesive surface model were set to 0.58 MPa and 50 J/m^2, respectively. These values were determined from normal pull-off adhesion tests (section 4.3.1) on PMMA discs and flat Aluminum molds at 135°C (see section 5.4.1). The stiffness is set to 1×10^{12} N/m/m^2 (the cohesive stiffness is stated per unit area). This parameter has relatively little effect on the simulation results, and this value was found to aid

convergence. The parameters for the normal and shear directions are identical, and the normal and shear stiffnesses are uncoupled.

The damage status (ranging from 0% to 100% degraded) of each element on the surface is available as an output from the finite element software [112]. This variable is plotted as a contour in Figure 3.35 for the results at 25°C. Darker colors indicate greater damage to the adhesive bond. Most of the bond in the flat areas of the mold has failed and is almost completely degraded. The outer sidewall of the feature is still comparatively well bonded.
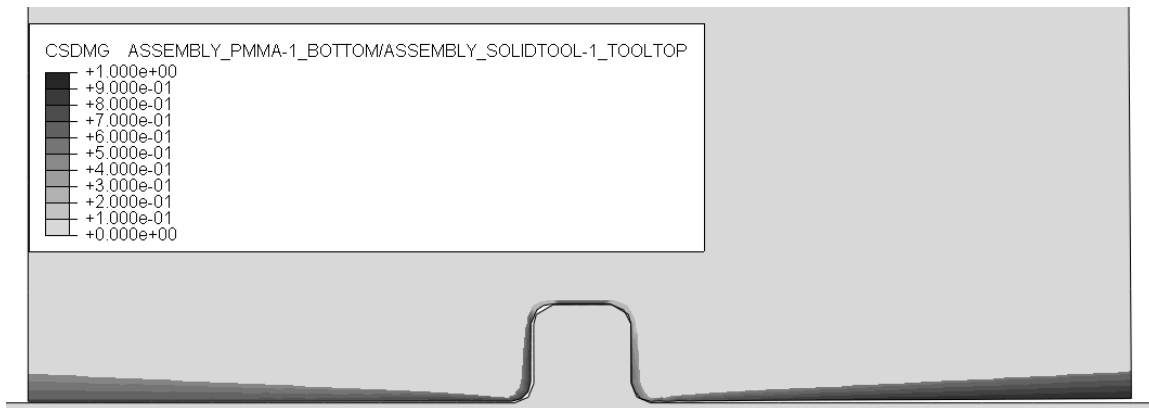
Figure 3.35 Contour plot of damage status variable for cohesive surface between PMMA and Aluminum cooled from 120°C to 25°C. Darker areas indicate greater local degradation of adhesion.

The damage status along the surface of the part is plotted as curves in Figure 3.36 for several temperatures. Initially, the entire surface is undamaged. As the part and mold cool, the thermal stresses that develop begin to degrade the adhesion at the surface.

The remaining adhesive strength at a given temperature must be overcome during demolding. The external work required to demold the part for the cohesive surface model is plotted in Figure 3.37. The demolding work decreases with temperature because a greater fraction of the surface has had its bond degraded. Once nearly all of the surface adhesion has been degraded, the demolding work drops dramatically. The temperature at which this abrupt transition occurs increases with decreasing adhesion strength. This transition causes convergence difficulties in the simulation, so demolding at lower temperatures generally cannot be simulated.
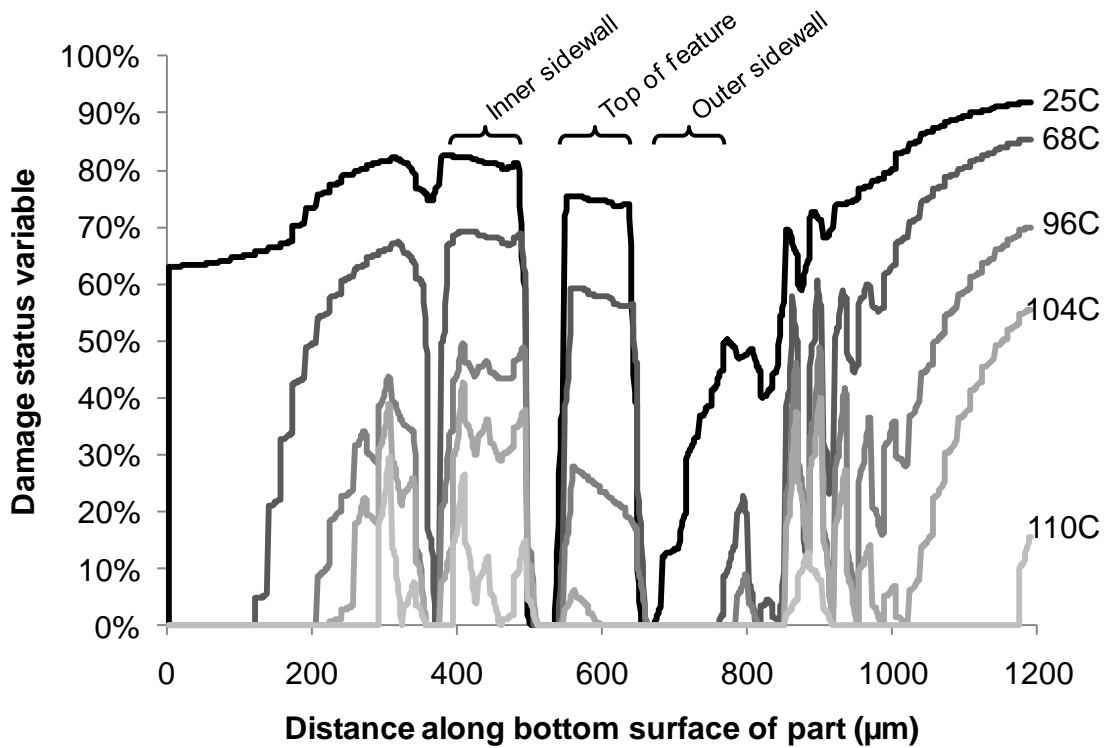
Figure 3.36 Plot of damage status along the bottom surface of the part while cooling from 120°C. The nodes near the upper feature corners were never in contact, causing a jump in damage status.
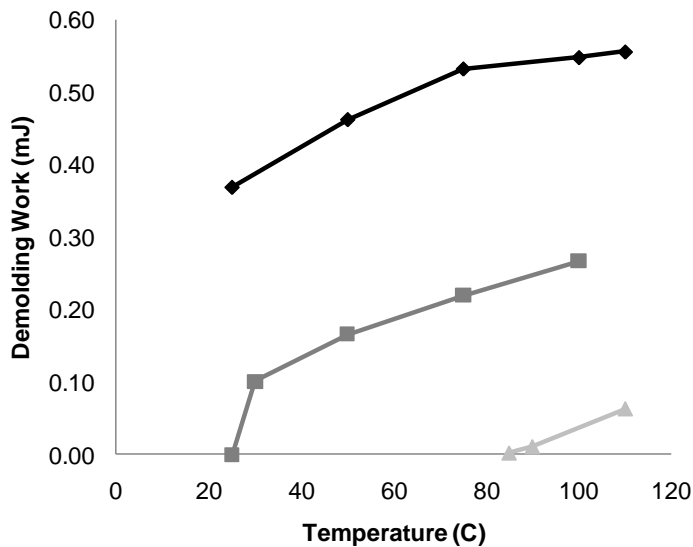
Figure 3.37 Demolding work at different temperatures for the cohesive surface model with a PMMA part 1.1 mm wide and Aluminum mold cooling from 120°C. As the adhesion strength decreases, the demolding work also decreases. Once the whole interface has failed, the demolding work drops rapidly to zero. The temperature at which adhesion fails completely increases with decreasing adhesion strength.

The feature spacing also affects how the adhesive bond between the part and the mold is degraded. Figure 3.38 compares the demolding work for two cohesive surface models 1 mm and 3 mm wide, along with the demolding work for the 1 mm friction model. Comparing Figure 3.38 with Figure 2.29, the demolding toughness models and the finite element simulations predict similar trends, with adhesion-dominant demolding transitioning to friction-dominant demolding at a certain temperature.
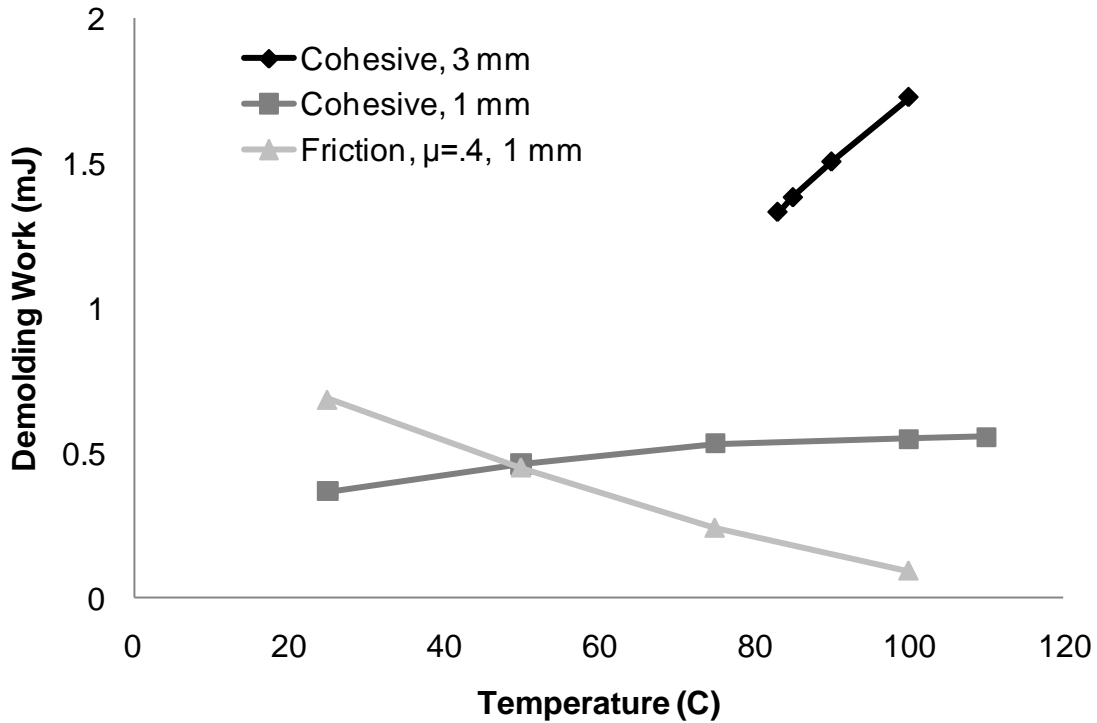
Figure 3.38 Comparison of demolding work for narrow and wide spacing cohesive models and narrow friction model. The demolding work associated with the different mechanisms show opposite trends with temperature. For the 3 mm spacing model, the demolding work due to adhesion decreases to zero rapidly below 80°C.

The demolding work associated with adhesion for the 3 mm model vanishes below about 80°C because the surface is almost fully degraded (Figure 3.39). The 3 mm wide model with frictional behavior could not converge.
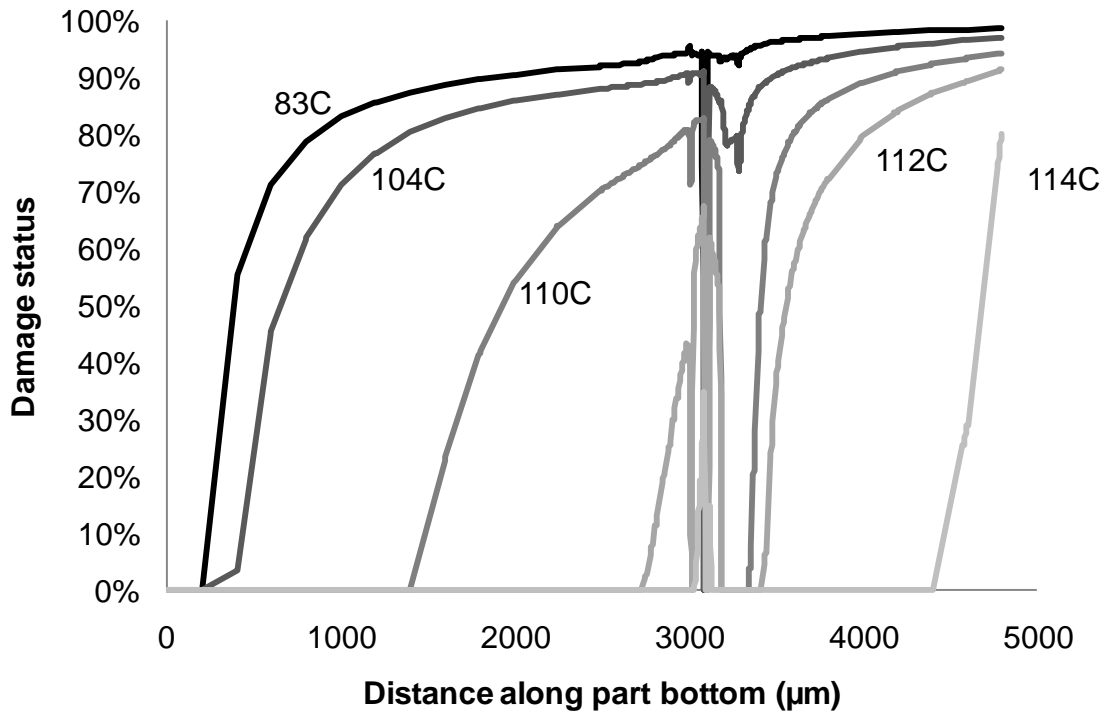
Figure 3.39 Plot of damage status of adhesive bond along bottom of 3 mm spacing PMMA part cooling from 120°C. The nodes near the upper feature corners were never in contact, causing a jump in damage status.

3.7 Conclusions from simulations

The finite element method makes it possible to probe the local stresses and deformations near features, as well as the behavior of different surface interaction models (friction and adhesion). The finite element results for single-feature models show good agreement with those of the analytical models from Chapter 2. Because the finite element models account for the local stress distribution near the feature, this agreement helps to validate the equivalent stiffness model of the local deflection near features based on contact mechanics. The multi-feature finite element model does not agree with the multi-feature analytical models, but it does agree as far as the trend of decreasing sidewall force for inner features, and for lower maximum sidewall force for multiple features compared with single-feature models. Increasing the number of features in the finite element model may lead to better agreement.

Because of the abrupt change in the condition of the model during demolding, this process is more difficult to simulate by the finite element method. Demolding work results could be computed for the narrowest model. These results show that, when the interaction between the part and mold is modeled as Coulomb friction, the resulting demolding work is proportional to

feature height, and the demolding work increases in tandem with sidewall force as the demolding temperature is lowered.

The results of the adhesion-based models also conform to the models in Chapter 2, in that the adhesion between the part and mold is degraded as they are cooled. For molds with wider feature spacing, this effect is more pronounced, and the adhesion is completely overcome at a higher temperature. Unfortunately, the effects of adhesion and friction could not be combined in a single finite element simulation, but their joint effect can be extrapolated from their separate behavior (see Figure 3.38). At higher temperatures, adhesion is the dominant mechanism, but as the part cools, sidewall friction takes over. The transition between these effects is influenced by the feature spacing and adhesion strength.

4 Experimental equipment and methods

4.1 Introduction to the chapter

A common aphorism has it that one cannot control what one cannot measure. Similarly, one cannot study what one cannot measure. With this in mind, an important contribution of this thesis is a metric by which demolding can be characterized. Such a metric should be descriptive of the difficulty or ease of demolding, should be straightforward to determine from experimental results, and, once determined, should be applicable to practical demolding situations. The demolding work defined in section 2.7 is proposed as this metric.

This chapter describes the experimental equipment and methods used to characterize the demolding of hot embossed polymer microstructures by measuring the demolding work. Commonly used methods for measuring adhesion are discussed and compared to demolding conditions in practical hot embossing applications. The functional requirements and detailed design of the experimental apparatus are discussed, and the fabrication methods for producing test specimens and test molds are described. The procedures followed in carrying out demolding experiments are described, along with methods for processing the resulting data and extracting metrics of interest. Finally, the reliability of this method is assessed by carefully analyzing the results of repeated tests under identical conditions. Chapter 5 discusses the results of these experiments for different processing conditions and micro-feature geometries.

4.2 Demolding in practice

When hot embossing is used for volume production, demolding is likely to be effected by ejector pins, strike-plates, or other mechanical means similar to those used for macroscopic polymer molding processes. A demolding system using strike plates was developed as part of the μFAC project described by Hardt [36]. In this system, thin metal strips along opposite edges of the mold push the part off of the mold as the embossing load is released and the upper platen is withdrawn. This demolding system is shown in a diagram in Figure 4.1 and in a photo in Figure 4.2. The strips are at the ends of slightly bent fingers, and if the resulting spring force is

insufficient for complete demolding, the strips contact hard stops that displace them further away from the surface of the mold as the upper platen is withdrawn. When demolding begins, the strips initiate cracks between the part and the mold, which then propagate as the strips bend further away from the mold until the part is completely demolded. This system is similar to strike plates used for demolding in macroscopic molding processes like injection molding.
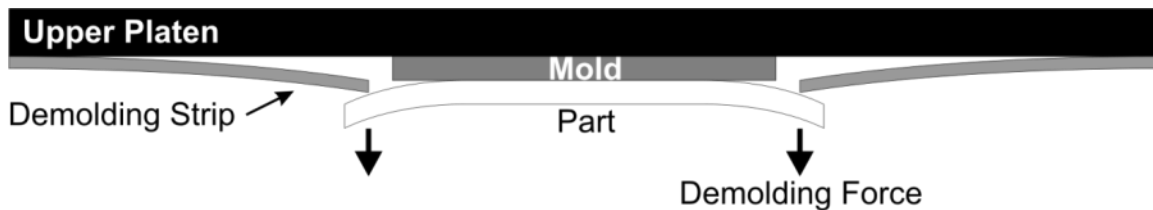
Figure 4.1 Schematic diagram showing the operation of the demolding fixture designed for the µFAC project. As the upper platen is withdrawn, the part is demolded automatically by the demolding strips.
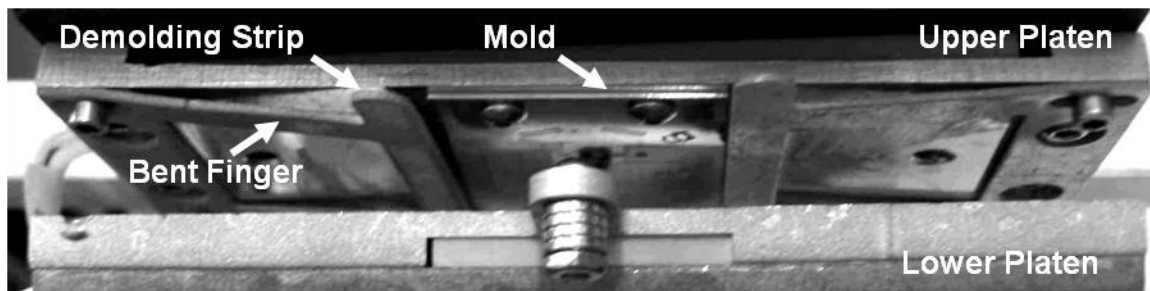
Figure 4.2 Photo of the platens of the embossing machine used in the µFAC project. Note the demolding tabs along the edges of the mold. As the upper platen is withdrawn, the part is demolded automatically by the demolding strips and either the spring force from the bent fingers or hard stops (not shown).

In the successor project, µFAC II, these strips have been replaced with stops connected to the lower platen (Figure 4.3). There is a small clearance between the stops and the part so the part can be loaded and unloaded. Again, as the upper platen is withdrawn, the part is demolded automatically.
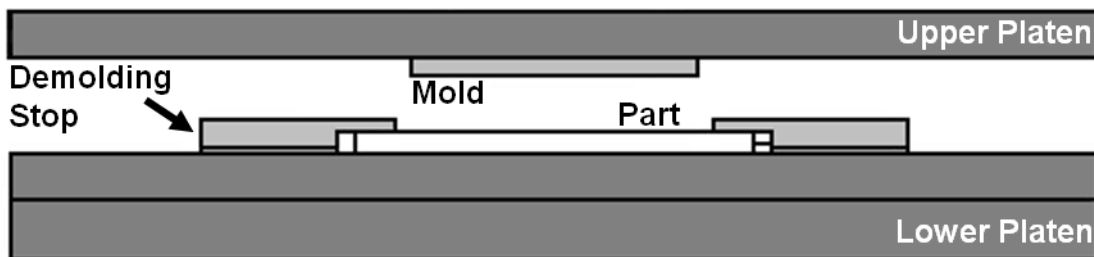
Figure 4.3 Diagram of µFAC II platens with demolding stops. There is a small clearance between the part and the stops. As the upper platen is withdrawn, the part is demolded automatically. Line drawing courtesy Melinda Hale, labels added.

112

Commercially available embossing machines often employ a perimeter clamp to fix the part to one platen, while the mold is fixed to the opposite platen (see, for example, Figure 1 in Trabadelo et al. [61]). Since the part is constrained at its edges but not over its area, it can deform as a plate or a membrane (Figure 4.4). Stress concentration near the edge of the mold will serve to initiate a crack here, which will propagate across the interface. Since the part is clamped, it is more firmly constrained in this system and demolding forces are likely to be higher.
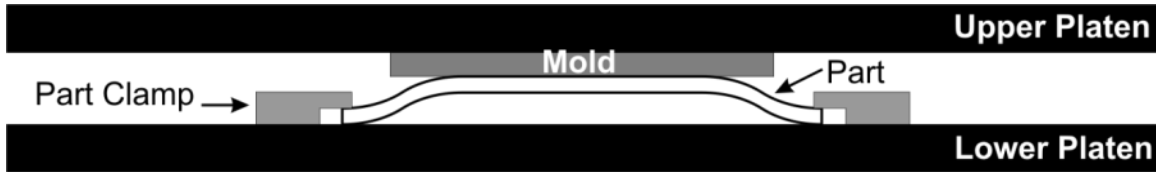
Figure 4.4 Schematic diagram of demolding a part clamped at its edges, as is often the case in commercial embossing machines. The firm constraint of the perimeter clamp increases the bending stiffness of the part, so demolding forces may be higher.

Macroscopic polymer molding processes often employ ejector pins to demold parts (Figure 4.5). These pins penetrate through one platen (or one side of a mold set). As the pin is pushed against the part, the concentrated load from the pin initiates cracks at the interface region around the pin, which propagate across the interface as the pin is pushed further. Ejector pins can be located in the interior of the part (Figure 4.5a) or near the edges (Figure 4.5b).
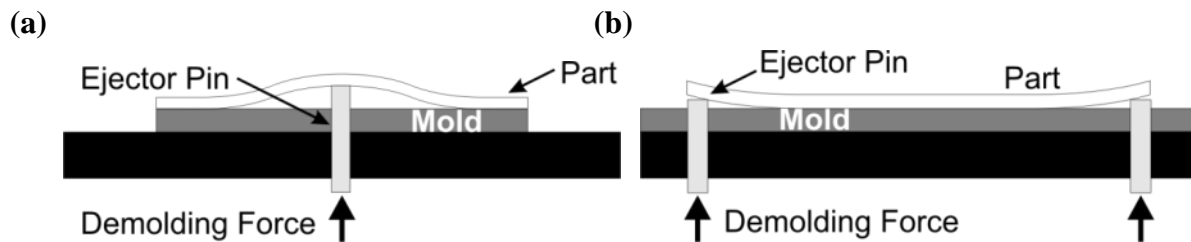
Figure 4.5 Schematic diagram of demolding with ejector pins. As the pins are pushed up, a crack is initiated and propagated, demolding the part. (a) Interior ejector pin, (b) Ejector pins near edges.

Microfluidic chips and similar products are largely planar (that is, they are much larger in two dimensions than in the third), and are embossed against planar molds. Whether accomplished by strike plates, perimeter clamps, or ejector pins, the process of demolding proceeds in a similar way. A crack between the part and the mold initiates near the point of application of the demolding force (usually near the edge), and propagates across the part until it is completely released from the mold. When both sides to the part are embossed by molds, the

113

part will preferentially adhere to the mold with the pattern that is more difficult to demold. The part must then be removed from this mold via strike plates or similar means.

4.3 Adhesion test methods

A huge variety of different methods has been developed for assessing the strength of adhesive bonds between materials [115-117] (these three references are especially helpful compendia of common test methods). The ideal measure of adhesion would be applicable to many different situations, would be measurable by simple and unambiguous means, and would have useful descriptive and predictive power (that is, it would sufficiently characterize adhesive strength and could predict when and how an adhesive bond would fail).

Practitioners make a key distinction between "fundamental" adhesion, which is taken to be an intrinsic and unvarying property of the material pair in question, and "practical" or "experimental" adhesion, which is the strength that is measured by a specific method [100, 115, 116, 118], which may be different from that measured in a different way. An important criterion for a method of assessing adhesion strength is, therefore, the degree to which it accurately simulates the conditions of the real situation of interest. With this criterion in mind, some well-established adhesion measurement methods are evaluated primarily by how well they emulate the conditions of demolding in practical applications.

4.3.1   Tension or Pull Test

Pull tests are straightforward in concept and simple in execution. This type of test is described by ASTM C633, D2095 and other standards. The ends of two cylinders (or substrates of other geometries) are bonded, and the specimen is subjected to a normal tensile load. The tensile stress (engineering stress) at which the bond fails is taken to be the strength of the adhesive joint. Figure 4.6 depicts a simple diagram of a pull test. Many variations on this geometry exist, some of which are discussed by Vallin et al. [117].
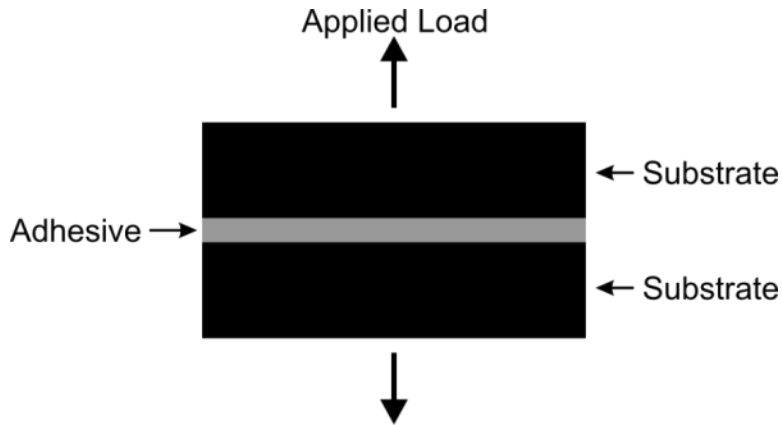
Figure 4.6 Diagram of a pull test for measuring adhesive strength. The substrates are pulled apart in the normal direction, and the maximum force (or stress) before failure is taken as a measure of the bond strength. Many other configurations are possible, see text for references.

Pull tests have the significant advantage of simplicity, and the stress at failure is a convenient measure of bond strength. The difference in elastic properties of the two materials induces shear stresses, however, so the stress at failure depends on the geometry of the specimen [119]. Pull tests are also known to give a large degree of variation in the measured strength. The load is applied to the whole volume of the specimen and is not localized to the interface, and failure proceeds in a rapid, uncontrolled manner [116, 117]. Pull tests have been used to measure the intrinsic adhesion between polymers and mold materials in nanoimprint lithography [46, 58], and to measure demolding forces in NIL [61-63].

Hot embossed parts are generally not demolded by pure normal forces, but are pushed or pried off by loads applied near their edges (section 4.2). Indeed, Trabedelo et al. mention that in many of their pull-type demolding tests, the demolding forces were too low to be measured because the part peeled off of the mold [61]. An exception is the moment when the embossing platens first begin to separate. This motion is normal to the plane of the part (to the extent that the embossing machine is well aligned). In most cases, the part adheres to the patterned mold and detaches from the flat backing plate in a manner similar to a pull test. In the case of double-sided embossing, the part is likely to adhere preferentially to the mold with the more difficult to demold pattern (or the more difficult areas of each mold). While pull tests have some relevance for practical demolding, the often-cited variation in the resulting data and the inability to control the location and progress of failure would make pull tests a poor vehicle for studying feature-level processes during demolding.

4.3.2 Peel Test

Peel tests are very commonly used to evaluate the strength of adhesion between a stiff substrate and a flexible adherend. Figure 4.7 depicts one common configuration, but many others exist.
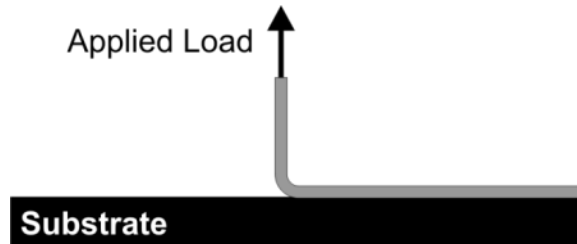
Figure 4.7 Schematic diagram of a 90° peel test. The measured peel force divided by the width of the specimen is taken as the "peel strength."

Peel test specimens are simple to prepare, and the ability to control the rate of peeling permits the study of time-dependent phenomena (such as viscoelastic effects) [116]. Peel tests are widely applied, and are described by several ASTM standards including D3330 (pressure-sensitive tape), D903 (180° peel tests for adhesion to metals), and many others. The measured peel force divided by the width of the specimen (the "peel strength") is useful for comparing the results of peel tests, and principles of elastic fracture mechanics can be used to relate this to the toughness.

The geometry of the test produces localized stresses along the peel front, so the location and progress of failure is well controlled. The test also produces large strains in the specimen near the bend. This fact limits the applicability of peel tests to flexible, tough materials. A peel test would not be suitable for studying demolding of stiff amorphous thermoplastics commonly used in hot embossing (except for very thin layers that have low bending stiffness). Peel tests have been used to study the demolding of microstructures cast in flexible materials such as UV-cured acrylate [120] and PDMS [45].

4.3.3 Blister Test

In a blister test, hydrostatic pressure is applied to the adherend through an opening in the substrate. Figure 4.8 depicts a common configuration, and others have been reported as well [116, 121]. Blister tests have the advantage of localized stress concentration, so crack initiation is controllable. The principles of elastic fracture mechanics can be applied to the blister test to

calculate the interface toughness based on the elastic properties of the adherend, the applied pressure, and the radius of the blister [121].
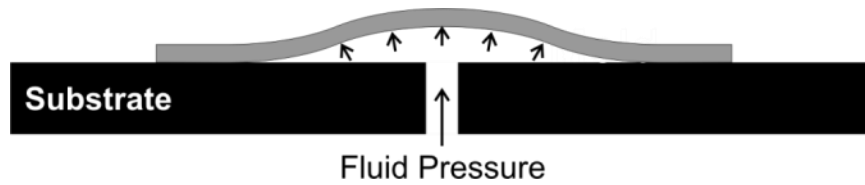
Figure 4.8 Schematic diagram of a blister test. Compare with Figure 4.5(a). Fluid pressure applied through an opening in the substrate initiates a crack around the opening, which propagates across the interface. The applied pressure and the blister radius can be related to the interfacial toughness.

Demolding by fluid pressure itself has been demonstrated for PDMS casting [25, 122, 123]. One difficulty with this method is the fact that the port for introducing the pressurized fluid must not allow penetration of the cast or embossed material before demolding. Another difficulty lies in the fact that the strain energy release rate (see section 2.3.1) increases with increasing blister radius, resulting in an unstable test condition (that is, the crack front is prone to "runaway") [121]. This fact also requires very accurate measurement of the blister radius in order to determine the interface toughness.

Comparing Figure 4.8 with Figure 4.5a, one can see a resemblance suggesting that blister tests may be a useful model for demolding via ejector pins. One can imagine a variation of the blister test where fluid pressure is replaced by an ejector pin. The applied load and displacement of the pin could be monitored during demolding and, along with the blister dimensions and elastic properties of the specimen, could be related to the toughness of the interface. Such a test has potential for quantitatively studying demolding; however, an embossing machine with an instrumented ejector pin that penetrates a platen would be mechanically more complicated than the cantilever design adopted in the present work (sections 4.3.5 and 4.5.6). The need to accurately measure the blister radius also presents some difficulty in developing a simple and reliable test method. In many practical cases, ejector pins are placed outside the patterned area of the mold, rather than amongst the features, and so once the crack has propagated to the main patterned area (the area most of interest during demolding), the demolding conditions resemble those of a cantilever test more than a blister test.

4.3.4 Razorblade or Wedge Test

One cantilever type test that has received a great deal of interest is the wedge, or "razorblade" test. This method is described by ASTM D3762 (adhesives for bonding aluminum). This method was introduced to the field of microfabrication by Maszara for evaluating the strength of bonded silicon wafers [124]. A wedge of a known thickness (quite often a razorblade) is inserted between two bonded layers, as shown in Figure 4.9 [116, 117]. The length of the resulting crack can then be used along with the elastic properties and geometry of the beams to calculate the toughness of the interface (Eq. 4-1) [117]. This calculation depends on the fourth power of the crack length, so this length must be measured very precisely to produce a useful estimate of the toughness.
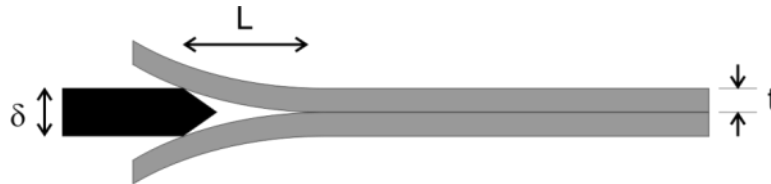
Figure 4.9 Schematic diagram of a wedge, or razorblade test. A wedge is inserted between bonded layers, and the length of the resulting crack is related to the interfacial toughness.

$$2\Gamma = \frac{3E'\delta^2 t^3}{8L^4}$$ **4-1**

where

Γ	Toughness
E'	Effective modulus ($E' = E$ for plane stress and $E/(1-v^2)$ for plane strain)
δ	Wedge thickness
t	Beam thickness
L	Crack length

As discussed in section 1.5.3, the razorblade test was adopted by Landis et al. [60] to study demolding in nanoimprint lithography (in their paper, they refer to the method as the Double Cantilever Beam or DCB method). They found that applying this method for quantitative characterization of demolding required fastidious attention to detail. For instance, variation in the insertion angle of the blade by as little as one degree introduced significant variation in the test results. The calculated toughness was also found to depend on the blade insertion distance and insertion speed.

One can imagine a variation of the symmetrical razorblade test where one beam is replaced by the (practically rigid) embossing mold. The razorblade type cantilever test has demonstrated usefulness for studying demolding; however, the sensitivity of the test to experimental parameters (insertion angle, speed, distance), and the need to measure the crack length very precisely, make this method difficult to implement in practice, as Landis et al. experienced [60].

4.3.5 Cantilever Beam Test

Many adhesion test methods are based on the cantilever geometry [116]. Cantilever beams have simple, well-known bending mechanics, so analyzing the results of these test methods is straightforward. The stresses induced by the test are also analytically manageable. The archetype of this category of tests is the Double Cantilever Beam or DCB test, which is described in ASTM D3433 (for adhesives for bonding metal) and D3807 (for adhesives for bonding polymers) and depicted in Figure 4.10(a). Two bonded strips with an initial crack are loaded normal to their long dimension near the pre-cracked end, as shown in Figure 4.10a. Usually, the displacement of the beam ends is controlled to a constant rate. The maximum force before the crack extends can be used to determine the interfacial toughness.
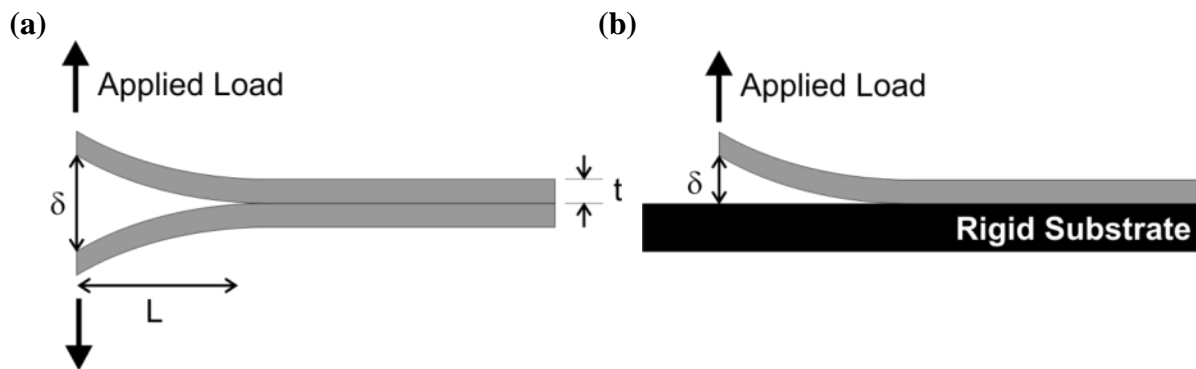
Figure 4.10 Diagram of cantilever test configurations. Bonded specimens with an initial crack are pulled apart at their ends, and the maximum force before the crack extends is related to the interfacial toughness. (a) DCB test as described in ASTM D3433, (b) asymmetric cantilever beam test with a rigid substrate (compare to Figure 4.1).

According to ASTM D3433, the toughness is calculated from the maximum load at failure and the specimen dimensions and properties by Equation 4-2. This relation is derived from simple beam theory, and it illustrates the straightforward analysis enabled by the cantilever test geometry.

$$G = \frac{4P^2\left(3L^2 + t^2\right)}{Eb^2t^3}$$ **4-2**

where
G   Toughness
P   Applied load
L   Initial crack length
t   Cantilever thickness
E   Elastic modulus
b   Cantilever width (into the page in Figure 4.10)

An alternative arrangement with great relevance to demolding is the asymmetric cantilever test, shown in Figure 4.10(b). In this test, one cantilever is replaced by a beam with different elastic constants and/or dimensions [125, 126], or a rigid (or effectively rigid) substrate [127, 128]. The beam-bending mechanics of an asymmetric cantilever test are quite similar to those of a double-cantilever test. Following the strain-energy approach (2.3.1) and assuming a rigid substrate that does not contribute to the strain energy of the system and that the cantilever is built-in at the root, the toughness can be calculated from Equation 4-2, which includes the effects of shear stress in the beam. Gillis and Gilman [129] relaxed the assumption of perfect constraint at the cantilever root, and their model can be used to produce Equation 4-3. Other researchers [130, 131] have also produced augmented models that incorporate higher order effects or use a different approach to account for the elastic foundation, but these models are more complex without appreciably increasing accuracy.

$$G = \frac{P^2}{E'b^2t}\left(3(\nu + 1) + \frac{12L^2}{t^2} + \frac{84L}{5t}\right)$$ **4-3**

where
G   Toughness
E'   Effective modulus: E'=E/(1-ν^2) for plane strain, E'=E for plane stress
ν Poisson's Ratio
P   Applied load
L   Initial crack length
t   Cantilever thickness
b   Cantilever width (into the page in Figure 4.10)

4.4 Demolding experiment concept

One of the major contributions of this work is the characterization of demolding of polymer microstructures produced by hot embossing through demolding experiments. The demolding work is proposed as the metric by which demolding can be characterized. The goals of demolding experiments are therefore to accurately and consistently measure the demolding work, and to assess the effect of varying process parameters and mold geometry on the demolding work.

One important criterion for a useful experiment is that it is representative of the real-world system that is the object of study. The results of demolding experiments should be relatable to practical demolding. Comparing Figure 4.10(b) with Figure 4.1 and Figure 4.5(b), one can see a clear resemblance that suggests this type of adhesion test could be applied to studying demolding. Indeed, because typical molds are much stiffer in bending than typical embossed parts, and molds are firmly mounted to platens, the asymmetric cantilever test geometry is nearly identical to the conditions experienced in practical demolding. The strong similarity with practical demolding, the ease of analysis, and the ease of adapting a hot embossing machine for this type of test combine to favor asymmetric cantilever tests as a method for studying demolding in hot embossing. This test method is adopted for the present work.

The experimental method implemented in this work begins with a typical embossing cycle of heating, pressing, holding, and cooling. Once the part is cooled to the demolding temperature, it is demolded by a controlled displacement of one edge, as in an asymmetric cantilever test. The load and displacement are measured and recorded during demolding, and this data is used to determine the demolding work. In a compromise between perfect realism and straightforward analysis, the test specimens are much longer in one dimension so that they can be modeled as cantilevers, facilitating comparison with the models and simulations discussed earlier. The experimental molds are not real microfluidic chip designs, but are simplified patterns that are designed to probe specific effects of feature geometry, such as height and width. The machine that was developed for these tests is described in the following section, while the molds are described in sections 4.5.5, 4.6, and 5.2, the experimental procedure is described in section 4.7, and the data analysis process is described in section 4.8.

4.5 Demolding Machine

A specialized apparatus (Demolding Machine) has been developed for demolding experiments. The demolding machine should mimic practical demolding as closely as possible so that experimental results will be relevant and applicable to real hot embossing applications, such as the manufacture of microfluidic chips. This machine must also be able to accurately measure and record the results of each demolding experiment.

4.5.1 Functional Requirements

The demolding machine used in this work must first complete a hot embossing cycle in order to produce the conditions for demolding. The machine must therefore be able to reach and maintain a specified temperature within the range commonly used for hot embossing and demolding (room temperature to ~150°C for PMMA, and hotter for some other materials). The demolding machine must apply sufficient, controlled embossing force to ensure good replication of the mold features. During demolding, the machine must be able to apply and measure the demolding force while monitoring and controlling the displacement of the part and/or demolding fixtures. Control of temperature, embossing pressure, and the demolding process must be consistent and repeatable to reduce experimental variation.

4.5.2 Motion system

Load and motion control in the demolding machine is accomplished by mounting the platen assemblies in an electromechanical load frame (Instron 5869), as shown in Figure 4.11. The lower platen is fixed to the frame base, while the upper platen is connected through the load cell to the moving crosshead.
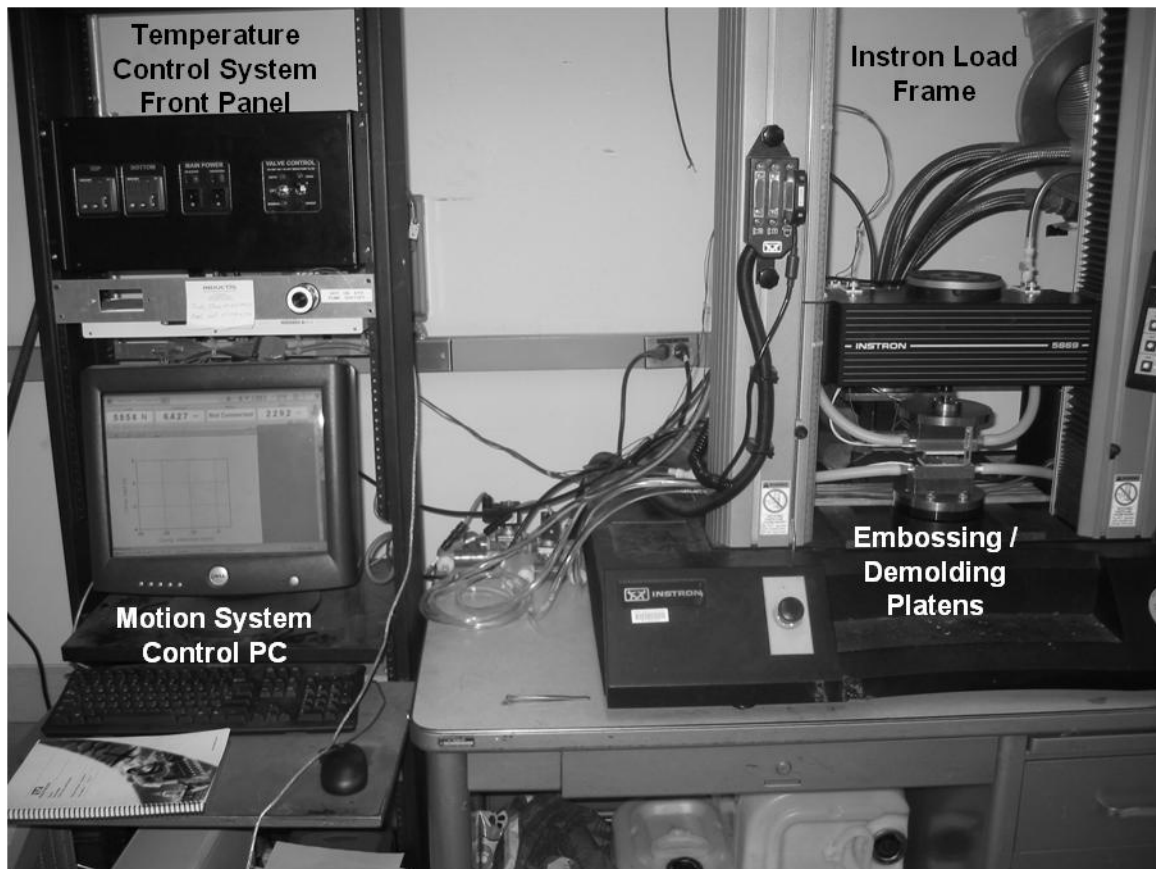
Figure 4.11 Photo showing demolding machine including platens mounted in Instron load frame, motion system control PC, and thermal system front panel.

The load frame is controlled through proprietary software (Merlin v 5.53). Both the embossing load and the demolding load are measured via a 1kN-rated load cell. The load cell has a quoted accuracy of 0.5% of its reading down to 0.5% of the full-scale range (0.025 N at 5 N), and a constant accuracy of 0.025 N below 5 N. The position of the platens (and the demolding bar during demolding) is measured through the internal axis position encoder in the load frame. The quoted resolution of the position control system is sub-micrometer.

4.5.3 Temperature control system

As in typical hot embossing, the temperature of the part and mold during embossing and demolding is determined by controlling the temperature of the embossing platens. The heating and temperature control system is modeled after that designed by Hale [34]. The manufacturer, model numbers, and relevant characteristics of the various components discussed below are listed in appendix 0. Figure 4.12 depicts a schematic diagram of the system.
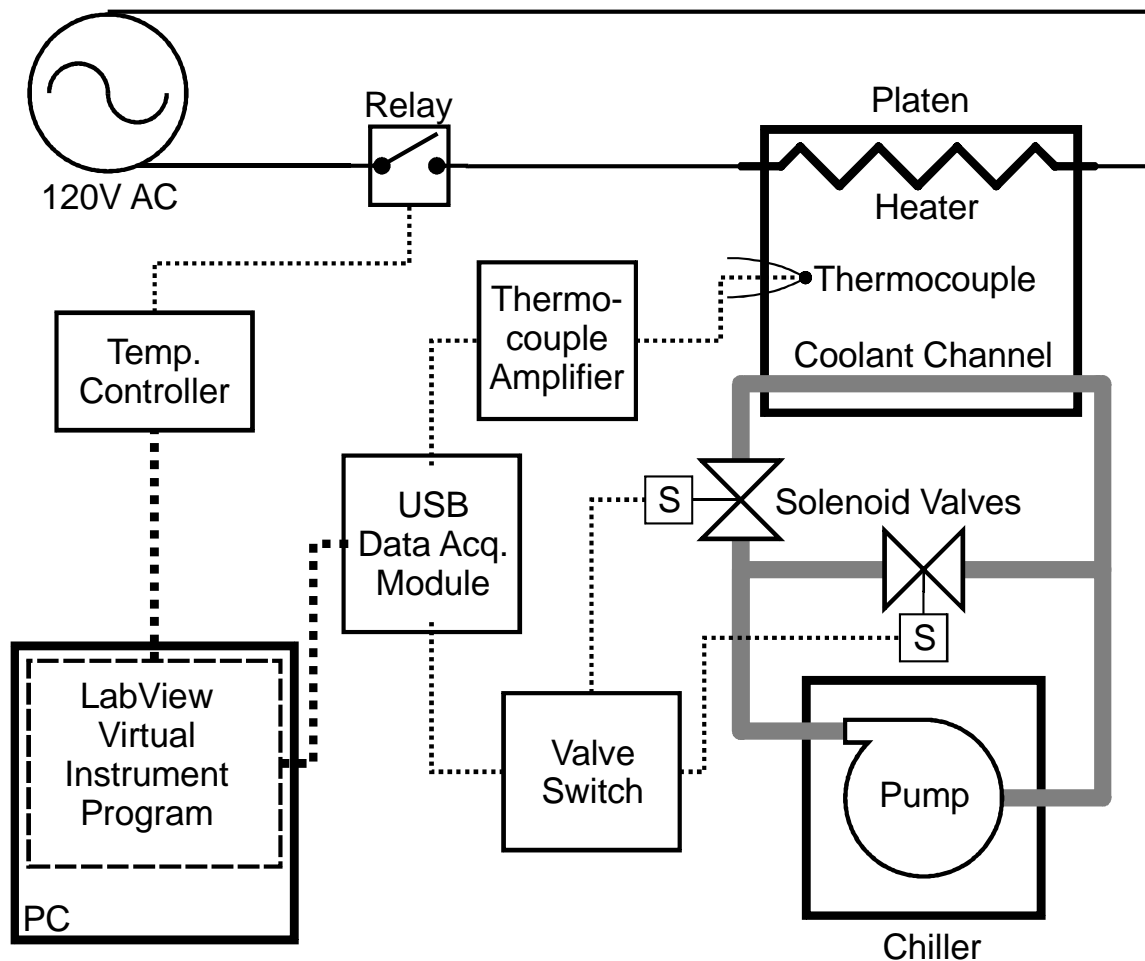
Figure 4.12 Schematic diagram of the temperature control system. For simplicity, only one platen is shown.

For thermal isolation, the platens are separated from the structure of the machine by ceramic insulation blocks. Each platen contains a ceramic heater with a resistive heating element. These heaters are connected to electrical power through a solid-state relay. The power supplied to the heaters is controlled by a pulse-width-modulated signal generated by temperature control modules, one for each platen. The temperature control module monitors the temperature of the heater via an embedded thermocouple, and adjusts the power level according to a PID control scheme. Each platen is cooled by a solution of water and ethylene glycol flowing through an internal passage. The coolant is circulated and cooled by a laboratory chiller. The coolant temperature is regulated to be 5°C, and the flow rate is roughly 4 L/min. The flow of coolant through the platens is started and stopped by solenoid valves, which can be activated either automatically via the control program running on the PC or manually using switches on the temperature control system front panel (Figure 4.13).

Figure 4.13 Photo of the temperature control system front panel. The PID heater controllers are at left, and the manual override switches for controlling the coolant flow are at right.

The temperature of each platen is monitored through a separate thermocouple mounted within the mold. The voltage from each thermocouple is amplified and adjusted by integrated circuits to a DC signal calibrated to 0.1 V per degree Celsius, with 0°C set to 0.0 V. The calibrated platen temperature voltages are measured via a data acquisition board containing an analog-to-digital converter.

The platen temperature is monitored and controlled through a virtual instrument (VI) program running in LabView. A PI control routine within the VI continuously adjusts the setpoint of the temperature control modules via a digital interface to reach and maintain the desired platen temperature. The solenoid valves that control the flow of coolant are also switched by a signal within the temperature control VI. When the controller gains are chosen appropriately, the temperature control system is capable of heating to typical embossing temperatures in 60-120 s, maintaining the desired temperature within 2°C, and cooling to typical demolding temperatures in 60-120 s. Heating and cooling times depend on the difference between the beginning and ending temperatures, since for most of the transient the temperature rate of change is limited by either the heater output power or the convective cooling capacity of the coolant passage.

As an example, some temperature data logged by the control VI is plotted in Figure 4.14. The temperature of a PMMA sample was monitored for this test using an embedded thermocouple. Because the two heaters used in the system (upper and lower platen) do not

125

perform identically, the transient responses of the two platens to a change in setpoint temperature are not the same. The closed-loop temperature control system accounts for these differences, so the steady-state temperatures of the platens are effectively the same.
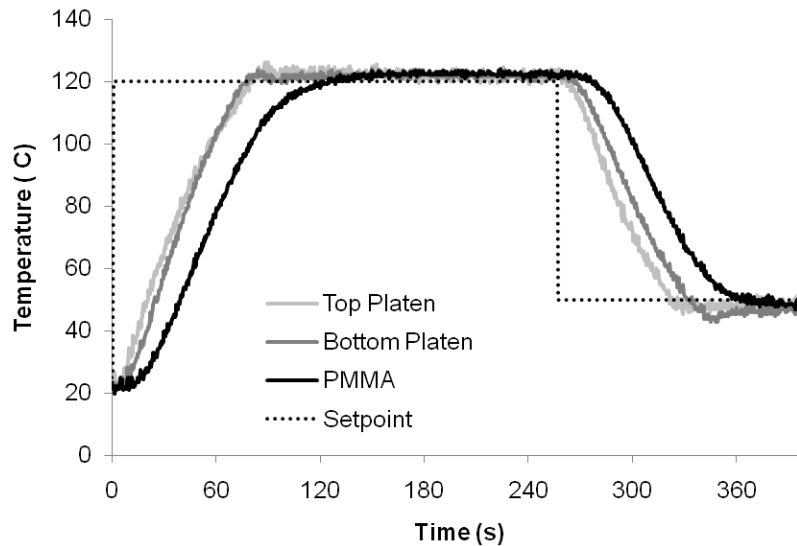
Figure 4.14 Plot of temperature data recorded by the temperature control VI showing closed-loop performance of the temperature control system. The temperature of a 3.2 mm thick PMMA sample between the platens was measured for this test with an embedded thermocouple.

4.5.4 Platens

Each platen is built up from three metal pieces (stainless steel 316): the platen body plus two cover-plates. A diagram of a platen and a platen assembly can be found in Figure 4.15 and Figure 4.16, respectively. The platen bodies were custom-fabricated by the Central Machine Shop at MIT, while the cover plates were water-jet cut from sheet stock, with additional machining in a drill press. The platen bodies have thick sidewalls to carry the embossing loads, an upper chamber to accept the ceramic heater, and a lower chamber that serves as the coolant flow passage. The coolant passage has a central island to help carry the embossing loads and protect the ceramic heater from distortion under load, which could cause it to crack. The sidewalls contain clearance holes for mounting the platens in the embossing machine, tapped holes for attaching the cover-plates and molds, and threaded holes for pipe fittings for connecting the coolant hoses. The cover plates have windows for accessing the platen mounting screws and countersunk holes for attaching the cover plates to the platens with flat-head screws flush with the surface.

126
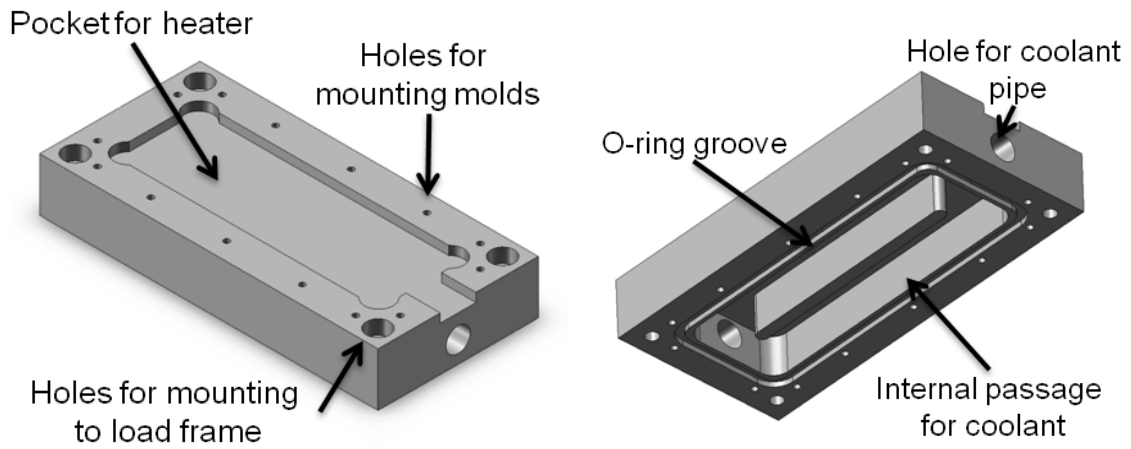
Figure 4.15 Diagram of a platen body.
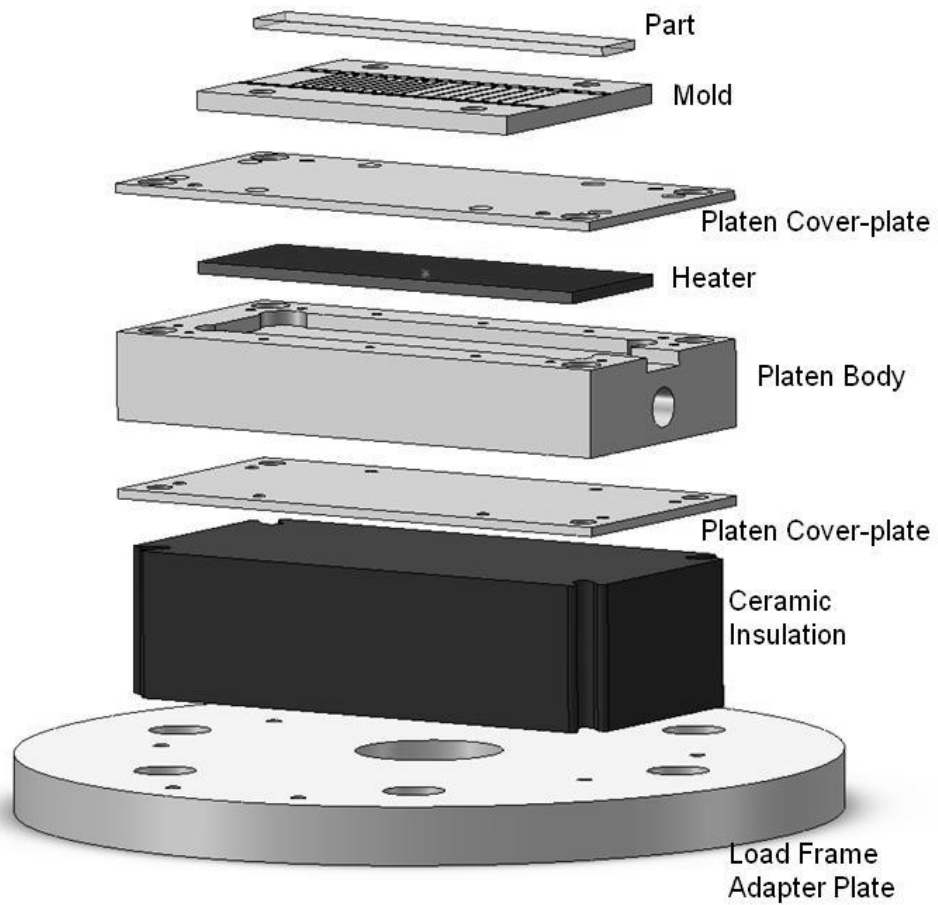
Figure 4.16 Diagram of the bottom platen assembly. The top platen assembly is similar.

4.5.5　Molds

The demolding machine includes means of mounting molds to the platens. The typical mold consists of a metal plate 45 mm by 62 mm, and between 3 mm and 5 mm thick. Molds are mounted to the platens by four screws near their corners. For most experiments, the mold with features of interest is mounted to the lower platen and a featureless, flat mold (backing plate) is mounted to the upper platen. All molds have a 0.8 mm diameter by ~10 mm deep hole drilled into one edge to allow insertion of a thermocouple for temperature measurement and control during experiments. A photo of a mold is shown in Figure 4.17. The specific feature layouts tested are discussed in section 5.2.
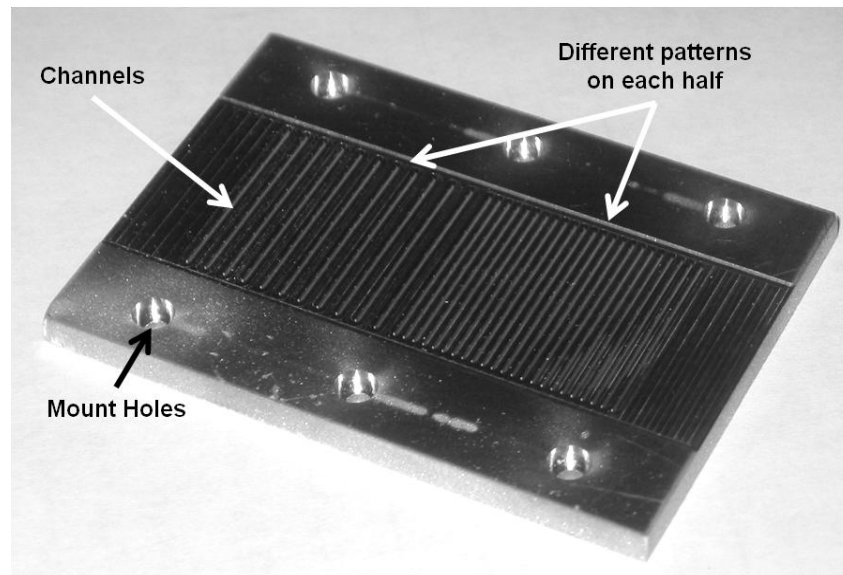
Figure 4.17 Photo of a mold used in demolding experiments. This mold has several parallel ridges (for embossing channels) 100 μm high, 100 μm wide, and spaced 1 mm and 2 mm apart.

4.5.6　Demolding fixture

The demolding force is applied to the embossed part by a steel bar at one edge of the mold. The demolding bar is positioned through holes at the ends of sliding links on each side of the platen. The sliding links allow the platens to be closed for embossing (Figure 4.18a). After the platens are cooled to the demolding temperature and the platens separate, the links slide until they come against adjustable stops attached to the upper platen assembly. Once the sliding links reach the stops, the demolding bar begins to move upwards, and is soon in contact with the part.

The bar lifts the end of the part, initiating a crack between the part and the mold, which propagates along the interface as the upper platen continues to move upwards (Figure 4.18b).

(a)

(b)
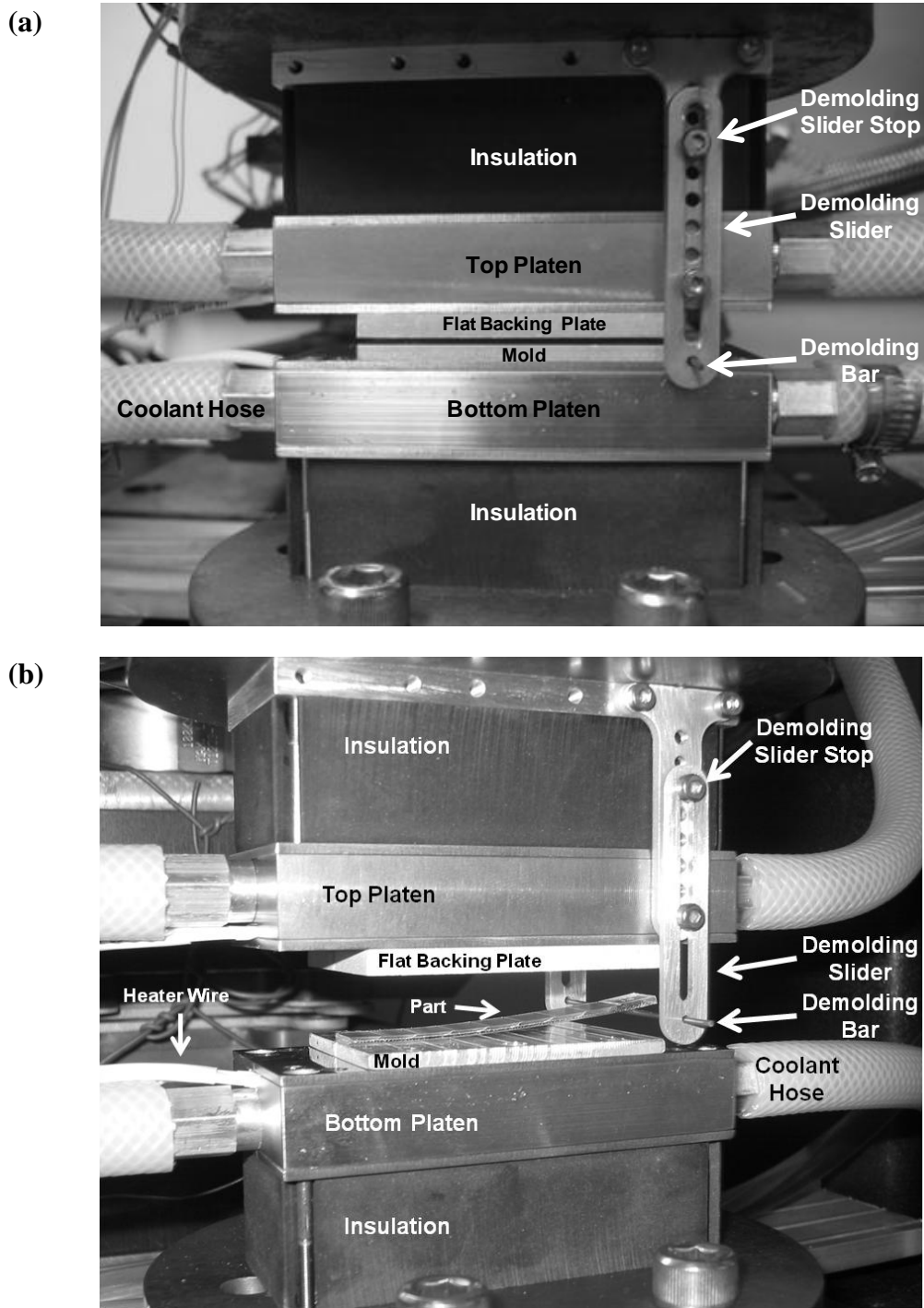
Figure 4.18 Photos of demolding fixture and platen assembly (a) during embossing (b) during demolding.

4.6 Mold fabrication

Test molds were produced by water-jet cutting rectangular blanks from a sheet of Aluminum 6061-T6 (McMaster-Carr). Mounting holes were drilled during water-jet cutting, while the thermocouple port was drilled using a standard vertical milling machine. For some molds, such as the brass molds, blanks were machined from stock using a standard vertical milling machine. The microchannel features on the molds were produced using a Microlution 363-S horizontal micro-milling machine. Carbide square end mills with diameters from 3.175 mm down to 0.397 mm were used. The numerical code for machining the molds was generated using MasterCAM. The specific machining parameters used are listed in Appendix D.2.

After machining, molds were cleaned with water-based degreaser (Simple Green™), then rinsed with acetone and dried with compressed tetrafluoroethane (VWR Whoosh-Duster™). Molds were then inspected with an optical microscope. If metal chips or other debris was evident, the molds were gently brushed with a plastic bottlebrush, and the acetone rinse / dry process was repeated. Finished molds were labeled with a permanent marker and stored in polystyrene Petri dishes. If at any time a mold became contaminated (fingerprints, dust, extended storage outside a container), the acetone rinse / dry process was repeated.

4.6.1 Micro-machining parameters

During this work, it was found that under some circumstances micro-milling produced burrs along the edges of micro-features on the mold. These burrs had a detrimental impact on demolding (see section 5.9.2). At low feed rates, the displacement of the part between the passage of each cutting edge of the tool (feed per tooth) was small enough that material was plowed instead of cutting cleanly, leaving large burrs on the parts. At higher feed rates (higher feed per tooth), there is enough material for the cutting edge to "bite" and create a chip. Very high feed rates, however, degrade the surface finish of the final part because the cutting marks are widely spaced. A range of feed rates was tested with sample mold blanks. A fresh 1.588 mm diameter carbide square end mill was used for these tests, and the spindle speed was fixed at 50000 rpm. The results of these tests are shown in Figure 4.19.
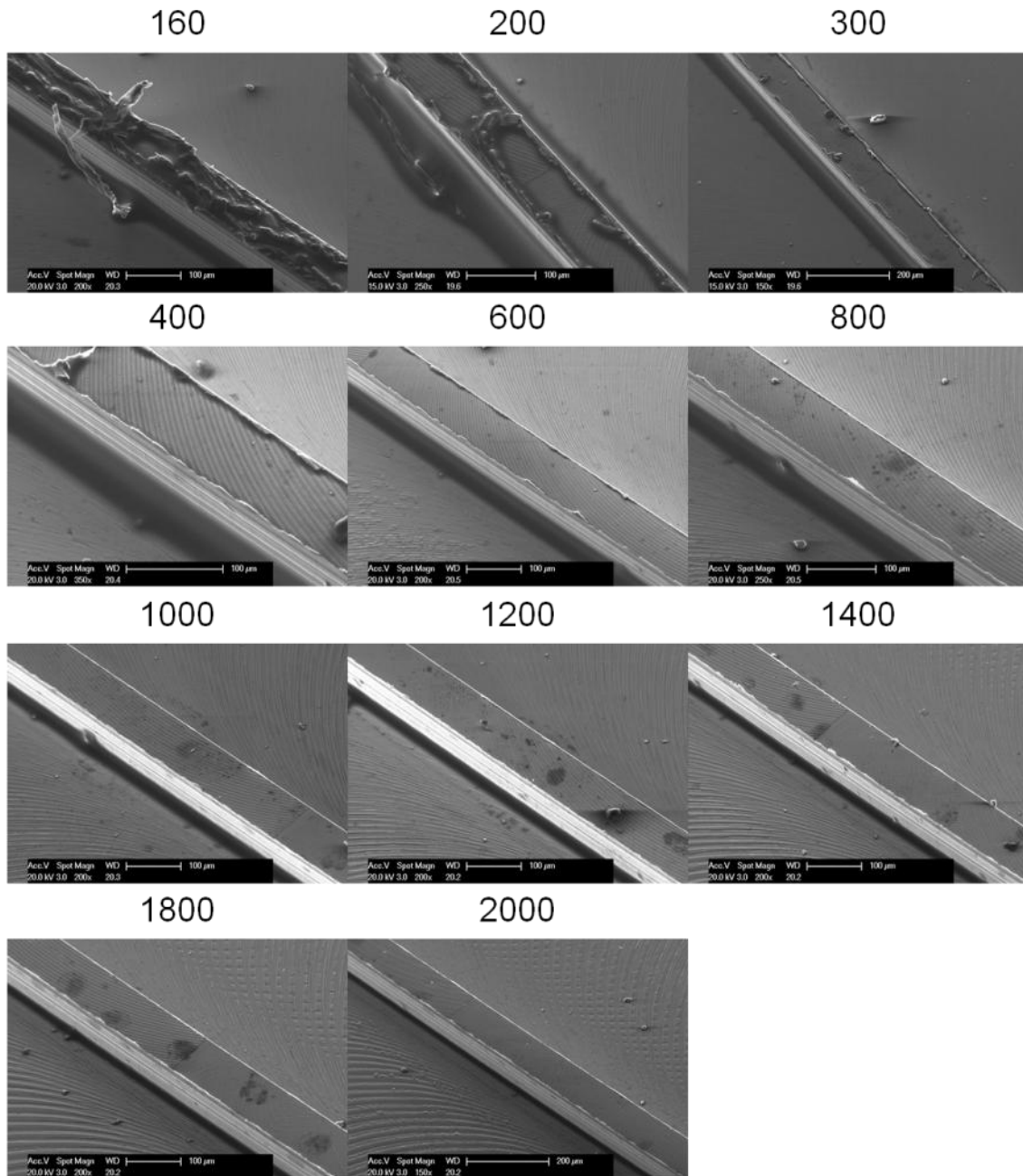
Figure 4.19 Scanning Electron Micrographs of results of machining parameter study.
Features are 100 μm high square protrusions (for embossing channels). Numbers are feedrate in mm/min.
Note the large burrs on the features machined at low feed rates, and the increasingly rough surface finish
with increasing feed rates. Based on these results, a feed rate of 1000 mm/min was used with 1.588 mm end
mills for machining molds. Feed rates for other size end mills were extrapolated from this value. Specific
machining parameters are listed in Appendix D.2.

Cutting parameters for machining test molds (spindle speed, feed rates, and depth of cut)
have been chosen based on these results, as well as from the recommendations of the online feed
and speed calculator provided by Robb Jack Corp, a supplier of cutting tools

(www.robbjack.com). Specific machining parameters used to produce test molds are listed in Appendix D.2.

4.7 Experimental procedure

The sections below describe the typical process for conducting experiments.

4.7.1 Specimen preparation

The specimens for the cantilever demolding tests consist of long strips of the part material (PMMA or polycarbonate). Specimens were produced by cutting from larger sheets using a CNC CO_2 laser system (Epilog Laser Mini24 with 45W laser). During cutting, unique numbers are laser-engraved in the surface of each specimen for identification and record keeping. The polyethylene backing films were retained on both sides during laser cutting. These backing films were not removed until immediately before an experiment to ensure that the specimens' surface remained clean. Specimens were usually laser-cut in large batches prior to a set of experiments. The standard specimens are 10 mm wide by 70 mm long and 1.59 mm thick. The extra length, compared with the 62 mm long mold (section 4.5.4), allows the specimen to project past one edge of the mold and cross over the demolding bar (section 4.5.6), and provides extra space to engrave the part number without interfering with the embossed pattern. A photo of a specimen is shown in Figure 4.20.
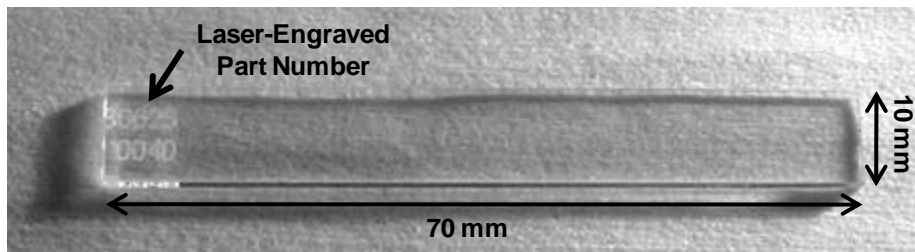
Figure 4.20 Photo of an unused PMMA specimen (part).

4.7.2 Experiment setup

Prior to an experiment, the computers that control the Instron load frame and the temperature control system are booted and the control software is executed (Merlin and the LabView VI, respectively). The mold set is mounted to the platens (patterned mold to the lower platen, and flat backing plate to the upper platen) and the thermocouples are inserted into the

132

ports in the molds (see section 4.5.5). The gauge length of the extension measurement for the load frame is set so that extension is zero when the demolding bar is just below the surface of the mold. This setting ensures that all demolding activity occurs for extension > 0, which simplifies data analysis (see section 4.8). The control software is configured to match the intended experimental parameters (see section 4.7.4).

Once the demolding machine is prepared as above, a specimen is selected, its backing film is removed, and it is placed onto the mold by hand (or, if the mold is at an unsafe temperature, the specimen is placed using tweezers). The specimen is aligned along the centerline of the mold by eye. This visual alignment is facilitated by the fact that the patterned area of the mold is not much wider than the specimen, so misalignment between the part and the mold is readily apparent. Once the part is loaded, the platens are manually brought together using the load frame's rapid jog function so that less than 2 mm gap remains between the part and the upper mold (flat backing plate). This action is taken to help ensure thermal uniformity through the thickness of the part at the beginning of embossing.

4.7.3   Process for each experiment

Once the machine and part are set up, the experiment can begin. The setpoint for the platen temperature control system is set to the desired embossing temperature, and the platens begin to heat up. The platen temperature rate of change is determined by the maximum power output of the electric heaters and by the thermal time constant of the platens. Section 4.5.3 discusses the transient performance of the temperature system. Once the platens have reached the embossing temperature (usually within 120 s), the test profile is activated in the motion control software (Merlin). Load and extension data is recorded throughout the test profile. The test profile begins by bringing the platens together at a constant speed until a load above a certain threshold is measured, indicating that the part is in contact with the upper platen. After this threshold is reached, the motion control system switches to load-control, and the load is ramped at a constant rate (N/s) up to the set embossing load.

Once the embossing load is reached, a timer is manually activated to count down the intended hold time. Once this hold time elapses, the platen temperature set point is switched to the intended demolding temperature. The platen temperature rate of change is determined by the convection cooling capacity of the paten coolant passage, the cooling capacity of the chiller, and

the thermal mass of the platen/mold assembly (section 4.5.3). The motion control test profile includes a constant-load hold whose duration is long enough to cover both the embossing hold time (at the embossing temperature) and the time to cool to the demolding temperature (usually within 120 s).

After this constant-load hold time has elapsed, the crosshead begins to move upward at a constant speed, separating the platens. The current temperature readings for the top and bottom platen at this moment are recorded as the actual demolding temperature. As this motion proceeds, the demolding bar fixture slides along its guides until it reaches the mechanical stop. After this point, the demolding bar moves upwards along with the upper platen. As the demolding bar moves, it contacts the bottom of the part and begins to apply the demolding load. Once the part has been completely demolded, the motion control software is stopped and the recorded data is saved. The demolded part is removed, and the next experiment may be set up

4.7.4 Experimental parameters

The configurations of the temperature and motion control programs, as well as the relevant parameters used for the majority of experiments are described below. Where any experiment deviated from these standard procedures or parameters, it is noted in the discussion of experimental results (Chapter 5). Demolding temperature has a very important effect on demolding, and so this parameter was set over a range of temperatures for various experiments. The other experimental parameters were held constant to isolate the more important effects of temperature, geometry and others that were the focus of this work. The embossing temperature, load, and hold time were chosen to ensure adequate replication of the mold features. Previous studies have found that many of the other parameters have little effect on embossing results [132].

Table 4.1 List of experimental parameters and typical values.

Parameter	Value
Embossing temperature	135°C for PMMA specimens 160°C for PC specimens
Pre-contact platen closing speed	10 mm/min
Contact load threshold	20 N
Embossing load ramp rate	4000 N/min
Embossing load	620 N (1 MPa) for PMMA, 930 N (1.5 MPa) for PC
Constant-load hold duration	120 s
Hold time at embossing temperature	30 s
Demolding temperature	25-135°C for PMMA 25-160°C for PC
Platen opening / demolding speed	15 mm/min
Extension & Load data recording	Data recorded every 2 μm in extension (125 samples/s during demolding)

4.8 Data analysis methods

All the relevant metrics of demolding are calculated from the load and displacement data recorded during each experiment. The goal of data analysis is to identify the locations in the load-displacement curve corresponding to demolding events associated with individual features on the mold. This is easy to do by eye, but for convenience and consistency, this task has been automated in MatLab. The scripts used are copied in Appendix C, and the operation of these scripts is described below.

4.8.1   Characteristics of experimental data

The load frame control software saves the recorded load and displacement data as comma-separated values in a text file. The data file is grouped into columns for each recorded load, displacement, and the time stamp for each data point. A data point is recorded for every 2 μm change in displacement, which corresponds to 125 samples/s while demolding at a rate of 15 mm/min. The load data recorded over the full duration of a combined embossing and demolding run is shown in Figure 4.21a. Some features of interest that are visible in this plot are the increasing compressive load ramp at the beginning of embossing, the constant-load hold during embossing and cooling, and a brief tensile force when the platens are first opened at the beginning of the demolding phase. Figure 4.21b shows a more detailed view of the load data

135

recorded during the demolding phase of the test, here plotted against the recorded displacement (extension) of the upper platen assembly. This plot shows the brief but strong tensile force recorded when the platens first open (the sticking force) along with the load data recorded during demolding of the mold features.

Figure 4.22 shows a detailed view of the load data recorded as the mold features were demolded. A small jump in load is visible corresponding to the weight of the demolding slider assembly when it reaches the hard stop and begins to move with the upper platen. Once the demolding bar comes into contact with the bottom of the part, the load increases rapidly as the part begins to bend. The peaks and troughs in load as each successive feature is demolded are clearly visible, along with a large drop in load associated with the change in pattern from one half of the mold to the other (see Figure 4.17). There is a small bias evident in the recorded load before the demolding bar comes into contact with the part, which is also visible in the recorded load value after the part has been completely demolded.
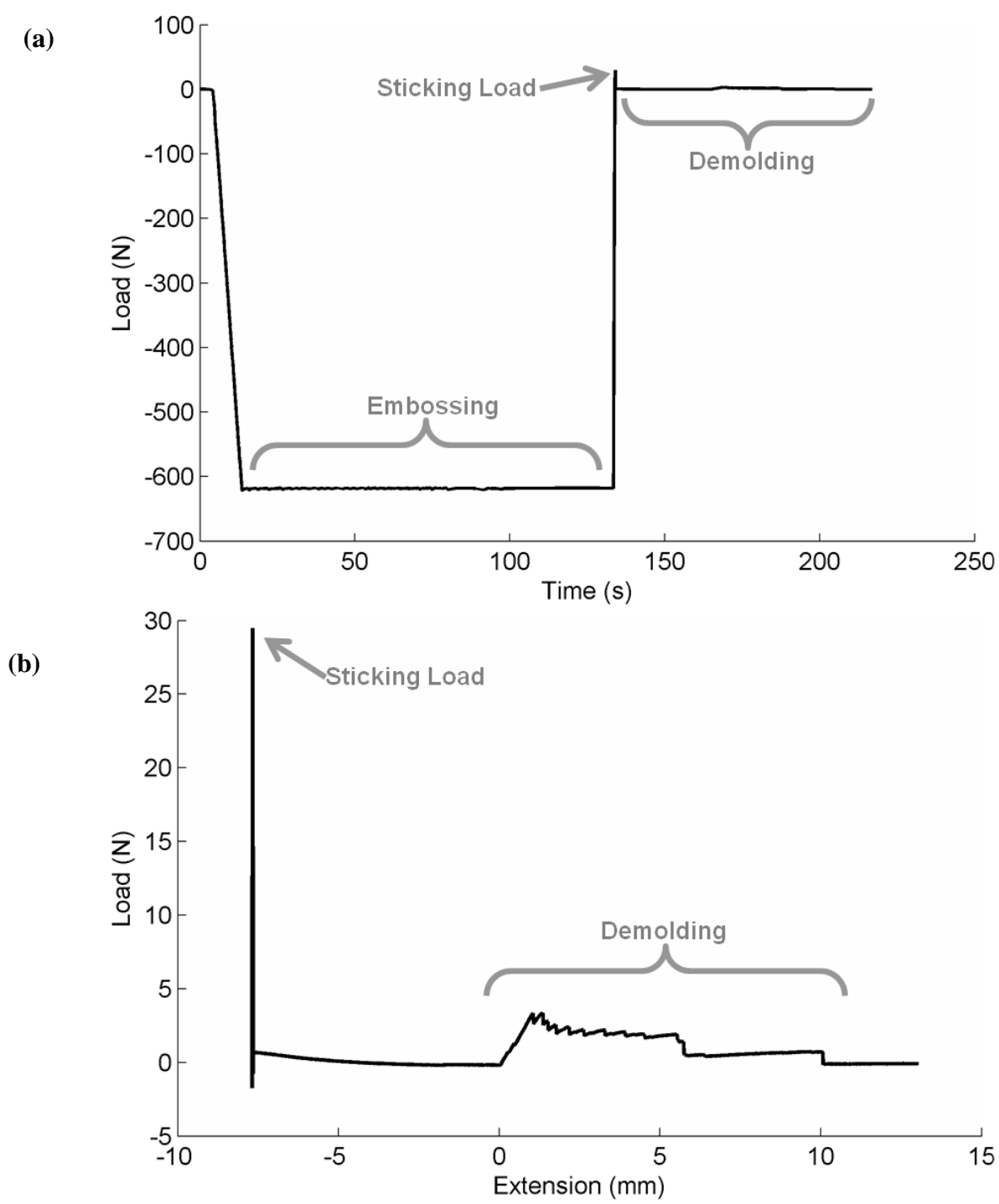
Figure 4.21 Plots of data recorded during an embossing / demolding test for PMMA embossed with a mold with 100μm high channels 2mm apart demolded at 73°C. (a) Load vs. time for the whole test (tensile loads are positive), (b) Load vs. displacement (extension) during separation of the top plate and demolding, including a strong, brief tensile load when the platens are first opened (sticking load) and the tensile loads associated with demolding.
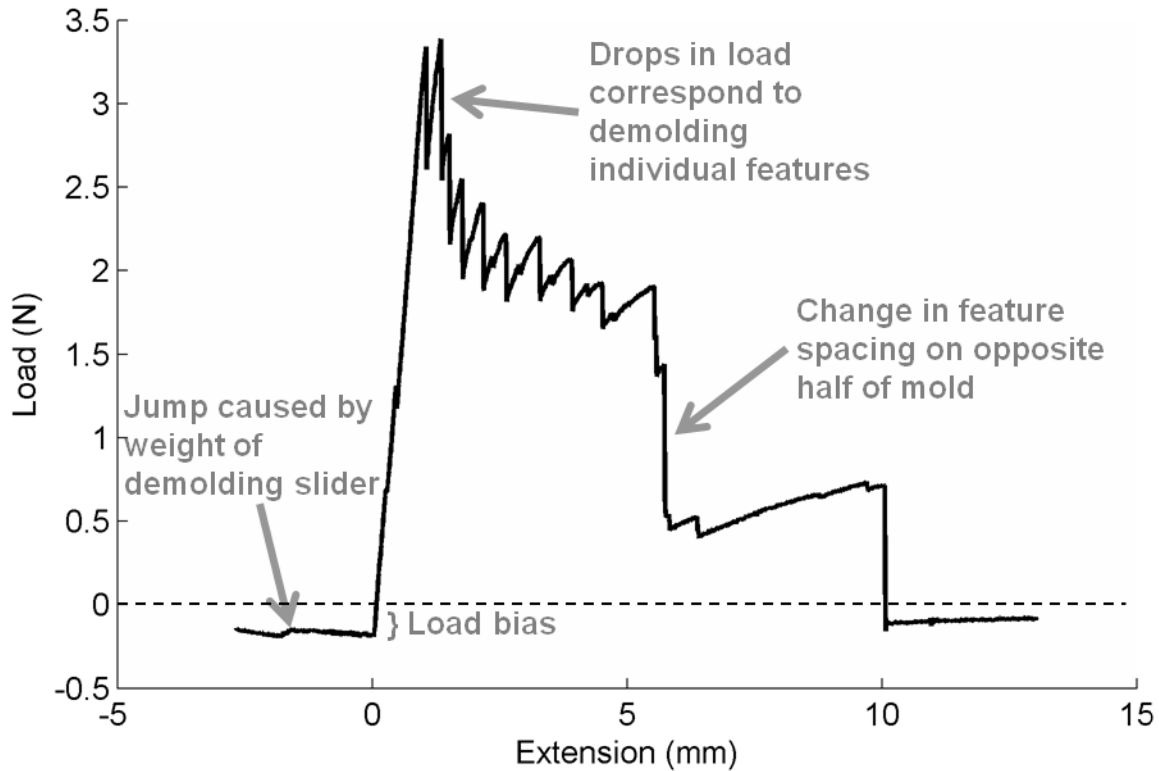
Figure 4.22 Detail of load and extension data for a PMMA part embossed with a mold with 100 μm high channels 2 mm apart demolded at 73°C.

4.8.2 Identifying points of interest and adjusting load and extension

In the first step of data analysis, a script is run that loads all of the data files in a given folder and converts them into MatLab structure variables with fields containing vectors of the time, load, and displacement data. These variables are saved to a MatLab-formatted data file for later retrieval.

In the second step of data analysis, a script is run that loads each data variable and processes it to calculate the metrics of interest. The data is partitioned based on the value of the recorded extension. Because the gauge length is set with the demolding bar just below the plane of the mold, all the demolding data will have extension greater than zero. The sticking load associated with separating the part from the flat backing plate is found from the maximum tensile load recorded for extension less than zero (Figure 4.21b).

The calculation of demolding work requires the beginning of demolding to be identified. This is accomplished by examining the slope of the recorded load ($\Delta P/\Delta x$). Calculating the slope between neighboring data points would amplify low-level noise in the load signal, so a finite difference calculation spanning ten samples is used instead: $(P_{i+10}-P_i)/(x_{i+10}-x_i)$. As an example,

138

the slope calculated in this way from demolding data for a PMMA part embossed with a mold with 100 μm high channels spaced 2 mm apart demolded at 73°C is plotted in Figure 4.23a. The point where this calculated slope first exceeds a set threshold (2 N/mm) is taken as an initial guess for the beginning of demolding, highlighted by the star symbol (⋆) in Figure 4.23a. The average load over the 70 data points before this point is recorded as the load bias (identified in Figure 4.22 and Figure 4.23b), and this load is subtracted from all the recorded loads to produce the adjusted load. The first point where the adjusted load is greater than zero immediately before the initial guess for the beginning of demolding is recorded as the beginning of demolding (highlighted by the star symbol in Figure 4.23b). The extension at this point is subtracted from all the recorded values of extension to produce the adjusted extension. The result of these adjustments is that the beginning of demolding is set to zero load and zero extension for every experiment, facilitating comparative plots and calculating the demolding work. A similar approach is used to identify the end of demolding (that is, the point where the part was completely released from the mold), highlighted in these figures by the filled circle symbol (●).

(a)

(b)
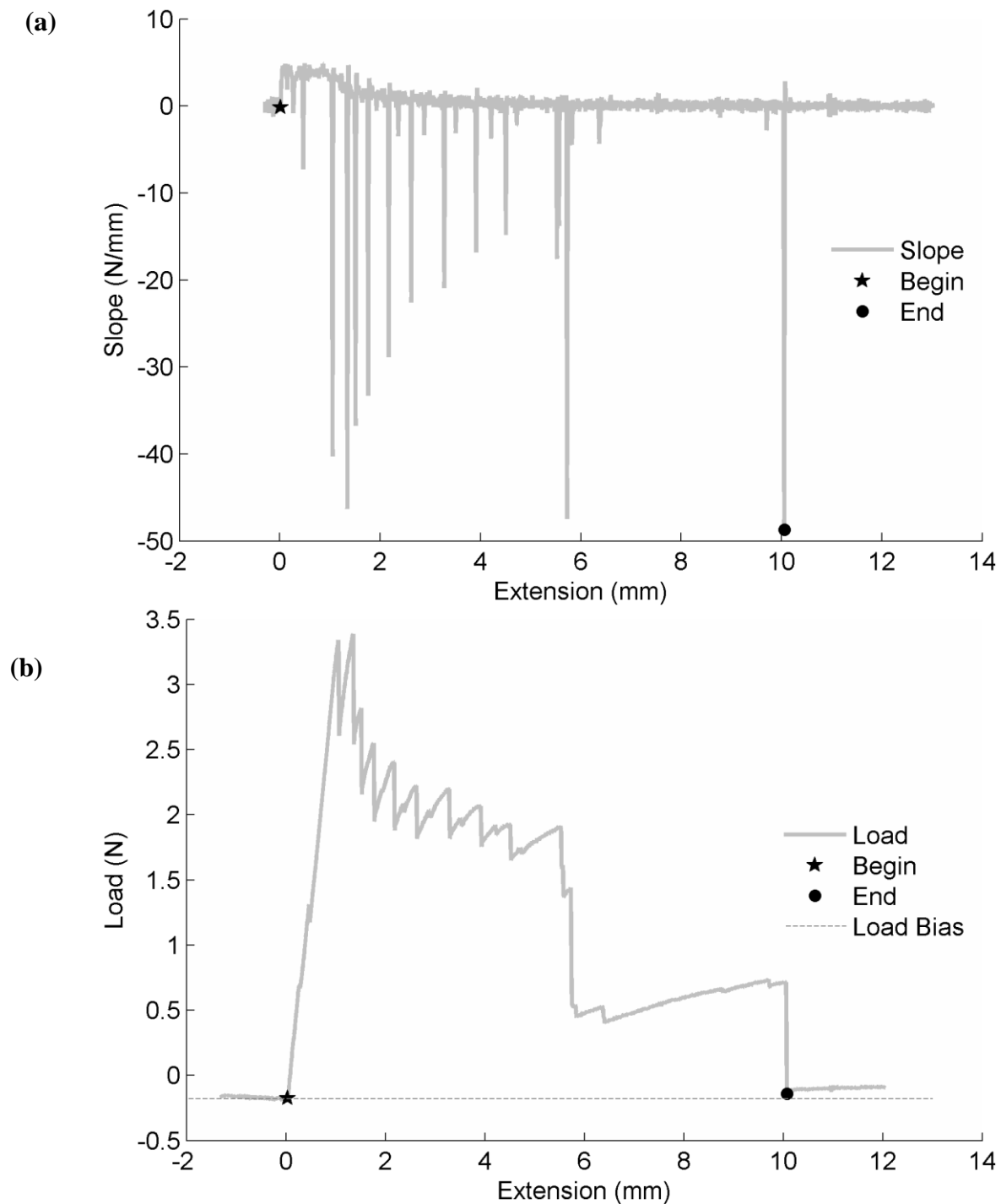
**Figure 4.23 Method of identifying beginning and ending of demolding and calculating load bias.
(a) Plot of calculated slope showing beginning and ending points identified as the first and last points,
respectively, to exceed threshold slope values. (b) Beginning, ending, and load bias superimposed on load-
displacement data. Load bias is found from the average load over a range of extension immediately preceding
the beginning point.**

4.8.3 Identifying demolding events

The next task is to identify demolding events associated with individual features on the mold. The beginning and ending points define the window within which demolding events will be identified. Two functions from the MatLab image processing toolbox are used to identify local extrema (imregionalmax for maxima and imregionalmin for minima). Because of low-level noise in the measured load signal, there are very many local extrema. Individual demolding events are associated with large, fast drops in load. Such large drops can be identified by the large difference between neighboring extrema. The difference between each local maximum and the following local minimum is calculated. The points with the largest difference between neighboring extrema are expected to be the demolding events. The number of expected demolding events is determined from the number of features on the mold, and is a user input to the data analysis script. If a particular mold produced 16 feature-associated demolding events, then the 16 points with the largest neighboring extrema are identified as potential demolding events. As an example, the extrema differences for load data recorded while demolding a PMMA part from a mold with 100 µm high channel features spaced 2 mm apart at 73°C are plotted in Figure 4.24a, where the identified demolding events are highlighted with open circle symbols (○). These points are superimposed on the load-displacement data in Figure 4.24b, showing that this approach does a good job of locating the demolding events.
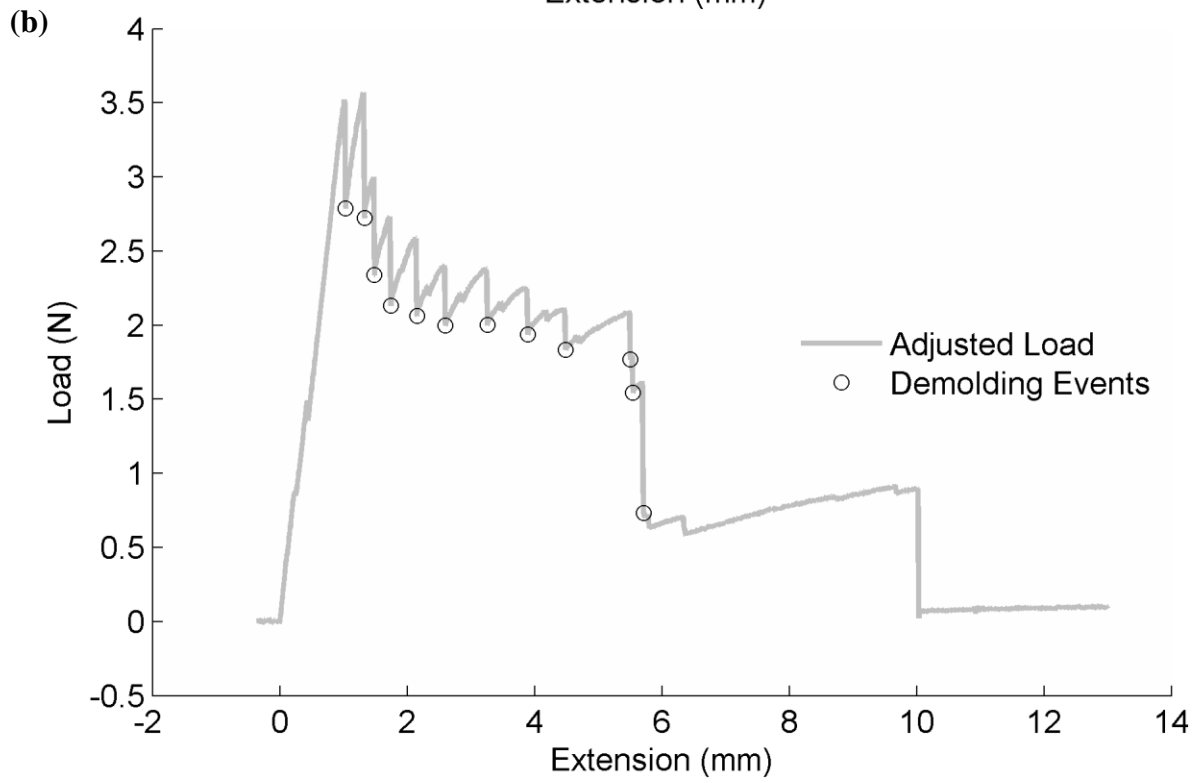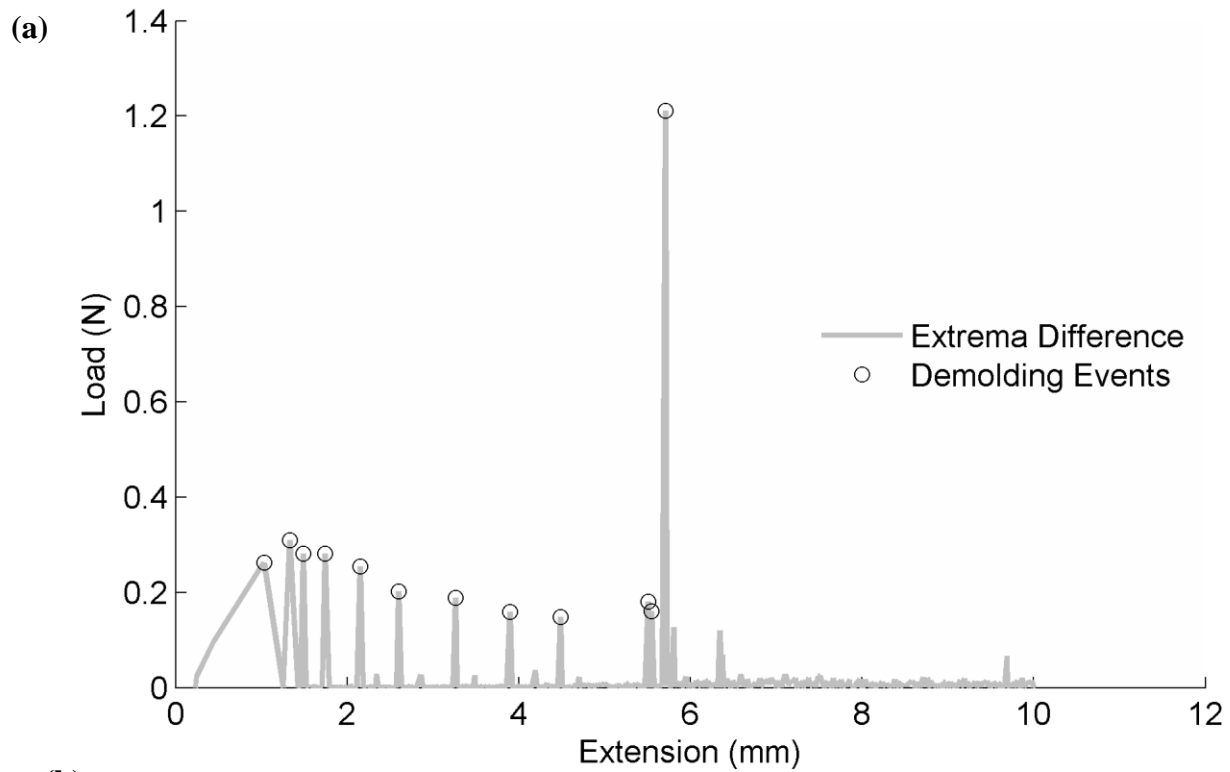
Figure 4.24 Method of identifying demolding events for a mold with 100µm high channels 2mm apart demolded at 73°C. (a) Plot of extrema differences with identified demolding events. (b) Identified demolding events superimposed on load-displacement data.

4.8.4   Calculating demolding work

The demolding toughness could be calculated from the maximum load before each demolding event according to, for instance, the relation given in ASTM D3433 (Equation 4-2). Load-based methods such as this rely on modeling the demolding part according to beam theory. The simple relation given by ASTM D3433 has been augmented by many researchers to account for additional effects such as shear stress and rotation at the beam root [129-131]. Even these more extensive models, however, require additional corrections because no model can fully account for the behavior of a real specimen [133]. In the present work, demolding work is calculated by the area method given by Equation 4-4 and depicted schematically in Figure 4.25. The area method does not rely on a model of the beam's behavior, and depends entirely on the recorded data and the assumption that all deformations are elastic.

$$\text{DMW} = \text{Area of region OAB in Figure 4.25}$$
$$\text{DMW} = \frac{1}{2}\, P_A x_A + \int_{x_A}^{x_B} P\; dx - \frac{1}{2} P_B x_B \qquad \textbf{4-4}$$

where
DMW   Demolding work
P   Load
x   Extension

The calculated demolding work for each demolding event is plotted in Figure 4.26. The large value of demolding work near the end of the series corresponds to the large drop in load associated with a change in pattern from one side of the mold to the other. Most molds used in this work have different patterns on each half, so only the demolding works from the first half are of interest in a given experiment. In calculating the mean demolding work for this part, only the first eight values are used, corresponding to the pattern on the first half of the mold. The mean demolding work per feature for the first half of the mold is used as an overall measure of demolding difficulty for that particular pattern and set of experimental conditions (such as demolding temperature). The mold would be mounted in the reversed direction to study the pattern on the other half.
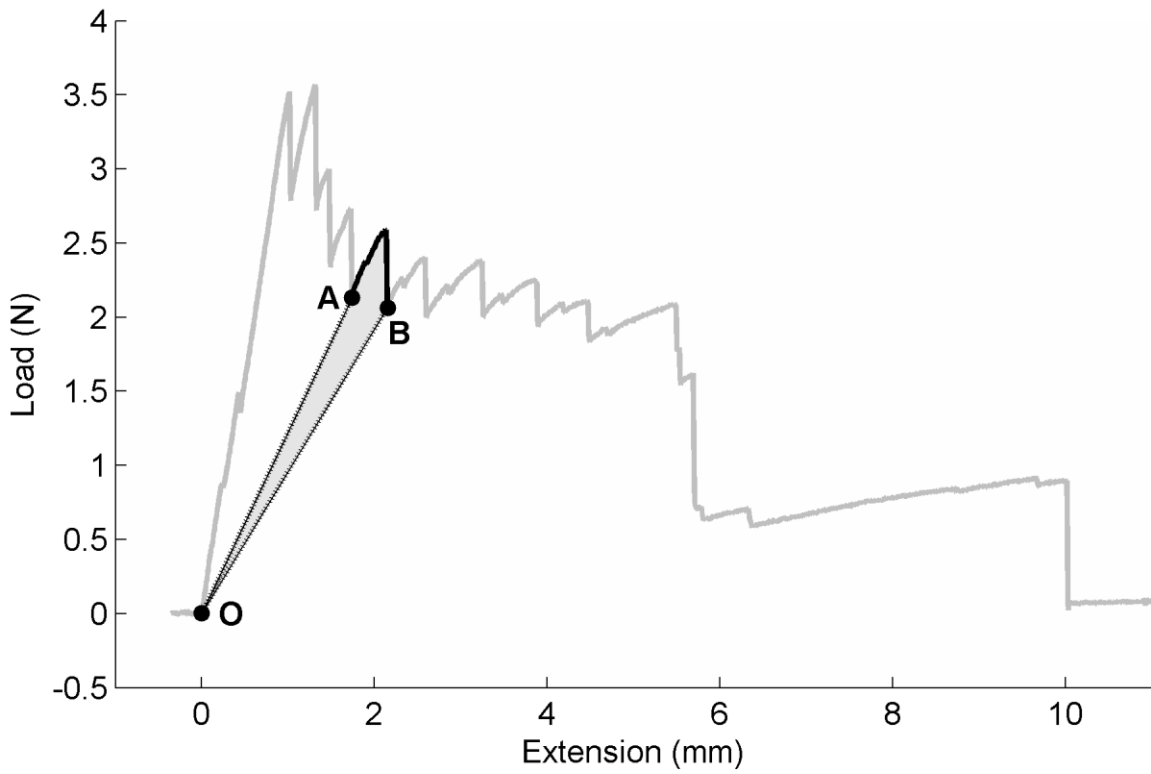
Figure 4.25 Diagram of determining demolding work by the area method.
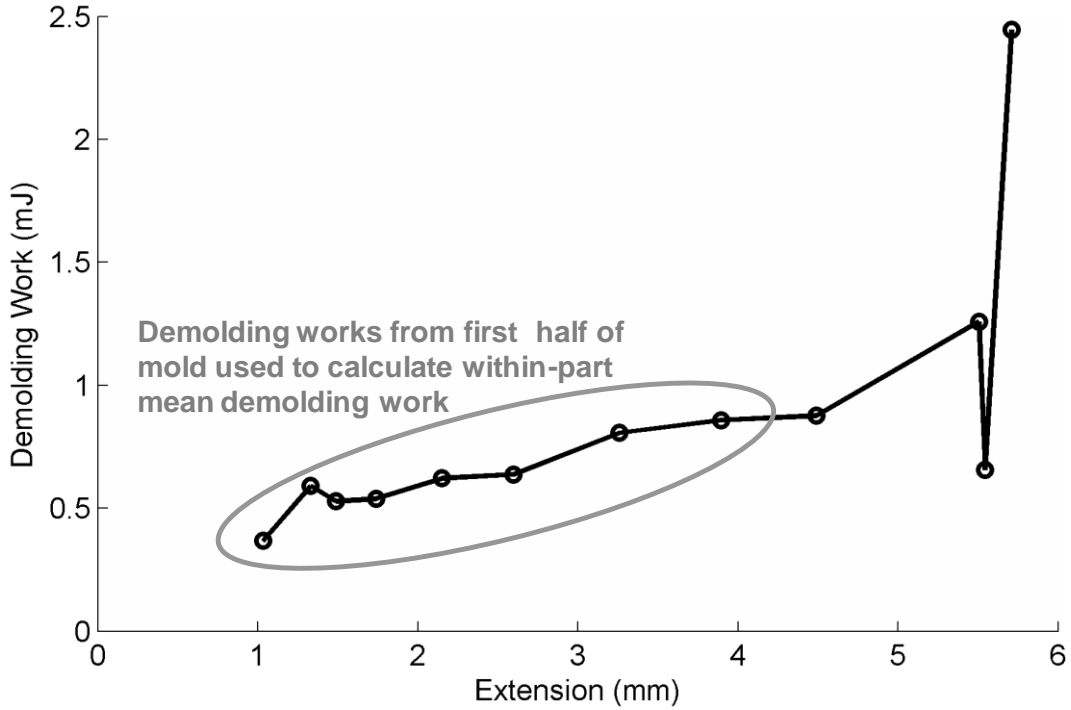
Figure 4.26 Plot of calculated demolding works for a mold with 100µm high channels 2mm apart demolded at 73°C. The extreme value of the last point corresponds to the change in pattern from one side of the mold to the other. Only the first 8 points are used to calculate the within-part mean demolding work.

Some experiments record strong demolding loads and large, noticeable drops in load for each demolding event, while for others the load signal is more subtle. The above method of identifying individual demolding events has been found to be reliable and robust to these differences between experiments. All of the calculations are deterministic, so repeated runs of the analysis scripts produce identical results. The data analysis script will sometimes identify a spurious demolding event, or fail to recognize a real event. These failures are readily apparent in the diagnostic plots produced by the script, and these points are manually censored from further calculations (such as the within-part mean demolding work) that are performed in Excel.

All of the identified points of interest, along with the adjusted load and extension, the identified demolding events, the calculated energy for each demolding event, and the adjusted load and extension at each demolding event are stored as fields in the MatLab variable for each experiment and saved to a MatLab formatted data file for later retrieval. The experiment identifiers (part numbers), demolding works, demolding loads and extensions, and sticking loads are exported to an Excel spreadsheet for additional manual examination and analysis.

Within Excel, demolding work and sticking force results are grouped along with the recorded demolding temperatures for each experiment. Since the top and bottom platen temperatures sometimes differ slightly from each other and from the intended setpoint, each value is recoded at the time of the experiment. The average of the top and bottom platen temperatures is taken as the demolding temperature for a given test.

4.8.5 Calculating demolding toughness

To compare across geometries, and to produce a metric that may be generalized to other situations, the calculated demolding work can be normalized by area to estimate the demolding toughness. Fracture energy is normalized by the area of crack enlargement to calculate the average toughness over the area. This normalization scheme can be checked by comparing with the results of load-based calculations of demolding toughness, such as those given by the formula in ASTM D3433 (Equation 4-2). From Figure 4.27 it can be seen that there is good agreement in general between the toughness calculated by the area method and that calculated by the load-based relations, although the load-based methods underestimate the toughness. Hashemi et al. found that demolding toughness determined from load-based calculations required empirical correction factors to match those found by the area method [133].

145
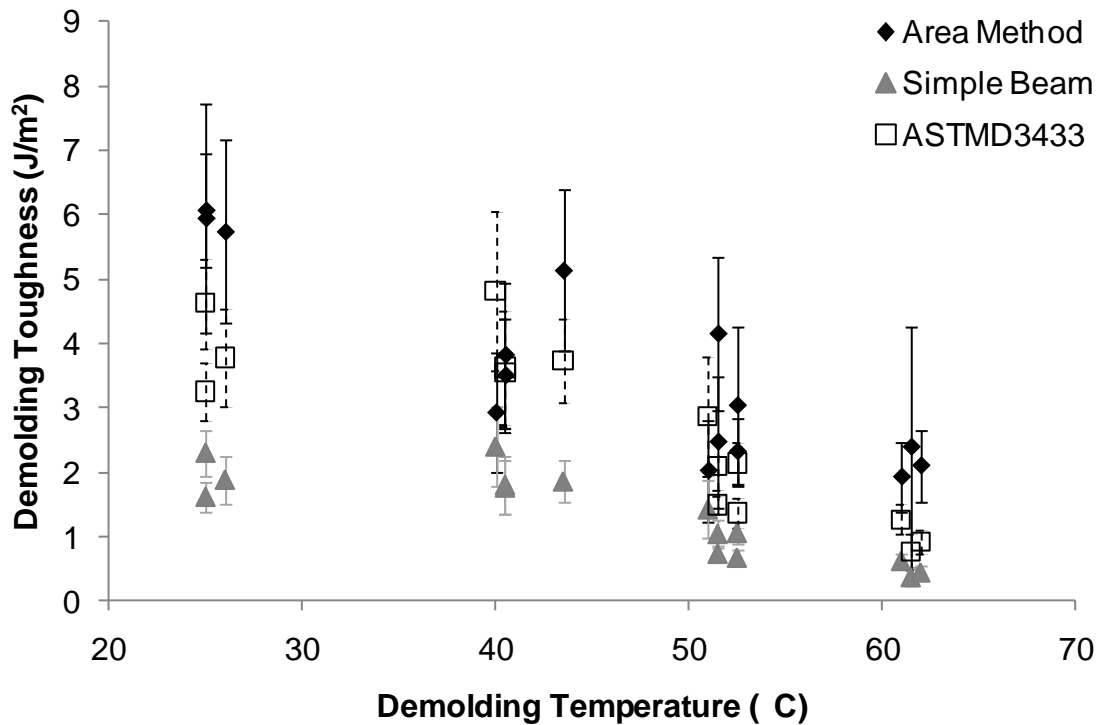
Figure 4.27 Plot comparing toughness calculation methods at several temperatures.
Each point represents the within-part average toughness for demolding tests on a mold with 7 channels
100 μm high and 3.2 mm apart. Error bars are the 95% confidence interval calculated from each within-part
standard deviation. Error bar colors match marker colors.

4.9 Repeatability of demolding work

Before interpreting the experimental results, the reliability of the test method must be assessed. Variation is inherent to any real-world process, and adhesion tests in particular are known to produce highly variable results [116]. Several experiments were replicated to assess the variation in the measured demolding work. Figure 4.28 shows the demolding work determined for individual features from several repeated demolding experiments at 50°C with a PMMA specimen on a mold with 100 μm high, 100 μm wide channel features spaced 2 mm apart that extend across the full width of the part (pattern H100E2). Each point represents the demolding work for a single feature, and the data is grouped by runs. A large degree of variation between runs is evident for individual channels, but this variation is comparable to the variation between channels within a given run.
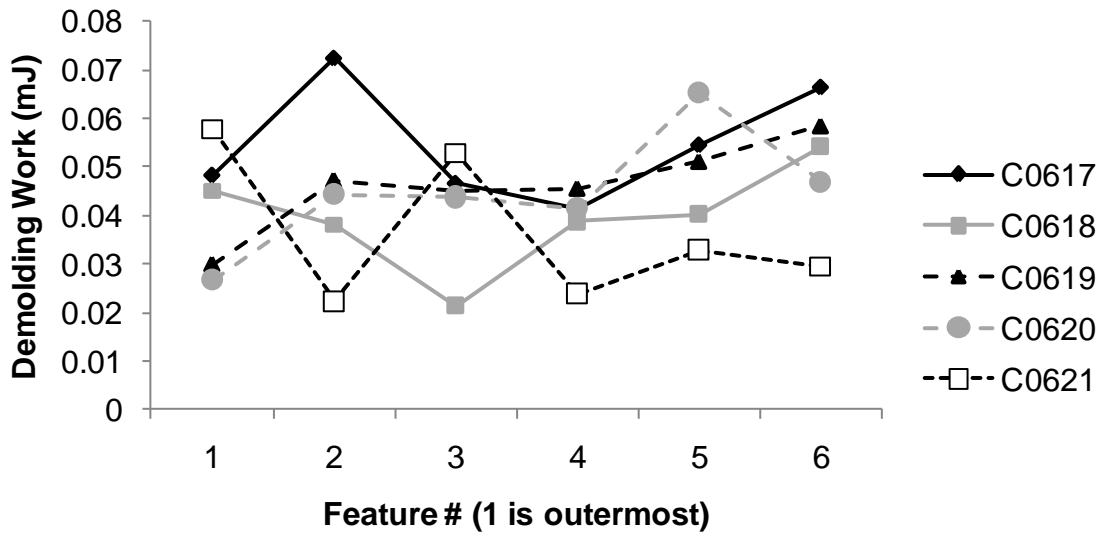
Figure 4.28 Demolding work results from five repeated demolding experiments at 50°C on a mold with 100 µm high channels spaced 2 mm apart that extend across the full width of the part. Each point represents the demolding work for a given feature, and the data is grouped by part #.

The hypothesis underlying this test method is that the demolding work measured in an experiment is a combination of the actual demolding work with some random "noise." The actual demolding work should be identical for all the features on a given mold, and also should not vary with time. This is equivalent to the hypothesis that all the demolding works measured for individual features in repeated experiments are independent random variables from the same population with a constant mean and variance. This hypothesis can be evaluated qualitatively by plotting the data as in Figure 4.28, or as a box plot in Figure 4.29. From this box plot, it is evident that demolding work for a given feature is highly variable across repeated experiments, but that this variation is comparable to the variation between features. The within-part mean demolding work is less variable since it "smoothes" some of the variation between features.
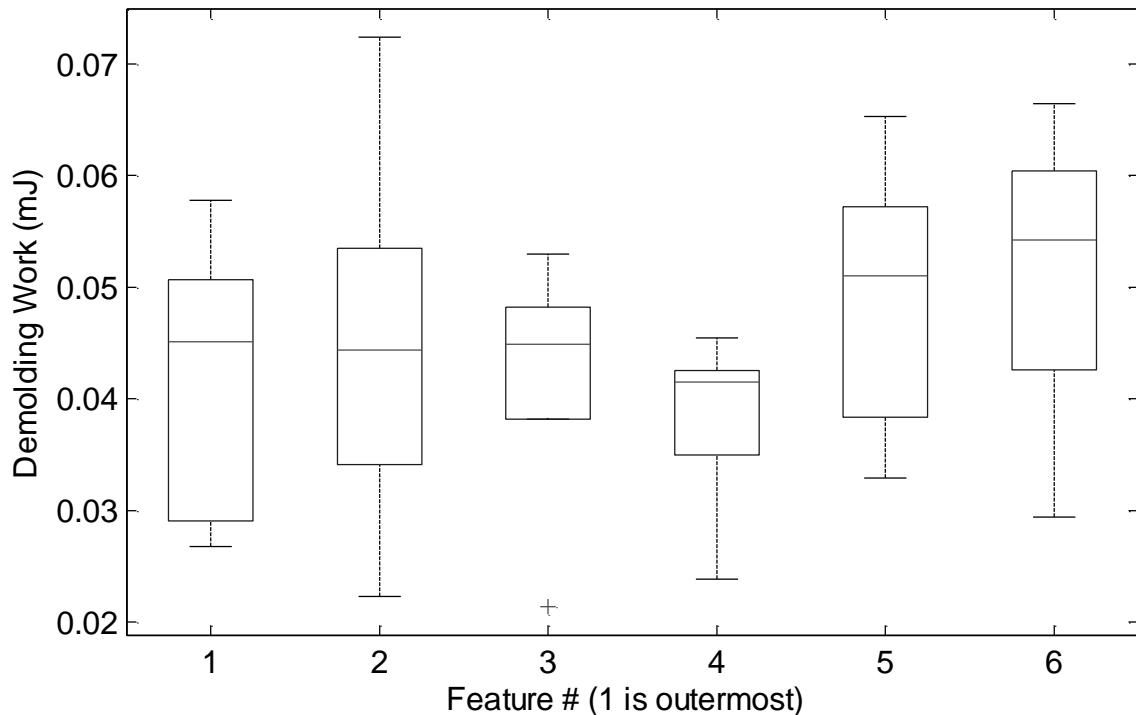
Figure 4.29 Box plot of data from five repeated demolding experiments at 50°C on a mold with 100 μm high channels spaced 2 mm apart that extend across the full width of the part. Boxes span between the 25th and 75th percentile, with a horizontal line at the mean. Whiskers extend to the extreme values, while crosses represent outliers further than 1.5 times the inter-quartile distance.

This hypothesis can be tested quantitatively by a two-way analysis of variance (ANOVA), which compares the variation between different groups (the main effects) to the variation attributed to random noise (the error). The results of the 2-way ANOVA are given in Table 4.2. The relevant outputs of this analysis are the two P-values in the right-hand column. The P-value for the effect of features (0.59) means there is no significant difference in the demolding work between the channels. Similarly, the P-value for the effect of runs (0.14) means there is no significant difference in demolding work between different runs.

Table 4.2 Results of 2-way ANOVA for five parts demolded at 50C from mold H100E2 (full-width channels 100 μm high and 2 mm apart).

Source	Sum of Squares	Degrees of freedom	Mean Square	F statistic	P-value
Features	5.83×10^{-4}	5	1.17×10^{-4}	0.76	0.59
Runs	1.20×10^{-3}	4	3.00×10^{-4}	1.94	0.14
Error	3.08×10^{-3}	20	1.54×10^{-4}		
Total	4.86×10^{-3}	29			

Overall, these results can be interpreted to support the hypothesis that the demolding work for any given channel is a measure of the true value combined with some random noise. Similar conclusions can be made for the other mold geometries tested, and at other temperatures. Analysis of variance results for selected experiments are shown below. Figure 4.30 and Table 4.3 show the results for three demolding experiments at 60°C for a mold with 100 µm high channels spaced 3.2 mm apart and interrupted with 0.5 mm period for 50% total projected area, and Figure 4.31 and Table 4.4 show the results for five repeated demolding experiments at 50°C on a mold with 200 µm high channels spaced 2 mm apart that extend across the full width of the part. In both cases, the effects of features and runs are not significant, confirming that the experimental variation is caused by the inherent variability of demolding, rather than any systematic variation.

In demolding, the magnitude of the noise component can be quite large, so repeated measurements are needed to make firm conclusions. The ability to determine demolding work for several individual channels on the mold for each experiment also helps to overcome the large variation in demolding work for individual features, since the average across several channels for a given run will be less sensitive to noise.
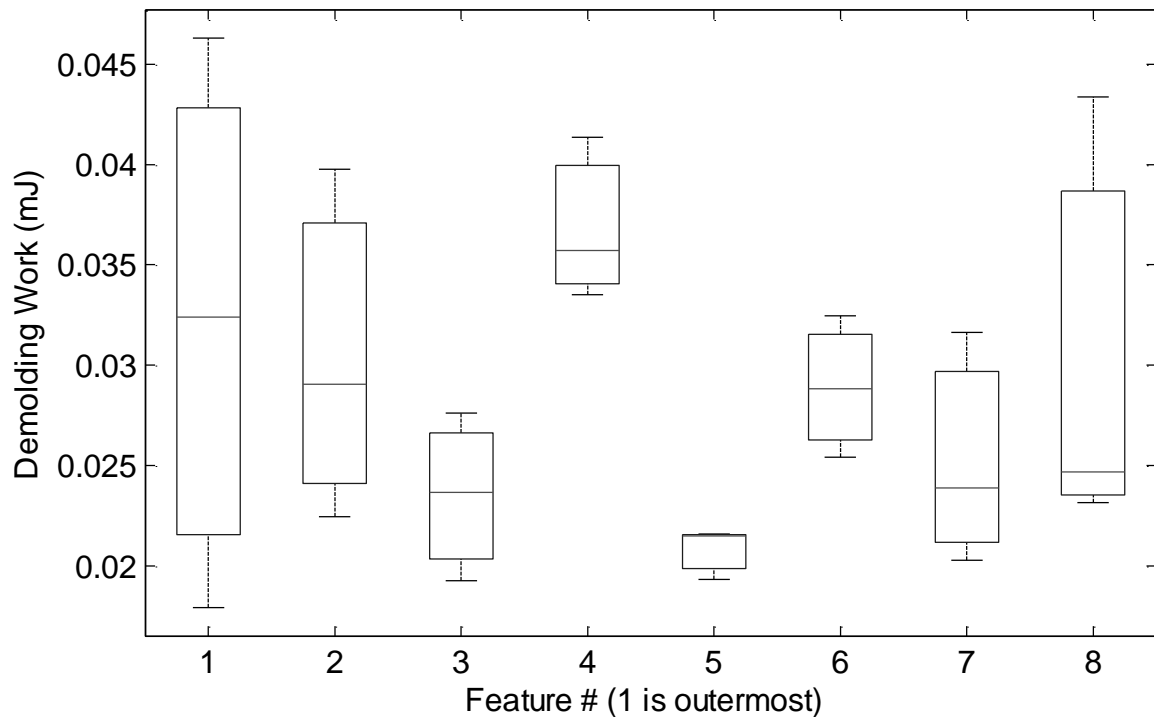
Figure 4.30 Box plot of data from three demolding experiments at 60°C for a mold with 100 µm high channels spaced 3.2 mm apart and interrupted with 0.5 mm period for 50% total projected area.

149

Table 4.3 Results of 2-way ANOVA for three parts demolded at 60C from a mold with interrupted channels 100 μm high and 3.2 mm apart with 50% projected area.

Source	Sum of Squares	Degrees of freedom	Mean Square	F statistic	P-value
Features	5.58×10^{-4}	7	7.97×10^{-5}	1.24	0.34
Parts	7.58×10^{-5}	2	3.79×10^{-5}	0.59	0.57
Error	8.97×10^{-4}	14	6.40×10^{-5}		
Total	1.53×10^{-3}	23			
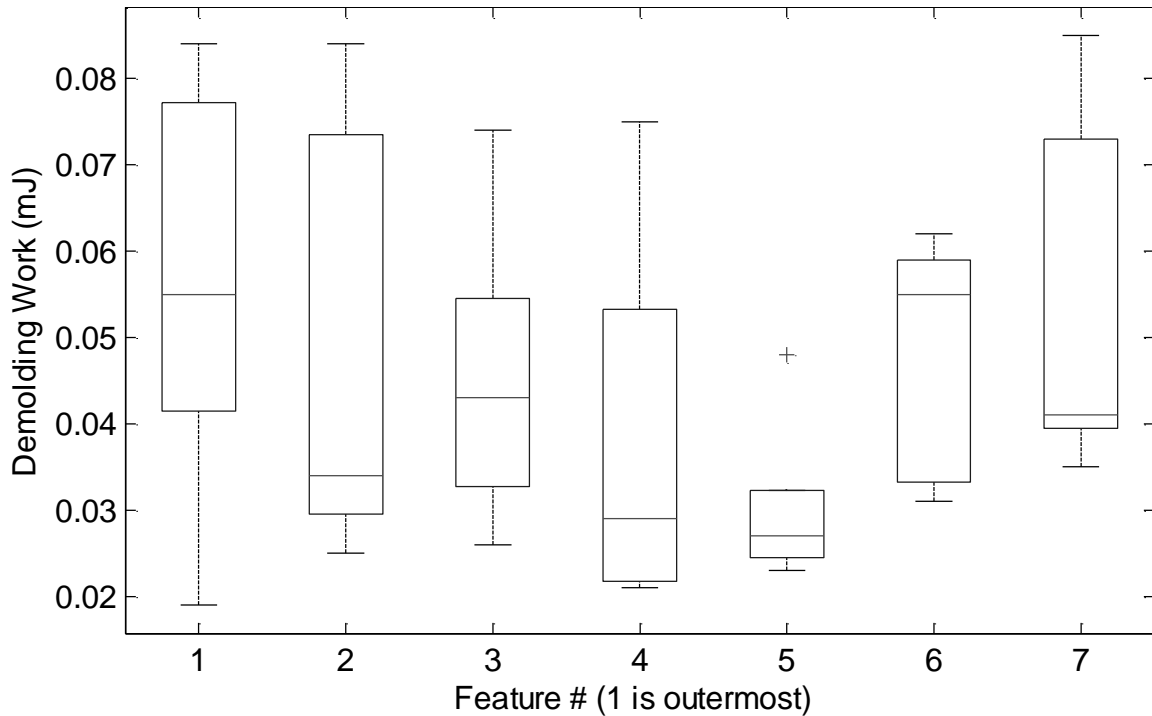
Figure 4.31 Box plot of data from five repeated demolding experiments at 50°C on a mold with 200 μm high channels spaced 2 mm apart that extend across the full width of the part.

Table 4.4 Results of 2-way ANOVA for five parts demolded at 50C from a mold with full-width channels 200 μm high and 2 mm apart.

Source	Sum of Squares	Degrees of freedom	Mean Square	F statistic	P-value
Features	2.50×10^{-3}	6	4.16×10^{-4}	1.13	0.37
Parts	3.00×10^{-3}	4	7.59×10^{-4}	2.07	0.12
Error	8.80×10^{-3}	24	3.68×10^{-4}		
Total	1.44×10^{-2}	34			

4.9.1 Mold-to-mold variation

It is also possible that differences between the machined molds might contribute to apparent differences in demolding work. In order to study the effect of channel spacing (discussed in section 5.8.1), molds were machined with 100 µm high channels with different spacing. One mold combined channels with 1 mm and 2 mm spacing, another had 3.2 mm and 7.5 mm spacing, and a third had 2 mm and 3.2 mm spacing. Within these three molds, it is possible to compare identical geometry in two cases: 2 mm and 3.2 mm spacing. Analysis of variance results for these two cases are shown in Table 4.5 and Table 4.6. No significant effect on the demolding work at 50°C is observed, and so it is not expected that mold-to-mold variation will contribute significantly to observed differences in demolding work.

Table 4.5 Results of ANOVA for the effect of mold-to-mold variation for 100 µm deep channels spaced 2 mm apart demolded at 50°C.

Source	Sum of Squares	Degrees of freedom	Mean Square	F statistic	P-value
Molds	2.60×10^{-5}	1	1.00×10^{-4}	1.44	0.26
Error	1.98×10^{-4}	11	1.10×10^{-3}		
Total	2.24×10^{-4}	12			

Table 4.6 Results of ANOVA for the effect of mold-to-mold variation for 100 µm deep channels spaced 3.2 mm apart demolded at 50°C.

Source	Sum of Squares	Degrees of freedom	Mean Square	F statistic	P-value
Molds	8.00×10^{-5}	1	8.00×10^{-5}	1.02	0.34
Error	7.04×10^{-4}	9	7.83×10^{-5}		
Total	7.84×10^{-4}	10			

5 Experimental results and discussion

5.1 Introduction to the chapter

The analysis of demolding mechanics in Chapter 2 and the simulations results presented in Chapter 3 provide insight into the process of demolding, as well as predictions of expected trends in the observed demolding work. While there have been other efforts at modeling demolding, experimental validation has apparently been lacking (see section 1.5). An important component of the present work, and a major contribution of this thesis, is the development of the experimental method described in Chapter 4, and its use in testing the predictions of the analytical and finite element models. The experimental findings themselves represent another major contribution of this work.

This chapter presents the experimental results and discusses how they relate to the mechanics of demolding and the simulated results presented earlier. Overall, there is considerable agreement in terms of the relationship between demolding work and feature geometry, as well as the related phenomenon of feature distortion. The observed trends of demolding work with temperature are consistent with the model combining adhesion degradation and sidewall friction developed in section 2.7. While the models and simulations are one- or two-dimensional, these experiments provide insight into the real, three-dimensional, non-ideal process of demolding. Just as importantly, the experimental method developed for this work makes it possible to evaluate the effects of mitigation strategies such as low-adhesion coatings and changes in feature edge quality on the demolding work.

5.2 Mold features

Several different molds were designed to test specific effects, and they can be grouped into three families. The first family consists of molds with channel features that extend across the width of the specimen perpendicular to the direction of crack propagation such as the mold in Figure 4.17. These molds were intended to test the effect of channel height and spacing, and were made at heights of 200, 100, 50, and 10 μm. The molds have two halves with different

inter-feature spacing of 2 mm and 3.2 mm. Molds were also made with 1 mm and 7.5 mm spacing at 100 µm height.
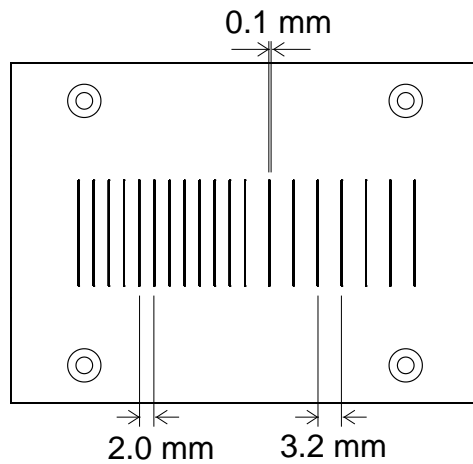
Figure 5.1 Diagram of mold with full-width channels designed to test the effect of inter-feature spacing.

The second family consists of molds with channel features that are interrupted, which were designed to study the effect of feature width (Figure 5.2). These molds were also made at heights of 200, 100, and 50 µm, and all had 3.2 mm spacing. The channel features have total widths of 25% and 50% of the width of the part (2.5 and 5 mm for the standard 10 mm wide part), and one mold at 75% width and 100 µm height. Molds were also made to test the effect of the distribution of width (Figure 5.3), with a single feature that is either 50% or 75% of the width of the part and centered with respect to the part, or two features at the edges of the part with total width of 50%.
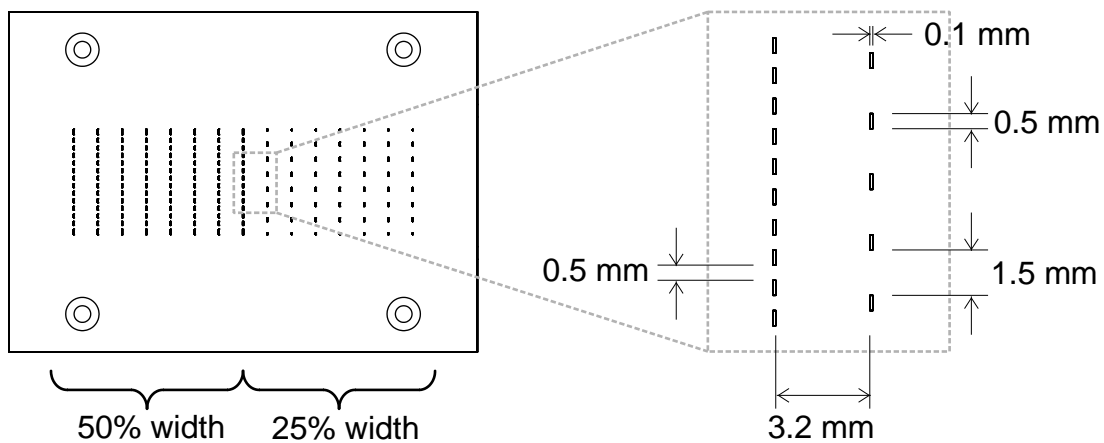
Figure 5.2 Diagram of mold pattern designed to test effect of width with interrupted channel features.
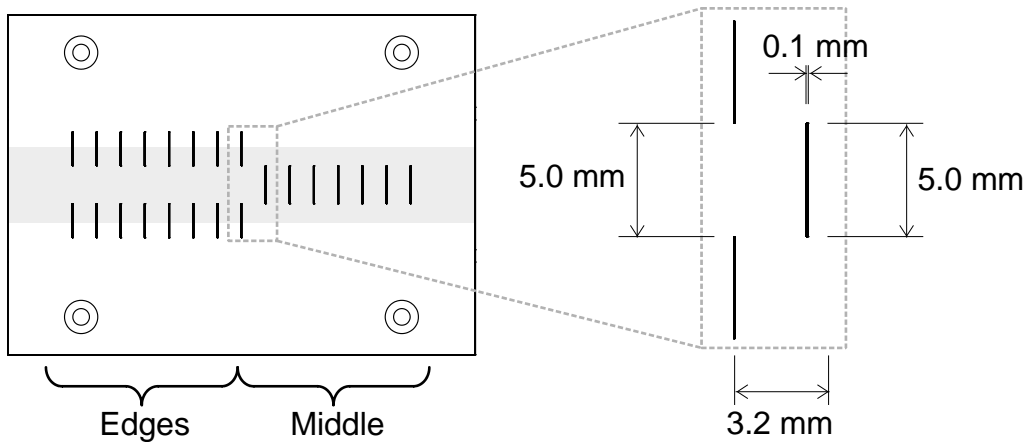
Figure 5.3 Diagram of mold pattern designed to test effect of distribution of width. The shaded area corresponds to the footprint of the test specimen.

The third family consists of molds with features parallel to the direction of crack extension ("longitudinal"). These molds were also made at heights of 200, 100, and 50 µm, and the two halves of each mold have either three or five features across the width of the part (the part is 10 mm wide) for a total width of 300 and 500 µm respectively. The longitudinal channel features are 4 mm long and spaced 2 mm apart (Figure 5.4).
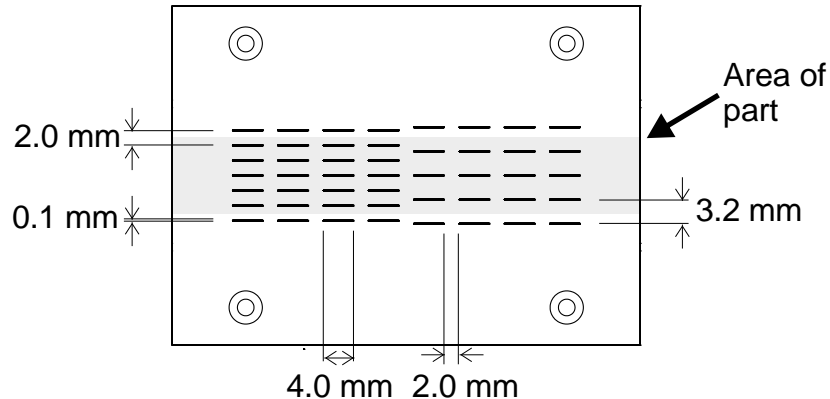
Figure 5.4 Diagram of mold pattern with longitudinal features. The shaded area corresponds to the footprint of the test specimen.

5.3 Feature distortion at low temperatures

Defects such as the one shown in Figure 5.5 have been observed many times [39, 42, 74], and are widely hypothesized to be caused by thermal stress during cooling and demolding. The local deformation includes a bulge that is pushed above the original surface of the part, as shown in Figure 5.6 and Figure 5.7 (see sections 3.4.4 and 3.4.5 for similar results from FEA models).

These bulges are problematic for bonding because they can prevent the cover plate from sealing channels. Local deformation such as this can cause a part to be unusable.
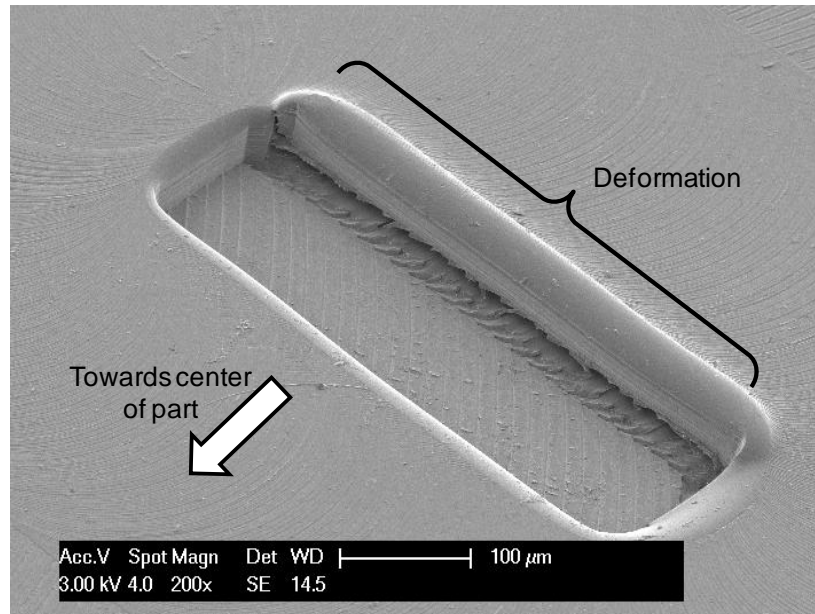
Figure 5.5 Scanning electron micrograph of a distorted feature in an embossed PMMA part. The part was cooled to 25°C before demolding. Thermal contraction towards the center caused large thermal stresses, which deformed the feature and created a bulge on the outer side.
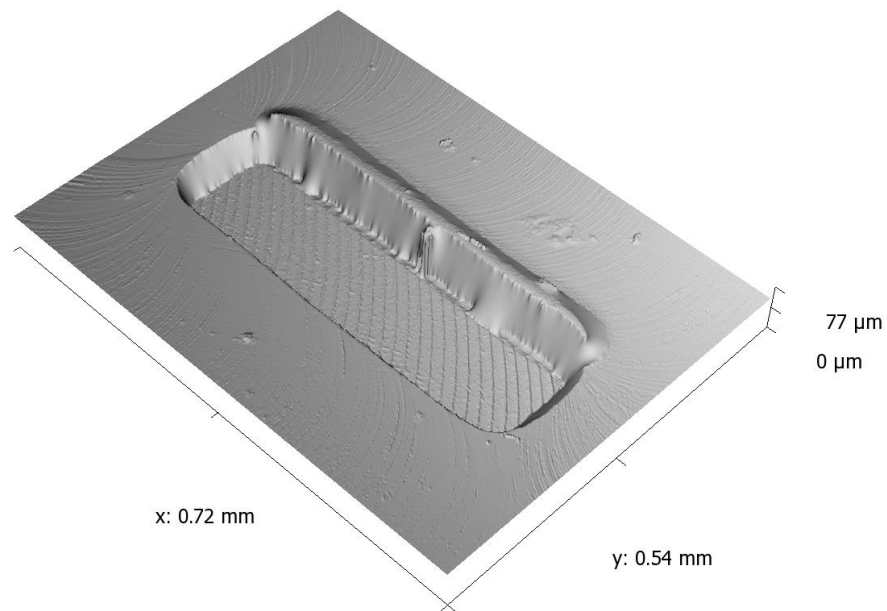
Figure 5.6 Rendered projection of data from white light profilometer for a feature embossed in PMMA and demolded at 25°C. The instrument cannot view vertical sidewalls, so missing data is interpolated. Compare to Figure 5.5.
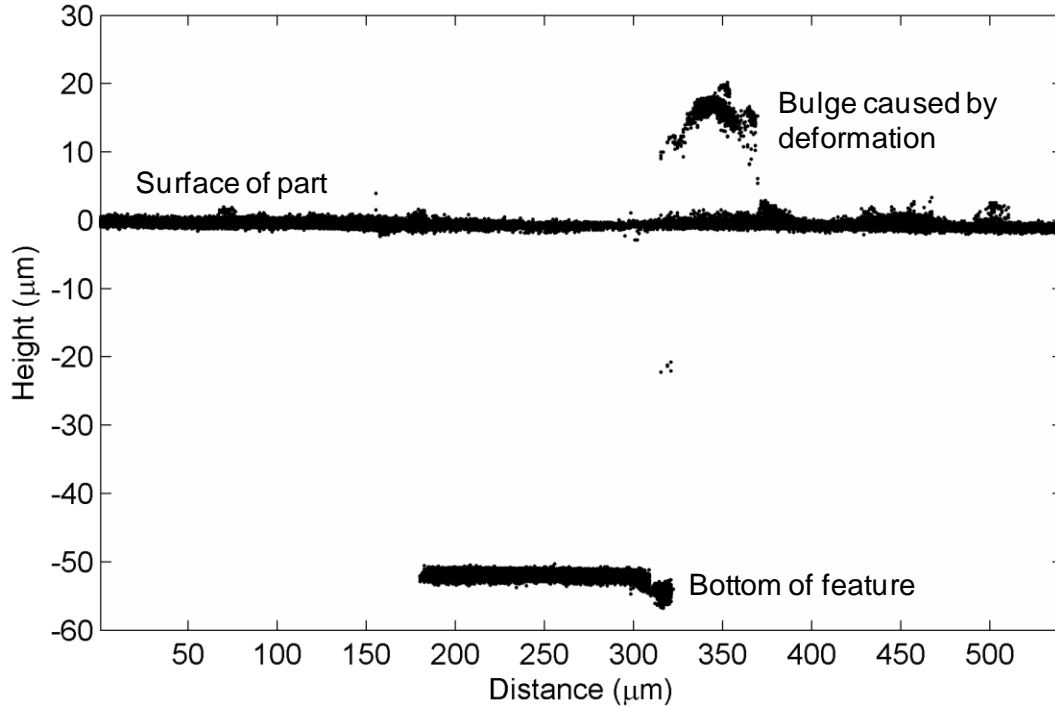
Figure 5.7 Profilometer data shown in Figure 5.6 projected edge-on to show the cross-section of a feature embossed in PMMA and demolded at 25°C along with the bulge defect.

5.3.1 Effect of temperature and geometry on feature distortion

The local deformation of features is related to both the demolding temperature and the feature geometry. Figure 5.8 depicts several microscope photos of the end of a longitudinal channel of three different heights embossed in PMMA parts and demolded at different temperatures between 25°C and 70°C. Distortion becomes more severe at lower temperature, evidenced by a larger and more distinct bulge at the end of the channel. The deeper channels show less severe distortion, with the deepest 200 μm channel showing no distortion at even the lowest temperature.

156
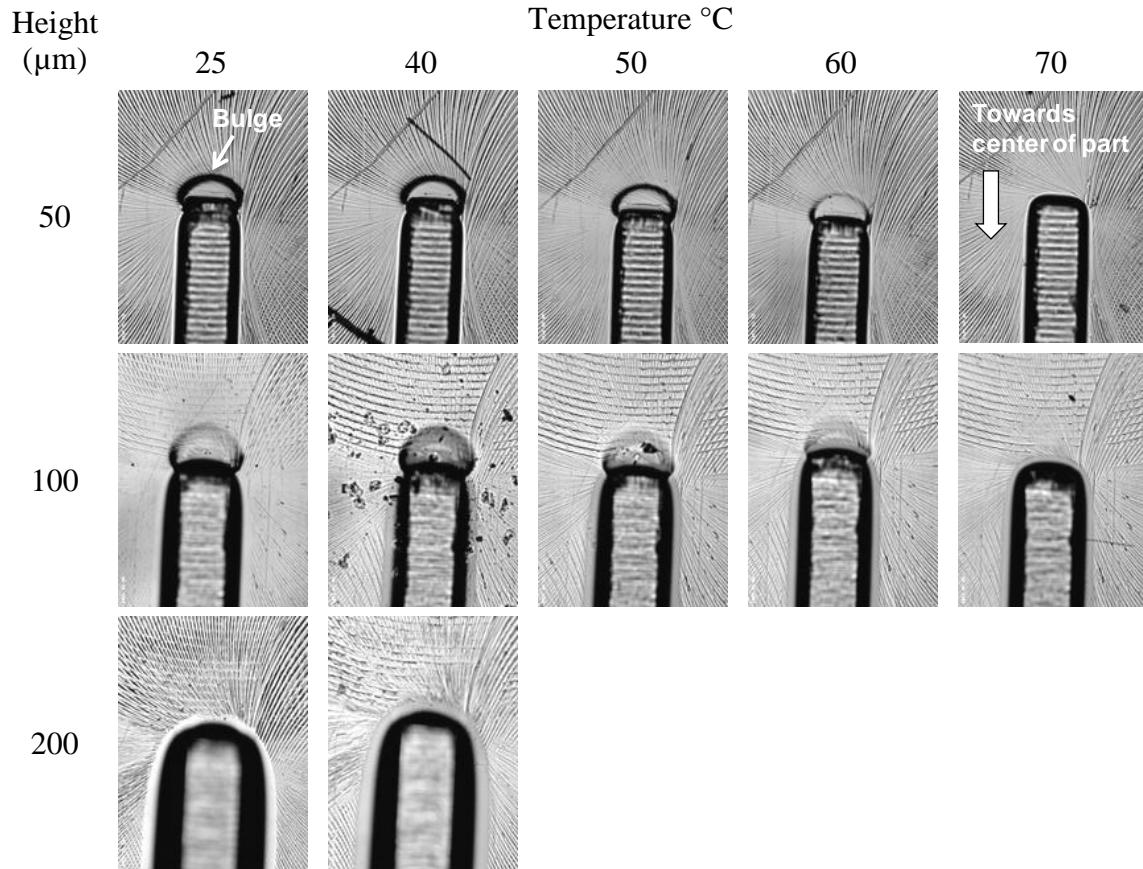
Figure 5.8 Optical micrographs of 100 μm wide longitudinal channels of thee different depths embossed in PMMA and demolded between 25°C and 70°C. The rectangular object is the outer end of the feature, and the large arcs are machining marks. The small arcs at the end of the channel are evidence of local distortion. Distortion increases at lower temperatures. The deeper channels show less severe distortion, with the 200 μm deep channel showing no distortion even at the lowest temperature. Overall thermal contraction is towards the bottom of the images.

Along with height, the total width of the features across the part also affects the severity of distortion and the temperature at which it is first evident. Figure 5.9 depicts several microscope photos of the end of a 100 μm deep longitudinal channel embossed in PMMA parts and demolded at different temperatures between 25°C and 70°C. The mold has two halves with three and five channels across the part respectively (Figure 5.4). The half with more features, and thus greater total width of features, shows less severe distortion. Furthermore, the distortion is not evident until lower temperatures are reached.
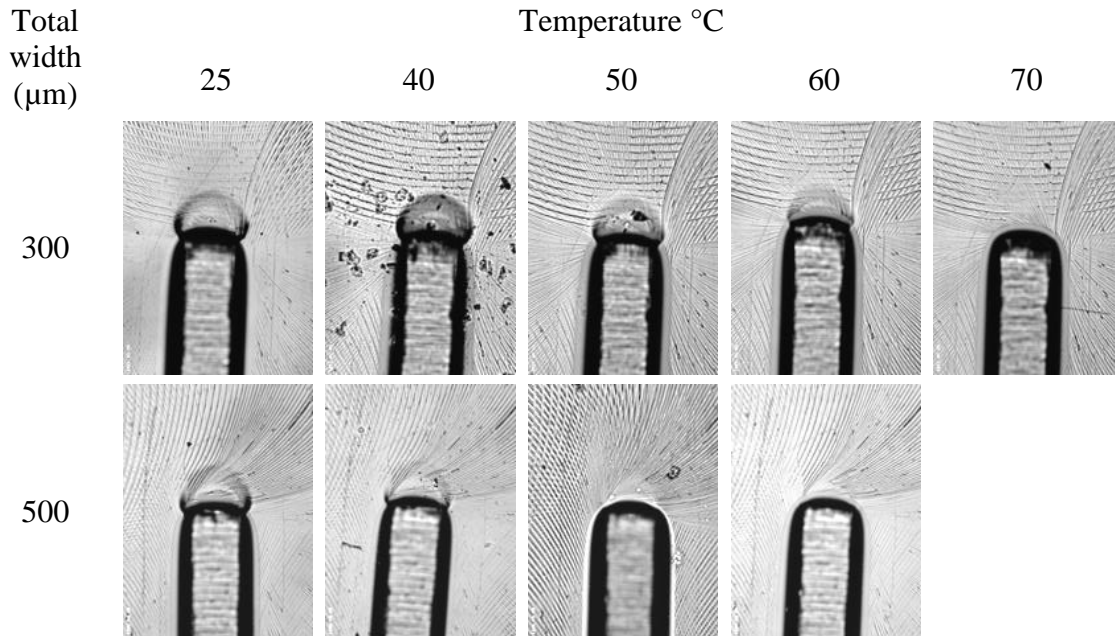
Figure 5.9 Optical micrographs of 100 μm wide and 100 μm deep longitudinal channels embossed in PMMA and demolded between 25°C and 70°C.

The height of the bulge (as in Figure 5.7) can be used to assess the amount of local distortion. The height is taken from the white light profilometer data for each part using the script listed in Appendix C.4. This script first removes any slight out-of-plane tilt in the data, and then locates the cross-section with the greatest height to identify the location of the bulge. The height of the bulge is measured relative to the surface of the part. The bulge height for PMMA parts embossed with 50 μm deep interrupted channels with 25% total width (2.5 mm) and demolded at various temperatures is plotted in Figure 5.10. As shown by these curves, no distortion is evident for demolding temperatures of 80°C and higher. The outermost features are the first to show distortion, and show the greatest amount of distortion. This observation is consistent with the distribution of sidewall forces among multiple features predicted from the model given by Equation 2-30 (compare Figure 5.10 with Figure 2.26).
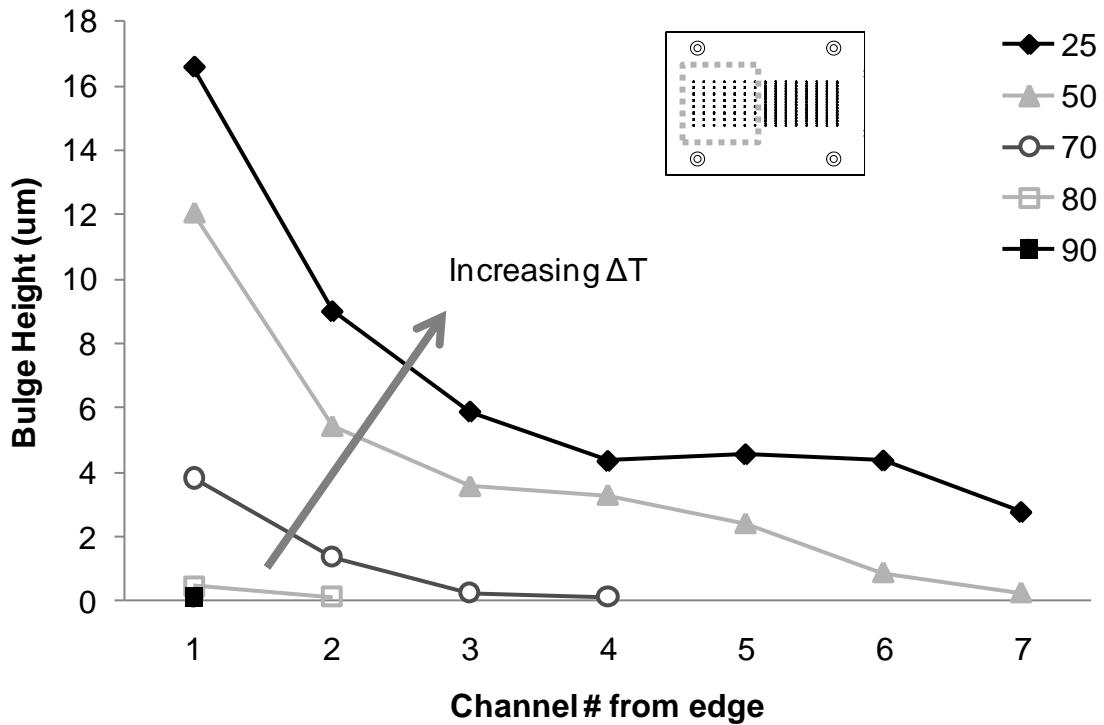
Figure 5.10 Bulge height measured from profilometer data for PMMA parts embossed with 50 μm deep interrupted channels with 2.5 mm total width (shown in inset) and demolded at five temperatures (one part at each temperature). Distortion is evident at 70°C and below, and increases with ΔT. The outermost features are the first to show distortion, and show a greater amount of distortion.

The temperature at which bulge defects are first evident (the distortion temperature) is related to the feature geometry. The bulge height for the outermost channel measured from profilometer data for various molds with interrupted channels is plotted against demolding temperature in Figure 5.11. As shown in this plot, the molds with greater height and width have lower distortion temperatures, and the tallest molds did not show any distortion at the lowest demolding temperature tested of 25°C. Longitudinal features have similar results, as shown in Figure 5.12.
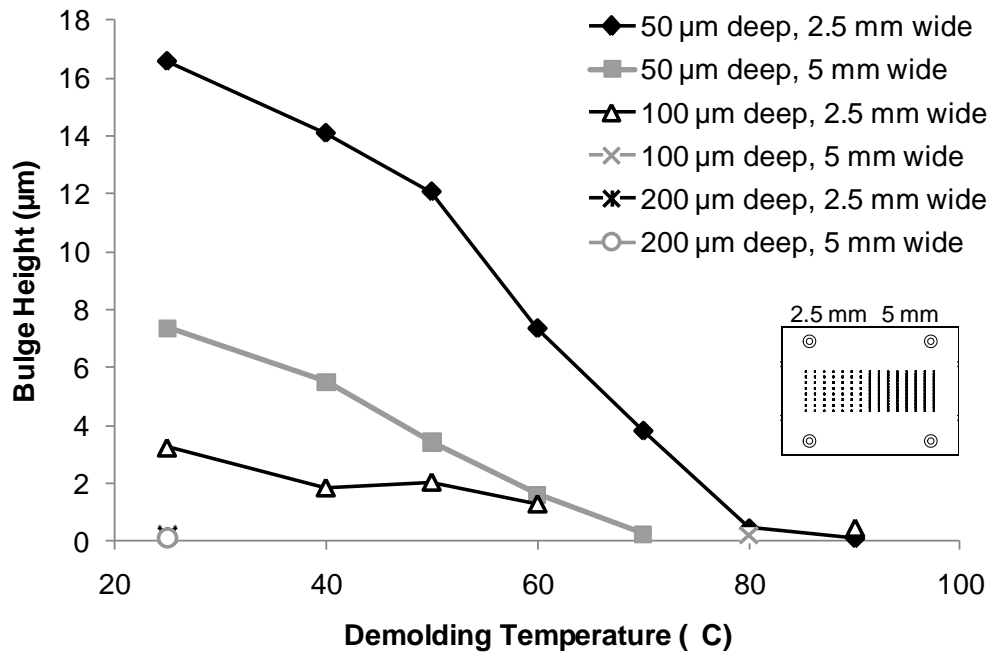
Figure 5.11 Bulge height at outermost feature on PMMA parts embossed with different molds with interrupted channels (shown in inset) at demolding temperatures of 25-90°C. Deeper and wider channels have lower distortion temperatures and show less overall distortion. Measured bulge heights of less than 2 μm are not significant.
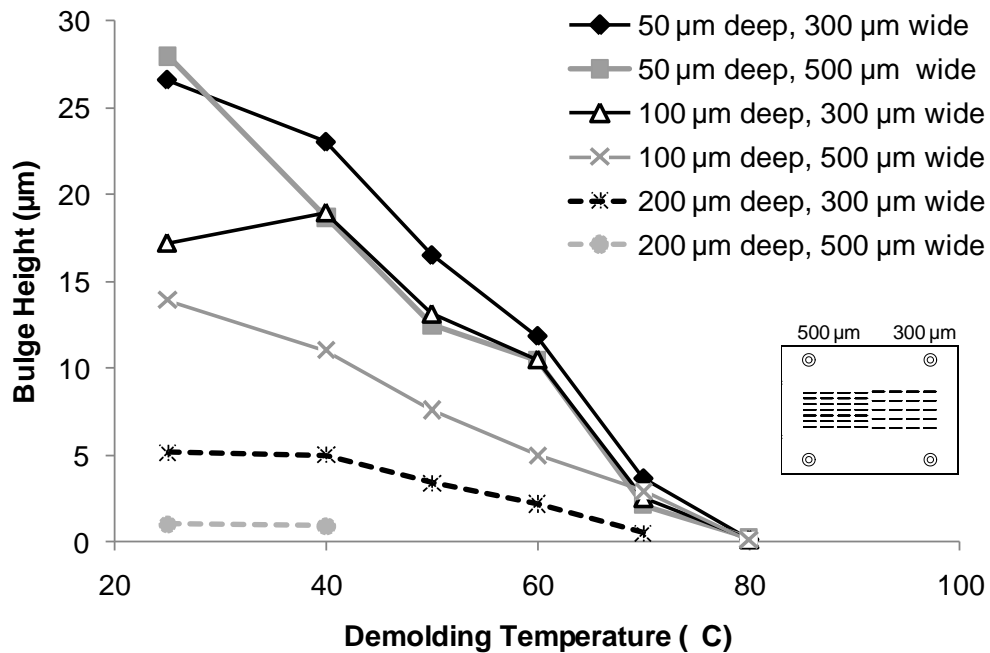
Figure 5.12 Bulge height for PMMA parts embossed with different molds with longitudinal channels (shown in inset) at demolding temperatures of 25-80°C. Deeper and wider patterns have lower distortion temperatures and show less overall distortion.

5.3.2 Quantifying the relationship between feature geometry and distortion

A reasonable hypothesis would be that local distortion occurs when the local stress exceeds the yield strength of the polymer. The local stress can be roughly estimated as the force on the feature caused by thermal stress divided by the projected area of the feature. At this point, it is useful to define dimensions that characterize the pattern of features on the mold. Considering a repeated pattern, L_c and w_c are defined as the length and width of a "unit cell," while w_f is the width of the feature. These parameters are illustrated in Figure 5.13a for a pattern of interrupted channels and Figure 5.13b for longitudinal channels.

Figure 5.13 Diagram illustrating the local pattern dimensions for (a) interrupted channels (b) longitudinal channels. The grey rectangle represents a single unit cell of the pattern. Overall contraction is towards the left in these diagrams.

Using these parameters, the criterion for local distortion can be stated as Equation 5-1.

$$\frac{F_{SW}}{w_f h_f} > \sigma_y$$

5-1

where

F_{SW}	Force on feature sidewall
w_f	Width of feature perpendicular to direction of contraction
h_f	Height of feature
σ_y	Yield strength of the part material

161

Recalling Equation 2-26 for estimating the force on a feature, and substituting Equation 2-27 and 2-29 for the stiffnesses and using the local dimensions defined above (the length of the pattern unit cell, L_c is equivalent to feature spacing), the criterion for local distortion can be re-stated as Equation 5-2. The criterion can be solved for the ΔT at which yielding begins as in Equation 5-4, where material properties and geometric parameters have been grouped.

$$F_{SW} = \frac{k_p k_f}{k_p + k_f} L_c \alpha \Delta T \qquad \textbf{2-26}$$

$$k_p = \frac{E w_p t_p}{L_c} \qquad \textbf{2-27}$$

$$k_f \approx \frac{\pi E w_f}{(1 - v^2) 2 \ln\left(\frac{r_0}{r}\right)} \qquad \textbf{2-29}$$

$$\frac{F_{SW}}{w_f h_f} = \frac{1}{w_f h_f} \frac{k_p k_f}{\left(k_p + k_f\right)} L \alpha \Delta T = \frac{1}{w_f h_f} \frac{\dfrac{E t_p w_c}{L_c} \dfrac{\pi E w_f}{(1 - v^2) 2 \ln\left(\frac{r_0}{r}\right)} L_c \alpha \Delta T}{\left[\dfrac{E t_p w_c}{L_c} + \dfrac{\pi E w_f}{(1 - v^2) 2 \ln\left(\frac{r_0}{r}\right)}\right]} > \sigma_y \qquad \textbf{5-2}$$

$$\frac{\pi t_p w_c L_c E \alpha \Delta T}{h_f (1 - v^2) 2 \ln\left(\frac{r_0}{r}\right) \left[w_c t_p + w_f L_c \dfrac{\pi}{(1 - v^2) 2 \ln\left(\frac{r_0}{r}\right)}\right]} > \sigma_y \qquad \textbf{5-3}$$

$$\underbrace{\frac{\sigma_y (1 - v^2)}{E \alpha}}_{\text{material properties}} \underbrace{\left\{ \frac{2 \ln\left(\frac{r_0}{r}\right)}{\pi} \frac{h_f \left[w_c t_p + w_f L_c \dfrac{\pi}{(1 - v^2) 2 \ln\left(\frac{r_0}{r}\right)}\right]}{t_p w_c L_c} \right\}}_{\text{geometric parameters}} < \Delta T \qquad \textbf{5-4}$$

where
F_{SW} Sidewall force
k_p Equivalent stiffness of the bulk part
k_f Equivalent local stiffness of the region of the part near the feature
t_p Thickness of part
w_c Width of unit cell
L_c Length of unit cell
h_f Height of feature
w_f Width of feature
v Poisson's ratio
E Elastic modulus
α Linear coefficient of thermal contraction
r_0, r Boundary condition parameters, r_0=1 mm, r=1 μm (see section 2.6.2)
ΔT Change in temperature

On the left side of Equation 5-4, the quantity in braces contains all the information related to geometry. The quantity $2\ln(r_0/r)/\pi$ is approximately 4.4, and since most polymers that might be hot embossed have a Poisson's ratio between 0.3 and 0.4 at temperatures below their glass transition, the quantity $\pi/(1-v^2)2\ln(r_0/r)$ can be approximated as 0.52. The term containing the geometric parameters can then be stated as the dimensionless geometric ratio $\mathcal{D}$, defined in Equation 5-5. The distortion criterion can then be re-stated as Equation 5-6.

$$4.4\frac{h_f\left(w_c t_p + 0.52 w_f L_c\right)}{t_p w_c L_c} \equiv \mathcal{D} \qquad\qquad \textbf{5-5}$$

$$\frac{\sigma_y(1-v^2)}{E\alpha}\mathcal{D} < \Delta T \qquad\qquad \textbf{5-6}$$

where

t_p	Thickness of part
w_c	Width of pattern unit cell
L_c	Length of pattern unit cell
h_f	Height of feature
w_f	Width of feature
$\mathcal{D}$	Dimensionless geometric ratio related to feature distortion
σ_y	Yield strength
v	Poisson's ratio
E	Elastic modulus
α	Linear coefficient of thermal contraction
ΔT	Change in temperature

The ratio $\mathcal{D}$ is related to pattern density. Sparse patterns will have relatively small features and large unit cells, which together reduce the value of $\mathcal{D}$, while denser patterns with larger, closely spaced features have higher $\mathcal{D}$. Increasing sidewall area for a given pattern by increasing feature height also increases the value of $\mathcal{D}$. Intuition would suggest that sparser patterns would be more sensitive to thermal stress and more apt to show feature distortion, and experimental observations support this expectation.

Experimental observations show that there is a clear relationship between the distortion temperature and $\mathcal{D}$, and the trend is consistent for the three very different feature patterns tested (full-width, interrupted, and longitudinal channels), as shown in Figure 5.14 in which the ΔT below T_g at which feature distortion is first observed is plotted against the dimensionless ratio $\mathcal{D}$ for all of the feature patterns tested. Demolding tests were conducted at 10°C intervals, which

accounts for the step-wise changes in observed distortion temperature. Distortion was not observed in the mold patterns with $\mathfrak{D}>0.2$ at the lowest temperature tested of 25°C ($\Delta T = 85$°C).
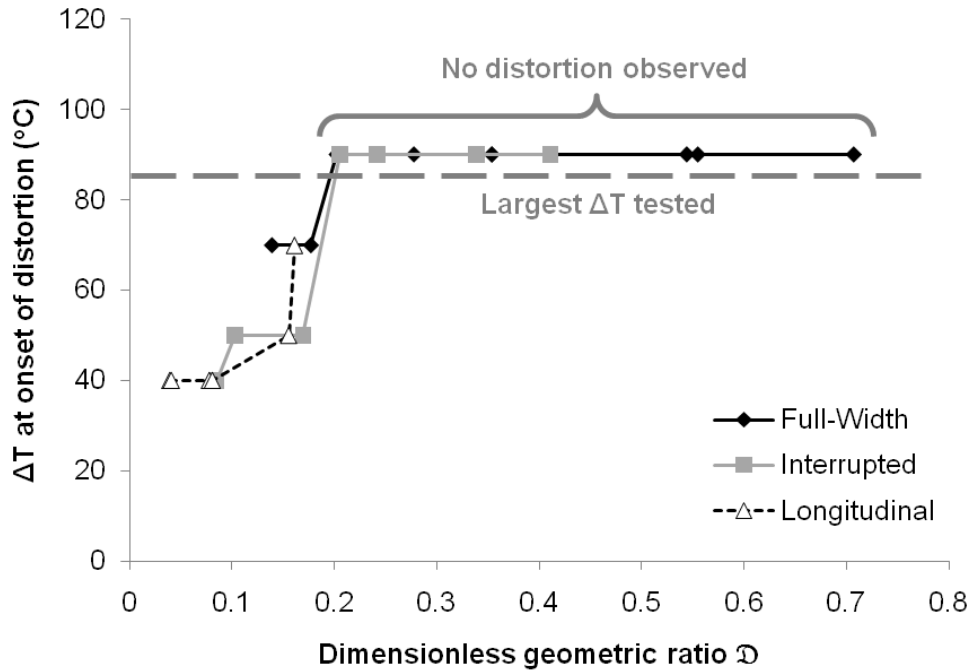
Figure 5.14 ΔT below T$_g$ at which feature distortion is first observed in embossed PMMA parts plotted against the dimensionless geometric ratio $\mathfrak{D}$ for the various mold geometries tested. There is a clear relationship between $\mathfrak{D}$ and the distortion temperature.

The ΔT at which local stress exceeds the yield stress can be estimated using temperature dependent material properties for PMMA from the models developed by Ames [105]. The ΔT estimated from Equation 5-4 is plotted in Figure 5.15 along with the observed distortion temperatures from experiments with PMMA parts. There is good agreement between the trend in observed distortion temperature with $\mathfrak{D}$ and the calculated distortion threshold. Demolding experiments were conducted at 10°C intervals, accounting for the grouping of experimental observations and some of the departure from the model line. Also, there is some departure from the model for very sparse patterns ($\mathfrak{D}<0.1$), which are somewhat more resistant to distortion than expected. The overall good agreement between the model and the experimental observations supports the importance of the ratio $\mathfrak{D}$ as well as the physical reasoning that underlies the distortion criterion given by Equation 5-6. Similar results are shown in Figure 5.16 for polycarbonate parts. Again, there is good agreement between the experimentally observed distortion temperature and the estimate from Equation 5-6.

164
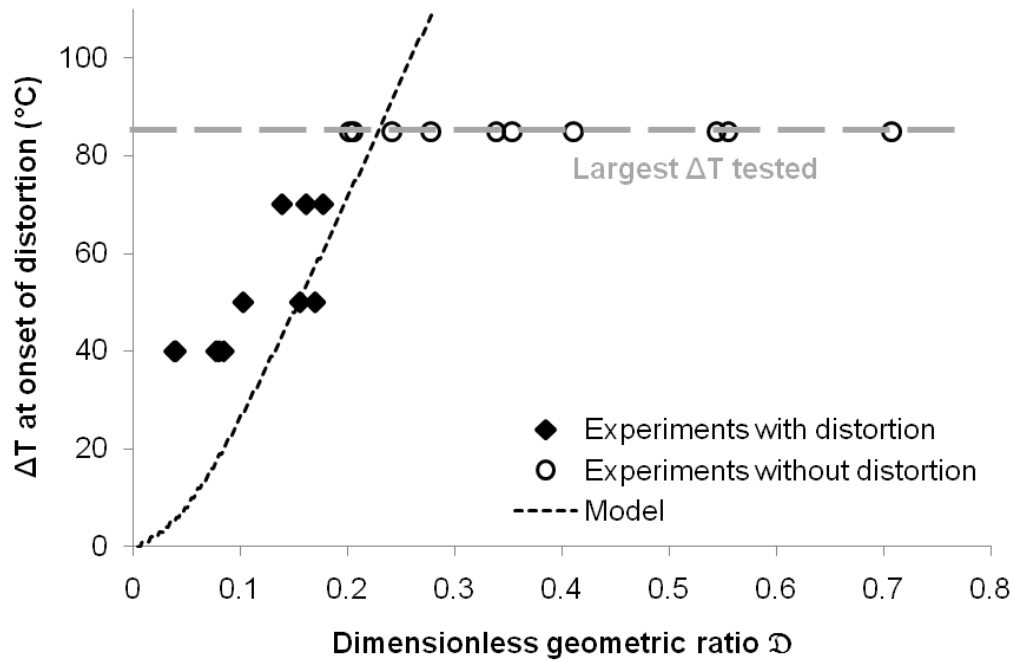
Figure 5.15 Comparison of feature distortion temperature observed in experiments on PMMA parts with the estimate from Eq. 5-4.
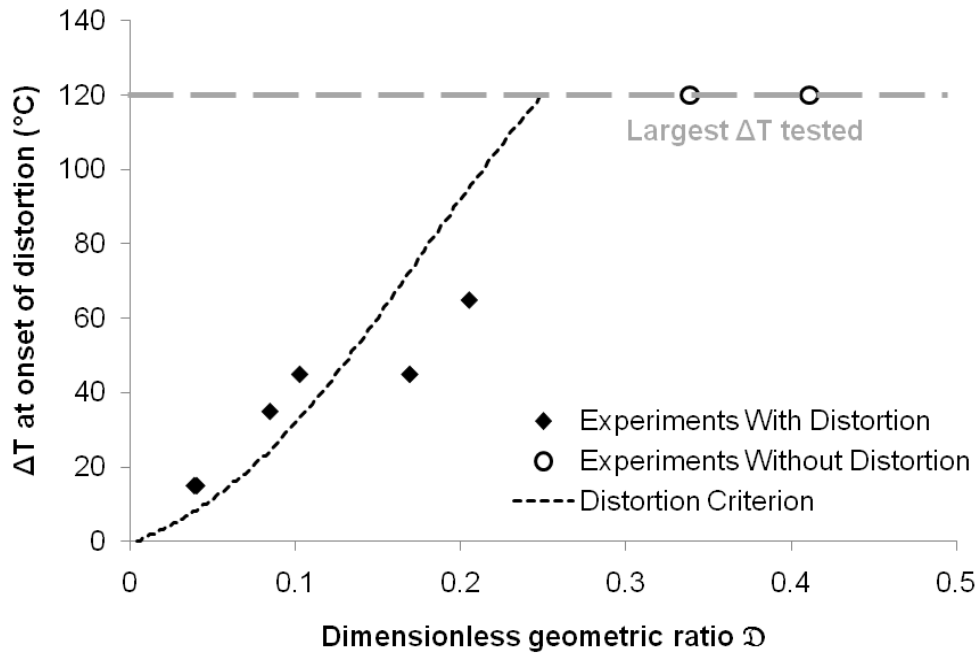
Figure 5.16 Comparison of feature distortion temperature observed in experiments on polycarbonate parts with the estimate from Eq. 5-4.

165

The ratio $\mathcal{D}$ is also related to the amount of distortion at a given temperature, as shown by Figure 5.17 in which the bulge height for the outermost feature at 25°C is plotted against $\mathcal{D}$ for both the interrupted and longitudinal mold patterns. The consistent trend of increasing distortion with decreasing $\mathcal{D}$ for several different patterns provides additional evidence reinforcing the role of this ratio in predicting feature distortion.
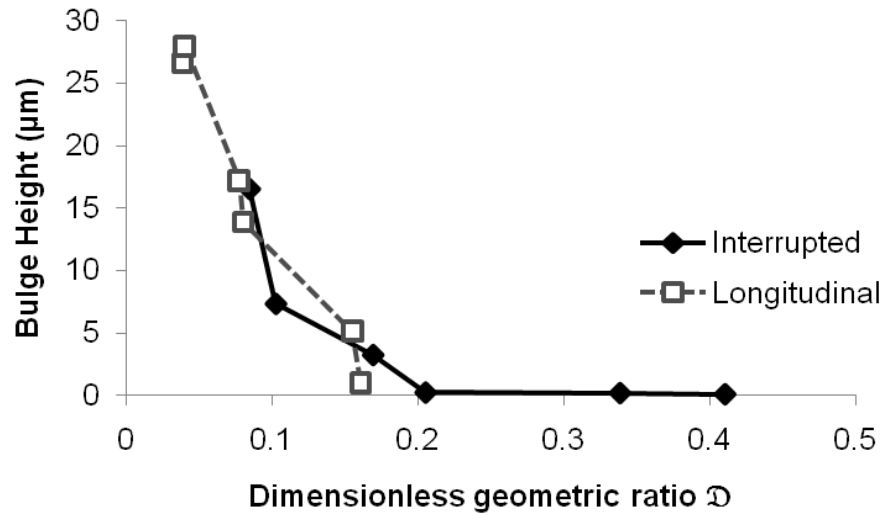
Figure 5.17 Bulge height of outermost feature in PMMA parts at 25°C plotted against $\mathcal{D}$ for interrupted and longitudinal mold patterns.

Another test of the influence of $\mathcal{D}$ would be to change it for a given pattern by varying the thickness of the part. For instance, with the standard 1.58 mm thick test specimen, the 100 µm high interrupted channel with 50% total width has $\mathcal{D}=0.205$ and no distortion is observed at the lowest demolding temperature tested of 25°C ($\Delta T=85°C$). When the part thickness is doubled to 3.16 mm (by embossing and demolding two stacked and bonded specimens), $\mathcal{D}=0.169$ and distortion is evident at 60°C ($\Delta T=50°C$), as shown in Figure 5.18.
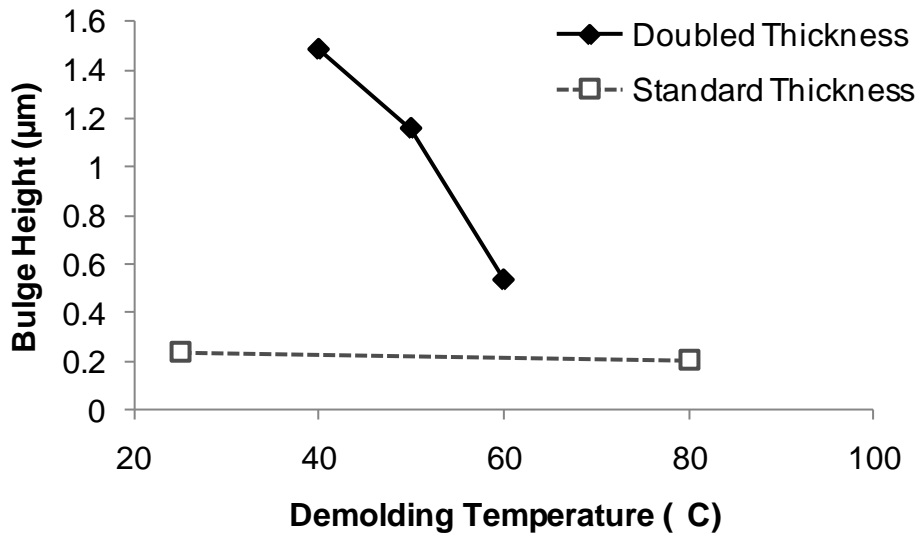
Figure 5.18 Comparison of feature distortion for standard and double-thick PMMA specimens embossed with 100 μm deep interrupted channels with 5 mm total width. No distortion was evident in the standard thickness part (the 0.2 μm bulge height is within the range of the surface roughness), but doubling the specimen thickness reduces the value of 𝔇, and distortion is now evident at 60°C as expected.

Experimental observations have shown that the amount of local feature distortion and the temperature at which it is first evident (the distortion temperature) are related to the geometry of features. The distortion criterion given by Equation 5-4 is derived from the equivalent stiffness model developed in section 2.6.2, along with some physical intuition. By grouping the parameters in this criterion, the effects of pattern geometry can be aggregated into the dimensionless geometric ratio 𝔇 defined in Equation 5-5. The role of 𝔇 in determining feature distortion is confirmed by the consistent trends in both the distortion temperature and the amount of distortion across several disparate feature patterns. These observed effects are also consistent with predictions from the simple models of demolding mechanics developed in section 2.6, in terms of the onset of distortion and the distribution of distortion among features.

5.4 Effect of temperature on demolding work

One of the most notable and consistent phenomena observed in this experimental study is the relationship between demolding temperature and demolding work for a given mold pattern. As an example, the measured demolding work for three different molds is plotted against demolding temperature in Figure 5.19. Despite differences in the magnitude of the demolding work, the trend with temperature has three features in common for all molds. As demolding

temperature decreases, the demolding work is initially high, but steeply drops to the minimum value, then gradually increases. An example of the demolding work results for polycarbonate parts is shown in Figure 5.20. The trend of demolding work with temperature is similar for both polycarbonate and PMMA.

Comparing the experimental data shown in Figure 5.19 with the trend predicted by the combined adhesion and friction model developed in section 2.7, shown in Figure 2.29 (repeated below), it is clear that the observed trends are consistent with this model. From this correspondence, it can be postulated that the observed transition from a decreasing trend in demolding work to an increasing trend is related to a transition from adhesion-dominated to friction-dominated demolding, as in the analytical model. Such a transition is also expected based on the results of finite element simulations discussed in sections 3.5 and 3.6.
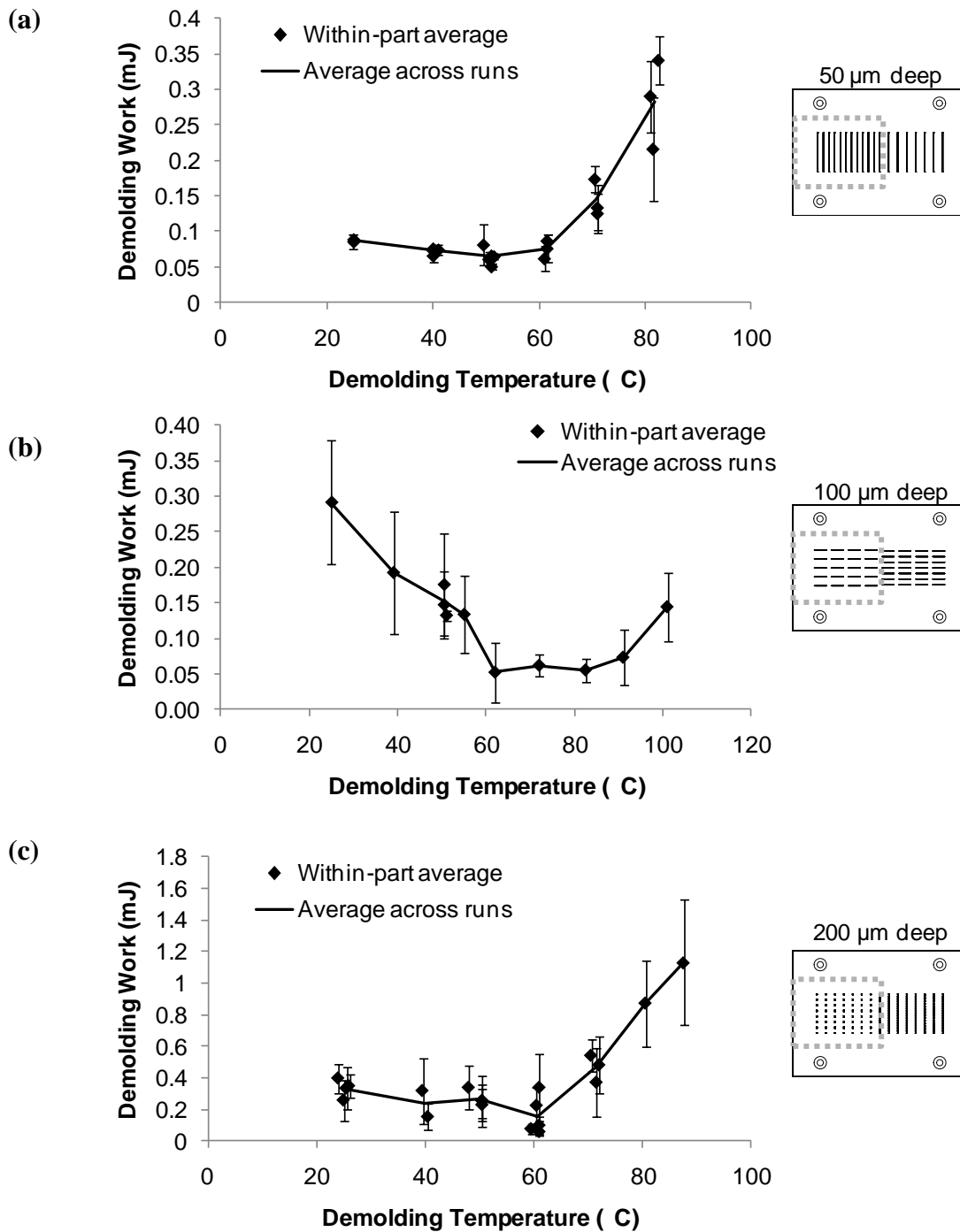
Figure 5.19 Measured demolding work for PMMA parts at various demolding temperatures for three different molds (see insets). Each point represents the within-part average for one run, while error bars represent the 95% confidence interval for each run based on the within-part standard deviation and lines connect the across-runs average. Demolding work at higher temperatures is high, then steeply decreases to the minimum value, then gradually increases as temperature decreases. (a) 50 μm deep full-width channels spaced 2 mm apart, (b) 100 μm deep longitudinal channels, with a combined width of 300 μm, (c) 200 μm deep interrupted channels with total width 2.5 mm.
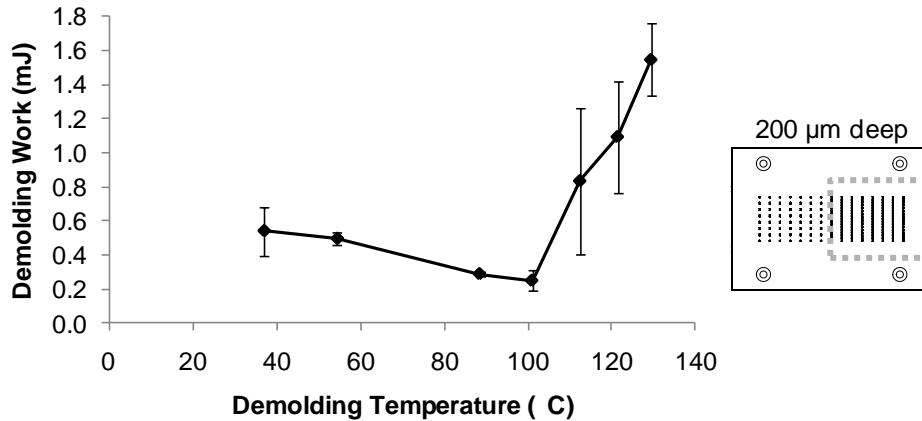
Figure 5.20 Measured demolding work for PC parts at various demolding temperatures for a mold with 200 μm deep interrupted channels with total width 5 mm. Each point represents the within-part average for one run, while error bars represent the 95% confidence interval for each run based on the within-part standard deviation. Demolding work for PC shows the same trend with temperature as for PMMA.
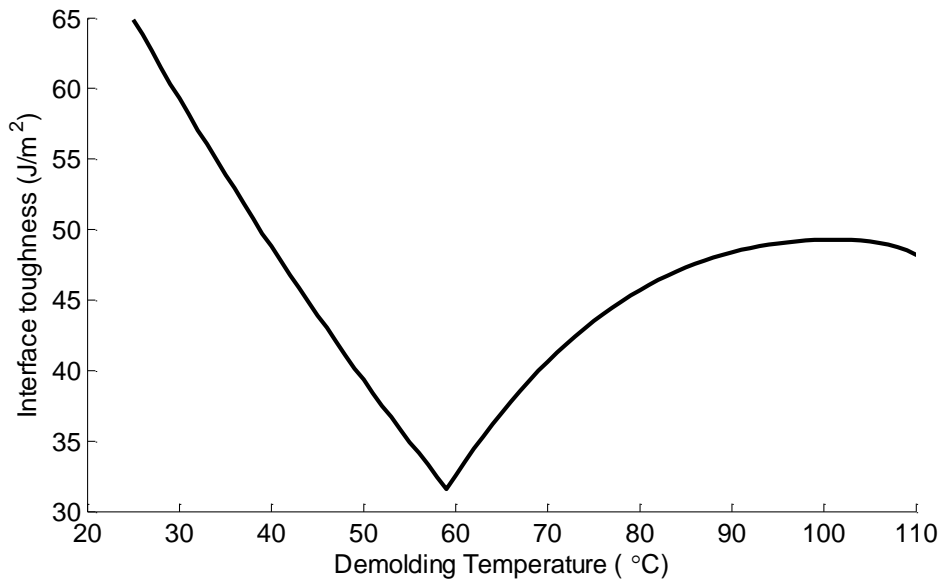
Figure 2.29 Combined effects of friction and adhesion in demolding at temperatures from 25-110°C. There is a clear minimum demolding toughness at the transition between adhesion-dominant and friction-dominant demolding. This point at ~60°C would be the optimal demolding temperature.

5.4.1   Effect of temperature on adhesion

When the demolding phase of an experiment begins and the platens first begin to separate, a brief tensile force, termed the "sticking force" is often observed (see Figure 4.21). The sticking force is associated with breaking the adhesion between the featureless upper mold (backing plate) and the top surface of the part, and so the observed sticking force can be taken as an indication of the degree of adhesion between the mold and the part. Like the demolding work,

170

the sticking force shows a consistent trend with temperature across all mold patterns. This trend can be seen in Figure 5.21, which shows the sticking force for three types of patterns (six molds total) of 100 μm deep features at demolding temperatures from 25-100°C. The sticking force drops off rapidly with decreasing temperature, and it has effectively vanished at ~60°C. This trend is consistent across all the mold patterns tested. Similar results for polycarbonate are shown in Figure 5.22. For polycarbonate, the measured sticking force decreases rapidly as demolding temperature decreases from 150°C, and has effectively vanished at ~90°C.

The observation that the adhesion of the top surface of the part is decreasing over the same range in which the demolding work is decreasing agrees with the proposed model of adhesion-dominated demolding giving way to friction-dominated demolding as the adhesion is degraded by increasing thermal stress.
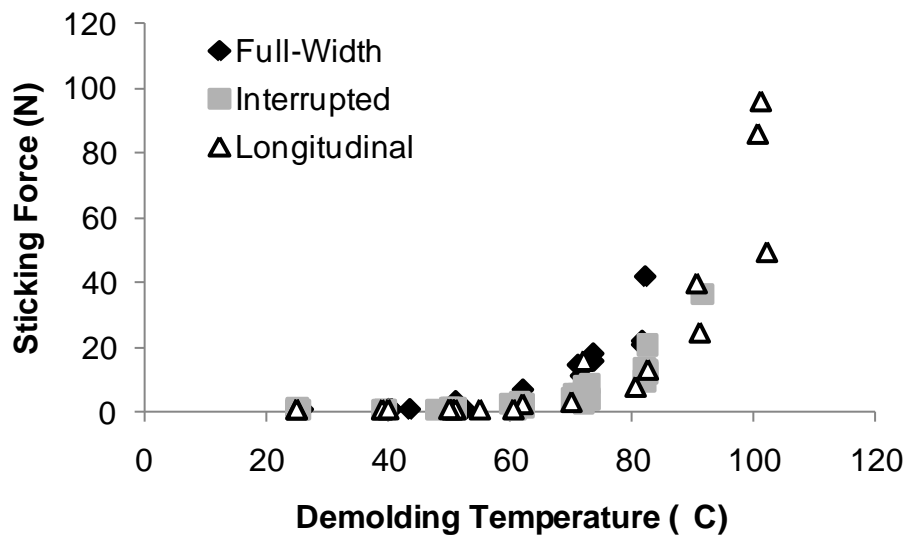
Figure 5.21 Sticking force vs. demolding temperature for three different types of patterns (six molds total) of 100 μm deep features embossed into PMMA.
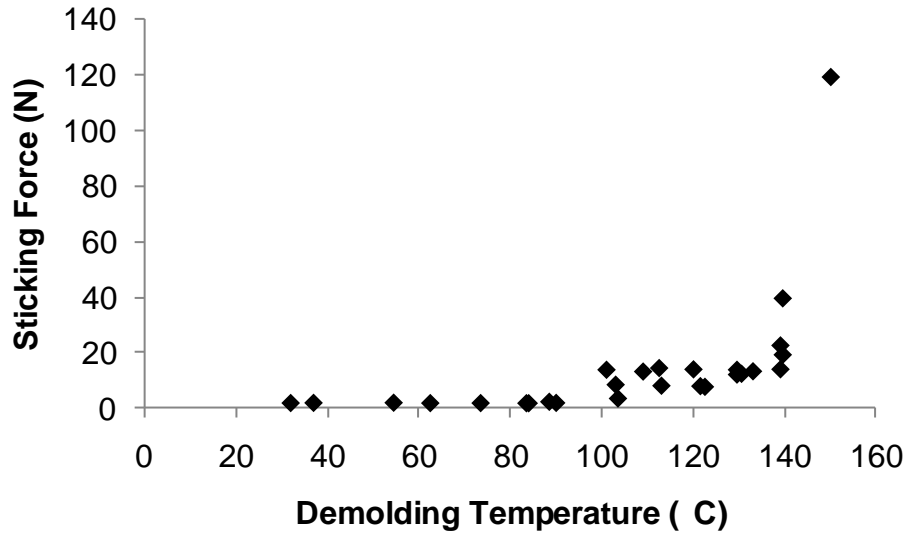
Figure 5.22 Sticking force vs. demolding temperature for polycarbonate parts embossed with molds with interrupted channels 100 μm and 200 μm deep.

Both the analytical and finite element adhesion models (sections 2.7 and 3.6) depend on the original adhesive strength between the part and mold. To calibrate these models, an experimental measurement of the adhesion strength is needed. Because they could be easily performed using the same apparatus, pull tests (see section 4.3.1) were performed to measure the adhesion strength between PMMA and Aluminum across the relevant temperature range. The test specimens were 20 mm diameter discs that were 1.58 mm thick, and the featureless aluminum molds from the other demolding tests were used as both the top and bottom mold. The heating, pressing, and demolding portions of the adhesion tests were the same as for demolding tests, including the temperature, pressure, hold time, and displacement rate of the upper platen. The measured adhesion force at temperatures from 135°C down to 25°C is plotted in Figure 5.23. As with the sticking force, there is a decreasing trend, with the adhesion force effectively vanishing at ~60°C. Similar adhesion tests were conducted using 20 mm diameter and 1.58 mm thick polycarbonate discs. Because of polycarbonate's higher glass transition temperature, these tests were performed at 160°C.
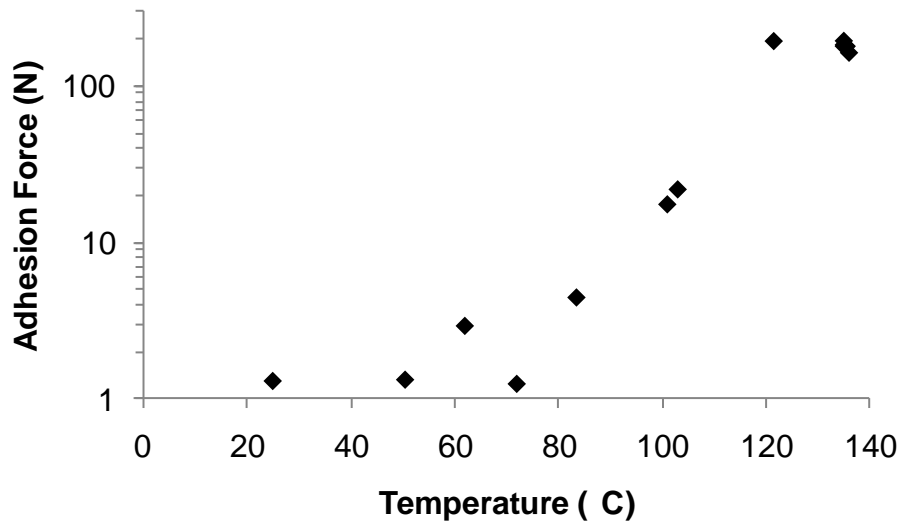
Figure 5.23 Adhesion force vs. temperature for 20 mm diameter 1.58 mm thick PMMA discs on flat aluminum. Note the log scale of the vertical axis, which exaggerates small variation in the very low forces measured below 80°C. Six tests were performed at 135°C.

The adhesion toughness can be estimated from the adhesion force according to the relation in Equation 5-7, which was developed by Yang and Li [134]. Using the average adhesion force for PMMA at 135°C of 182 N, the adhesion toughness can be estimated as 49.7 J/m^2.

Based on the average adhesion force for polycarbonate at 160°C of 146 N, the adhesion toughness can be estimated as 12.4 J/m^2. Although the polycarbonate discs had similar measured adhesion forces to the PMMA discs, the greater elastic modulus of polycarbonate at the embossing temperature (11.7 MPa at 160°C for PC versus 4.0 MPa at 135°C for PMMA) results in lower calculated adhesion toughness compared with PMMA. These values are used in the analytical and finite element modeling of adhesion in sections 2.7 and 3.6.

$$G_0 = \frac{t_p(1 - v^2)}{2E}\left(\frac{F_A}{\pi r^2}\right)^2 \qquad\qquad \textbf{5-7}$$

where
G_0 Adhesion strength (toughness)
t_p Thickness of part
v Poisson's ratio
E Elastic modulus
F_A Adhesion force
r Radius of part

The adhesion toughness for the PMMA discs calculated from the measured forces and Equation 5-7 and accounting for the temperature dependence of the elastic modulus is plotted in Figure 5.24. Again, the adhesion strength has been completely degraded by ~60°C, which agrees with the temperature predicted by the model developed in section 2.7 (also see Figure 2.27), which was calibrated using the initial adhesion toughness at 135°C measured in these tests. This evidence for the degradation of adhesion also suggests that below a critical temperature, another mechanism, most likely sidewall friction, must account for the demolding work at lower temperatures.
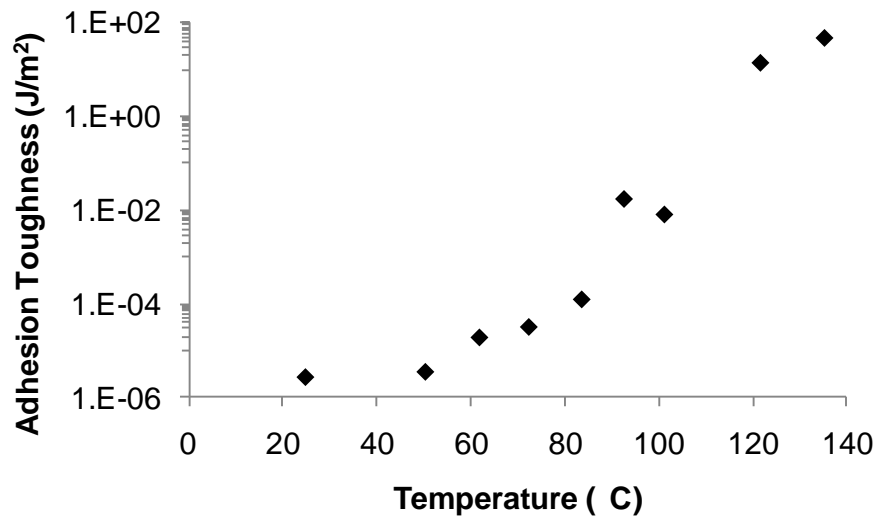
Figure 5.24 Adhesion toughness vs. temperature for 20 mm diameter 1.58 mm thick PMMA discs on flat aluminum. Note the log scale of the vertical axis. The measured adhesion strength effectively vanishes below ~60°C. The point at 135°C is the average toughness across six tests, while the other points are for single tests.

5.4.2   Effect of feature distortion on demolding work at low temperatures

As discussed previously, molds with sparse patterns have been observed to suffer from feature distortion at lower demolding temperatures. Recalling the simulation results presented in sections 3.4.4 and 3.5.4, plastic deformation in the region near the features partially relieves the thermal stress in the part, which in turn reduces the forces on the feature sidewalls. According to the model of friction-dominated demolding (see section 2.7 and Eq. 2-34), a reduction in sidewall forces should reduce the demolding work.

This effect has been observed in the experiments on sparse patterns, as shown in Figure 5.25. This plot shows the demolding work for molds with interrupted channels with heights of 50

and 100 µm and widths of 2.5 and 5 mm. The demolding work for these patterns was found to depart from the increasing trend with decreasing demolding temperature at the lowest temperatures. This departure coincides with the onset of feature distortion, as shown in Figure 5.11. This observed effect is consistent with the finite element simulations and the analytical model of friction-dominated demolding. These results highlight the importance of sidewall forces in determining the demolding work at lower temperatures, helping to confirm that sidewall friction is the dominant mechanism in this regime.
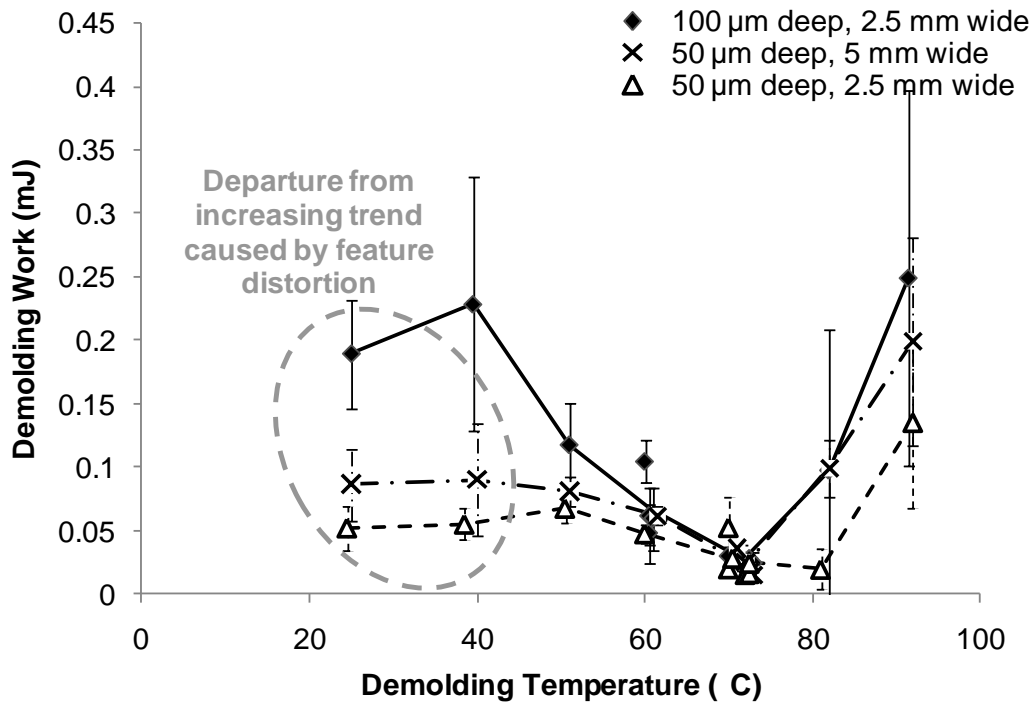
Figure 5.25 For sparse patterns, demolding work at low temperatures departs from the increasing trend with decreasing demolding temperature. This effect is attributed to local feature distortion relieving some thermal stress, which in turn reduces sidewall forces. Points represent within-part mean demolding work; lines connect the across-run mean work; error bars represent 95% confidence intervals on the within-part means based on the within-part variance.

5.5 Part warping at high temperatures

At higher demolding temperatures, parts were sometimes permanently warped during demolding, as shown in Figure 5.26 which depicts four PMMA parts embossed with an aluminum mold with 100 µm deep channels spaced 7.5 mm apart and demolded at temperatures from 77-104°C.
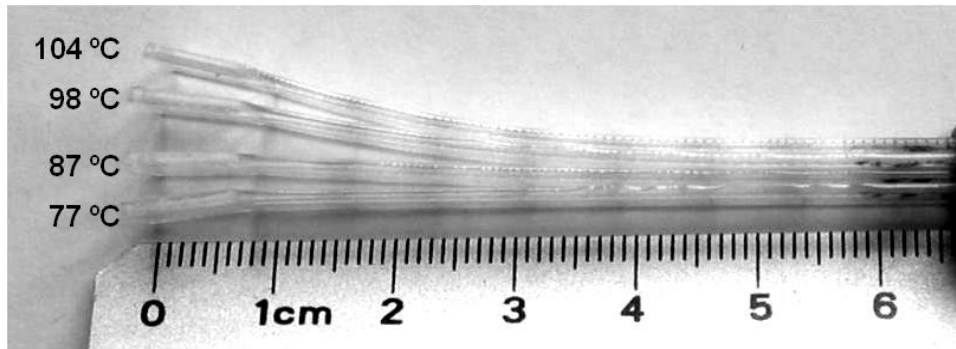
Figure 5.26 Photo of four PMMA parts demolded from an aluminum mold with 100 μm deep channels spaced 7.5 mm apart. The parts demolded at higher temperatures were permanently warped because of strong adhesion with the mold.

It is possible that the energy consumed in deforming these warped parts is partially contributing to the observed demolding work (recall the deformation component included in Equation 2-32). This possibility does not contradict the hypothesis that adhesion causes higher demolding work at high temperatures. In fact, it is the combination of strong adhesion and low material strength—as illustrated in Figure 5.27—that leads to part warping at high temperatures. Because of the possibility of warping, demolding in the presence of strong adhesion is not recommended.
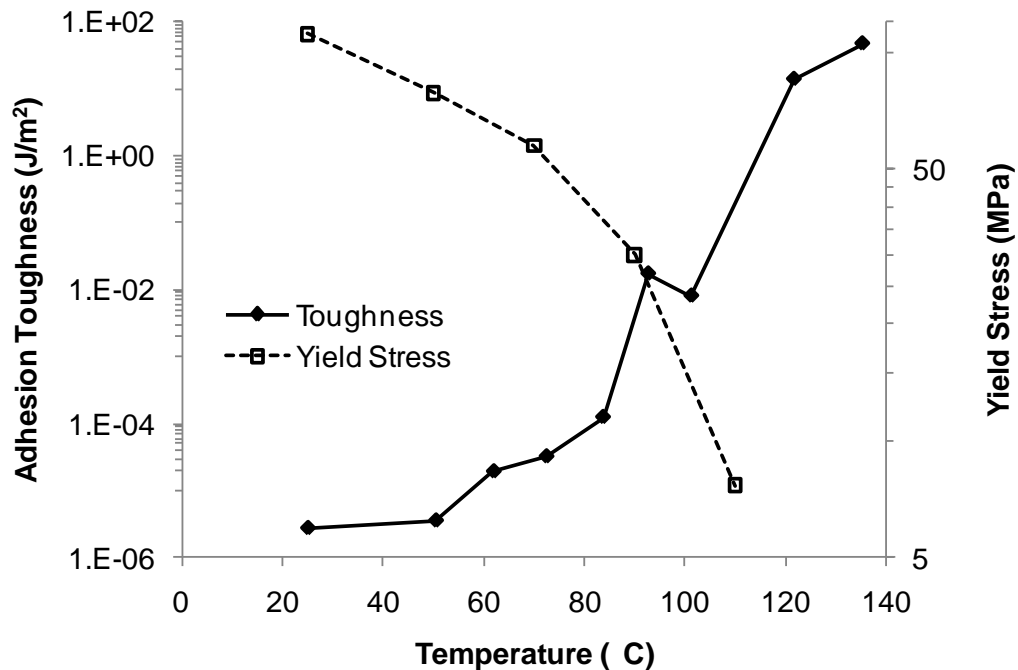
Figure 5.27 At high temperatures, a combination of strong adhesion and low material strength can result in part warping. Note the log scale of the vertical axes.

5.6 Effect of mold geometry on optimum demolding temperature

As evidenced by the demolding work results for the various molds (Figure 5.19), there is a clear minimum in the demolding work at a specific temperature. Based on the models of demolding mechanics developed in section 2.7, the finite element simulation results discussed in 3.5 and 3.6, and the observed trend in adhesion strength discussed in 5.4.1, it can be concluded that the minimum demolding work coincides with the transition from adhesion-dominated to friction-dominated demolding.

The temperature at which demolding work is minimized can be considered the optimal demolding temperature. As shown in Figure 5.28, this optimal temperature is related to the pattern of features on the mold. The optimum temperature shows a decreasing trend with increasing $\mathfrak{D}$, the dimensionless ratio defined in Equation 5-5.
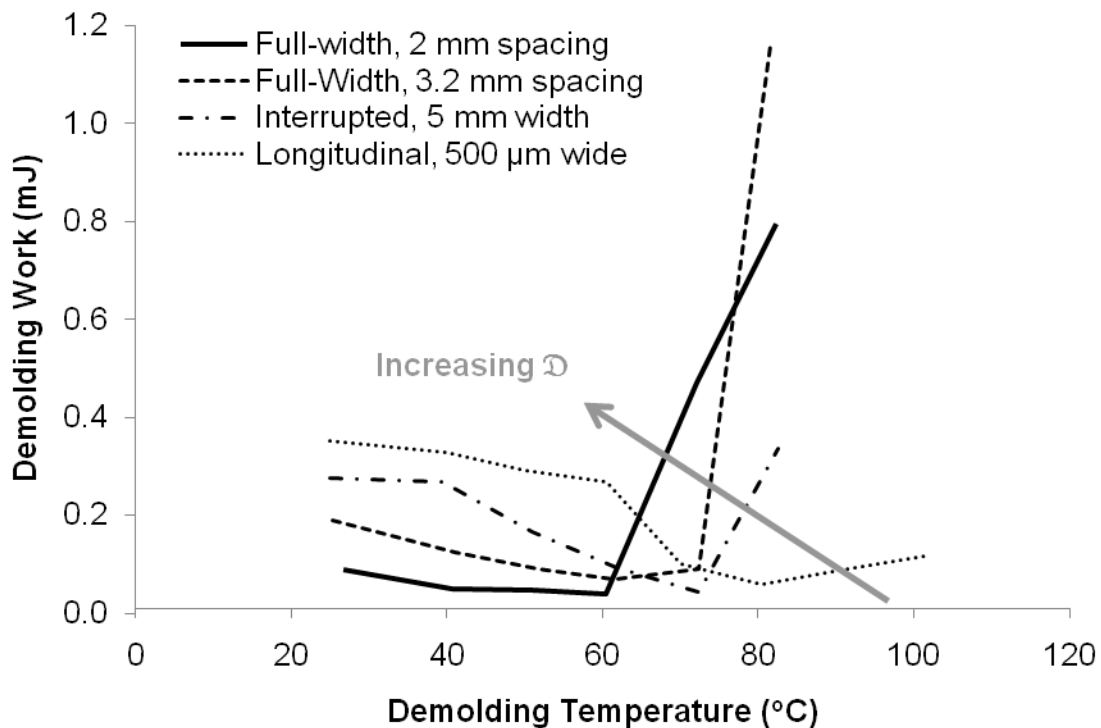
Figure 5.28 Average demolding work across 3-5 runs at various temperatures for five different patterns of 100 μm deep features. The optimal demolding temperature is related to the dimensionless ratio $\mathfrak{D}$.

The relationship between optimal demolding temperature (lowest demolding work) for all of the mold patterns tested and $\mathfrak{D}$ is clear from Figure 5.29. Because demolding experiments were conducted at 10°C intervals, the optimal temperature cannot be identified precisely,

accounting for some of the scatter in this plot. Even so, the trend with $\mathfrak{D}$ is consistent across all the mold patterns. For the densest patterns (largest $\mathfrak{D}$), the optimal ΔT is equal to that predicted by the adhesion-degradation model of section 2.7 (corresponding to a demolding temperature of 60°C).
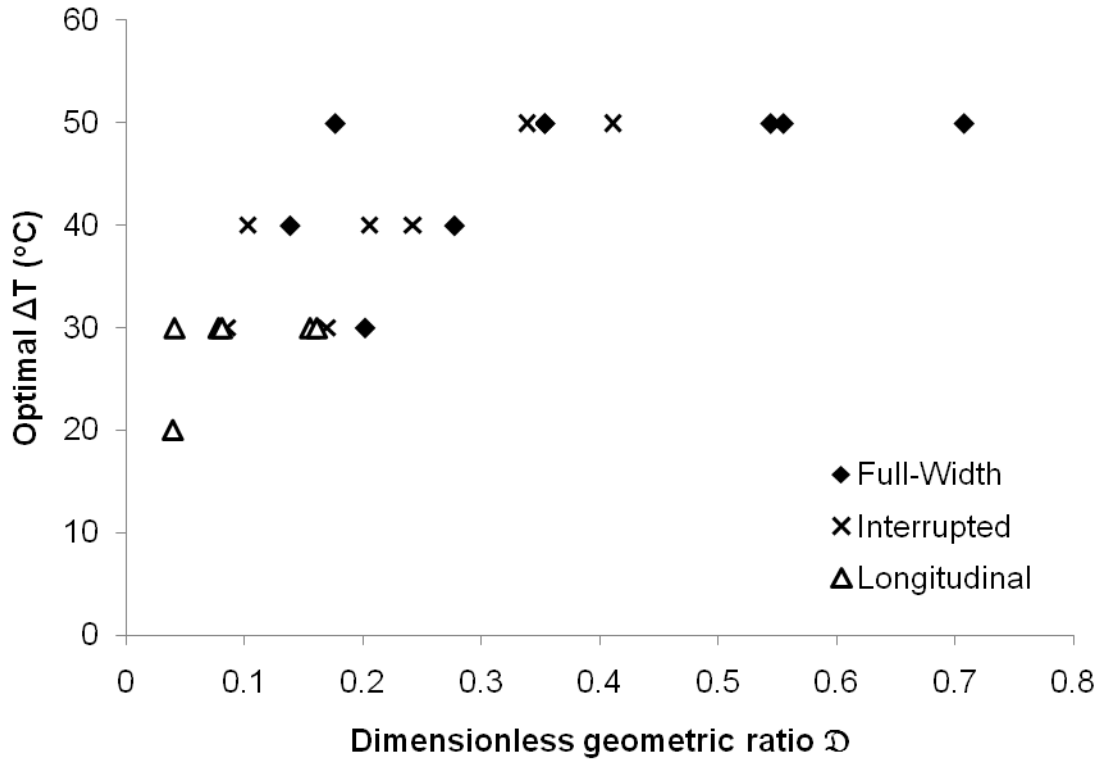
Figure 5.29 Optimal demolding ΔT vs. geometric ratio $\mathfrak{D}$ for all of the mold patterns tested.

These results also imply that the critical temperature below which adhesion gives way to friction is also related to $\mathfrak{D}$. A possible explanation for this trend with $\mathfrak{D}$ is the inhibiting effect of dense patterns on the degradation of adhesion between the part and the mold. When there are many features, the features help support the thermal stress, and so adhesion in the flat areas may be less severely degraded. Sparser patterns (lower $\mathfrak{D}$) will tend to support less of the thermal stress, so adhesion is quickly degraded. This effect is consistent with the results of finite element simulations of adhesion degradation presented in section 3.6.

178

5.7 Demolding process window

The temperature at which local distortion becomes evident (the distortion temperature, see section 5.3) sets the lower boundary for acceptable demolding. Similarly, the temperature below which demolding transitions from adhesion-dominant to friction-dominant (critical temperature, see section 5.4.1 and 5.5) sets the upper boundary for acceptable demolding, since above this temperature mold-part adhesion can be strong enough to warp the part. Furthermore, these temperatures are related to the dimensionless geometric ratio $\mathfrak{D}$, defined in Equation 5-5 in section 5.3.2. Highlighting this relationship, the distortion temperature, optimal temperature, and critical temperatures for all the mold patterns tested are plotted vs. $\mathfrak{D}$ in Figure 5.30. From this plot, it is evident that there is a window for acceptable demolding bounded by the distortion temperature and the critical temperature and containing the optimal temperature. This window of acceptable demolding temperatures (the demolding process window) is also clearly related to $\mathfrak{D}$.
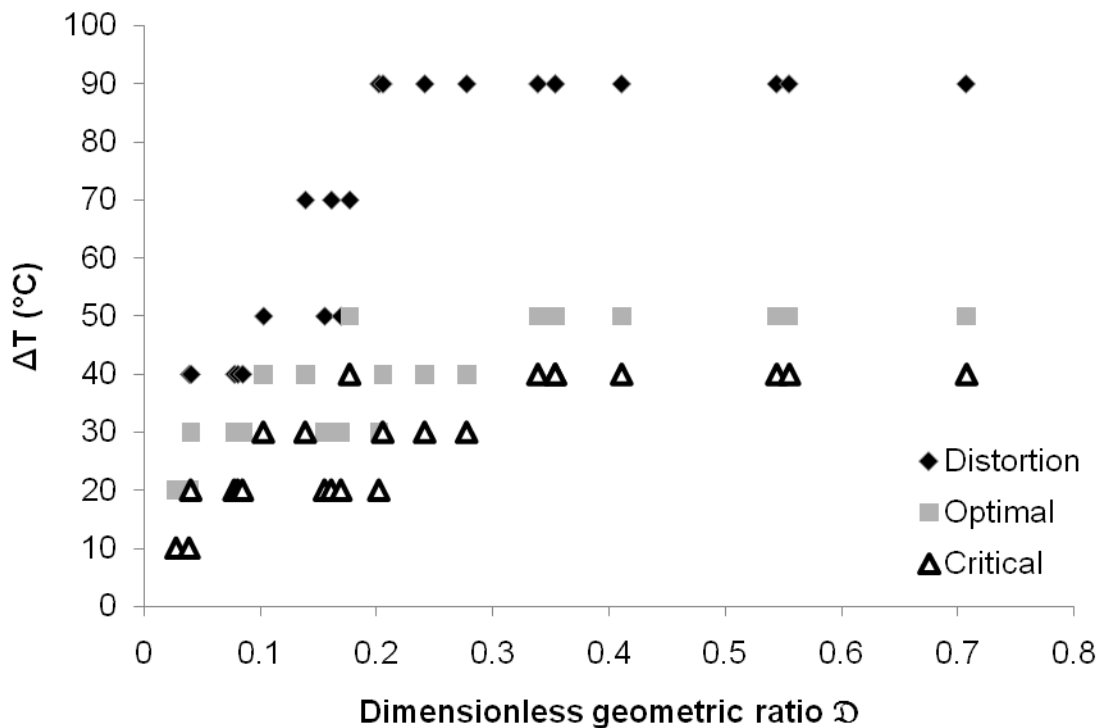
Figure 5.30 Distortion temperature, optimal temperature, and critical temperature vs. $\mathfrak{D}$ for all mold patterns tested. The relationship between $\mathfrak{D}$, feature distortion, and the optimal demolding temperature is consistent across the different mold patterns. The distortion temperature and the critical temperature along with $\mathfrak{D}$ define the window of acceptable demolding temperatures (process window).

The generalized demolding process window for PMMA on aluminum molds is given in Figure 5.31. The lines in this figure are roughly based on a moving average of the observed boundary temperatures. Acceptable demolding is possible anywhere between the limits defined by the potential for feature distortion and part warping. The optimal temperature is recommended, since the lowest demolding works (and lowest demolding forces) occur here. Special care should be taken when $\mathcal{D}<0.2$ because the demolding process window can be as narrow as 10°C. Importantly, there is no single demolding temperature that is acceptable for all mold patterns, so knowledge of the pattern (in terms of $\mathcal{D}$) and the demolding process window is required to select the appropriate demolding temperature.
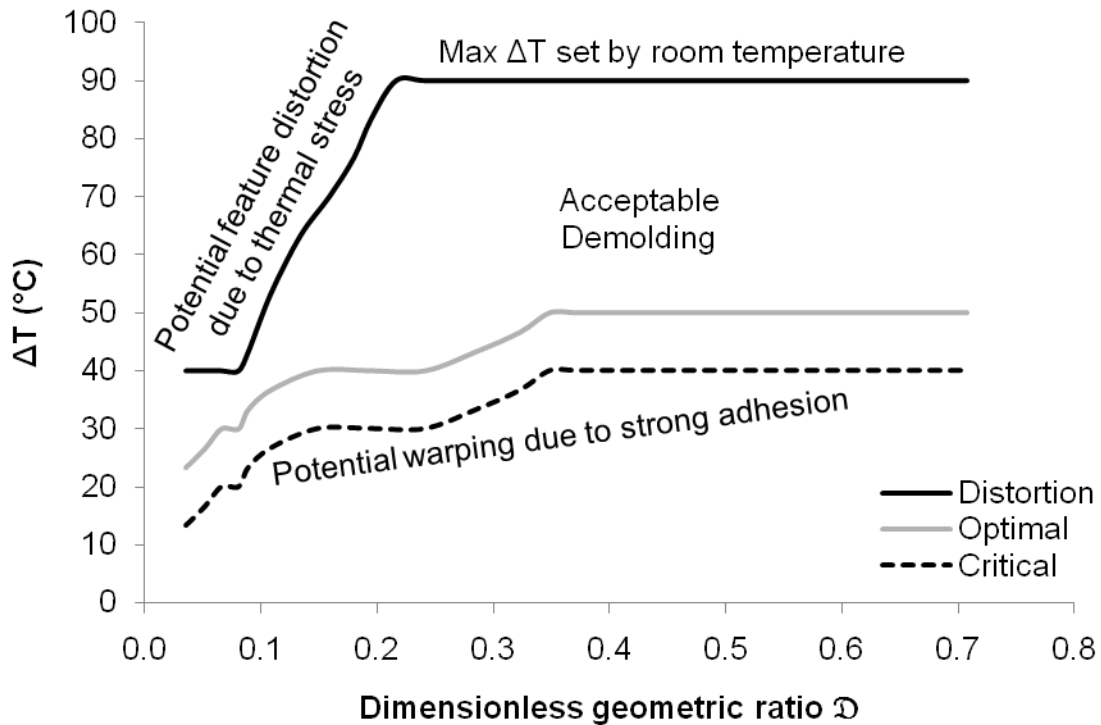
Figure 5.31 Demolding process window for PMMA on Aluminum molds based on experimental observations.

Considering both the critical temperature and the distortion temperature, it can be seen that the ratio $\mathcal{D}$ is related to the "severity" of thermal stresses. Sparser patterns of smaller features have low values of $\mathcal{D}$ and exhibit more feature distortion at lower ΔT (higher demolding temperatures). Denser patterns of larger features have higher values of $\mathcal{D}$ and are more resistant to thermal stress, but this resistance also has the effect of delaying the degradation of adhesion and increasing the ΔT required for acceptable demolding. This effect was anticipated in the finite

180

element simulations of molds with different feature spacing (compare Figure 3.36 and Figure 3.39), where the sparser pattern showed more degradation of adhesion strength at higher temperatures.

The generalized demolding process window for polycarbonate is shown in Figure 5.32. As was the case for PMMA, there is no single demolding temperature that is recommended for all values of $\mathfrak{D}$. The weaker initial adhesion toughness between PC and Aluminum (see section 5.4.1) results in a lower adhesion limit ΔT for all values of $\mathfrak{D}$ compared with the adhesion limit ΔT for PMMA. The effect is consistent with the adhesion degradation model developed in section 2.7 (Eq. 2-33) and the finite element simulations for different initial adhesion strengths presented in section 3.6 (see Figure 3.37). For polycarbonate, the sparsest mold patterns ($\mathfrak{D} \lesssim 0.18$) had such weak adhesion that they could be easily demolded near the embossing temperature.
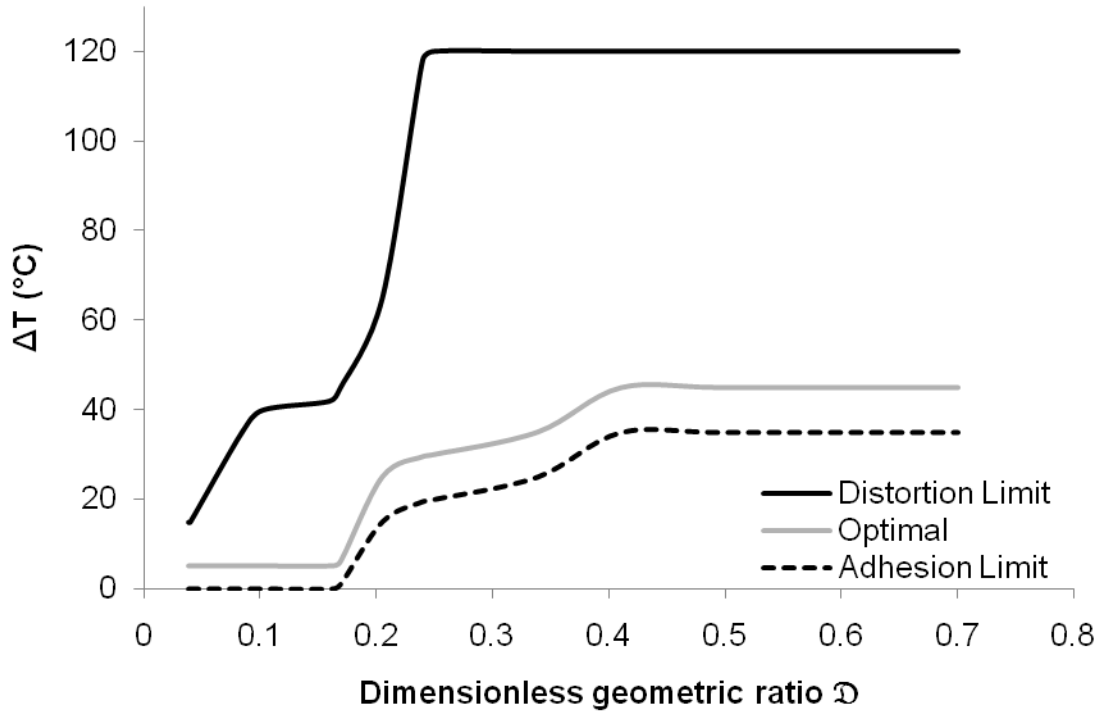
Figure 5.32 Demolding process window for PC on Aluminum molds based on experimental observations. Note that the lower initial adhesion toughness between PC and Aluminum (see section 5.4.1) results in a lower adhesion limit ΔT for all values of $\mathfrak{D}$ compared with PMMA.

5.8 Feature geometry and demolding work

Recalling the results of analytical models in section 2.7 and finite element simulations in section 3.6, it is expected that feature geometry will have an effect on the magnitude of the demolding work in the friction-dominated regime.

5.8.1 Effect of spacing

The spacing between rows of features that are oriented perpendicular to the direction of thermal contraction has a strong effect on the forces on those features according to both analytical models (Equation 2-27) and finite element simulations (Figure 3.12). Higher sidewall forces in turn lead to higher demolding work in Coulomb friction dominated demolding (Equation 2-34).

To test this effect, molds were produced with 100 μm high full-width channels and spacing of 1, 2, 3.2, and 7.5 mm, and between 5 and 13 PMMA parts were embossed with each mold and demolded at 50°C. For all of these patterns, 50°C is within the friction-dominant demolding range. The within-part average demolding work at 50°C for all of these tests is plotted against the feature spacing in Figure 5.33. The demolding work clearly increases with feature spacing.
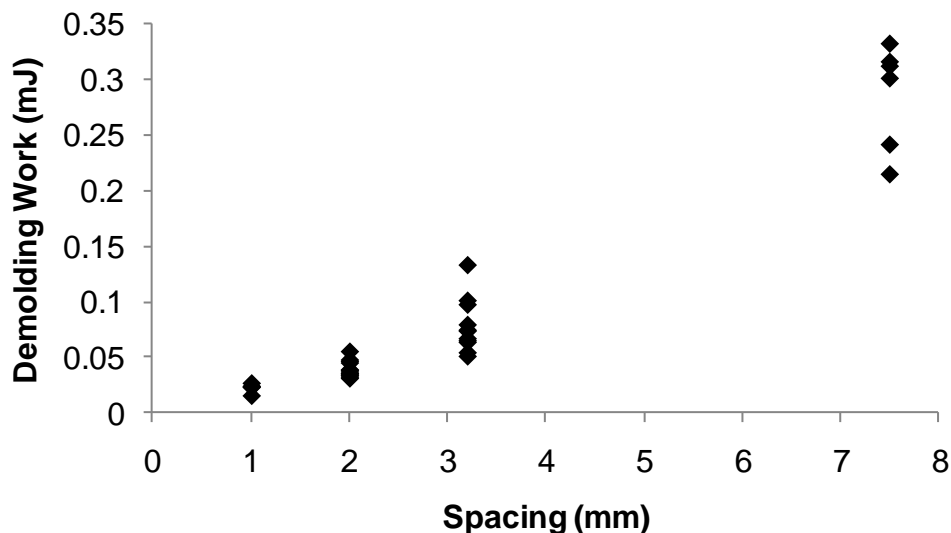
Figure 5.33 Within-part mean demolding work for 100 μm deep channels of different spacing at 50°C.

Because the spacing varies, the area of crack extension between features also varies. From a macroscopic perspective, if two surfaces have the same toughness (energy/area) but cracks in one of the surfaces extend with longer increments, that surface will exhibit higher measured fracture energy. When the fracture energy is normalized by the area of crack extension (to compute the toughness), the difference will disappear. To test whether the overall demolding difficulty at 50°C (due to sidewall friction) increases with feature spacing, the demolding work should be normalized by the area of crack extension and the demolding toughness should be compared for these different patterns. The demolding toughness for these tests is plotted in Figure 5.34. The trend of demolding toughness with spacing is less steep, but is still apparent.
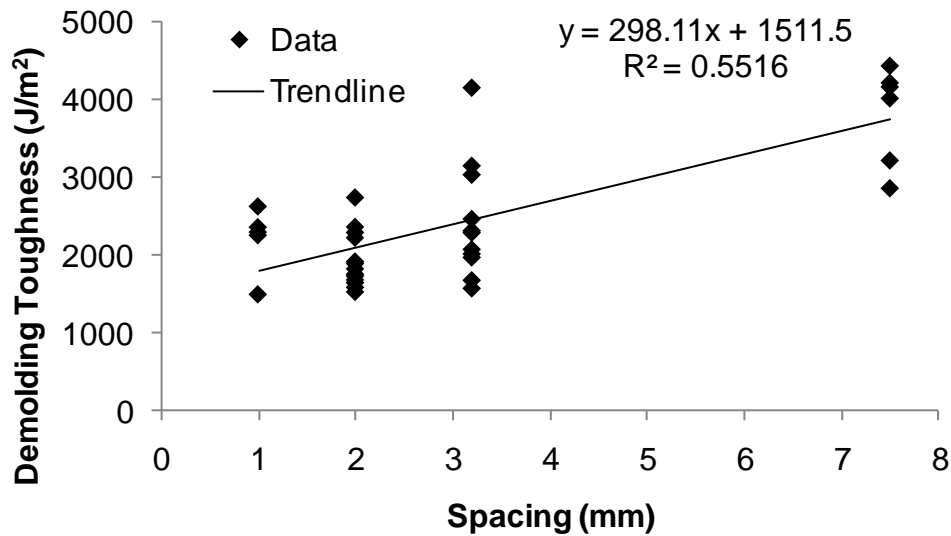
Figure 5.34 Within-part mean demolding toughness for 100 µm deep channels of different spacing at 50°C, along with least-squares linear fit. There is an increasing trend of demolding toughness with increasing feature spacing, which can be explained by the increasing forces on feature sidewalls.

A statistical analysis can verify the significance of the relationship between spacing and toughness. If there is a strong quantitative relationship between spacing and demolding toughness, then these two parameters should be strongly correlated. The linear correlation coefficient for spacing and within-part mean demolding toughness is r=0.743 (square root of R^2=0.552 from Figure 5.34; the calculation of R^2 can be found in many statistics texts [135]). The significance of this correlation can be evaluated using the test statistic defined in Equation 5-8, which has a Student's distribution with n-2 degrees of freedom [135].

$$r_t \equiv \frac{r\sqrt{n-2}}{\sqrt{1-r^2}}$$

5-8

where

r_t Test statistic for correlation coefficient
r Linear correlation coefficient
n Number of observations used to compute r

The sample linear correlation coefficient r is an estimate of the population correlation coefficient ρ, and the statistic r_t is used to test the null hypothesis H_0: $\rho=0$ against the alternate hypothesis H_1: $\rho>0$. In the current case, the null hypothesis can be rejected with a one-tailed p-value of 1.6×10^{-7}. It can therefore be concluded that $\rho>0$ (that is, there is a real correlation between spacing and toughness) with a very high confidence.

According to the models and simulations discussed earlier (section 2.6.2 and 3.4.3 respectively), increasing feature spacing increases the sidewall force. In the Coulomb friction model of demolding mechanics, higher sidewall forces should result in greater demolding toughness. The experimental results discussed above indicate that there is a clear and significant positive relationship between spacing and toughness, which lends support to the theory of demolding mechanics combining the equivalent stiffness model of sidewall forces with the Coulomb friction model of demolding.

5.8.2 Effects of height and width

For demolding where Coulomb friction is the primary mechanism of energy dissipation, the demolding work is expected to be proportional to feature height, since this is the sliding distance for the sidewall friction force during demolding (see Eq. 2-34 and Figure 3.31). Under these conditions, feature width is not expected to have a strong effect because Coulomb friction is independent of apparent contact area.

To test this effect, molds have been produced with several combinations of total feature width (2.5-10 mm, or 25-100% of the width of the parts) and feature height (50-200 μm), and PMMA parts have been embossed with these molds and demolded at temperatures of 25-100°C. All of these patterns have the same feature spacing (3.2 mm). In practice, it is difficult to compare the effects of geometry across a broad range of feature dimensions because of the relationship between pattern geometry and the demolding process window. Recalling the generalized demolding process window shown in Figure 5.31, there are some demolding

temperatures at which sparse patterns are beginning to suffer local distortion, while dense patterns are still within the adhesion-dominated regime and so have much higher demolding works. There is thus no single temperature at which the effects of geometry can be isolated across a wide range of patterns.

With this in mind, the effects of geometry can be deduced by examining the trends of demolding work with feature width and height at selected temperatures and for limited, overlapping ranges of dimensions. A slight increasing trend in demolding work with feature height is visible at 60°C and at 70°C for interrupted channels with total width 2.5 mm, as shown in Figure 5.35. It should be noted that at 60°C the 50 μm deep interrupted channels have just begun to show local distortion, while at 70°C the 200 μm deep pattern is still within the adhesion-dominated regime. The correlation between height and demolding work at 60°C is significant with a p-value of 0.047 based on seven observations (n=7), and at 70°C it is significant with a p-value of 0.029 based on nine observations (n=9).

A similar increasing trend of demolding work with feature height at 60°C and 70°C for interrupted channels with total width 5 mm is apparent in Figure 5.36. Again, it should be noted that at 60°C the 50 μm deep interrupted channels have just begun to show local distortion, while at 70°C the 200 μm deep pattern is still within the adhesion-dominated regime. The correlation between height and demolding work at 60°C is significant with a p-value of 0.002 (n=6), and at 70°C it is marginally significant with a p-value of 0.059 (n=9)

The positive relationship between demolding work and feature height is also apparent for the full-width channels, as shown in Figure 5.37. The correlation between height and demolding work is significant with a p-value of 0.004 (n=10).

The significance levels of the correlations between feature height and demolding work for the three different feature widths are summarized in Table 5.1. Overall, the positive correlation between feature height (channel depth) and demolding work is in line with expectations based on a Coulomb friction model of demolding as proposed in section 2.7.

(a)

$y = 0.0002x + 0.0379$
$R^2 = 0.4599$

(b)

$y = 0.0001x + 0.0145$
$R^2 = 0.4217$
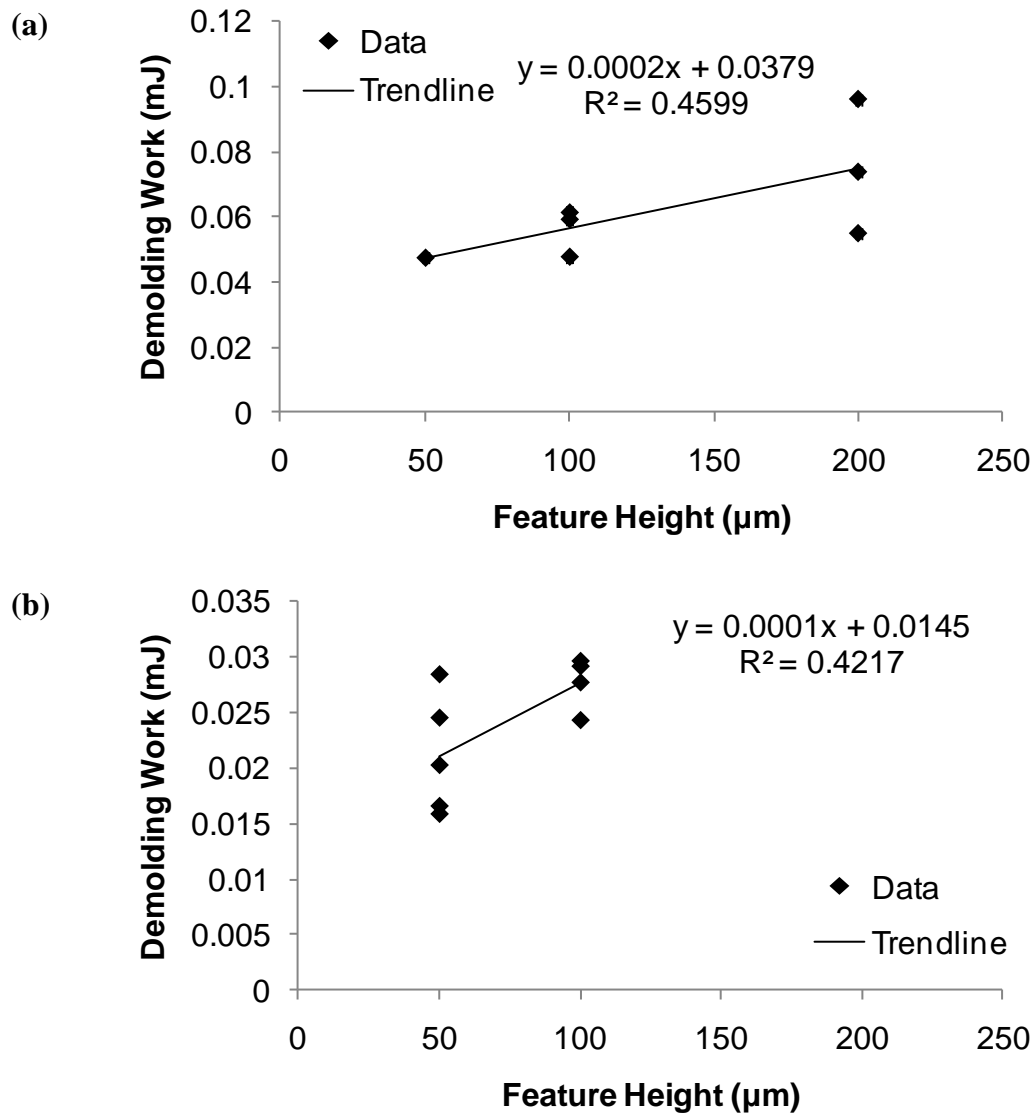
Figure 5.35 Effects of feature height for channels with 2.5 mm total width at (a) 60°C, and (b) 70°C. Note: at 60°C the 50 μm high pattern has just begun to show local distortion, while at 70°C the 200 μm deep pattern is still within the adhesion dominated regime and so this data is not included. In both cases, the correlation between height and demolding work is significant.

(a)

y = 0.0003x + 0.0516
R² = 0.8967

(b)

y = 0.0004x + 0.0038
R² = 0.3125
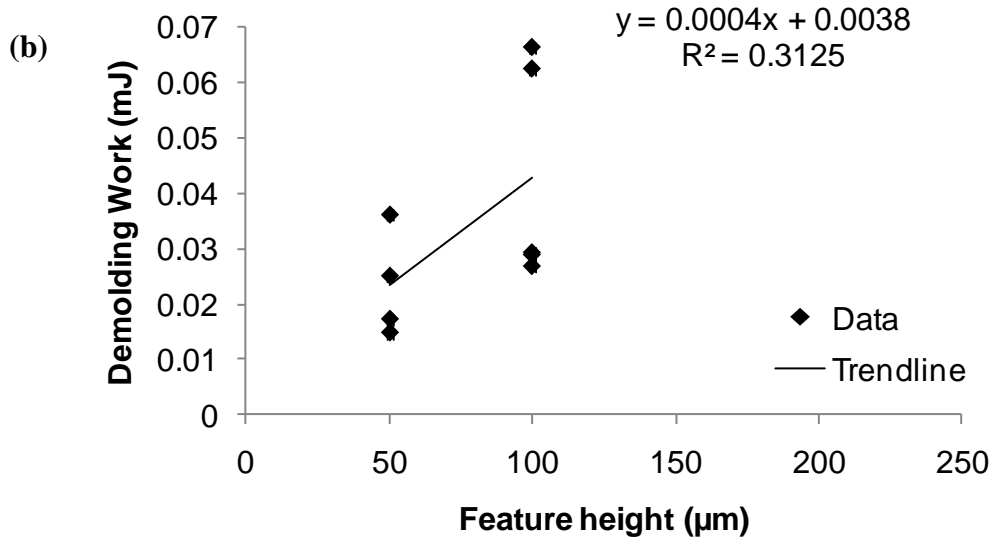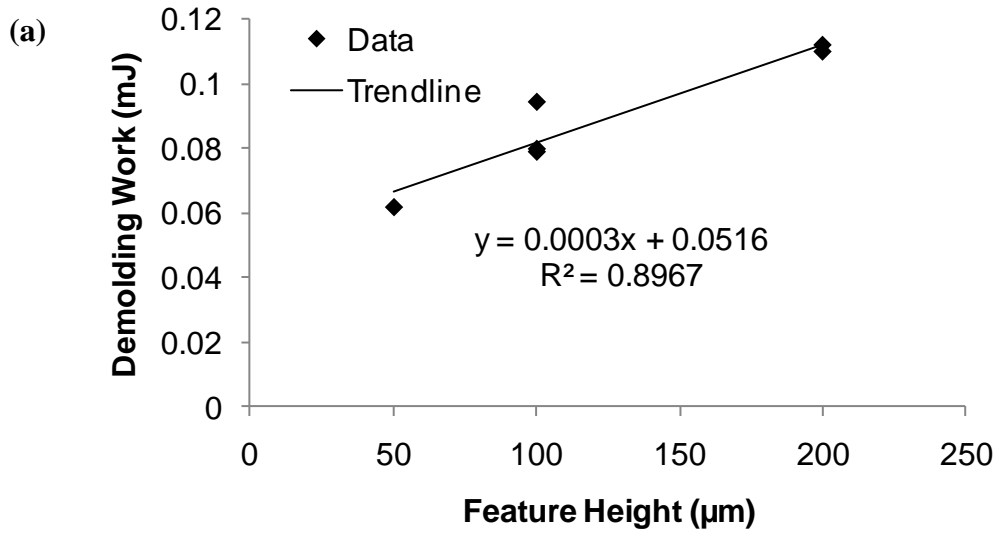
Figure 5.36 Effects of feature height for channels with 5 mm total width at (a) 60°C, and (b) 70°C. Note: at 60°C the 50 μm high pattern has begun to show distortion, while at 70°C the 200 μm deep pattern is within the adhesion dominated regime and so this data is not included. In both cases, the correlation is significant.
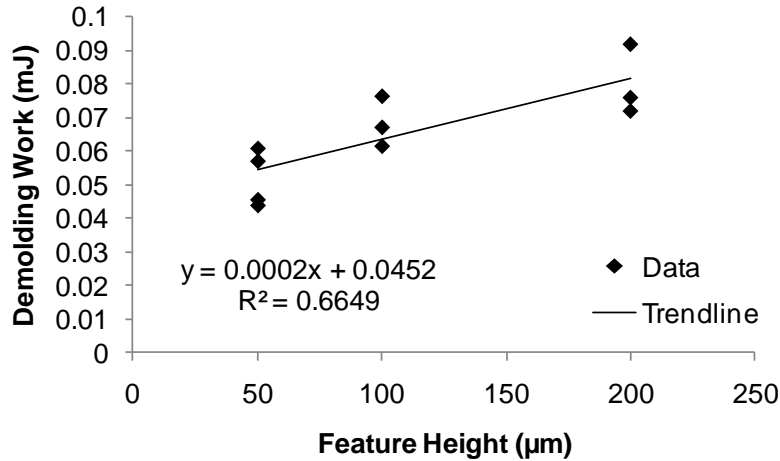
Figure 5.37 Effects of feature height for full-width channels (10 mm total width) at 60°C.

Table 5.1 Summary of correlation P-values between feature height and within-part mean demolding work along with number of observations for various widths at 60°C and 70°C. Values less than 5.0% are considered statistically significant.

Total Width	60°C	70°C
2.5 mm	4.7%, n=7	2.9%, n=9
5 mm	0.2%, n=6	5.9%, n=9
10 mm	0.4%, n=10	

The Coulomb friction model of demolding predicts that there should be no strong relationship between total feature width and demolding work, since Coulomb friction is independent of apparent contact area. The results of demolding experiments on molds with different total feature widths are consistent with this prediction. As shown in Figure 5.38, there is no apparent relationship between total feature width and demolding work at 60°C for the three feature heights tested. At 60°C, all of the patterns are within the friction-dominated regime, although the sparsest patterns (2.5 and 5 mm total width for 50 μm high and 2.5 mm total width for 100 μm high) have just begun to show distortion of the outermost features.

Table 5.2 summarizes the significance levels of the correlations between feature width and demolding work. These are two-tailed p-values because the correlation coefficients are near zero, and so the alternate hypothesis is H_1: $\rho \neq 0$. For all three heights, there is no significant correlation between width and demolding work. This result is consistent with the Coulomb friction model of demolding, which predicts that the friction force, and therefore the demolding work, is independent of apparent contact area and so should not be related to total feature width.
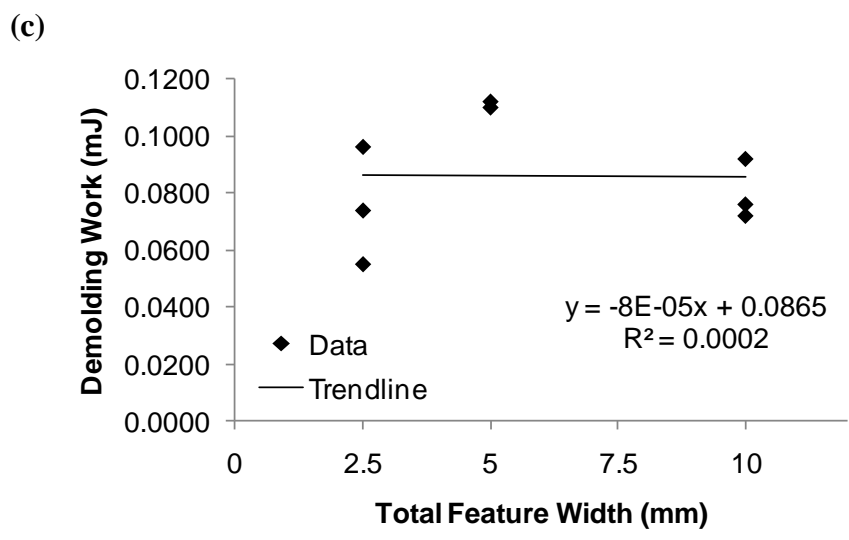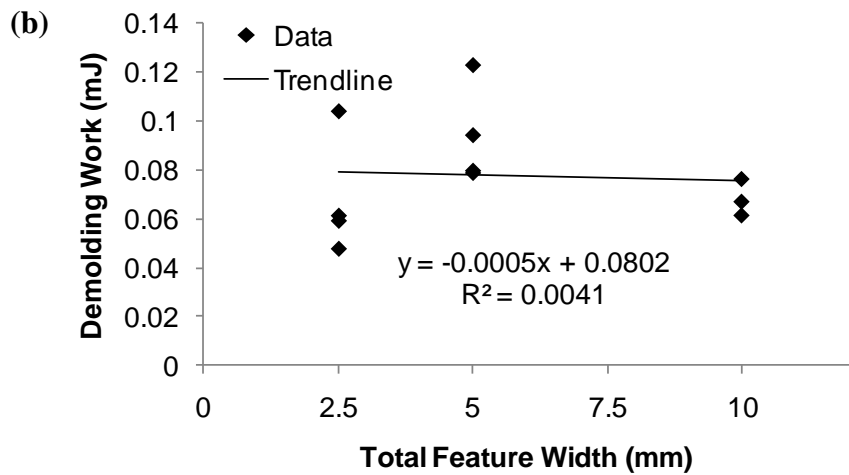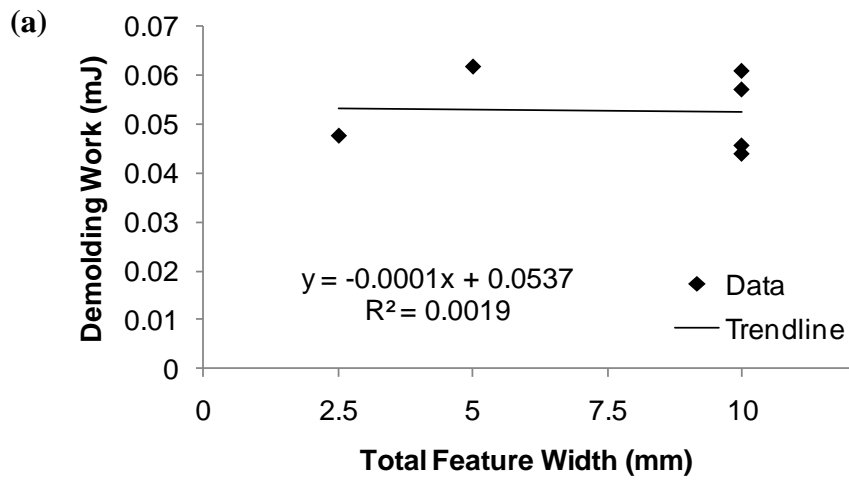
Figure 5.38 Effect of total feature width on demolding work at 60°C for (a) 50 μm, (b) 100 μm, and (c) 200 μm deep channels. In all three cases, the correlation between width and demolding work is not significant.

189

Table 5.2 Summary of correlation P-values between feature width and within-part mean demolding work for various heights at 60°C. None of these correlations is considered significant.

Feature Height	60°C
50 μm	98%, n=6
100 μm	85%, n=11
200 μm	97%, n=8

The layout of the channel features also does not affect the demolding work. Some molds were made with channels that were interrupted so that the total width was reduced, while other molds were made with one feature in the middle of the part or two features at the edges of the part with the same total width (see Figure 5.3). Figure 5.39 shows box plots of the within-part mean demolding work at 50°C for different layouts, and ANOVA results for different layouts are given in Table 5.3 and Table 5.4. From the ANOVA results, it can be concluded that there is no significant difference among the different layouts, which supports the hypothesis that feature width does not affect the demolding work and is consistent with the Coulomb friction model of demolding.
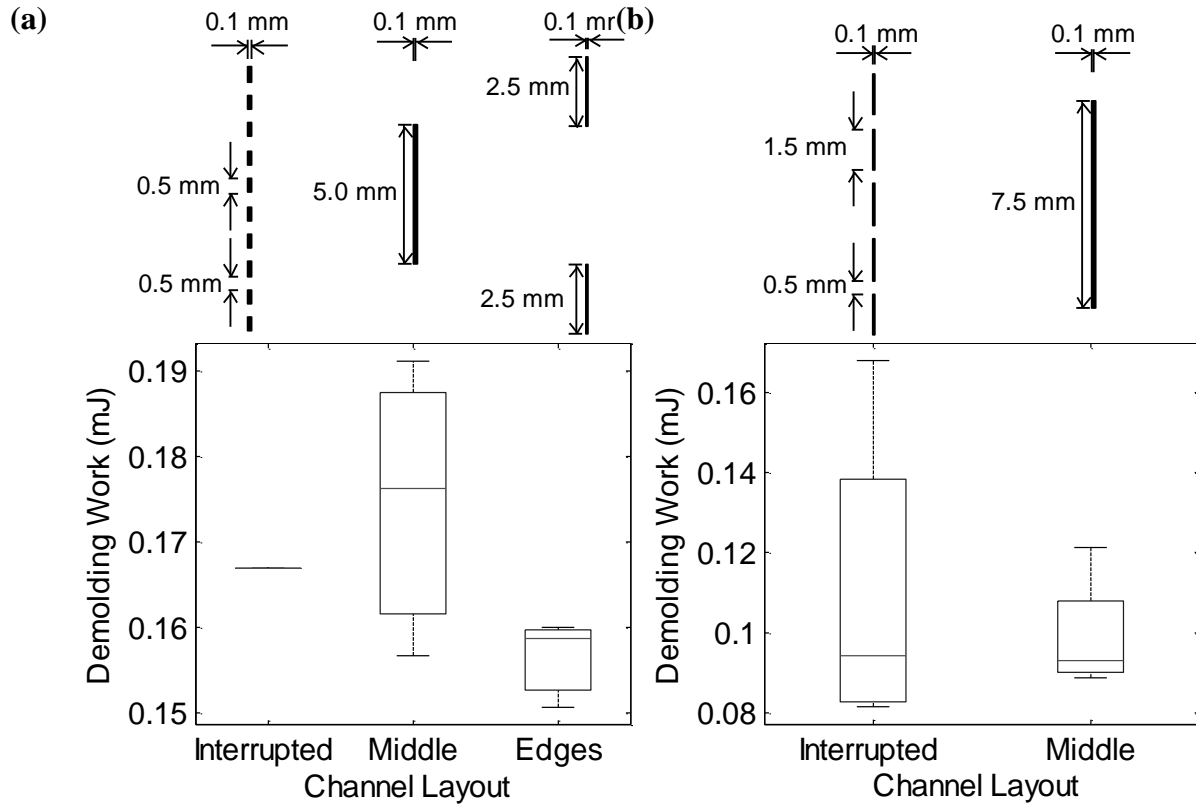
Figure 5.39 Box plots showing effect of pattern layout on within-part mean demolding work at 50°C for (a) 50% total feature width (5 mm) (Note: there is only one observation for the 50% width Interrupted channel at 50°C), and (b) 75% total feature width (7.5 mm).

Table 5.3 Results of ANOVA for effect of pattern layout on within-part mean demolding work at 50°C for 50% total feature width (5 mm).

Source	Sum of Squares	Degrees of freedom	Mean Square	F statistic	P-value
Layout	5.04×10^{-4}	2	2.52×10^{-4}	1.55	0.32
Error	6.51×10^{-4}	4	1.63×10^{-4}		
Total	1.15E-03	6			

Table 5.4 Results of ANOVA for effect of pattern layout on within-part mean demolding work at 50°C for 75% total feature width (7.5 mm).

Source	Sum of Squares	Degrees of freedom	Mean Square	F statistic	P-value
Layout	3.22×10^{-4}	1	3.22×10^{-4}	0.37	0.56
Error	6.15×10^{-3}	7	8.79×10^{-4}		
Total	6.47×10^{-3}	8			

5.9 Evaluating methods of mitigating demolding

The development of the demolding work and toughness as metrics for the difficulty of demolding, along with the experimental method described previously, make it possible to evaluate methods for mitigating demolding, such as coatings applied to molds or changes to feature geometry.

5.9.1 Effect of coatings

Several researchers have suggested various anti-adhesive and low-friction coatings to improve demolding of polymer microstructures [45, 53, 81, 136, 137]. It has also been found that some of these coatings can have a finite lifetime [78]. While mold coatings have been found to be effective in macroscopic polymer molding [138, 139], their effect has rarely been quantitatively evaluated in molding of microstructures [45]. Quantitative evaluation is necessary to compare the effectiveness of these treatments and to analyze their costs and benefits to determine their usefulness.

The effect of mold coatings was studied in collaboration with Biswajit Saha, a doctoral student at Nanyang Technological University in Singapore and a member of the Singapore-MIT Alliance Programme in Manufacturing Systems and Technology. Biswajit Saha designed and produced the silicon molds for this study, applied the coatings, and participated in conducting the demolding experiments. He also performed measurements of the surface energies of the coatings.

The silicon molds were produced using conventional microfabrication techniques including photolithography and dry etching. The coatings consist of Molybdenum Disulfide doped with varying amounts of Titanium, and were deposited by sputtering. Each silicon mold is a rectangle 36 mm long by 20 mm wide. The features are 100 µm high square channels that are 8 mm wide across the mold. The features are spaced 0.5 mm apart, and the first feature is 3.6 mm from the edge. This pattern has $\mathcal{D}=0.81$, the highest value tested so far. A special fixture was made to mount the silicon tools in the demolding machine. A photo of one (broken) silicon mold clamped in this fixture is shown in Figure 5.40.The test specimens were 8 mm wide by 40 mm long and 1.58 mm thick.
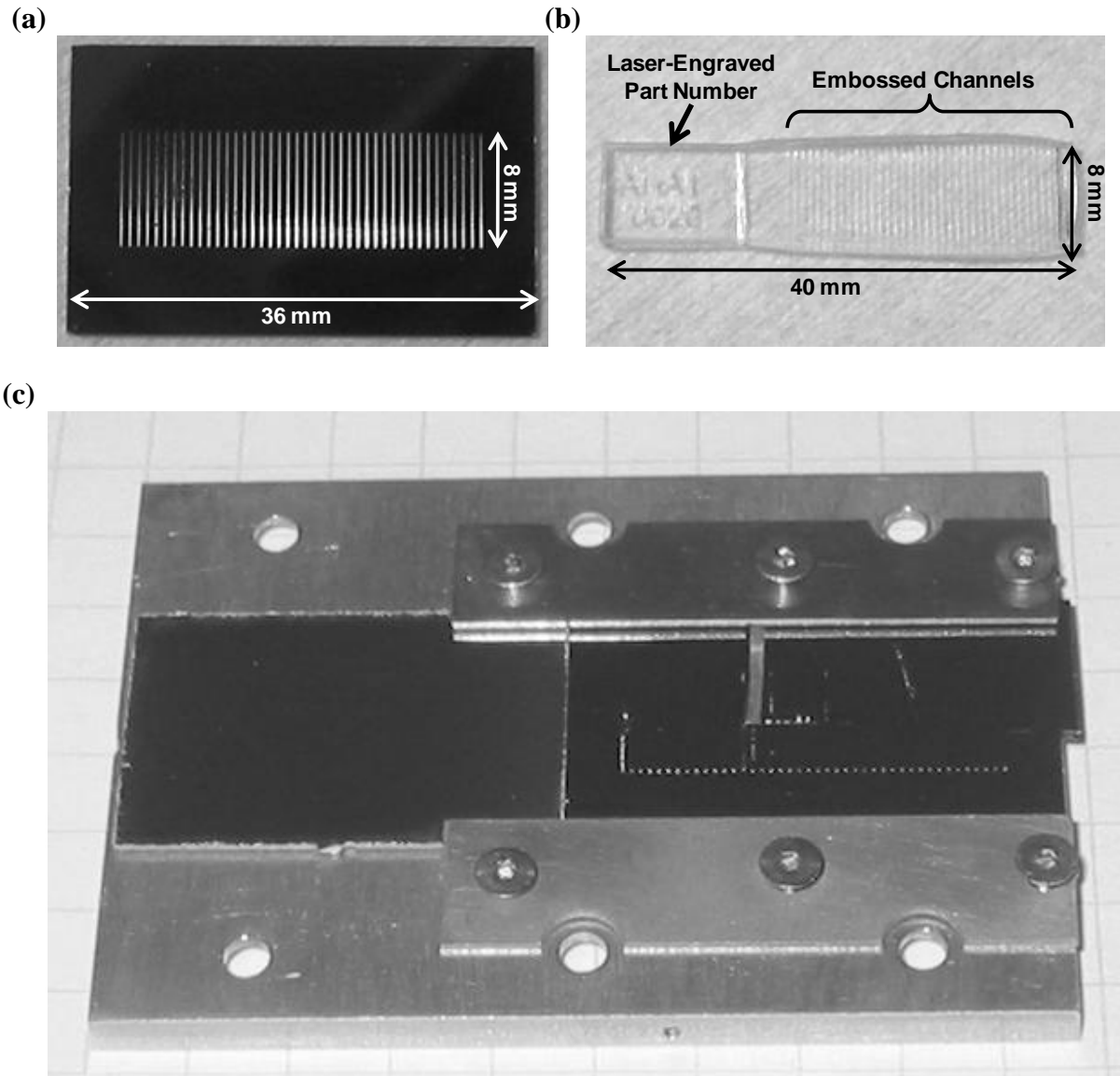
Figure 5.40 (a) Photo of a silicon test mold, the bright lines are the features. (b) Photo of a test specimen embossed with the silicon mold, note the embossed channels. (c) Photo of a silicon mounted in the clamp fixture used for demolding trials. The silicon mold is the dark rectangle on which bright dots (the ends of features) are visible. The silicon mold has broken—a not uncommon experience during this study.

The data for these tests was analyzed using a slightly different script, which identified demolding events by locating peaks in the second derivative of the load-vs-extension curve. As an example, the data from a demolding experiment on an uncoated silicon mold at 50°C is shown in Figure 5.41.
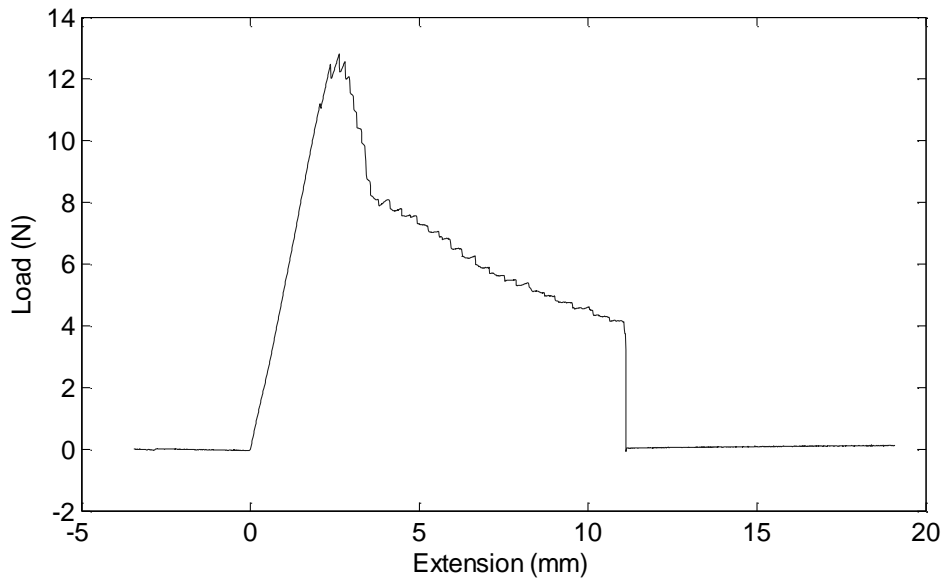
Figure 5.41 Plot of load vs. extension data from a demolding experiment on an uncoated silicon mold at 50°C. The silicon mold has dense feature spacing, so there are many more channels than on the aluminum molds.

The mold coatings were found to have a profound effect on the demolding work, as can be seen in the box plot of demolding work data in Figure 5.42. The results for ANOVA on the effect of mold coatings on demolding work are presented in Table 5.5. The effect of mold coatings is significant, with a p-value of 1.52×10^{-12}.
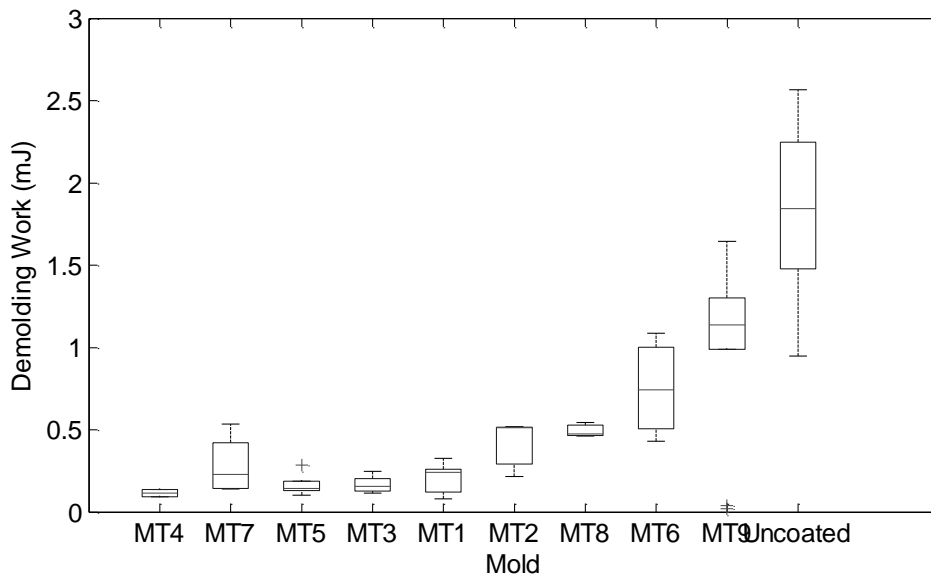
Figure 5.42 Box plot of demolding work at 50°C for several silicon molds. Molds have been sorted according to the average demolding work.

Table 5.5 Results of ANOVA for the effect of mold coatings on demolding work at 50°C.

Source	Sum of Squares	Degrees of freedom	Mean Square	F statistic	P-value
Coating	21.6	9	2.40	19.3	1.52×10^{-12}
Error	5.48	44	0.12		
Total	27.1	53			

Most demolding tests on the silicon molds were conducted at 50°C. For three molds, demolding tests were also performed at temperatures from 40 to 80°C. The demolding work measured in these tests is plotted in Figure 5.43. For all three molds, demolding work followed a decreasing trend with temperature, indicating that these patterns are still within the adhesion-dominated regime at 50°C. This condition could be a result of the high value of $\mathcal{D}$ for this pattern combined with strong initial adhesion to the molds.
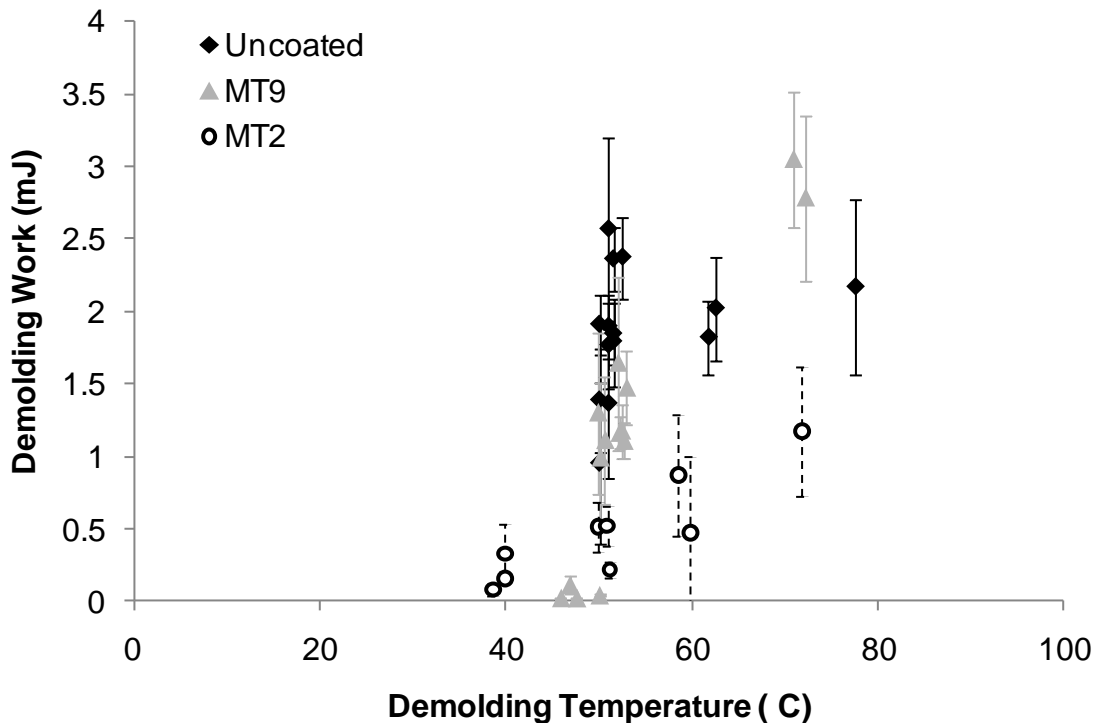
Figure 5.43 Plot of demolding work for three different molds at a range of temperatures. Demolding work shows a decreasing trend with temperature, indicating that these patterns are still within the adhesion-dominated regime at 50°C. Error bars represent the 95% confidence interval on the within-part mean based on the within-part variance.

Since the demolding tests were conducted within the adhesion-dominated regime, it is expected that the adhesion strength between PMMA and the mold coatings would affect the

demolding work. The adhesion strength was not measured, but it should be related to the work of adhesion between PMMA and the coatings, which can be estimated from surface energy measurements using Equation 2-9. The estimated works of adhesion for the coating materials are listed in Table 5.6. Surface energy components for the coatings were measured by Biswajit Saha from the contact angles with water and ethylene glycol following procedures described by him elsewhere [53], while the values for uncoated silicon are from Illie [140] and for PMMA are from Wu [104].

Table 5.6 Surface energy components and estimated work of adhesion with PMMA for coated silicon molds. Surface energy data for coatings is courtesy Biswajit Saha. Surface energy values for Silicon are from Illie [140] and for PMMA are from Wu [104].

Coating	Dispersive component	Polar component	Total surface energy	Work of Adhesion with PMMA
MT5	11.7	3.8	15.5	45.0
MT4	10.9	4.8	15.6	45.3
MT7	13.5	3.4	17.0	47.7
MT1	17.3	3.1	20.4	53.4
MT6	28.0	2.4	30.4	65.4
MT2	36.1	2.1	38.3	72.2
MT9	39.7	2.1	41.8	74.8
MT8	44.0	1.9	45.9	77.2
MT3	54.2	1.7	55.9	82.5
Silicon	19	16	35	73.1

The within-part mean demolding work for several experiments on these coated molds at 50°C is plotted against the estimated work of adhesion with PMMA in Figure 5.44. The demolding work for mold MT3 was anomalously low considering its high work of adhesion with PMMA, so this data has been left out of the plot. The correlation shown in the plot is significant, with a p-value of value of 2.9×10^{-7} (corresponding to a confidence of better than 99.99%). These results are consistent with the expectation that the demolding work in the adhesion-dominated regime would be related to the work of adhesion between the mold and part materials. These results could be made more firm if the actual adhesion strength between these mold coatings and PMMA is measured directly, such as by pull tests or peel tests (section 4.3), and if additional demolding experiments over a range of temperatures are conducted.
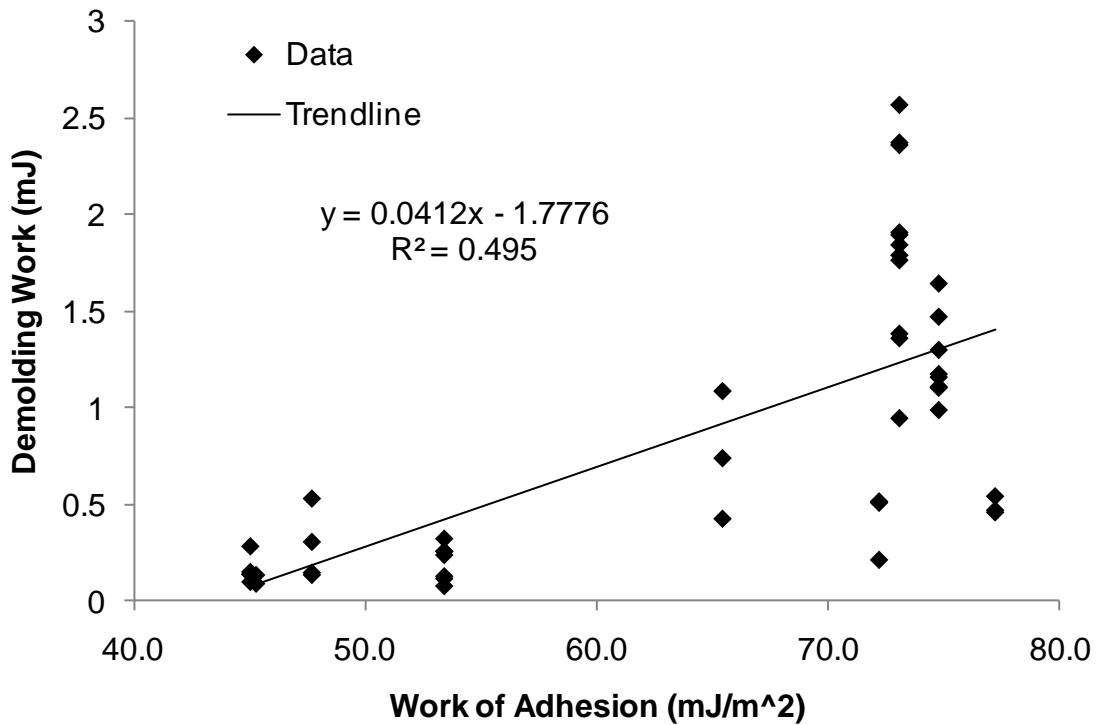
Figure 5.44 Demolding work at 50°C plotted against estimated work of adhesion for the coated molds. The correlation is significant, with a p-value of 2.9×10⁻⁷.

Demolding within the adhesion-dominated regime is not recommended. Indeed, because of strong adhesion and high demolding forces, uncoated silicon molds failed during some experiments (partly accounting for the large scatter in the demolding work for these molds). At the same time, the effect of low-adhesion coatings has been confirmed in these experiments, and the apparent reduction in the adhesion strength between the part and mold coating will likely reduce the temperature change required to overcome adhesion. The higher demolding temperatures that are made possible through the use of low-adhesion coatings can reduce the risk of feature distortion and increase production rates by reducing cooling time.

5.9.2   Effects of feature edge quality

The quality of the edges of the machined features on the molds has a very strong effect on the demolding work. This effect was first observed inadvertently, since some molds were produced with burrs on the edges of the features, which were not visible in visual inspections using a microscope. Figure 5.45 shows an example of a mold with burrs compared with a mold with good edge quality.

(a)

(b)
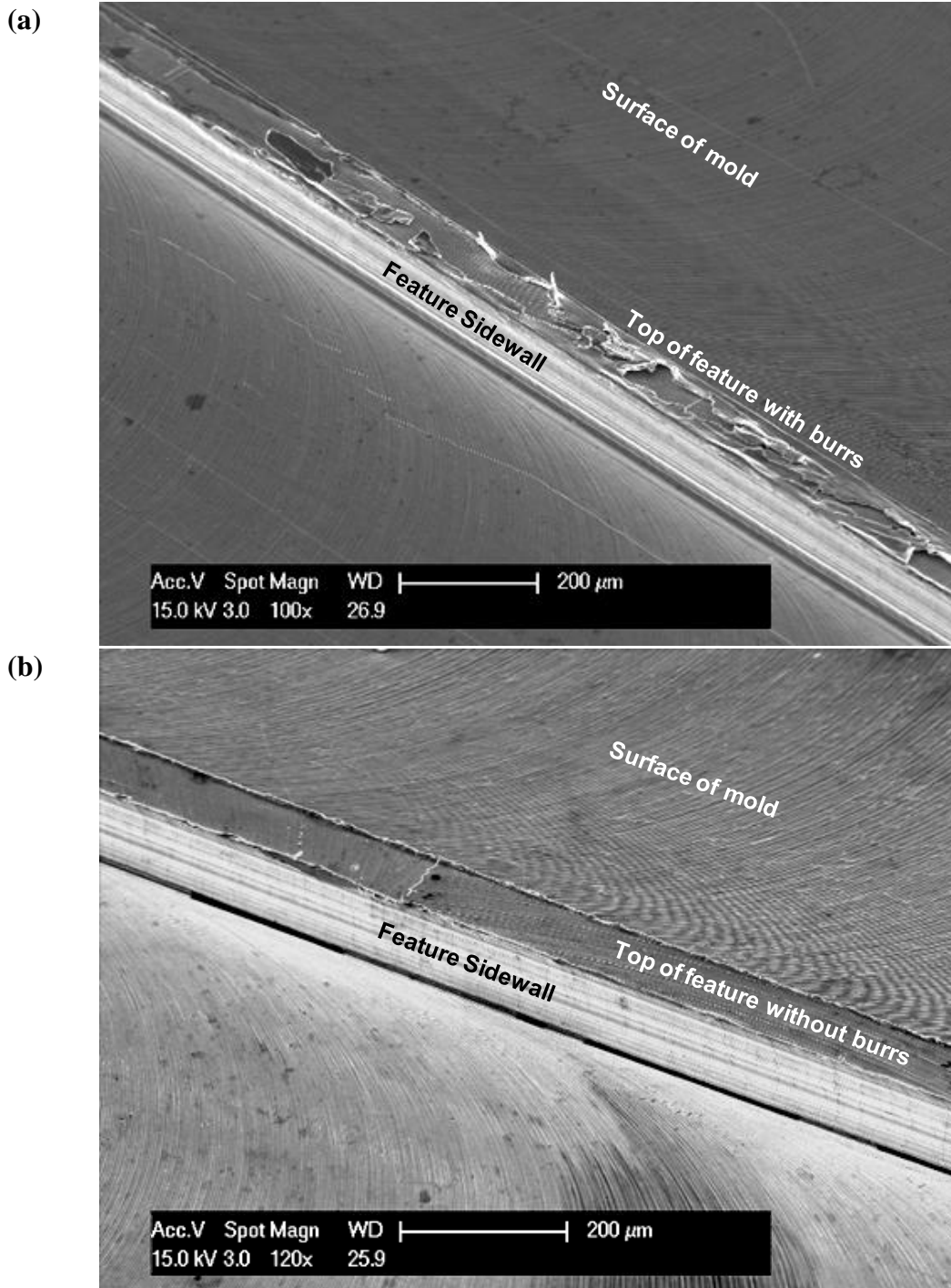
Figure 5.45 Scanning electron micrographs of machined aluminum molds with 100 µm high square channels (a) with burrs along the top edges, and (b) with good edge quality.

The effect of burrs on demolding work is quite dramatic, especially at low temperatures, as can be seen in Figure 5.46. This effect could be attributed to additional energy dissipated by deformation of the part material that is interlocked with the burr. The demolding work shows a

decreasing trend with temperature, possibly because the increased thermal stress at lower temperatures is helping to break the interlocked material free. At higher temperatures, the demolding work is not significantly different from the adhesion-dominated regime because the strength of the part material is much lower and the deformation component of the demolding work is small. In effect, the burrs on the mold features have added a deformation-dominated regime of demolding.
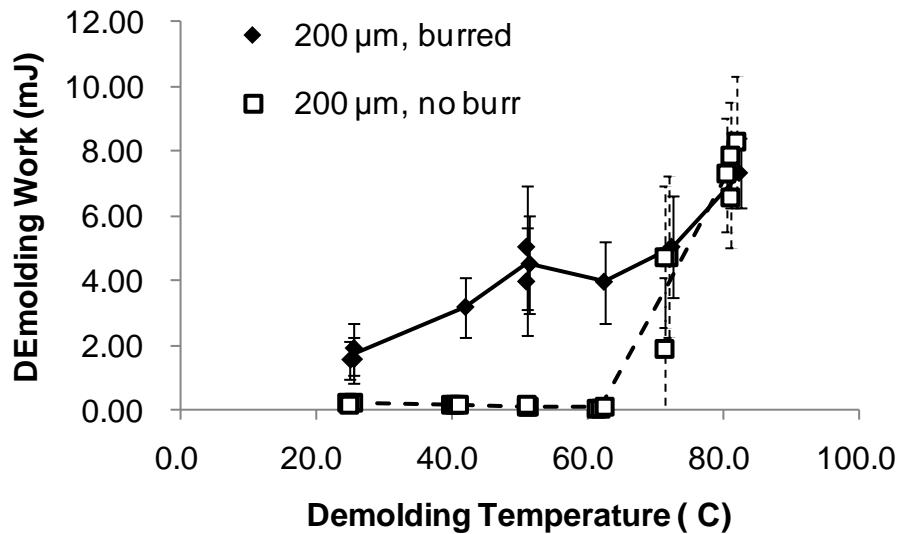
Figure 5.46 Demolding work at a range of temperatures for 200 μm deep channels embossed in PMMA. The channels with burrs have dramatically higher demolding work at low temperatures.

Close examination of the embossed features supports the idea that deformation is increasing the demolding work. As shown in Figure 5.47, the channel produced by the burred mold shows gouges and other evidence of deformation in it sidewall. This part also has a deep trench along the edge of the channel, corresponding to a tall burr on the mold. By comparison, the channel produced by the normal mold does not show evidence of deformation in the feature sidewall.

(a)

Channel sidewall showing gouging

Surface of part

Bottom of channel

Acc.V Spot Magn   Det WD |————————————| 20 μm
3.00 kV 4.0   1000x   SE   15.9

(b)

Surface of part

Channel sidewall

Bottom of channel

Acc.V Spot Magn   Det WD |————————————| 20 μm
3.00 kV 4.0   1200x   SE   14.1
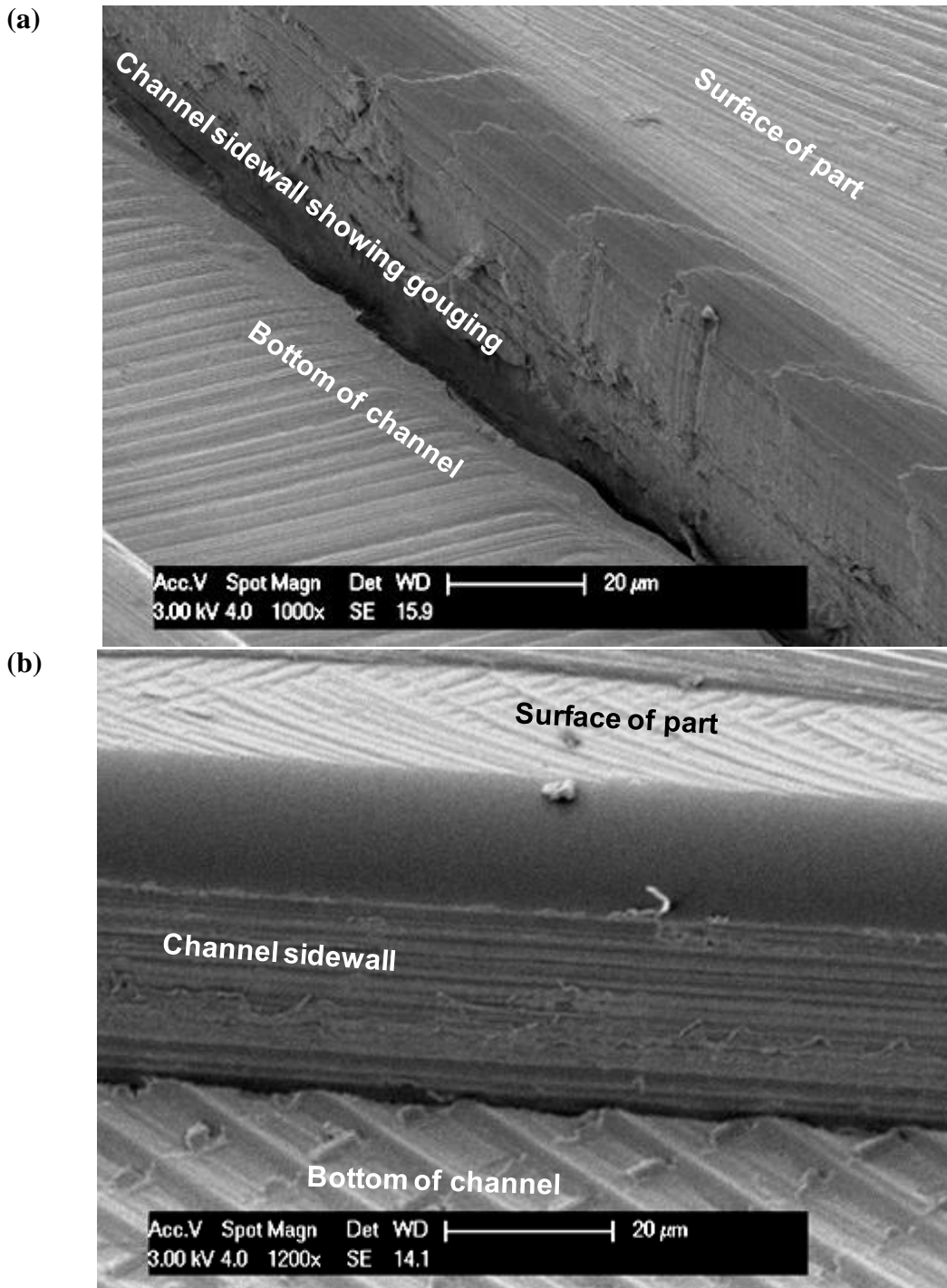
Figure 5.47 Scanning electron micrographs comparing of 50 μm deep channels embossed by molds (a) with burred features, and (b) with normal features. The burred mold produced gouges in the sidewall, and left a deep trench at the edge of the channel.

The effects of burrs on demolding, along with the observation that the stress in the mold

and part during demolding is always highest near the mold feature edge (see section 3.5 and

Figure 3.22), suggests that rounding or angling the edges of the features might reduce the demolding work. This hypothesis was tested by polishing a mold with 50 µm high channel features using jeweler's rouge with a felt wheel and a handheld grinding tool, and performing demolding tests on the polished mold. Polishing rounded the feature edges without significantly altering the height of the feature, as shown in Figure 5.48, which compares the cross sections of channels in parts embossed with these molds. The polished mold channel is somewhat less wide, possibly because of machining variation. The normal mold shows some small (<5 µm) burrs along the edges, similar to those in Figure 5.45b. A feature on the polished mold is shown in Figure 5.49.
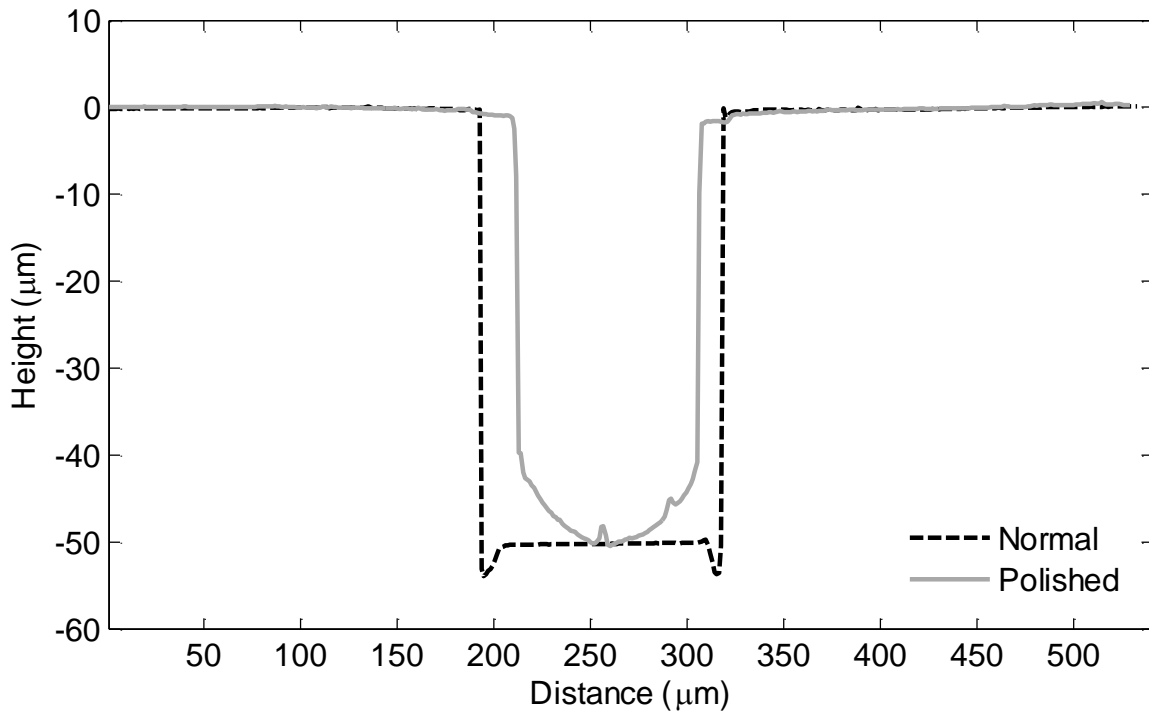
Figure 5.48 Comparison of the cross-section of channels embossed in PMMA using a normal mold and a polished mold. Polishing did not significantly reduce the channel's depth, so changes in demolding work can be attributed to the change in edge quality.

The demolding work for the polished mold is compared with that for the normal mold and a burred mold in Figure 5.50. Similar to the 200 µm deep channel pattern, the burred 50 µm deep channel has much higher demolding work, especially at lower temperatures. In contrast, the polished mold has lower demolding work at the temperatures tested. Recalling the cross-sections of mold features shown in Figure 5.48, the polished mold feature is the same height as the normal feature, but the vertical portion of its sidewall has been reduced by about 10 µm, or 20%.

The difference in demolding work for the two molds at 50°C is much greater, at 0.044 mJ for the polished mold vs. 0.112 mJ for the normal mold (a 60% reduction). One possible explanation for this difference is that the sloped corner of the feature actually promoted demolding, since during the final stages of demolding only this portion of the feature would be in contact and the contact load cause by the thermal stress would have a vertical component. It is also possible that polishing the mold reduced the effective friction coefficient. The polished mold also has much lower demolding work at high temperatures, where demolding is expected to be dominated by adhesion. Since it is known that surface roughness can affect apparent adhesion strength [100, 103, 109], it is possible that the polished mold has lower apparent adhesion to the part, which would reduce the demolding work in the adhesion regime and increase the optimal demolding temperature.
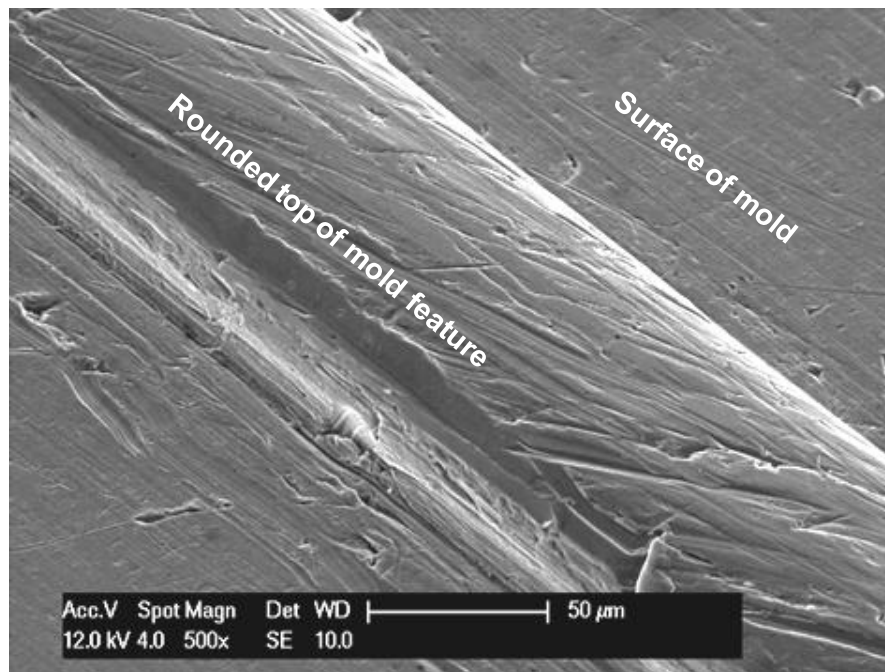
Figure 5.49 Scanning electron micrograph of a 50 μm high channel feature on the polished aluminum mold.

The effect of feature edge quality on the within-part mean demolding work is statistically significant, as shown by the box plot in Figure 5.51 and the ANOVA results in Table 5.7. From the results of these tests, it is clear that the characteristics of machine mold features are very important for demolding, and that mold treatments such as polishing can have beneficial effects.
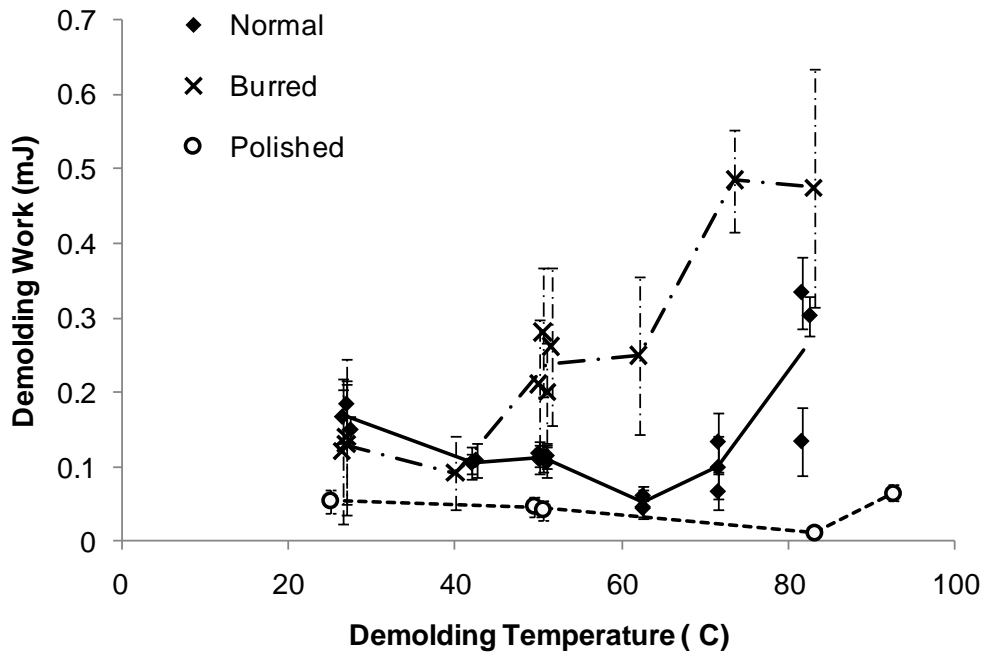
Figure 5.50 Comparison of demolding work for different mold edge qualities.
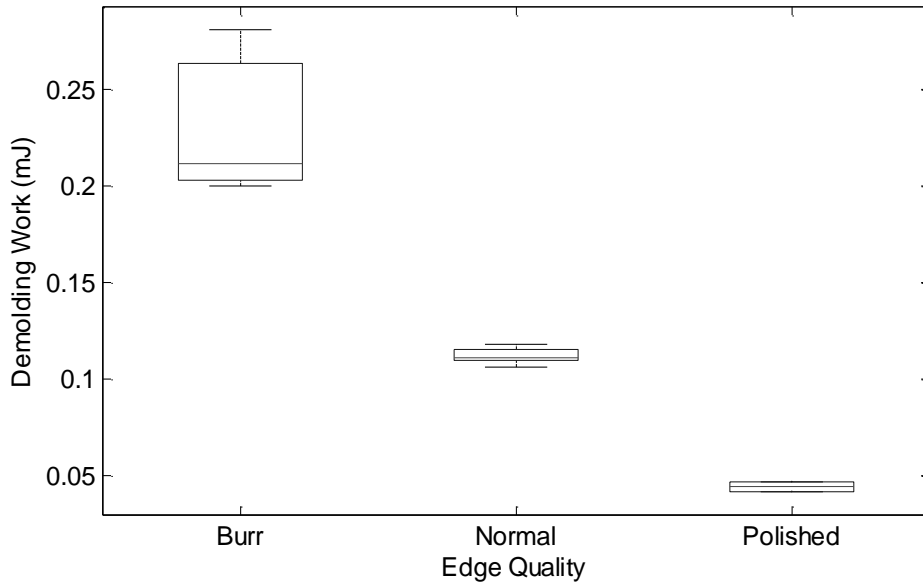
Figure 5.51 Box plot of within-part demolding work at 50°C for molds with different edge quality.

Table 5.7 Results of ANOVA for effect of edge quality on within-part mean demolding work at 50°C.

Source	Sum of Squares	Degrees of freedom	Mean Square	F statistic	P-value
Edges	4.66×10^{-2}	2	2.33×10^{-2}	41.7	1.30×10^{-4}
Error	3.92×10^{-3}	7	5.60×10^{-4}		
Total	5.05×10^{-2}	9			

6 Conclusions, applications, and future work

6.1 Summary

This thesis presents a study of demolding of hot embossed polymer microstructures—such as microfluidic channels—including a theory of demolding mechanics, finite element simulations of demolding, a demolding test method, and the results of demolding experiments. The basic theoretical approach has been validated through comparisons among theoretical models, finite element simulations, and demolding experiments using a standard test method developed in this work. These results have been generalized to provide useful guidelines for industrial application of hot embossing as well as other polymer micro-molding processes, especially with respect to selecting appropriate demolding conditions.

This work was motivated by the potential of microfluidic devices in medical diagnostics, high-throughput biomedical screening, and several other promising applications. To be economically successful, such devices must be manufactured in large numbers, at low cost, and with excellent quality. Polymer micro-molding processes, such as hot embossing, are the best candidates for manufacturing microfluidic devices to meet these volume, cost, and quality requirements. This work has aimed to facilitate the industrial application of hot embossing by improving the understanding of demolding.

6.1.1 Importance of demolding

All polymer micro-molding processes involve a demolding step in which the part is removed from the mold. Demolding-related defects are frequently observed, including localized distortion of features in parts, damage and wear of features on molds, and catastrophic failure of individual features or whole molds during demolding. Despite these problems, there does not seem to have been any comprehensive effort at developing an over-arching theory of demolding mechanics or at systematically characterizing demolding through experiments. Most research on demolding of polymer microstructures to date has taken the form of finite element studies of the forces and stresses in a small region near an individual feature, or of qualitative comparisons of

the quality of parts embossed with different molds, mold coatings, or demolded under different conditions. A small number of experimental studies have been undertaken, but these have not tested the effects of pattern geometry, and have involved only coarse changes in demolding temperature. The present work has aimed to address the need for a comprehensive approach to demolding, and well as the need to generalize research findings to produce useful guidance for industrial application.

6.1.2   Demolding mechanics and the demolding work

Destruction of the bond between the part and the mold is the goal of demolding. This bond is the result of the combined action of multiple mechanisms including surface-based adhesion and mechanical/frictional interaction of features. Through an analogy between demolding and interfacial fracture, the tools of fracture mechanics can be brought to bear in analyzing demolding. The broad mismatch in material properties between typical mold and part materials causes significant shear loads at the interface, especially as the demolding temperature is decreased. These shear loads cause mechanical interaction of the interlocked features. Thermal stress is a dominant phenomenon in demolding, both in degrading surface-based adhesion and in exacerbating frictional interaction of features. The combined effects of thermal stress, adhesion, and friction together constitute a theory of demolding mechanics that has been developed in the present work. This theory has produced testable predictions that have been compared with experimental observations.

In keeping with the analogy with fracture, the energy dissipated during demolding, or the demolding work, is proposed as a metric for evaluating demolding. Based on the theory of demolding mechanics developed in this work, it is expected that the demolding work will follow a decreasing trend with decreasing demolding temperature until frictional effects are stronger than adhesion effects, whereupon the demolding work will begin to increase. The transition between the two demolding regimes coincides with the minimal value of demolding work (defined herein as the optimal demolding temperature). It is expected that the demolding work will increase with increasing feature spacing and height, and will not depend on feature width. These predictions are largely confirmed by the experimental results.

6.1.3   Simulations of demolding

Complementing these analytical models, demolding has also been modeled using the finite element method. For practical computation times, a two-dimensional model of a small region of a part and mold is used, along with isotropic rate-independent elastic (and elastic-perfectly-plastic) material models with temperature-dependent properties. There is good general agreement between the finite element results and the analytical, lumped parameter models. Demolding simulations with frictional interaction between the part and mold predict a trend of increasing demolding work with decreasing temperature and increasing feature height. Simulations with adhesive interactions predict decreasing demolding work with decreasing temperature and increasing feature spacing. These two trends agree with those predicted by the analytical models, and agree with observed trends in experiments. Simulations using elastic-perfectly-plastic material models predict local deformations similar to those observed in experiments.

6.1.4   Development of a useful demolding test method

A test method has been developed to measure the demolding work. The test method combines an embossing step with a controlled demolding step, and involves a similar demolding process to those used in real situations. A controlled displacement is applied to the end of the part, and a crack between the mold and part is initiated at the edge of the mold and then propagated. A specialized demolding machine has been developed to implement the test method. The machine uses an Instron load frame for displacement and load control as well as measurement. The embossing molds are mounted to temperature-controlled platens in the load frame. The recorded load and displacement data is analyzed using methods similar to those developed for asymmetric cantilever fracture tests. The demolding work for individual features on the mold can be calculated from the data, and the average demolding work across features within a part is used to characterize demolding for that part. The resulting measure of demolding work has been found to be consistent across runs, and experimental variation is small enough that the effects of other parameters, such as demolding temperature and feature geometry, can generally be discriminated.

6.1.5   Findings from demolding experiments

The development of this test method enables experiments that can support or disprove the hypotheses on the mechanisms responsible for the demolding work and the effects of process parameters and feature geometry. Overall, the experimental results show good qualitative agreement with the proposed models and with finite element simulations based on these models in terms of the trends of demolding work with temperature and feature geometry. Theoretical estimates of the expected demolding work based on one dimensional analytical models and two-dimensional finite element models leave out potentially important effects, such as the influence of pattern density on adhesion degradation, the effects of transverse thermal stress, or the non-ideal constraint of the demolded portion of the part (treated as a built-in cantilever in the models), and rely on parameters such as the intrinsic adhesion and the friction coefficient between the part and the mold, which are not known precisely (and may also depend on temperature, surface roughness, humidity, etc.). Despite these shortcomings, the estimates of the theoretical models and the finite element simulations are of similar magnitude to the measured demolding works, indicating that un-modeled effects are most likely of lesser importance. The consistent agreement in terms of trends and effects between theory and experiment supports the validity of the basic theoretical approach, at least as a first effort. The experiments also provide insight into effects that cannot be captured in the one- and two-dimensional models and simulations, such as the effects of feature width, layout, and pattern density.

Defects associated with lower demolding temperatures similar to those observed by others have been studied. These defects, consisting of bulges on the outside of features, are caused by thermal stresses that result from thermal contraction mismatch between the mold and the part. The amount of distortion increases with decreasing demolding temperature, and outer features are distorted more severely, as expected from the sidewall force models developed earlier. The effect of pattern density, which is not entirely captured in the analytical models or finite element simulations, has been characterized. A dimensionless parameter combining local geometric measures, $\mathfrak{D}$, has been derived from the sidewall force model. This parameter is related to the temperature at which distortion is evident, and this relationship is consistent across the different mold patterns and part materials that have been tested.

The existence of a hypothetical optimal demolding temperature has been confirmed through demolding experiments over a range of temperatures. The trend of demolding work with

decreasing temperature (decreasing to an optimal value, and then increasing) agrees with the proposed model of adhesion that is degraded by thermal stress combined with Coulomb friction on feature sidewalls. The optimal temperature coincides with the transition between adhesion-dominated demolding to a friction-dominated regime. The temperature at which this transition is observed also shows a trend with the parameter $\mathfrak{D}$ that is consistent across the different mold patterns and part materials tested. The distortion temperature and the adhesion-to-friction transition together define the process window for demolding. This window is also related to $\mathfrak{D}$, and is consistent across the different patterns. The identification of the processing window, and the phenomena that define it, is a significant contribution of this work.

The effects of mold geometry, including feature spacing, height, width, and layout on the demolding work have also been studied. High experimental variation is characteristic of adhesion tests in general, and this variation limits the ability to make firm conclusions as to the quantitative effects of feature geometry on the precise value of the demolding work. At the same time, the observed trends are statistically significant and agree with the predictions of the models of demolding that have been proposed. These trends include a positive correlation between demolding work and feature spacing as well as feature height, and a lack of a correlation between demolding work and feature width. The layout of features, in terms of the distribution of feature width across the part, also does not have a significant effect.

The development of a useful and reliable test method, along with a metric by which demolding can be characterized (the demolding work), also enables the evaluation of measures that might mitigate demolding. An effect associated with anti-adhesive coatings on molds has been observed, in which the demolding work is positively correlated with the work of adhesion between the part material and the mold coating when demolding in the adhesion-dominated regime. While demolding under these conditions is not recommended, the observed reduction in adhesion strength through the use of low-adhesion coatings would reduce the temperature change required to degrade adhesion and enable higher demolding temperatures. An effect associated with feature edge quality has also been observed. Poor edge quality, such as the presence of burrs, cause gouges and other local defects, and this deformation dramatically increases the demolding work. Conversely, features with rounded edges exhibit reductions in demolding work, suggesting that polishing or other mold treatments can be used to mitigate demolding.

6.2 Application of findings

The goal that has animated this work is to facilitate the manufacturing of microfluidic chips and other polymer-based devices with micro-scale features. In particular, the findings of this work should be related to the issues that are important in manufacturing, namely: production rate, quality, cost, process flexibility, and environmental impact.

6.2.1 Demolding guidelines

Considering all the ways that a hot embossing machine might be configured, and the ways that parts and molds might be fixed in a machine, demolding will most often be accomplished by applying a force (or controlled displacement) to a small region of the part, initiating a crack between the part and mold, and propagating the crack until the part is fully demolded. The magnitudes of demolding work (and associated demolding toughness) observed in the current study suggest that the forces required in demolding are nearly always much lower than those required for embossing, and so are less likely to be driving factors in machine design or tool lifetime. However, there are circumstances where strong demolding forces or thermal stresses cause damage to the part or the mold.

To minimize demolding forces, the crack should be initiated near the edge of the part and, as much as feasible, remote from features. Initiating a crack with an ejector pin that is near the middle of the part (Figure 4.5) will require higher initial forces. Parts that are large in extent would benefit from multi-point demolding, where cracks are initiated as several locations (for instance, at all edges). Overly constraining the part, such as by firmly clamping its edges, will increase the stiffness of the part during demolding, which will increase demolding forces but also reduce the amount of displacement required to propagate the crack completely across the part. The high sticking force observed when the platens initially open corresponds to an extreme case of part constraint during demolding (see section 5.4.1). Ejector pins or strike plates located along the edges of the part would be very effective means of demolding.

6.2.2 Demolding process window

One of the most significant contributions of this thesis is the identification of the demolding process window and the factors that define its boundaries (shown in Figure 5.31 and repeated below). The relationship between feature distortion and adhesion degradation—which

form the lower and upper bounds of the demolding process window—and the mold geometry as characterized by the ratio $\mathfrak{D}$ provides a "rule of thumb" for selecting the appropriate demolding temperature for a given mold design.
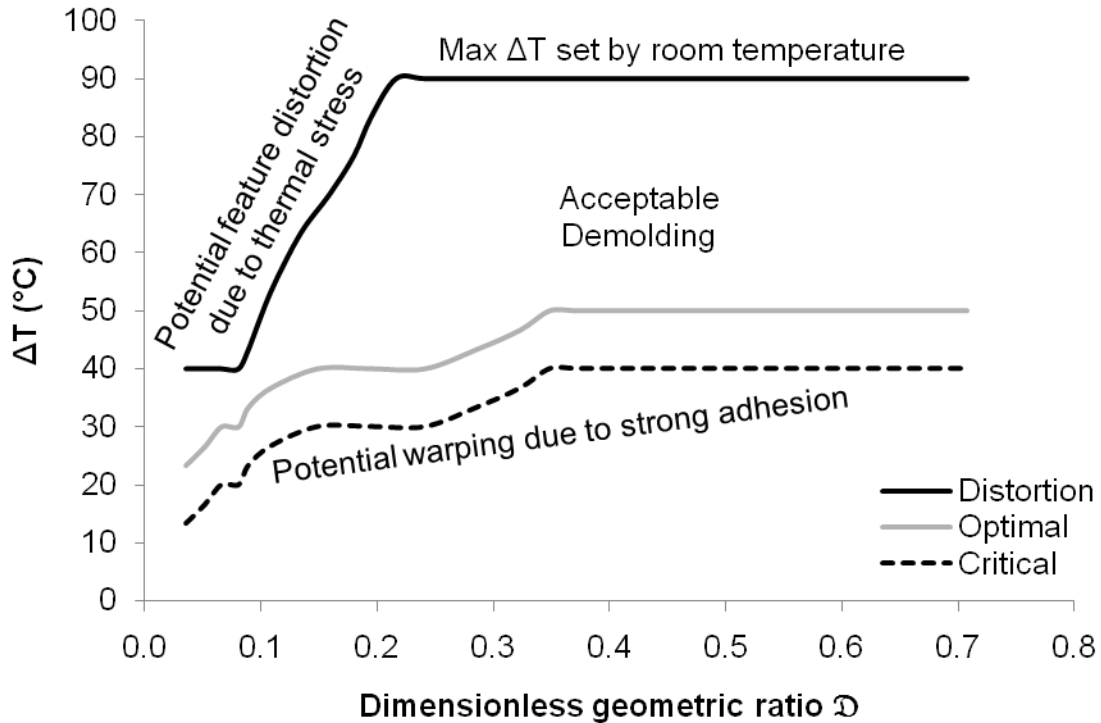
Figure 5.31 Demolding process window for PMMA on Aluminum molds based on experimental observations.

The processing window has been defined for PMMA and polycarbonate parts and aluminum molds based on experimental observations. When faced with a new material combination, the process window can be sketched out using the simple models developed in this work. Equation 5-6, along with knowledge of the part's material properties at T_g and below, can be used to estimate the distortion temperature. Similarly, Equation 2-33, along with the adhesion strength between the part and mold at the embossing temperature, can be used to estimate the temperature at which adhesion will be fully degraded, and thus the optimal demolding temperature for dense patterns. The adhesion strength can be characterized through pull tests with flat molds, as in section 5.4.1. Similarly, the optimal demolding temperature for lower values of $\mathfrak{D}$ could be found for a particular pair of part and mold materials using a small number of specially designed test patterns. If the demolding fixtures in a production embossing machine are instrumented to measure the demolding force, the optimal demolding temperature could be

located using a "hill-climbing" type algorithm by monitoring the change in demolding force after small perturbations in the demolding temperature. Such an approach, combined with cycle-to-cycle control techniques, would permit "adaptive" selection of the demolding temperature for novel patterns.

Whenever possible, a demolding temperature at or slightly below the optimal temperature is recommended. This temperature is optimal in the sense that the demolding work is at its lowest value. At the same time, this temperature is the highest temperature at which acceptable demolding (without warping or local distortion) is expected. Because heating and cooling time are usually the largest components of the hot embossing process cycle time, the highest possible demolding temperature is also optimal in terms of production rate. A smaller temperature swing between embossing and demolding also reduces the energy inputs required for heating and cooling, reducing both the operating cost and environmental impact.

Quality defects such as local feature distortion and part warping can be avoided by choosing an appropriate demolding temperature. Both of these defects are particularly problematic for bonding cover-plates to enclose microfluidic channels, since they may prevent the cover plate from sealing properly. Because the transition between adhesion-dominant and friction-dominant demolding is fairly abrupt and occurs just warmer than the optimal temperature, a compromise between production rate and quality may be required where temperature control is imperfect (or where material properties or mold adhesion are variable for some reason). Demolding somewhat below the optimum temperature will help ensure that demolding always occurs within the process window. Similarly, demolding near the distortion temperature is not recommended, since inadvertent excursions below this temperature may occur. The onset of local distortion is more gradual, and is initially limited to the outermost features, so the lower bound of the process window is somewhat "softer." Part quality is also related to cost and environmental impact, since avoiding defects reduces wasted material and energy associated with scrapped parts.

The relationship between the processing window, material properties, and mold geometry ($\mathfrak{D}$) also means that there is no single demolding temperature that is acceptable for every material and every mold design, so hot embossing equipment needs the capability to select a specific demolding temperature, and to accurately and repeatably cool the part and mold to that

temperature. Controllable demolding temperature is a requirement for a flexible embossing process.

6.2.3   Design for demolding

There are many cases where design decisions can have important ramifications for demolding. Considering the demolding process window (Figure 5.31), there is no demolding temperature that is acceptable for the whole range of mold patterns tested. The ratio $\mathcal{D}$, which helps define the processing window, only depends on local pattern dimensions and the part thickness. Thus, $\mathcal{D}$ can vary across a mold with a heterogeneous pattern. It is therefore very important that $\mathcal{D}$ not vary too much across a mold, or some areas will begin to suffer local distortion while other areas are still strongly adhered. Small regions with strong adhesion can also exacerbate part warping. Molds should be designs to maintain uniform $\mathcal{D}$ over their area. This can be accomplished by spreading out dense regions of features, or adding "dummy fill" to sparse regions.

Barrier features have also been proposed for reducing sidewall forces and preventing feature distortion [42, 49]. Such features can be effective, but they must be carefully designed. A barrier feature that is similar in size to the functional feature it protects may prevent distortion of the functional feature, but any distortion of the barrier feature could still produce a bulge that would hamper bonding. Furthermore, an improperly designed barrier feature could increase the local value of $\mathcal{D}$ too much and cause stronger local adhesion. The width and height of the barrier feature, and its separation from the feature it protects, should be chosen so that the local value of $\mathcal{D}$ is closely matched to the rest of the mold, and so that the barrier feature itself does not suffer distortion.

The feature pattern design itself can be included in any trade-offs between production rate and quality. For example, sparser patterns (lower $\mathcal{D}$) have higher optimal demolding temperatures which could allow faster production rates by minimizing heating and cooling time, but such patterns also have higher distortion temperatures and narrower demolding windows. In contrast, denser patterns (higher $\mathcal{D}$) have wider processing windows and are less sensitive to small variations in the local value of $\mathcal{D}$, but have lower critical temperatures and are more prone to warping at high temperatures, so will require longer cooling time to reach their demolding process window.

Pattern density will also enter into trade-offs involving part size, since making a given layout sparser will tend to increase the required part area, while denser patterns are more compact. Denser molds are likely to be more expensive to fabricate, while sparser patterns will require more material in the mold and part. Larger parts also require more heating and cooling power, greater embossing force, and better alignment in the embossing machine. While a denser pattern may require a cooler demolding temperature, the reduction in part size may result in an overall reduction in energy consumption, cycle time, and machine cost. Such trade-offs might favor smaller machines producing individual parts over larger machines producing arrays of parts that are then diced.

The orientation of a pattern with respect to the direction of thermal contraction determines which dimensions are used for the width and length in calculating $\mathcal{D}$, so feature orientation can also affect the process window. With respect to the center of contraction, "radial" features produce lower values of $\mathcal{D}$ than "circumferential" features. All else being equal, shorter features demold more easily, so low feature aspect ratios are preferred (in microfluidics, wide and shallow channels vs. narrow and deep channels).

The specific pattern layout and processing window can also guide decisions about mold treatments. For instance, low-adhesion coatings will tend to increase the optimal demolding temperature, and the cost of applying the coating to the mold can be weighed against the increase in production rate or the ability to demold at higher temperatures and avoid distortion in sparser regions of the pattern. Similarly, the costs and benefits of feature edge treatments such as polishing can be weighed in light of their effect on the demolding forces and the processing window. Mold coatings and feature edge treatments can be helpful for adjusting the demolding process window when changes to the pattern layout are not possible. Reducing the part thickness has the effect of globally increasing $\mathcal{D}$, so this could also be helpful in otherwise difficult demolding situations, since the demolding process window is generally wider for higher $\mathcal{D}$.

6.3 Applicability to other areas

Because of the common features among the several processes that are used to produce polymer-based devices with micro-scale functional features, many of the findings on demolding of hot embossed parts may be more broadly applicable.

6.3.1 Injection molding of polymer microstructures

Thermal stress and friction are the main mechanisms that are important in macroscopic demolding [73], and this is likely to be the case as well in injection molding of microstructures. Because the polymer is cooling from its melting temperature, thermal stress may even be more severe. At the same time, adhesion may be less important in injection molding because of the inherently greater ΔT involved. The test method presented here could be adapted for injection molding by, for instance, monitoring the load and displacement of ejector pins or other demolding fixtures.

In order to successfully replicate microstructures, it is sometime necessary to heat the mold above the polymer's glass transition temperature during injection, then cool the mold to the demolding temperature [12, 14]. Demolding temperature is a critical process parameter in injection molding just as in hot embossing. Local distortion defects are observed in injection molding (Figure 1.3), so local feature distortion will set the lower boundary of the demolding temperature in injection molding. If adhesion is too strong or is not uniform across the part, warping and other defects are also possible [43]. The geometric parameter $\mathcal{D}$ will be important in determining the demolding window for injection molding, and in evaluating designs to ensure uniform demolding characteristics. Unlike in hot embossing, the part is also subject to very high hydrostatic pressure during packing. Volumetric expansion when this pressure is released can partially offset thermal contraction, so this mechanism must also be considered in demolding, as found by Fu et al. [44].

6.3.2 Casting of curable liquid resins

Curable liquid resins are subject to shrinkage as they cure, and this process may play a similar role to thermal contraction in hot embossing, degrading adhesion and increasing sidewall loads. The work of Yeo et al. anticipates this effect [64, 65]. In fact, curing-related shrinkage is comparable in magnitude to thermal contraction in hot embossing. For instance, for PMMA cooling by 50°C, the total volumetric shrinkage is ~1.3%. Elastomers can resist more strain before yielding, so local feature distortion may be less important when casting PDMS and polyurethane. Less-elastic materials, however, may experience local distortion when shrinkage is severe, and $\mathcal{D}$ can be used to relate these effects to pattern geometry. Yeo et al. suggest that there may be an optimal cure time that is related to a certain amount of shrinkage, and this optimal

time may also be related to pattern geometry through $\mathcal{D}$. In any event, it is adviseable to reduce adhesion as much as is feasible, and to avoid unnecessary shrinkage while the part is adhered to the mold (by, e.g. demolding thermal-cure resins at the curing temperature rather than cooling to room temperature). The test method developed in the present work is not suitable for elastomer materials, but the peel tests employed by Yeo et al. have proved to be a useful method for studying demolding [45, 64].

6.3.3 Nanoimprinting

Nanoimprint lithography (NIL) is accomplished by two different means: thermal imprinting and UV imprinting. Thermal imprinting is, essentially, hot embossing on a polymer layer that is adhered to a substrate and is thin relative to the pattern geometry. UV imprinting is more similar to casting of curable liquid resins. In both cases, the thin layer adhered to the wafer is not able to contract (thermally or due to curing shrinkage) much in the in-plane directions, so more contraction will be evident in the out-of-plane (normal) direction. As in hot embossing (and casting), this strain will serve to degrade adhesion. In thermal NIL, there is evidence for an optimal demolding temperature [61-63]. So far no one has tested whether this temperature is related to pattern geometry, adhesion strength, material properties, or other factors, although there is evidence that the presence of features and their orientation does have an effect on the demolding toughness [60]. The theory of demolding mechanics presented in this work could inform future studies of demolding mechanics in NIL.

Because NIL stamps and substrates are rigid, the test method developed here can be of use in studying demolding for nanoimprint. Existing studies of demolding have adapted pull tests [61-63] and razor-blade tests [60], but have faced difficulties related to these methods' repeatability. Controlled double-cantilever tests were used by Houle et al. [59] to study the adhesion strength between imprint stamps and resist materials, and a similar approach can be used to test the effects of feature geometry. Since nanoimprinted features are often densely spaced and much smaller than microfluidic features, it will probably be necessary to monitor the crack length to calculate the demolding work. Another option could be to design test stamps with "stripes" of dens features, and use the drop in load as each stripe is demolded along with the area method employed in this work to determine the demolding work (or toughness).

6.4 Future work

Prior to the present work, the relationship between the difficulty of demolding and characteristics such as mold geometry, material properties, and processing parameters such as demolding temperature, was largely unknown. While qualitative observations had been made (often in the course of studies with other goals), there was no systematic effort at studying demolding and no over-arching theory relating demolding to these characteristics. As the first major effort in this area, this work was necessarily exploratory and in some ways limited in scope. Along with questions still unanswered, the answers provided by the present work have spawned many new questions. Some of these questions, along with the means by which they might be answered, are discussed below.

6.4.1 Demolding mechanics

The microscopic origins of friction have long been mysterious and controversial [141, 142], and the scale of microfluidic channels (and nanoimprint stamp features) is small enough that better knowledge of these micro-mechanisms, such as stick-slip transitions and nano-asperity adhesion and deformation, might contribute to the understanding of demolding. The present experiments could not distinguish effect of static and dynamic friction, but these mechanisms could be studied through probe-based microscopy of common microfluidic chip materials (PMMA, PC, COP, etc.) over a range of temperatures. Such studies could then inform more detailed simulations of demolding. The effects of surface roughness and release layers on the demolding mechanics could also provide further insight into the potential benefits of mitigation strategies such as polishing molds or applying low-friction coatings.

6.4.2 Finite element studies

Finite element simulations are easily adaptable to test the effect of different interaction models, material properties, and feature geometries. Finite element simulation of demolding of other materials, such as polycarbonate and cyclo-olefin polymers can provide further insight into their demolding characteristics. Mold material parameters can also be changed, for instance, to simulate the demolding characteristics of molds made from polymers. The effect of feature edge quality and draft angles could also be simulated.

In the modeling approach adopted here, adhesion and friction could not be combined in the same simulation. Alternative surface interaction formulations, such as user-defined interaction subroutines or cohesive surface elements could enable combined simulations of demolding.

This work relied on two-dimensional models of small regions of parts, so these simulations could not capture the effects of out-of-plane characteristics such as feature width. Three-dimensional and larger scale simulations would be useful in this regard.

The simulations presented here began with an existing channel in the part that replicated the mold feature. Others have developed thermo-mechanically coupled models of amorphous thermoplastics over a range of temperatures that can be implemented in finite element simulations of hot embossing and cooling [113, 143-145]. These simulations may be extended to include adhesion and friction, producing comprehensive embossing and demolding models. These comprehensive models could also be used to check for any effects of demolding rate.

6.4.3 Experiments

The test method that has been developed in the present work can be used to study a wide variety of additional factors that might impact demolding. Some interesting candidates for further study include other part materials (polystyrene, COP), other mold materials (brass, silicon, nickel, tool steel, polymers), and the many potentially helpful surface coatings (metal oxides & nitrides, fluorocarbons, self-assembled monolayers). The effects of feature treatments such as polishing and draft angles could be studies systematically.

All of the molds in the present work had orthogonally oriented features (parallel or perpendicular to the direction of crack extension). Non-orthogonal feature orientation, such as 30° or 45° would also be interesting to study. The projected width of a non-orthogonal feature could be used to calculate $\mathfrak{D}$, but this hypothesis needs experimental validation. Feature deformation and optimal demolding for very sparse ($\mathfrak{D}<0.02$) and very dense ($\mathfrak{D}>0.8$) patterns also merit further study.

The present experiments all used micro-machined aluminum molds, which had machining marks on their surface. The effect of mold surface roughness can be studied using the test methods developed here. Smooth molds, such as those produced by nickel electroforming,

217

may present slightly different demolding characteristics, since surface roughness is known to affect interfacial adhesion behavior.

Finally, hot embossing can be used to pattern both sides of the part, and even to produce through-holes [27]. In double-sided embossing, one side will be demolding in a manner similar to a pull test. The factors that affect which side is demolded first, the magnitude of the demolding force, and potential demolding defects such as warping and feature pull-out, should be studied.

References

[1] Whitesides, G. M., "The origins and the future of microfluidics," *Nature*, **442**(7101), pp. 368-373. 2006.

[2] Hansen, C. L., Skordalakes, E., Berger, J. M. and Quake, S. R., "A robust and scalable microfluidic metering method that allows protein crystal growth by free interface diffusion," *Proceedings of the National Academy of Sciences of the United States of America*, **99**(26), pp. 16531-16536. 2002.

[3] Yager, P., Edwards, T., Fu, E., Helton, K., Nelson, K., Tam, M. R. and Weigl, B. H., "Microfluidic diagnostic technologies for global public health," *Nature*, **442**(7101), pp. 412-418. 2006.

[4] Manz, A., Graber, N. and Widmer, H. M., "Miniaturized total chemical analysis systems: A novel concept for chemical sensing," *Sensors and Actuators B: Chemical*, **1**(1-6), pp. 244-248. 1990.

[5] Thorsen, T., Maerki, S. J. and Quake, S. R., "Microfluidic large-scale integration," *Science*, **298**(5593), pp. 580-4. 2002.

[6] Gravesen, P., Branebjerg, J. and Jensen, O. S., "Microfluidics-a review," *Journal of Micromechanics and Microengineering*, **3**(4), p. 168. 1993.

[7] Grodzinski, P., Liu, R. H., Chen, B., Blackwell, J., Liu, Y., Rhine, D., Smekal, T., Ganser, D., Romero, C., Yu, H., Chan, T. and Kroutchinina, N., "Development of plastic microfluidic devices for sample preparation," *Biomedical Microdevices*, **3**(4), pp. 275-83. 2001.

[8] Becker, H. and Locascio, L. E., "Polymer microfluidic devices," *Talanta*, **56**(2), pp. 267-287. 2002.

[9] Hupert, M. L., Witek, M. A., Wang, Y., Mitchell, M. W., Liu, Y., Bejat, Y., Nikitopoulos, D. E., Goettert, J., Murphy, M. C. and Soper, S. A., "Polymer-based microfluidic devices for biomedical applications," *Microfluidics, BioMEMS, and Medical Microsystems, Jan 27-29 2003,* pp. 52-64. 2003.

[10] Fiorini, G. S. and Chiu, D. T., "Disposable microfluidic devices: Fabrication, function, and application," *BioTechniques*, **38**(3), pp. 429-446. 2005.

[11] J. Cooper McDonald, D. C. D., Janelle R. Anderson, Daniel T. Chiu, Hongkai Wu, Olivier J. A. Schueller, George M. Whitesides,, "Fabrication of microfluidic systems in poly(dimethylsiloxane)," *Electrophoresis*, **21**(1), pp. 27-40. 2000.

[12] Piotter, V., Hanemann, T., Ruprecht, R. and Hausselt, J., "Injection molding and related techniques for fabrication of microstructures," *Microsystem Technologies*, **3**(3), pp. 129-133. 1997.

[13] Schift, H., David, C., Gabriel, M., Gobrecht, J., Heyderman, L. J., Kaiser, W., Koppel, S. and Scandella, L., "Nanoreplication in polymers using hot embossing and injection molding," *Microelectronic Engineering*, **53**(1), pp. 171-174. 2000.

[14] Huang, C. K., "Polymeric nanofeatures of 100 nm using injection moulding for replication," *Journal of Micromechanics and Microengineering*, **17**(8), p. 1518. 2007.

[15] Attia, U., Marson, S. and Alcock, J., "Micro-injection moulding of polymer microfluidic devices," *Microfluidics and Nanofluidics*, **7**(1), pp. 1-28. 2009.

[16] Becker, H. and Dietz, W., "Microfluidic devices for micro-TAS applications fabricated by polymer hot embossing," *Proceedings of the 1998 Conference on Microfluidic Devices and Systems, Sep 21-22 1998,* pp. 177-182. 1998.

[17] Lee, G.-B., Chen, S.-H., Huang, G.-R., Sung, W.-C. and Lin, Y.-H., "Microfabricated plastic chips by hot embossing methods and their applications for DNA separation and detection," *Sensors and Actuators, B: Chemical*, **75**(1-2), pp. 142-148. 2001.

[18] Heckele, M., Gerlach, A., Guber, A. and Schaller, T., "Large area polymer replication for microfluidic devices," *Design, Test, Integration, and Packaging of MEMS/MOEMS 2001, Apr 25-27 2001,* pp. 469-477. 2001.

[19] Gerlach, A., Knebel, G., Guber, A. E., Heckele, M., Herrmann, D., Muslija, A. and Schaller, T., "Microfabrication of single-use plastic microfluidic devices for high-throughput screening and DNA analysis," *Microsystem Technologies*, **7**(5-6), pp. 265-268. 2002.

[20] Heckele, M., "Hot embossing - A flexible and successful replication technology for polymer MEMS," *Microfluidics, BioMEMS, and Medical Microsystems II, Jan 26-27 2004,* pp. 108-117. 2004.

[21] Park, D. S.-W., Hupert, M. L., Witek, M. A., You, B. H., Datta, P., Guy, J., Lee, J.-B., Soper, S. A., Nikitopoulos, D. E. and Murphy, M. C., "A titer plate-based polymer microfluidic platform for high throughput nucleic acid purification," *Biomedical Microdevices*, **10**(1), pp. 21-33. 2008.

[22] Becker, H., "Mind the gap!," *Lab on a Chip*, **10**(3), pp. 271-3. 2010.

[23] Mazzeo, A. D., Dirckx, M. and Hardt, D. E., "Process selection for microfluidic device manufacturing," *Society of Plastics Engineers Annual Technical Conference: Plastics Encounter at ANTEC 2007, May 6-11 2007,* pp. 1997-2001. 2007.

[24] Mazzeo, A. D. and Hardt, D. E., "Towards the Manufacture of Micro and Nano Features with Curable Liquid Resins: Mold Materials and Part-to-part Dimensional Variation," *International Symposium on Nanomanufacturing*. 2008.

[25] Mazzeo, A., *Centrifugal Casting and Fast Curing of Polydimethylsiloxane (PDMS) for the Manufacture of Micro and Nano Featured Components*, Ph.D. thesis in Mechanical Engineering, Massachusetts Institute of Technology, Cambridge, MA. 2009.

[26] Kalpakjian, S., *Manufacturing Engineering and Technology*, Prentice Hall, Upper Saddle River, NJ. 2001.

[27] Mazzeo, A. D., Dirckx, M. and Hardt, D. E., "Single-step through-hole punching by hot embossing," *Society of Plastics Engineers Annual Technical Conference: Plastics Encounter at ANTEC 2007, May 6-11 2007,* pp. 2931-2935. 2007.

[28] Kim, D. S., Lee, H. S., Han, J., Lee, S. H., Ahn, C. H. and Kwon, T. H., "Collapse-free thermal bonding technique for large area microchambers in plastic lab-on-a-chip applications," *Microsystem Technologies*, **14**(2), pp. 179-184. 2008.

[29] Dirckx, M., Taylor, H. K., Mazzeo, A. D. and Hardt, D. E., "Tooling for Micro- and Nano-Imprinting and its Consequences for Manufacturing," *4th International Symposium on Nano-Manufacturing*. 2006.

[30] Dirckx, M. and Hardt, D., "A review of hot micro-embossing manufacturing process research," *International Conference on Micro-Manufacturing*. 2006.

[31] Becker, H., "It's the economy," *Lab on a Chip*, **9**(19), pp. 2759-62. 2009.

[32] Dirckx, M., *Design of a Fast Cycle Time Hot Micro-Embossing Machine*, M.S. thesis in Mechanical Engineering, Massachusetts Institute of Technology, Cambridge, MA. 2005.

[33] Kimerling, T. E., Liu, W., Kim, B. H. and Yao, D., "Rapid hot embossing of polymer microfeatures," *Microsystem Technologies*, **12**(8), pp. 730-735. 2006.

[34] Hale, M. R., *Development of a Low-Cost, Rapid-Cycle Hot Embossing System for Microscale Parts*, M.S. thesis in Mechanical Engineering, Massachusetts Institute of Technology, Cambridge, MA. 2009.

[35] Wang, X., Wang, L., Liu, C., Ma, L. and Luo, Y., "Automatic fabrication system for plastic microfluidic chips," *Proceedings of the 2004 International Symposium on Micro-NanoMechatronics and Human Science, 31 Oct.-3 Nov. 2004,* pp. 331-6 BN - 0 7803 8607 8. 2004.

[36] Hardt, D. E., Anthony, B. W. and Tor, S. B., "A teaching factory for polymer microfabrication - µFAC," *International Symposium on Nanomanufacturing*. 2008.

[37] Worgull, M. and Heckele, M., "New aspects of simulation in hot embossing," *Design, Test and Packaging Microsystem Technologies*, **10**(5), pp. 432-437. 2004.

[38] He, Y., Fu, J.-Z. and Chen, Z.-C., "Research on modeling of hot embossing polymeric microfluidic chip," *Zhejiang Daxue Xuebao (Gongxue Ban)/Journal of Zhejiang University (Engineering Science)*, **39**(12), pp. 1911-1914. 2005.

[39] Dirckx, M., Taylor, H. K. and Hardt, D. E., "High-temperature de-molding for cycle time reduction in hot embossing," *Society of Plastics Engineers Annual Technical Conference: Plastics Encounter at ANTEC 2007, May 6-11 2007,* pp. 2926-2930. 2007.

[40] Dirckx, M., Mazzeo, A. D. and Hardt, D. E., "Production of micro-molding tooling by hot embossing," *International Manufacturing Science and Engineering Conference*. 2007.

[41] Guo, Y., Liu, G., Zhu, X. and Tian, Y., "Analysis of the demolding forces during hot embossing," *Microsystem Technologies*, **13**(5-6), pp. 411-15. 2007.

[42] Guo, Y., Liu, G., Xiong, Y. and Tian, Y., "Study of the demolding process & implications for thermal stress, adhesion and friction control," *Journal of Micromechanics and Microengineering*, **17**(1), pp. 9-19. 2007.

[43] Michaeli, W. and Gartner, R., "New demolding concepts for the injection molding of microstructures," *Journal of Polymer Engineering*, **26**(2-4), pp. 161-177. 2006.

[44] Fu, G., Tor, S. B., Loh, N. H., Tay, B. Y. and Hardt, D. E., "The demolding of powder injection molded micro-structures: Analysis, simulation and experiment," *Journal of Micromechanics and Microengineering*, **18**(7), p. 075024. 2008.

[45] Yeo, L. P., Yan, Y. H., Lam, Y. C. and Chan-Park, M. B., "Design of experiment for optimization of plasma-polymerized octafluorocyclobutane coating on very high aspect ratio silicon molds," *Langmuir*, **22**(24), pp. 10196-10203. 2006.

[46] Taniguchi, J., Kawasaki, T., Tokano, Y., Kogo, Y., Miyamoto, L., Komuro, M., Hiroshima, H., Sakai, N. and Tada, K., "Measurement of adhesive force between mold and photocurable resin in imprint technology," *International Microprocesses and Nanotechnology Conference,* pp. 4194-7. 2002.

[47] Hirai, Y., Yoshida, S. and Takagi, N., "Defect analysis in thermal nanoimprint lithography," *Journal of Vacuum Science and Technology B: Microelectronics and Nanometer Structures*, **21**(6), pp. 2765-2770. 2003.

[48] Schift, H., "Nanoimprint lithography: an old story in modern times? A review," *Journal of Vacuum Science & Technology B (Microelectronics and Nanometer Structures)*, **26**(2), pp. 458-80. 2008.

[49] Worgull, M., Heckele, M. and Schomburg, W. K., "Large-scale hot embossing," *Microsystem Technologies*, **12**(1-2 SPEC ISS), pp. 110-115. 2005.

[50] Worgull, M., Kabanemi, K., Marcotte, J.-P., Hetu, J.-F. and Heckele, M., "Modeling of large area hot embossing," *Microsystem Technologies*, **14**(7), pp. 1061-1066. 2008.

[51] Tian, Y., Zhang, P., Liu, G. and Tian, X., "The lifetime comparison of Ni and Ni-PTFE moulding inserts with high aspect-ratio structure," *Microsystem Technologies*, **11**(4-5), pp. 261-264. 2005.

[52] Guo, Y., Liu, G., Xiong, Y., Wang, J., Huang, X. and Tian, Y., "Study of hot embossing using nickel and Ni-PTFE LIGA mold inserts," *Journal of Microelectromechanical Systems*, **16**(3), pp. 589-597. 2007.

[53] Saha, B., Liu, E., Tor, S. B., Khun, N. W., Hardt, D. E. and Chun, J. H., "Replication performance of Si-N-DLC-coated Si micro-molds in micro-hot-embossing," *Journal of Micromechanics and Microengineering*, **20**(4), p. 045007. 2010.

[54] Worgull, M., Hetu, J.-F., Kabanemi, K. K. and Heckele, M., "Hot embossing of microstructures: Characterization of friction during demolding," *Microsystem Technologies*, **14**(6), pp. 767-773. 2008.

[55] Pouzada, A. S., Ferreira, E. C. and Pontes, A. J., "Friction properties of moulding thermoplastics," *Polymer Testing*, **25**(8), pp. 1017-23. 2006.

[56] Hsueh, C.-H., Lee, S., Lin, H.-Y., Chen, L.-S. and Wang, W.-H., "Analyses of mechanical failure in nanoimprint processes," *Materials Science and Engineering A*, **433**(1-2), pp. 316-322. 2006.

[57] Song, Z., Choi, J., You, B. H., Lee, J. and Park, S., "Simulation study on stress and deformation of polymeric patterns during the demolding process in thermal imprint lithography," *Journal of Vacuum Science and Technology B: Microelectronics and Nanometer Structures*, **26**(2), pp. 598-605. 2008.

[58] Hiroshima, H., "Release force reduction in UV nanoimprint by mold orientation control and by gas environment," *Journal of Vacuum Science and Technology B: Microelectronics and Nanometer Structures*, **27**(6), pp. 2862-2865. 2009.

[59] Houle, F. A., Guyer, E., Miller, D. C. and Dauskardt, R., "Adhesion between template materials and UV-cured nanoimprint resists," *Journal of Vacuum Science and Technology B: Microelectronics and Nanometer Structures*, **25**(4), pp. 1179-1185. 2007.

[60] Landis, S., Chaix, N., Gourgon, C. and Leveder, T., "Quantitative characterizations of a nanopatterned bonded wafer: force determination for nanoimprint lithography stamp removal," *Nanotechnology*, **19**(12), pp. 125305-1. 2008.

[61] Trabadelo, V., Schift, H., Merino, S., Bellini, S. and Gobrecht, J., "Measurement of demolding forces in full wafer thermal nanoimprint," *Microelectronic Engineering*, **85**(5-6), pp. 907-909. 2008.

[62] Song, Z., *Study of demodling process in thermal imprint lithography via numerical simulaton and experimental approaches*, M.S. thesis in Mechanical Engineering, Louisiana State University, Baton Rouge, LA. 2007.

[63] Park, S., Song, Z., Brumfield, L., Amirsadeghi, A. and Lee, J., "Demolding temperature in thermal nanoimprint lithography," *Applied Physics A: Materials Science & Processing*, **97**(2), pp. 395-402. 2009.

[64] Yeo, L., *Optimization of Micro-patterning Processes*, Ph.D. thesis in Innovations in Manufacturing Systems and Technology in the Singapore-MIT Alliance, Nanyang Technological University, Singapore. 2007.

[65] Yeo, L., Joshi, S., Lam, Y., Chan-Park, M. and Hardt, D., "Numerical analyses of peel demolding for UV embossing of high aspect ratio micro-patterning," *Microsystem Technologies*, **15**(4), pp. 581-93. 2009.

[66] Wang, H., Kabanemi, K. K. and Salloum, G., "Prediction of ejection force and ejection-induced stress in injection molding of plastics," *Proceedings of the 1997 55th Annual Technical Conference, ANTEC. Part 3 (of 3), April 27, 1997 - May 2, 1997,* pp. 692-696. 1997.

[67] Wang, H., Kabanemi, K. K. and Salloum, G., "Numerical and experimental studies on the ejection of injection-molded plastic products," *Polymer Engineering and Science*, **40**(3), pp. 826-840. 2000.

[68] Pontes, A. J. and Pouzada, A. S., "Ejection force in tubular injection moldings. Part 1: effect of processing conditions," *Polymer Engineering and Science*, **44**(5), pp. 891-7. 2004.

[69] Pontes, A. J., Pouzada, A. S., Pantani, R. and Titomanlio, G., "Ejection force of tubular injection moldings. Part II: a prediction model," *Polymer Engineering and Science*, **45**(3), pp. 325-32. 2005.

[70] Bhagavatula, N., Michalski, D., Lilly, B. and Glozer, G., "Modelling and verification of ejection forces in thermoplastic injection moulding," *Modelling and Simulation in Materials Science and Engineering*, **12**(3), pp. S239-S254. 2004.

[71] Bataineh, O. M. and Klamecki, B. E., "Prediction of local part-mold and ejection force in injection molding," *Journal of Manufacturing Science and Engineering, Transactions of the ASME*, **127**(3), pp. 598-604. 2005.

[72] Michaeli, W. and Helbich, B., "Coupled FEA simulation of the demoulding procedure of injection moulded parts," *66th Annual Technical Conference of the Society of Plastics Engineers, Plastics Encounter at ANTEC 2008, May 4, 2008 - May 8, 2008,* pp. 369-373. 2008.

[73] Glanvill, A. B., *The plastics engineer's data book*, Industrial Press, Inc., New York, NY. 1973.

[74] Worgull, M., Heckele, M., Hetu, J. F. and Kabanemi, K. K., "Modeling and optimization of the hot embossing process for micro- and nanocomponent fabrication," *Journal of Microlithography, Microfabrication, and Microsystems*, **5**(1), pp. 011005-13. 2006.

[75] Oberg, E., *Machinery's Handbook*, Industrial Press, Inc., New York, NY. 2008.

[76] Personal communication with Becker, H., received by M. Dirckx, April 22, 2009

[77] Allen, K. W., "Theories of Adhesion" in *Handbook of Adhesion* John Wiley & Sons Ltd., Chichester, pp. 535-538. 2005.

[78] Jaszewski, R. W., Schift, H., Schnyder, B., Schneuwly, A. and Groning, P., "Deposition of anti-adhesive ultra-thin teflon-like films and their interaction with polymers during hot embossing," *Applied Surface Science*, **143**(1), pp. 301-308. 1999.

[79] Park, S., Schift, H., Padeste, C., Schnyder, B., Kotz, R. u. and Gobrecht, J., "Anti-adhesive layers on nickel stamps for nanoimprint lithography," *Micro and Nano Engineering 2003, Sep 22-25 2003,* pp. 196-201. 2004.

[80] Roos, N., Schulz, H., Fink, M., Pfeiffer, K., Osenberg, F. and Scheer, H.-C., "Performance of 4" wafer-scale thermoset working stamps in hot embossing lithography," *Proceedings of the SPIE - The International Society for Optical Engineering,* pp. 232-9. 2002.

[81] Wissen, M., Bogdanski, N., Jerzy, R., Berrada, Z. E., Fink, M., Reuther, F., Glinsner, T. and Scheer, H.-C., "Silanized polymeric working stamps for hot embossing lithography," *Proceedings of the SPIE - The International Society for Optical Engineering,* pp. 998-1005. 2004.

[82] Yan, Y. H., Chan-Park, M. B., Ching, W. C. and Yue, C. Y., "Interaction of anti-adhesive silicone films with UV embossing resin," *Applied Surface Science*, **249**(1-4), pp. 332-339. 2005.

[83] Chou, S. Y., Krauss, P. R., Zhang, W., Guo, L. and Zhuang, L., "Sub-10 nm imprint lithography and applications," *Journal of Vacuum Science & Technology B: Microelectronics Processing and Phenomena*, **15**(6), p. 2897. 1997.

[84] Esch, M. B., Kapur, S., Irizarry, G. and Genova, V., "Influence of master fabrication techniques on the characteristics of embossed microfluidic channels," *Lab on a Chip*, **3**(2), pp. 121-7. 2003.

[85] Gates, B. D. and Whitesides, G. M., "Replication of Vertical Features Smaller than 2 nm by Soft Lithography," *J. Am. Chem. Soc.*, **125**(49), pp. 14986-14987. 2003.

[86] Becker, H. and Heim, U., "Silicon as tool material for polymer hot embossing," *Proceedings of the 1999 12th IEEE International Conference on Micro Electro Mechanical Systems, MEMS, Jan 17-21 1999,* pp. 228-231. 1999.

[87] Chan-Park, M. B., Lam, Y. C., Laulia, P. and Joshi, S. C., "Simulation and investigation of factors affecting high aspect ratio UV embossing," *Langmuir*, **21**(5), pp. 2000-2007. 2005.

[88] Griffith, A. A., "The phenomena of rupture and flow in solids," *Philosophical Transactions of the Royal Society of London*, **A221**pp. 163-198. 1921.

[89] Griffith, A. A., "The theory of rupture," *Proceedings of the 1st International Congress of Applied Mechanics*, pp. 55-93. 1924.

[90] Gdoutos, E. E., *Fracture mechanics: an introduction*, Springer, Dordrecht, The Netherlands. 2005.

[91] Orowan, E., "Energy criteria of fracture," *Welding Journal*, **34**(3), pp. 157-160. 1955.

[92] Williams, J. G., "Introduction to linear elastic fracture mechanics" in *Fracture mechanics testing methods for polymers, adhesives and composites.* Elsevier Science Ltd., Kidlington, Oxford, UK, pp. 3-10. 2001.

[93] Irwin, G. R., "Fracture" in *Handbuch der Physik* Springer, pp. 551-590. 1958.

[94] Erdogan, F., "Fracture mechanics of interfaces" in *Damage and Failure of Interfaces* Balkema, Rotterdam, The Netherlands, pp. 3-36. 1997.

[95] Wu, S., *Polymer Interface and Adhesion*, Marcel Dekker, Inc., New York, NY. 1982.

[96] *Handbook of Adhesion*, Edited by Packham, D. E., John Wiley & Sons, West Sussex, England. 2005.

[97] Rice, J. R., "Elastic fracture mechanics concepts for interfacial cracks," **55**(1), pp. 98-103. 1988.

[98] Hutchinson, J. W., Mear, M. E. and Rice, J. R., "Crack paralleling an interface between dissimilar materials," *Transactions of the ASME. Journal of Applied Mechanics*, **54**(4), pp. 828-32. 1987.

[99] Shih, C. F., "Cracks on bimaterial interfaces: elasticity and plasticity aspects," *Joint Japan-USA Seminar on Advanced Materials for Severe Service Applications,* pp. 77-90. 1991.

[100] Evans, A. G., Ruhle, M., Dalgleish, B. J. and Charalambides, P. G., "The fracture energy of bimaterial interfaces," *Symposium on Interface Science and Engineering,* pp. 2419-29. 1990.

[101] Liechti, K. M. and Chai, Y. S., "Asymmetric shielding in interfacial fracture under in-plane shear," *Transactions of the ASME. Journal of Applied Mechanics*, **59**(2), pp. 295-304. 1992.

[102] Liang, Y.-M. and Liechti, K. M., "Toughening mechanisms in mixed-mode interfacial fracture," *International Journal of Solids and Structures*, **32**(6-7), pp. 957-78. 1995.

[103] Evans, A. G. and Hutchinson, J. W., "Effects of non-planarity on the mixed mode fracture resistance of bimaterial interfaces," *Acta Metallurgica*, **37**(3), pp. 909-16. 1989.

[104] Wu, S., "Surface and Interfacial Tensions of Polymers, Oligomers, Plasticizers, and Organic Pigments" in *Polymer Handbook* John Wiley & Sons, New York, pp. 521-540. 2005.

[105] Ames, N. M., *A thermo-mechanical finite deformation theory of plasticity for amorphous polymers : application to micro-hot-embossing of poly(methyl methacrylate)*, Ph.D. thesis in Mechanical Engineering, Massachusetts Institute of Technology, Cambridge, MA. 2007.

[106] Kendall, K., "Shrinkage and peel strength of adhesive joints," *Journal of Physics D: Applied Physics*, **6**(15), pp. 1782-1787. 1973.

[107] Cannon, R. M., Fisher, R. M. and Evans, A. G., "Decohesion of thin films from ceramic substrates," *Thin Films - Interfaces and Phenomena. Part of the Fall 1985 Meeting of the Materials Research Society, 2-6 Dec. 1985,* pp. 799-804. 1986.

[108] Suo, Z. and Hutchinson, J. W., "Interface crack between two elastic layers," *International Journal of Fracture*, **43**(1), pp. 1-18. 1990.

[109] Cao, H. C. and Evans, A. G., "Experimental study of the fracture resistance of bimaterial interfaces," *Mechanics of Materials*, **7**(4), pp. 295-304. 1989.

[110] Johnson, K. L., *Contact Mechanics*, Cambridge University Press, Cambridge, UK. 1985.

[111] Bathe, K.-J., *Finite Element Procedures*, Prentice Hall, Upper Saddle River, NJ. 1996.

[112] *ABAQUS Documentation (version 6.8)*, Dassault Systèmes Simulia Corp., Providence, RI, USA. 2008.

[113] Srivastava, V., Chester, S. A., Ames, N. M. and Anand, L., "A thermo-mechanically-coupled large-deformation theory for amorphous polymers in a temperature range which spans their glass transition," *International Journal of Plasticity*, In Press. 2010.

[114] Wunderlich, W., "Physical Constants of Poly(methyl methacrylate)" in *Polymer Handbook* John Wiley & Sons, New York, pp. 87-89. 2005.

[115] Mittal, K. L., "Adhesion Measurement of Films and Coatings: A Commentary" in *Adhesion Measurement of Films and Coatings* VSP, Utrecht, The Netherlands, pp. 1-13. 1995.

[116] Lacombe, R., *Adhesion Measurement Methods: Theory and Practice*, Taylor & Francis Group, Boca Raton, FL. 2006.

[117] Vallin, O., Jonsson, K. and Lindberg, U., "Adhesion quantification methods for wafer bonding," *Materials Science & Engineering R-Reports*, **50**(4-5), pp. 109-165. 2005.

[118] Brown, S. D., "Adherence Failure and Measurement: Some Troubling Questions" in *Adhesion Measurement of Films and Coatings* VSP, Utrecht, The Netherlands, pp. 15-39. 1995.

[119] Packham, D. E., "Tensile tests" in *Handbook of Adhesion* John Wiley & Sons, Inc., Chichester, West Sussex, England, pp. 529-531. 2005.

[120] Yeo, L. P., Lam, Y. C., Chan-Park, M. B., Joshi, S. C. and Hardt, D. E., "Demolding of high aspect ratio polymeric micro-patterning," *International Journal of Nanoscience*, **4**(4), pp. 543-549. 2005.

[121] Lai, Y.-H. and Dillard, D. A., "A study of the fracture efficiency parameter of blister tests of films and coatings" in *Adhesion Measurement of Films and Coatings* VSP, Utrecht, The Netherlands, pp. 231-247. 1995.

[122] Kendale, A. M., *Automation of Soft Lithographic Microcontact Printing*, M.S. thesis in Mechanical Engineering, Massachusetts Institute of Technology, Cambridge, MA. 2002.

[123] Kendale, A. M. and Trumper, D. L., *Microcontact Printing*. U.S. Patent 7,117,790 B2. 2006.

[124] Maszara, W. P., Goetz, G., Caviglia, A. and McKitterick, J. B., "Bonding of silicon wafers for silicon-on-insulator," *Journal of Applied Physics*, **64**(10), pp. 4943-4950. 1988.

[125] Bennati, S., Colleluori, M., Corigliano, D. and Valvo, P. S., "An enhanced beam-theory model of the asymmetric double cantilever beam (ADCB) test for composite laminates," *Experimental Techniques and Design in Composite Materials (ETDCM8) with Regular Papers Composites Science and Technology*, **69**(11-12), pp. 1735-1745. 2009.

[126] Xiao, F., Hui, C.-Y. and Kramer, E. J., "Analysis of a mixed mode fracture specimen: the asymmetric double cantilever beam," *Journal of Materials Science*, **28**(20), pp. 5620-9. 1993.

[127] Bascom, W. D. and Bitner, J. L., "A fracture approach to thick film adhesion measurements," *Journal of Materials Science*, **12**(7), pp. 1401-1410. 1977.

[128] Brown, H. R., "Mixed-mode effects on the toughness of polymer interfaces," *Journal of Materials Science*, **25**(6), pp. 2791-2794. 1990.

[129] Gillis, P. P. and Gilman, J. J., "Double-cantilever cleavage mode of crack propagation," *Journal of Applied Physics*, **35**(3), pp. 647-658. 1964.

[130] Srawley, J. E. and Gross, B., "Stress Intensity Factors for Crackline-Loaded Edge-Crack Specimens," *Materials Research and Standards*, **7**pp. 155-162. 1967.

[131] Kanninen, M. F., "An augmented double cantilever beam model for studying crack propagation and arrest," *International Journal of Fracture*, **9**(1), pp. 83-92. 1973.

[132] Wang, Q., *Process Window Characterization and Process Variation Identification of Micro Embossing Process*, M.S. thesis in Mechanical Engineering, Massachusetts Institute of Technology, Cambridge, MA. 2006.

[133] Hashemi, S., Kinloch, A. J. and Williams, J. G., "Corrections needed in double-cantilever beam tests for assessing the interlaminar failure of fibre-composites," *Journal of Materials Science Letters*, **8**(2), pp. 125-9. 1989.

[134] Yang, F. and Li, J. C. M., "Adhesion of a Rigid Punch to an Incompressible Elastic Film," *Langmuir*, **17**(21), pp. 6524-6529. 2001.

[135] Spiegel, M. R., Schiller, J. J. and Srinivasan, R. A., *Probability and Statistics*, McGraw Hill, New York, NY, USA. 2009.

[136] Gao, J. X., Yeo, L. P., Chan-Park, M. B., Miao, J. M., Yan, Y. H., Sun, J. B., Lam, Y. C. and Yue, C. Y., "Antistick postpassivation of high-aspect ratio silicon molds fabricated by deep-reactive ion etching," *Journal of Microelectromechanical Systems*, **15**(1), pp. 84-93. 2006.

227

[137] Zhang, T., Kobrin, B., Wanebo, M., Nowak, R., Yi, R., Chinn, J., Bender, M., Fuchs, A. and Otto, M., "Vapor deposited release layers for nanoimprint lithography," *Emerging Lithographic Technologies X, Jan 21-23 2006,* p. 615117. 2006.

[138] Van Stappen, M., Vandierendonck, K., Mol, C., Beeckman, E. and De Clercq, E., "Practice vs. laboratory tests for plastic injection moulding," *Surface and Coatings Technology*, **142-144** pp. 143-145. 2001.

[139] Charmeau, J.-Y., Chailly, M., Gilbert, V. and Bereaux, Y., "Influence of mold surface coatings in injection molding. Application to the ejection stage," *International Journal of Material Forming*, **1**(SUPPL. 1), pp. 699-702. 2008.

[140] Ilie, M., Marculescu, B., Moldovan, N., Nastase, N. and Olteanu, M., "Adhesion between PMMA mask layer and silicon wafer in KOH aqueous solution," *Proceedings of the 1998 Conference on Materials and Device Characterization in Micromachining, Sep 21-22 1998,* pp. 422-430. 1998.

[141] Rabinowicz, E., *Friction and Wear of Materials*, John Wiley and Sons, Inc., New York, NY, USA. 1965.

[142] Suh, N. P., *Tribophysics*, Prentice-Hall, Inc., Englewood Cliffs, NJ, USA. 1986.

[143] Srivastava, V. and Anand, L., "On modeling the mechanical behavior of amorphous polymers for the micro-hot-embossing of microfluidic devices," *2008 ASME International Mechanical Engineering Congress and Exposition, IMECE 2008, October 31, 2008 - November 6, 2008,* pp. 113-120. 2009.

[144] Anand, L., Ames, N. M., Srivastava, V. and Chester, S. A., "A thermo-mechanically coupled theory for large deformations of amorphous polymers. Part I: formulation," *International Journal of Plasticity*, **25**(8), pp. 1474-1494. 2009.

[145] Ames, N. M., Srivastava, V., Chester, S. A. and Anand, L., "A thermo-mechanically coupled theory for large deformations of amorphous polymers. Part II: applications," *International Journal of Plasticity*, **25**(8), pp. 1495-539. 2009.

[146] Schrader, D., "Physical Constants of Poly(styrene)" in *Polymer Handbood* John Wiley & Sons, New York, pp. 91-97. 2005.

[147] *Zeonor Typical Properties*, Zeon Chemicals, Accessed 2007, http://www.zeonchemicals.com/zeonor.aspx#docs

[148] Personal communication with Grau, A., Applications Engineer at Zeon Chemicals, received by M. Dirckx, March 26, 2007

[149] *Zeonex 690R Typical Properties*, Zeon Chemicals, Accessed 2007, http://www.zeonchemicals.com/zeonex.aspx#docs

[150] Delassus, P. T. and Whiteman, N. F., "Physical and Mechanical Properties of Some Important Polymers" in *Polymer Handbook* John Wiley & Sons, New York, pp. 159-169. 2005.

[151] Greenwood, J. C., "Silicon in mechanical sensors," *Journal of Physics E: Scientific Instruments*, **21**(12), pp. 1114-1128. 1988.

[152] Fritz, T., Griepentrog, M., Mokwa, W. and Schnakenberg, U., "Determination of Young's modulus of electroplated nickel," *Electrochimica Acta*, **48**(20-22), pp. 3029-3035. 2003.

[153] Chan-Park, M. B., Gao, J. and Koo, A. H. L., "Surface characterization of nickel alloy plasma-treated by O2/CF4 mixture," *Journal of Adhesion Science and Technology*, **17**(15), pp. 1979-2004. 2003.

[154] Kaufman, J. G., *Aluminum Alloy Database*, Accessed May, 2010. http://knovel.com/web/portal/browse/display?_EXT_KNOVEL_DISPLAY_bookid=844 &VerticalID=0

[155] Salou, M., Yamazaki, S., Nishimiya, N. and Tsutsumi, K., "Wettability characteristics of treated aluminum surfaces," *Colloids and Surfaces A: Physicochemical and Engineering Aspects*, **139**(3), pp. 299-310. 1998.

Appendix

A Material Properties

A.1   Representative properties of selected materials

Material	Tg °C	Deflection Temp. °C (1.8MPa)	E GPa (25°C)	CTE μm/m°C (25°C)	Surface Energy J/m^2×10^{-3} (25°C)		References
					Polar	Disp.	
PS	90	83	3.2	80	6.7	33	[104, 146]
COP1	100	99	2.1	70	0	32	[147, 148]
PMMA	110	86	3.1	73	11.4	29.3	[104, 105, 114]
COP2	136	136	2.35	70	0	32	[148, 149]
PC	150	132	2.48	70	10.6	32.3	[104, 150]
Silicon	-	-	130*	2.5	19	16	[140, 151]
Nickel	-	-	205	13	0.28	44	[152, 153]
Aluminum	-	-	70	23	45	5	[154, 155]

COP1=Zeonor 1060R COP2=Zeonex 690R *<100> crystal plane

A.2   Material properties used in finite element simulations

Mold material models:

Material	Elastic Modulus (MPa)	Poisson's Ratio	Yield Stress (MPa)	Linear CTE
Aluminum	70.0	0.33	-	2.4E-05
Silicon	130.0	0.33	-	2.5E-06

PMMA part material model listed on following page.

Temperature (°C)	Elastic Modulus (MPa)	Poisson's Ratio	Yield Stress (MPa)	Linear CTE	Temperature (°C)	Elastic Modulus (MPa)	Poisson's Ratio	Yield Stress (MPa)	Linear CTE
25	3.10E+03	0.350	1.11E+02	8.40E-05	88	1.39E+03	0.350	3.37E+01	8.40E-05
26	3.07E+03	0.350	1.10E+02	8.40E-05	89	1.37E+03	0.350	3.25E+01	8.40E-05
27	3.04E+03	0.350	1.09E+02	8.40E-05	90	1.34E+03	0.350	3.13E+01	8.40E-05
28	3.01E+03	0.350	1.08E+02	8.40E-05	91	1.31E+03	0.350	3.01E+01	8.40E-05
29	2.99E+03	0.350	1.06E+02	8.40E-05	92	1.29E+03	0.350	2.89E+01	8.40E-05
30	2.96E+03	0.350	1.05E+02	8.40E-05	93	1.26E+03	0.350	2.77E+01	8.40E-05
31	2.93E+03	0.350	1.04E+02	8.40E-05	94	1.23E+03	0.350	2.65E+01	8.40E-05
32	2.91E+03	0.350	1.03E+02	8.40E-05	95	1.20E+03	0.350	2.53E+01	8.40E-05
33	2.88E+03	0.350	1.01E+02	8.40E-05	96	1.18E+03	0.350	2.41E+01	8.40E-05
34	2.85E+03	0.350	1.00E+02	8.40E-05	97	1.15E+03	0.350	2.29E+01	8.40E-05
35	2.83E+03	0.350	9.89E+01	8.40E-05	98	1.12E+03	0.350	2.17E+01	8.40E-05
36	2.80E+03	0.350	9.76E+01	8.40E-05	99	1.09E+03	0.350	2.05E+01	8.40E-05
37	2.77E+03	0.350	9.64E+01	8.40E-05	100	1.06E+03	0.350	1.93E+01	8.40E-05
38	2.74E+03	0.350	9.51E+01	8.40E-05	101	1.03E+03	0.351	1.81E+01	8.40E-05
39	2.72E+03	0.350	9.39E+01	8.40E-05	102	1.00E+03	0.351	1.69E+01	8.40E-05
40	2.69E+03	0.350	9.26E+01	8.40E-05	103	9.66E+02	0.352	1.57E+01	8.40E-05
41	2.66E+03	0.350	9.14E+01	8.40E-05	104	9.24E+02	0.353	1.45E+01	8.41E-05
42	2.64E+03	0.350	9.01E+01	8.40E-05	105	8.75E+02	0.356	1.33E+01	8.41E-05
43	2.61E+03	0.350	8.89E+01	8.40E-05	106	8.13E+02	0.361	1.21E+01	8.42E-05
44	2.58E+03	0.350	8.76E+01	8.40E-05	107	7.36E+02	0.369	1.10E+01	8.43E-05
45	2.56E+03	0.350	8.64E+01	8.40E-05	108	6.40E+02	0.381	9.76E+00	8.45E-05
46	2.53E+03	0.350	8.52E+01	8.40E-05	109	5.26E+02	0.399	8.57E+00	8.49E-05
47	2.50E+03	0.350	8.39E+01	8.40E-05	110	4.02E+02	0.420	7.38E+00	8.53E-05
48	2.47E+03	0.350	8.27E+01	8.40E-05	111	3.05E+02	0.441	3.55E+00	8.59E-05
49	2.45E+03	0.350	8.14E+01	8.40E-05	112	2.18E+02	0.459	2.48E+00	8.67E-05
50	2.42E+03	0.350	8.02E+01	8.40E-05	113	1.49E+02	0.471	1.80E+00	8.74E-05
51	2.39E+03	0.350	7.90E+01	8.40E-05	114	9.89E+01	0.479	1.34E+00	8.83E-05
52	2.37E+03	0.350	7.77E+01	8.40E-05	115	6.44E+01	0.484	1.03E+00	8.91E-05
53	2.34E+03	0.350	7.65E+01	8.40E-05	116	4.18E+01	0.487	8.09E-01	9.00E-05
54	2.31E+03	0.350	7.53E+01	8.40E-05	117	2.73E+01	0.488	6.48E-01	9.08E-05
55	2.29E+03	0.350	7.40E+01	8.40E-05	118	1.83E+01	0.489	5.27E-01	9.16E-05
56	2.26E+03	0.350	7.28E+01	8.40E-05	119	1.27E+01	0.490	4.36E-01	9.25E-05
57	2.23E+03	0.350	7.16E+01	8.40E-05	120	9.33E+00	0.490	3.66E-01	9.33E-05
58	2.20E+03	0.350	7.03E+01	8.40E-05	121	7.24E+00	0.490	3.10E-01	9.41E-05
59	2.18E+03	0.350	6.91E+01	8.40E-05	122	5.97E+00	0.490	2.66E-01	9.49E-05
60	2.15E+03	0.350	6.79E+01	8.40E-05	123	5.19E+00	0.490	2.30E-01	9.56E-05
61	2.12E+03	0.350	6.66E+01	8.40E-05	124	4.73E+00	0.490	2.01E-01	9.64E-05
62	2.10E+03	0.350	6.54E+01	8.40E-05	125	4.44E+00	0.490	1.77E-01	9.71E-05
63	2.07E+03	0.350	6.42E+01	8.40E-05	126	4.27E+00	0.490	1.57E-01	9.79E-05
64	2.04E+03	0.350	6.30E+01	8.40E-05	127	4.16E+00	0.490	1.40E-01	9.86E-05
65	2.02E+03	0.350	6.17E+01	8.40E-05	128	4.10E+00	0.490	1.25E-01	9.93E-05
66	1.99E+03	0.350	6.05E+01	8.40E-05	129	4.06E+00	0.490	1.13E-01	1.00E-04
67	1.96E+03	0.350	5.93E+01	8.40E-05	130	4.04E+00	0.490	1.03E-01	1.01E-04
68	1.93E+03	0.350	5.81E+01	8.40E-05	131	4.02E+00	0.490	9.34E-02	1.01E-04
69	1.91E+03	0.350	5.68E+01	8.40E-05	132	4.01E+00	0.490	8.55E-02	1.02E-04
70	1.88E+03	0.350	5.56E+01	8.40E-05	133	4.01E+00	0.490	7.85E-02	1.03E-04
71	1.85E+03	0.350	5.44E+01	8.40E-05	134	4.00E+00	0.490	7.23E-02	1.03E-04
72	1.83E+03	0.350	5.32E+01	8.40E-05	135	4.00E+00	0.490	6.69E-02	1.04E-04
73	1.80E+03	0.350	5.19E+01	8.40E-05	136	4.00E+00	0.490	6.20E-02	1.05E-04
74	1.77E+03	0.350	5.07E+01	8.40E-05	137	4.00E+00	0.490	5.77E-02	1.05E-04
75	1.75E+03	0.350	4.95E+01	8.40E-05	138	4.00E+00	0.490	5.38E-02	1.06E-04
76	1.72E+03	0.350	4.83E+01	8.40E-05	139	4.00E+00	0.490	5.03E-02	1.07E-04
77	1.69E+03	0.350	4.71E+01	8.40E-05	140	4.00E+00	0.490	4.71E-02	1.07E-04
78	1.66E+03	0.350	4.59E+01	8.40E-05	141	4.00E+00	0.490	4.43E-02	1.08E-04
79	1.64E+03	0.350	4.46E+01	8.40E-05	142	4.00E+00	0.490	4.17E-02	1.08E-04
80	1.61E+03	0.350	4.34E+01	8.40E-05	143	4.00E+00	0.490	3.93E-02	1.09E-04
81	1.58E+03	0.350	4.22E+01	8.40E-05	144	4.00E+00	0.490	3.71E-02	1.09E-04
82	1.56E+03	0.350	4.10E+01	8.40E-05	145	4.00E+00	0.490	3.52E-02	1.10E-04
83	1.53E+03	0.350	3.98E+01	8.40E-05	146	4.00E+00	0.490	3.33E-02	1.11E-04
84	1.50E+03	0.350	3.86E+01	8.40E-05	147	4.00E+00	0.490	3.17E-02	1.11E-04
85	1.48E+03	0.350	3.74E+01	8.40E-05	148	4.00E+00	0.490	3.01E-02	1.12E-04
86	1.45E+03	0.350	3.62E+01	8.40E-05	149	4.00E+00	0.490	2.87E-02	1.12E-04
87	1.42E+03	0.350	3.50E+01	8.40E-05	150	4.00E+00	0.490	2.73E-02	1.13E-04

B Demolding machine design

More information regarding the design, fabrication, and operation of the demolding machine, such as solid model files, circuit diagrams, and control program files, can be obtained by contacting the author.

B.1   Manufacturer and model of major components of the demolding machine

Item	Description	Vendor	Model
Load Frame	Electromechanical load frame for force & displacement control and measurement	Instron	5869
Load Frame Controller	Interface btw. PC and load frame	Instron	Fastrac 8800
Load Cell	+/-1 kN rating	Instron	2525-806
Load Frame Adapter	Spherical seat for alignment	Instron	T1223-1059
Chiller	Circulates & controls temperature of coolant	VWR	1175MD
Solenoid Valves	Controlling coolant flow to platens	Granzow	21HN4KY160
Heater	25x75mm 730W 110V	Watlow	Ultramic CER-1-01-00007
Heater Controller	PID heater controllers with serial interface	Watlow	SD6C-HKAA-ARG
RS-485 Adapter	Communicate w/heater controller	Easysync	ESU-2002M
Heater Relay	Switching heater power for temperature control	Carlo Gavazzi	RS123A23D25
Thermocouple probes, connectors and wires	For platen temp measurement	Omega	K-type, various
Thermocouple amplifier	IC's for thermocouple signal amplification	Analog Devices	AD595C
USB Data acquisition module	4 double-ended analog inputs plus 8 digital I/O	National Instruments	NI-USB-6008

C MatLab scripts

The most important MatLab scripts used in this work are given below. Electronic copies of these scripts and attendant functions, as well as other scripts used in this work can be obtained by contacting the author.

C.1   Calculation of Material properties from Ames/Srivastava model

The elastic modulus, Poisson's ratio, and yield strength of PMMA used in many calculations in this work, as well as many of the ABAQUS simulations, are derived from the models developed by Ames [105] and Srivastava et al. [113].

```
%Script for Material Props
%From Srivastava et al, "Thermo-mechanically-coupled...spans their glass
%transition." Article in press, International Journal of Plasticity 2010.

matlist={'Z690R','PC','PMMA'};
material=matlist(1)
switch char(material)
    case 'Z690R'
        Gg=482e6;
        Gr=3.4e6;
        Mg=0.16e6;
        Mr=.034e6;
        vg=0.40;
        vr=0.49;
        ag=7e-5;
        ar=12e-5;
        Delta=2.0;
        Te=140;
        Tg=136;
        T=[25:150];
        SY=-0.0021*T.^2-0.0853*T+66.686;
    case 'PC'
        Gg=640e6;
        Gr=4.0e6;
        Mg=0.73e6;
        Mr=.017e6;
        vg=0.37;
        vr=0.49;
        ag=6.5e-5;
        ar=12e-5;
        Delta=1.6;
        Tg=145;
        Te=160;
        T=[25:160];
        SY=-0.0023*T.^2-0.005*T+74.813;
    case 'PMMA'
        Gg=300e6;
        Gr=1.4e6;
```

```
        Mg=10e6;
        Mr=.003e6;
        vg=0.35;
        vr=0.49;
        ag=7e-5;
        ar=16e-5;
        Delta=1.7;
        Tg=110; %Note: Sriviastava et al use 115, but my material has 110
        Te=160;
        T=[25:135];
        SY=0.0004*T.^2-1.2776*T+143.08;
end %switch

M(find(T<=Tg))=Mg;
M(find(T>Tg))=Mr;
G=1/2*(Gg+Gr)-1/2*(Gg-Gr)*tanh(1/Delta*(T-Tg))-M.*(T-Tg);
v=1/2*(vg+vr)-1/2*(vg-vr)*tanh(1/Delta*(T-Tg));
E=2*G.*(1+v);
a=ag;
clear Gg Gr Mg Mr M vg vr ag ar Delta matlist material
```

C.2   Conversion of raw load-displacement data files

```
%Script to import Instron *.raw files into Matlab & save
%April 2009 Matt Dirckx, modified from "xyz2mat" by Hayden Taylor

clear

%User inputs target folder
folder='foldername'

%get list of files in target folder
path=strcat('../',folder);
LS = dir(path);
filecount = size(LS);
filecount = filecount(1);

for f = 1:filecount,
    %Display files as they are processed
    LS(f).name
    %Check if file is an Instron *.raw file
    if 1 == regexp((LS(f).name),'^.*\.raw$'),

        %Fix filename to be used as a matlab variable name
        scanname = regexprep((LS(f).name),'\.raw','');
        scanname = regexprep(scanname,'-','_');
        scanname = regexprep(scanname,',','_');

        %Read data from file
        A=importdata(strcat(path,'/',LS(f).name),',',41);
        A.time=A.data(:,1);
        A.ext=A.data(:,2);
        A.load=A.data(:,3);
        A.name=scanname;
        %Assign data to a matlab variable with same name as file
        assignin('base',scanname,A);
```

```
    end;
end;

%Save data to *.mat file in target folder with same name as folder
clear scanname filecount f ans LS A
save(strcat(path,'/',folder));
clear;
display 'Done'
```

C.3   Identification of demolding events and calculation of demolding work

This script is designed to analyze a single data file, and is the most flexible since it allows the user to protect certain fields from changing. This feature is useful when, for instance, some demolding events have been identified manually. Other scripts that process batches of data are available by contacting the author.

```
%Gen 3 script for processing demolding data based on comparing local extrema

%User inputs variable name
varname='varname';
data=evalin('base',varname);

%User inputs expected number of demolding events
expect=8;

%% Protections: set flags to 1 to protect values
protectbegin=0;
protectend=0;
protecttrind=0;
internalvars=;
savedata=0;
%User sets normalize or not flag
normalize=0;
%User sets plot or not flag and plot window width
plots=1; xwindow=[-.2,10];

%% Control variables
%width of window for slope calculation
wind=10;
%threshold value of slope for beginning detection
slopethresh=2; endslopethresh=-2;
%width of window for taking mean load bias
lbwin=30;

%% Find areas of interest in data
%Note: test protocol sets ext=0 with demolding bar just below plane of tool
%surface, so embossing occurs for ext<0 and demolding occurrs for ext>0
data.pind=find(data.ext>=-1); data.nind=find(data.ext<-1);

%% Find beginning of demolding data and load bias
```

237

```matlab
%Calculate slope over a window of load data
dy=data.load(data.pind(wind:end))-data.load(data.pind(1:end-wind+1));
dx=data.ext(data.pind(wind:end))-data.ext(data.pind(1:end-wind+1));
data.slope=dy./dx;

if ~protectbegin,
    %initial guess at beginning as first large positive slope
    bgx=data.pind(find(data.slope>slopethresh,1)+round(wind/2));
    %estimate load bias at beginning and calc adjusted load
    data.lb=mean(data.load(bgx-lbwin:bgx));
    data.aload=data.load-data.lb;
    %refine beginning as last zero crossing aload prior to initial guess
    data.begin=data.pind(find(data.aload(data.pind(3):bgx)<0,1,'last')+3);
else
    bgx=data.begin;
    data.lb=mean(data.load(bgx-lbwin:bgx));
    data.aload=data.load-data.lb;
end %if
%adjust extesion zero to beginning of demolding
data.aext=data.ext-data.ext(data.begin);

%initial guess at end of demolding as last large negative slope
enx=data.pind(find(data.slope<endslopethresh,1,'last')+round(wind/2));
%%estimate load bias at ending
if (enx+lbwin) < max(size(data.load)),
    data.lb2=mean(data.load(enx:enx+lbwin));
else
    data.lb2=mean(data.load(enx:end));
end %if

%refine end as first zero crossing aload after initial guess
if ~protectend,
    data.ending=find((data.load(enx:end)-data.lb2)<0,1,'first')+enx;
end %if

%define area of interest between beginning & ending
data.hind=[data.begin:1:data.ending];

%% Find initial "sticking" load
data.stick=max(data.aload(data.nind));

%% Find demolding events
%Find local extrema
data.minind=data.hind(find(imregionalmin(data.aload(data.hind))));
data.maxind=data.hind(find(imregionalmax(data.aload(data.hind))));
neighborsize=min(max(size(data.minind)),max(size(data.maxind)))-1;

%Adjust for skipped extrema
for s=1:neighborsize
newminind(s+1)=data.minind(find(data.aext(data.minind)>data.aext(data.maxind(
    s)),1,'first'));
end %for s
data.minind=newminind;

%calculate difference between neigboring extrema
if normalize
    %normalize by magnitude of maximum
```

```matlab
    %data.neighbordif=(data.aload(data.maxind(1:neighborsize-1))-
  data.aload(data.minind(2:neighborsize)))./data.aload(data.maxind(1:neighbor
  size-1));
    %normalize by magnitude of minimum
    data.neighbordif=(data.aload(data.maxind(1:neighborsize-1))-
  data.aload(data.minind(2:neighborsize)))./data.aload(data.minind(2:neighbor
  size));
else
    %don't normalize by magnitude of maximum
    data.neighbordif=(data.aload(data.maxind(1:neighborsize-1))-
  data.aload(data.minind(2:neighborsize)));
end %if normalize

%Find largest deltas up to number of expected
[sorted,ind]=sort(data.neighbordif,'descend');
if expect>max(size(data.neighbordif))
    nchan=max(size(data.neighbordif));
else
    nchan=expect;
end %if
%assign to trough index variable
if ~protecttrind,
    data.trind=sort(data.minind(ind(1:nchan)+1));
    data.pkind=sort(data.maxind(ind(1:nchan)));
end %if

%% Caclulate demolding energies
% note: new demolding energy will be stored in field dmen

%Calculate area under each point
data.int=data.aload(1:end-1).*diff(data.ext);

%Calculate demolding energy for each trough
data.dmen=zeros(size(data.trind));
chan=1;
A=0;
B=sum(data.int(data.begin:data.trind(chan)));
C=1/2*data.aload(data.trind(chan))*data.aext(data.trind(chan));
data.dmen(chan)=A+B-C;
for chan=2:max(size(data.trind))
    A=1/2*data.aload(data.trind(chan-1))*data.aext(data.trind(chan-1));
    B=sum(data.int(data.trind(chan-1):data.trind(chan)));
    C=1/2*data.aload(data.trind(chan))*data.aext(data.trind(chan));
    data.dmen(chan)=A+B-C;
end %for

%% Plotting
if plots
    xwindow=[data.aext(data.hind(1))-.2,data.aext(data.hind(end))+.2];
    scrsz = get(0,'ScreenSize');
    figure('Position',[2*(scrsz(3)/3),1,scrsz(3)/3,3*scrsz(4)/4]);
    subplot 311
    plot(data.aext(data.pind),data.aload(data.pind),'-
  b',data.aext(data.trind),data.aload(data.trind),'om',data.aext(data.begin),
  data.aload(data.begin),'og',data.aext(bgx),data.aload(bgx),'pg',data.aext(e
  nx),data.aload(enx),'pr',data.aext(data.ending),data.aload(data.ending),'or
  ');
```

```
    title(data.name);
    xlim(xwindow);
    subplot 312
    plot(data.aext(data.minind(2:neighborsize)),data.neighbordif,'.-
  b',data.aext(data.minind(ind(1:nchan)+1)),sorted(1:nchan),'om')
    title('Load Extrema Differences')
    xlim(xwindow);
    subplot 313
    plot(data.aext(data.trind),data.dmen,'p-b');
    title('Calculated Demolding Energies');
    xlim(xwindow);
    subplot
end; %if

%% Data fields for summary variables
data.dmxt=data.aext(data.trind);
data.dmld=data.aload(data.trind);
data.pkxt=data.aext(data.pkind);
data.pkld=data.aload(data.pkind);

%% Pad data with zeros if needed
if nchan~=expect
            data.dmen=[data.dmen,zeros(1,expect-nchan)];
            data.dmxt=[data.dmxt;zeros(expect-nchan,1)];
            data.dmld=[data.dmld;zeros(expect-nchan,1)];
            data.pkxt=[data.pkxt;zeros(expect-nchan,1)];
            data.pkld=[data.pkld;zeros(expect-nchan,1)];
end %if

%Assign back to variable
if savedata,
assignin('base',varname,data);
end %if savedata
if ~internalvars,
    clear bgx chan dx dy endslopethresh enx ind lbwin neighborsize normalize;
    clear plots protectbegin protectend protecttrind s scrsz slopethresh;
    clear internalvars A B C sorted xwindow data;
end %if
```

C.4   Determining bulge height for deformed features

```
%New function to analyze zygo data and find height of deformed hump
%Takes as input a *.mat file generated by xyz2mat
%Written by Matt Dirckx Dec 2009
%Some portions adapted from height_width_calculator by Aaron Mazzeo

hold off;

%% Load file
filename='filename';
wide=1;
M=load(filename);
M=getfield(M,filename);
if wide
```

```
    Y=M(:,:,1)*1e6; %units are microns
    X=M(:,:,2)*1e6; %units are microns
    Z=M(:,:,3); %units are microns
else
    X=M(:,:,1)'*1e6; %units are microns
    Y=M(:,:,2)'*1e6; %units are microns
    Z=M(:,:,3)'; %units are microns
end %if

%% De-rotate
%find valid values of Z
valid=find(not(isnan(Z)));
Zmean=mean(Z(valid));
Zpos=find(Z>Zmean);

%De-rotate Z data about X and Y axes
Yrot=polyfit(Y(Zpos),Z(Zpos),1);
ZlevY=Z-(Y*Yrot(1)+Yrot(2));
Xrot=polyfit(X(Zpos),ZlevY(Zpos),1);
ZlevX=ZlevY-(X*Xrot(1)+Xrot(2));

%% Find level of "field" and adjust Z
Zlevpos=find(ZlevX>0);
hfield=median(ZlevX(Zlevpos));
Zlev=ZlevX-hfield;

%% Find Average heights of slices parallel to X
[sX,sY]=size(Z);
if wide
    window=639;
else
    window=479;
end %if
begin=round((sX-window)/2);
for i=1:sY
%     vX=find(not(isnan(Zlev(begin:begin+window,i))));
%     sliceav(i)=median(Zlev(vX+begin,i));
    vX=find(not(isnan(Zlev(:,i))));
    sliceav(i)=median(Zlev(vX,i));
end %for i

%% Find max slice
[maxslice,maxind]=max(sliceav);
%[hump,humpind]=max(Zlev(:,maxind));
validmax=find(~isnan(Zlev(:,maxind)));
hump2=mean(Zlev(find(Zlev(:,maxind)>mean(Zlev(validmax,maxind))),maxind))

%% Plots

%Plot X-section parallel to Y
if 1
    scrsz = get(0,'ScreenSize');
    figure('Position',[2*(scrsz(3)/3),1,scrsz(3)/3,3*scrsz(4)/4]);
    subplot 311
contourf(Y(begin:begin+window,:)',X(begin:begin+window,:)',Zlev(begin:begin+w
   indow,:)');
subplot 312
```

```
plot(Y(begin:begin+window,:),Zlev(begin:begin+window,:),'b',Y(:,1),sliceav,'g
   ',X(maxind,1),sliceav(maxind),'.r');
xlim([Y(1,1),Y(end,end)]);
subplot 313
%plot(X(:,1),Zlev(:,maxind),X(humpind,1),Zlev(humpind,maxind),'om');
plot(X(:,1),Zlev(:,maxind),[X(1,1),X(end,1)],[hump2,hump2],'r')
subplot
end
if 0
    subplot 211

    plot3(Y,X,Zlev','c');
    hold on
    plot3(X(humpind,:),Y(humpind,:),sliceav,'b','LineWidth',2);
    plot3(X(:,maxind),Y(:,maxind),Zlev(:,maxind),'r','LineWidth',2);
    hold off
    subplot 212
    plot(X(:,1),Zlev(:,maxind),X(humpind,1),Zlev(humpind,maxind),'om');
    subplot
end
```

D Experimental Materials

D.1 Part materials and sources

PMMA: Lucite CP from GEpolymershapes originally 4 ft by 8 ft sheet

PC: Polycarbonate from McMaster-Carr, originally 1 ft by 2 ft sheet.

Aluminum 6061-T6 from McMaster-Carr

Brass 360 from McMaster-Carr

D.2 Machining parameters used to produce molds

The machining parameters used to produce the molds for this study are listed in the table below. Fresh, sharp tools were used for each mold. A 3.175 mm end mill was used to face off the scale from the stock before any other operations. Finish passes of 20 μm width were used when machining the mold features, and the maximum depth of cut (vertical direction) was 100 μm.

Aluminum			
Tool Diameter (mm)	Spindle Speed (rpm)	Feedrate (mm/min)	Plunge Rate (mm/min)
3.175	50000	1000	100
1.588	50000	800	80
0.397	50000	240	24
Brass			
Tool Diameter (mm)	Spindle Speed (rpm)	Feedrate (mm/min)	Plunge Rate (mm/min)
3.175	22000	220	22
1.588	45000	220	22

D.3 List of test molds used

The table on the following page lists the molds used in this study. Additional details are available by contacting the author. *An entry of 0 for distortion limit temperature indicates that distortion was not observed at the lowest temperature tested of 25°C. An entry of "-" indicates that a mold was not evaluated for adhesion, distortion, or minimal demolding work.

Mold	Description	Dimensions — hf (μm)	wf (mm)	wc (mm)	lc (mm)	Ɗ	Ɗ	PMMA Process Window Results — Adhesion Limit	Work Limit	Minimal Distortion Limit*	PC Process Window Results — Adhesion Limit	Work Limit	Minimal Distortion Limit*
Silicon_	Silicon mold for coating studies, see section X	100	8.0	8.0	0.6	0.8775		-	-	-	-	-	-
W100A75_M	Single 75% width features in middle of mold spaced 3.2 mm	100	7.5	10.0	3.3	0.2414		-	-	-	-	-	-
W100A75_I	Interruped channel for 75% width spaced 3.2 mm	100	0.75	1.0	3.3	0.2414		80	70	0	-	-	-
W100A50_M	Single 50% width feature @ middle of mold sp. 3.2 mm	100	5.0	10.0	3.3	0.2054		-	-	-	-	-	-
W100A50_E	Two features 50% width @ edges spaced 3.2 mm	100	2.5	5.0	3.3	0.2054		60	60	-	-	-	-
SWA200E_50	Interruped channel for 50% width spaced 3.2 mm	200	0.5	1.0	3.3	0.4108		70	60	0	110	100	0
SWA200E_25	Interruped channel for 25% width spaced 3.2 mm	200	0.5	2.0	3.3	0.3387		70	60	0	120	110	0
SWA100E_50_2Xthick	As above but with double-thickness PMMA part	100	0.5	1.0	3.3	0.2054		-	60	60	-	-	-
SWA100E_50	Interruped channel for 50% width spaced 3.2 mm	100	0.5	1.0	3.3	0.2054		80	70	0	130	120	0
SWA100E_25	Interruped channel for 25% width spaced 3.2 mm	100	0.5	2.0	3.3	0.1694		90	80	60	150	140	100
SWA050E_50	Interruped channel for 50% width spaced 3.2 mm	50	0.5	1.0	3.3	0.1027		80	70	60	150	145	100
SWA050E_25	Interruped channel for 25% width spaced 3.2 mm	50	0.5	2.0	3.3	0.0847		80	80	70	150	145	110
LH200A_3.2	Three longitudinal channels 4 mm long spaced 3.2 mm	200	0.1	3.3	6.0	0.1553		90	80	60	-	-	-
LH200A_2	Five longitudinal channels 4 mm long spaced 2 mm	200	0.1	2.0	6.0	0.1611		90	80	40	-	-	-
LH100A_3.2	Three longitudinal channels 4 mm long spaced 3.2 mm	100	0.1	3.3	6.0	0.0777		90	80	70	-	-	-
LH100A_2	Five longitudinal channels 4 mm long spaced 2 mm	100	0.1	2.0	6.0	0.0805		90	80	70	-	-	-
LH050A_3.2	Three longitudinal channels 4 mm long spaced 3.2 mm	50	0.1	3.3	6.0	0.0388		100	90	70	150	145	130
LH050A_2	Five longitudinal channels 4 mm long spaced 2 mm	50	0.1	2.0	6.0	0.0403		90	80	70	150	145	130
H200E_3.2	Full-width channels spaced 3.2 mm	200	10.0	10.0	3.3	0.5549		70	60	0	-	-	-
H200E_2	Full-width channels spaced 2.0 mm	200	10.0	10.0	2.1	0.7073		70	60	0	-	-	-
H100E_3.2	Full-width channels spaced 3.2 mm	100	10.0	10.0	3.3	0.2775		80	70	0	-	-	-
H100E_2	Full-width channels spaced 2.0 mm	100	10.0	10.0	2.1	0.3536		70	60	0	-	-	-
H050E_3.2	Full-width channels spaced 3.2 mm	50	10.0	10.0	3.3	0.1387		80	60	40	-	-	-
H050E_2	Full-width channels spaced 2.0 mm	50	10.0	10.0	2.1	0.1768		70	70	40	-	-	-
H010E_3.2	Full-width channels spaced 3.2 mm	10	10.0	10.0	3.3	0.0277		100	90	-	-	-	-
AlumDens3_3.2	Full-width channels spaced 3.2 mm	100	10.0	10.0	3.3	0.2020		90	80	0	-	-	-
AlumDens3_7.5	Full-width channels spaced 7.5 mm	100	10.0	10.0	7.6	0.2020		90	60	0	-	-	-
AlumDens_2	Full-width channels spaced 2.0 mm	100	10.0	10.0	2.1	0.3536		70	60	0	-	-	-
AlumDens_1	Full-width channels spaced 1.0 mm	100	10.0	10.0	1.1	0.5441		70	60	0	-	-	-